SEMI-ANNUAL REPORT

(for January – June 1999)

Contract Number NAS5–31363

OCEAN OBSERVATIONS WITH EOS/MODIS:

Algorithm Development and Post Launch Studies

Howard R. Gordon
University of Miami
Department of Physics
Coral Gables, FL 33124

(Submitted July 15, 1999)

Semi-Annual Report (1 January – 30 June 1999) NAS5–31363

Preamble

As in earlier reports, we will continue to break our effort into six distinct units:

- Atmospheric Correction Algorithm Development
- Whitecap Correction Algorithm
- In-water Radiance Distribution
- Residual Instrument Polarization
- Pre-launch/Post-launch Atmospheric Correction Validation
- Detached Coccolith Algorithm and Post-launch Studies

This separation has been logical thus far; however, as launch of AM-1 approaches, it must be recognized that many of these activities will shift emphasis from algorithm development to validation. For example, the second, third, and fifth bullets will become almost totally validation-focussed activities in the post-launch era, providing the core of our experimental validation effort. Work under the first bullet will continue into the post-launch time frame, driven in part by algorithm deficiencies revealed as a result of validation activities.

Prior to the start of the 1999 fiscal year (FY99) we were requested to prepare a brief plan for our FY99 activities. This plan is included as **Appendix I**. The present report describes the progress made on our planned activities.

Abstract

Significant accomplishments made during the present reporting period:

- Submitted version 4 of the Water-leaving Radiance ATBD.
- Submitted version 4 of the Detached Coccolith ATBD.
- Completed analysis of a whitecap data set acquired in the Tropical Pacific. The results showed (1) the whitecap augmented reflectance in the visible for a given wind speed in the 8-12 m/s range was about 2.5 times less than that predicted by whitecap reflectance models, and (2) the augmented reflectance in the NIR (860 nm) was approximately 80% that in the visible, and only slightly dependent on the wind speed.
- Participated in pre-INDOEX and INDOEX field experiments. Obtained sun photometer and micro pulse lidar data along 55 days of ship tracks, and in-water upwelling radiance distribution data at 27 stations.

Semi-Annual Report (1 January – 30 June 1999) NAS5–31363

Atmospheric Correction Algorithm Development

As we have successfully processed SeaWiFS imagery (reformatted to MODIS) using our MODIS code, we can be assured that the implementation is correct. Thus, we focussed on ensuring the correctness of the basic correction algorithm, improving the basic algorithm to provide for an accurate correction in the presence of strongly-absorbing aerosols, and addressing several MODIS-specific issues.

1. Validate/Improve the Basic MODIS Algorithm using SeaWiFS

We will begin the algorithm validation and improvement process using SeaWiFS imagery.

a. Task Progress:

We have been processing SeaWiFS imagery using both the SeaDAS processing software and the University of Miami processing system DSP (which affords us more control over the processing). The main focus of this processing has been the development of newer versions of the algorithm, and this is discussed in a later section.

We have processed significant amounts of imagery that show that the "6-8" band selection for SeaWiFS atmospheric correction retrieves water-leaving radiances that are less noisy than the "7-8" band selection. There are several reasons why this should be true (e.g., the 7-8 algorithm requires a correction to the band 7 radiances for O_2 absorption near 759 nm, and bands 7 and 8 are closer together than bands 6 and 8 which decreases the influence of sensor noise on the choice of candidate aerosol models); however, we believe that use of the 7-8 algorithm should be continued because there is less contaminating water-leaving radiance in band 7 than in band 6. This is relevant to the MODIS algorithm in that MODIS uses bands 15 and 16, which are similar to the SeaWiFS bands 7 and 8 except that there is no O_2 correction required for MODIS.

Recently, in collaboration with R. Evans, we have started to participate in a SeaWiFS effort to understand the causes of the negative water-leaving radiances in the blue (412, 443, and 490 nm) retrieved under certain conditions. Although relatively few images have been examined, it appears that this problem is associated with one of several occurrences: (1) a very clear atmosphere; (2) absorbing aerosols; (3) Case 2 waters; and (4) very large scan (viewing) angles.

In the case of item (1) we have found instances in which the residual radiance after removal of the Rayleigh component was very small, or even negative, (i.e., $\rho_t(865) - \rho_r(865) < 0$). The most likely cause of this behavior is a radiometric calibration in band 8 (865 nm). All of the radiometric calibration efforts relating to SeaWiFS to date have assumed that there is no error in the calibration of band 8, e.g., *Gordon et al.* [1998]. This assumption means that bands 1 through 7 are calibrated *relative* to band 8. However, it is clear that a calibration error of a few % could exist in band 8. Thus, we arbitrarily assumed that SeaWiFS band 8 was calibrated 5% too low, and used the surface and atmosphere data acquired during the SeaWiFS

initialization cruise to "recalibrate" the sensor. This effort resulted in fewer negative water-leaving radiances and eliminated most instances in which $\rho_t(865) - \rho_r(865) < 0$.

In the case of item (2), we are developing new versions of the correction algorithm that will address absorbing aerosols. These are discussed in a later section.

In the case of items (3) and (4), the atmospheric correction algorithm is being applied in situations in which it was *not* designed to operated. For Case 2 waters, the "spectral optimization algorithm" described in a later section my provide a processing alternative. The large scan angle problem (item (4)) is not an issue with MODIS because of a more restricted scan and the absence of sensor tilt.

b. Anticipated Future Actions:

We will continue to test the algorithm with SeaWiFS imagery. In particular, we will continue to examine the problem of negative water-leaving radiances, and will continue work on the "spectral matching" and "spectral optimization" algorithms as described below.

c. Publications: None.

2. Implement and Test the "Spectral Matching Algorithm"

We will continue our basic study of the "spectral matching" algorithm. Unlike the basic MODIS algorithm, the spectral matching algorithm has the potential for atmospheric correction in the presence of strongly-absorbing aerosols.

a. Task Progress:

Gordon [1997] has described the difficulties of atmospheric correction in the presence of absorbing aerosols. These include the fact that (1) it is impossible to distinguish between weakly and strongly absorbing aerosol using NIR bands because the spectral variation of the aerosol reflectance there depends mostly on the aerosol's size distribution, (2) some aerosols, e.g., Saharan dust are nearly nonabsorbing in the green, red, and NIR, but absorb strongly in the blue, (3) the impact of aerosol absorption depends strongly on the aerosol's vertical distribution, and (4) the impact of aerosol absorption is most significant in the blue and blue-green bands where Rayleigh scattering is largest. These facts imply that aerosol absorption can only be ascertained through measurements in the blue region of the spectrum — precisely the region most sensitive to the water's chlorophyll concentration. Thus, atmospheric correction cannot be effected in the absence of knowledge regarding the water-leaving radiance throughout the spectrum, which requires a model of the marine reflectance as a function of the chlorophyll concentration. Such models exist (e.g., *Gordon et al.* [1988]), and have been incorporated into two atmospheric correction procedures that we refer to as the "spectral matching algorithm" and the "spectral optimization algorithm."

The spectral matching algorithm (SMA) [*Gordon, Du and Zhang*, 1997] and the spectral optimization algorithm (SOM) [*Chomko and Gordon*, 1998] have been implemented within the SeaDAS image processing

environment. Both algorithms perform atmospheric correction and retrieve water properties simultaneously, and represent a significant departure from the basic MODIS algorithm. The SOA has been tested more throughly, because we believe that it is a more versatile in the sense that it does not require accurate aerosol models to effect a correction. However, in the long run the SMA will likely be more useful in that, given realistic aerosol models, it will allow an accurate estimate of the aerosol optical thickness.

We tested the SOA using SeaWiFS imagery and compared its performance with the basic MODIS algorithm. The results are presented in detail in **Appendix II**. Briefly, the imagery used the performance of the algorithms on a turbid day followed (two days later) by a very clear day in the Middle Atlantic Bight (MAB). As the water properties were not expected to change significantly over the two-day period of the imagery (October 1998), the stability of the derived pigment concentrations over the period provided an excellent test of the algorithms. It was found that the SOA and the MODIS algorithms performed equally well on the clear day, but the SOA was considerably better on the turbid day. This leads us to believe that the SOA approach is a viable alternative to the standard MODIS algorithm. It also provides what may be a viable approach to atmospheric correction on Case 2 waters.

b. Anticipated Future Actions:

We will continue to test the SOA under a variety of conditions; however, we will also continue to develop the SMA. There are several reasons why the SMA is more desirable than the SOA: (1) the SMA is capable of retrieving the aerosol optical depth if the candidate aerosol models are realistic; (2) the SMA is capable of being incorporated into the standard MODIS algorithm (at reduced resolution) in a relatively simple manner; (3) there are situations (e.g., Saharan dust) where the SOA will not perform well because of the assumption that the index of refraction of the aerosol is independent of wavelength; (4) as realistic models of aerosols are developed, they can be incorporated into the SMA environment in a simple manner, and (5) at a minimum it will be easy to use the SMA to provide a flag within the MODIS algorithm that will signal the probable presence of absorbing aerosols, and indicate that the quality of the derived products cannot be assured. We expect the SMA to be the approach of choice for atmospheric correction in the presence of wind-blown dust.

c. Publications: None.

3. Optical Properties of Wind-Blown Dust

We need quantitative estimates of the optical properties of wind-blown dust, e.g., from Africa, to provide a proper model to effect atmospheric correction using the standard MODIS algorithm.

a. Task Progress:

The optical properties of wind-blown dust are required to effect atmospheric correction using the standard MODIS algorithm, and possibly the spectral matching algorithm as well. In collaboration with post doctoral associate Cyril Moulin, the approach we have taken for development/improvement of a wind-blown dust

model is to utilize SeaWiFS imagery acquired off the African Coast (east of the Canary Islands and west of Dakar). In this region, the dust is mixed high in the atmosphere, and the optical thickness is often very large ($\tau_a(865) \gtrsim 2$) so the marine reflectance is small compared to the reflectance of the aerosol. In this situation, small errors in the marine reflectance will have an insignificant impact on the retrieved aerosol reflectance. We used marine reflectances computed from the *Gordon et al.* [1988] semi-analytic model for the marine reflectances corresponding to the SeaWiFS monthly mean chlorophyll concentrations, and extracted aerosol reflectances

$$\rho_t(\lambda) - \rho_r(\lambda) - t(\lambda)\rho_t(\lambda) \equiv \rho_A(\lambda),$$

where the subscripts t, r, and w, refer to total, Rayleigh, and water, respectively, and t is the diffuse transmittance of the atmosphere, along a track that passed through a dust plumb of varying opacity. The desert dust model size distribution proposed by *Shettle* [1984] was combined with the imaginary part of the refractive index proposed by *Patterson* [1981] to compute the variation of $\rho_A(\lambda)$ as a function of $\rho_A(865)$, for comparison with the observed values along the track. We call this the BDS model (Background Desert Shettle). This model was found by *Moulin et al.* [1997] to fit sun photometer aerosol optical depth data better than several other popular models in the literature. We found that the fit to the spectral data was very poor. This led us to believe that the *Patterson* [1981] absorption indices are too large. We are now trying a variety of absorption indices and modifications to the *Shettle* [1984] size distribution to develop a better dust model.

We tested the efficacy of a variant of the SMA for atmospheric correction in a region off the coast of Africa that was subjected to a high concentration of Saharan dust. In this case we used the BDS model with varying concentrations of large particles, and with varying thicknesses for the aerosol layer. The results were encouraging and suggested that atmospheric correction can be effected under dust conditions with aerosol optical thicknesses at 865 nm as high as unity.

b. Anticipated Future Actions:

We will continue to refine the dust models described above with the goal that they will be available for inclusion in the MODIS correction algorithm, or its SMA variant, by the end of the next reporting period. As described above, preliminary attempts to use the BDS model in atmospherically correcting imagery off the African coast have shown considerable promise. These will continue.

We also have a unique opportunity to use SeaWiFS imagery that was acquired over the Caribbean in 1998 during particularly intense dust periods of July and August, simultaneous with our surface measurements of the aerosol vertical profile (using our MPL) and aerosol optical thickness (using a CIMEL sun/sky radiometer) made from St. Johns, VI, to validate our model for African dust.

c. Publications: None.

4. MODIS-Specific Issues

We need to address the detection and removal of thin cirrus clouds, methods for efficiently including earth-curvature effects, out-of-band corrections, BRDF effects on the diffuse transmittance, correct for polarization sensitivity of MODIS, and the efficacy of atmospheric correction for removal of the aerosol effect from the measurement of the fluorescence line height.

a. Task Progress:

We have used the MODIS relative spectral response (RSR) functions to complete the out-of-band corrections to the algorithm using the *Gordon* [1995] methodology. These will be included in the at-launch version of the algorithm.

We have included the MODIS polarization-sensitivity correction in the MODIS processing code. This task will be complete when the SBRS/MCST polarization-sensitivity data are received from MSCT.

We are working to develop a model of the subsurface BRDF. These efforts are described below (under "In-water Radiance Distribution").

b. Anticipated Future Actions:

We know that there are difficulties atmospherically correcting SeaWiFS imagery when the scan angle exceeds $\sim 50°$. Although scan angles greater than 50° comprise only a minor portion of the MODIS scan, the larger the scan angle that can be successfully corrected, the larger the base of MODIS data that will be available. The primary of cause of algorithm failure at large scan angles may be the fact that earth-curvature is ignored in the algorithm. Thus, we will investigate the requirements of including earth-curvature effects in the MODIS algorithm following the *Ding and Gordon* [1994] approach. This involves a modification of the look-up tables for the top-of-the-atmosphere contribution from Rayleigh scattering. However, before actually embarking on an implementation, we will examine SeaWiFS imagery at high latitude and large scan angle to assess the impact of neglecting earth-curvature in the algorithm.

Finally, because of uncertainty in the performance of MODIS Band 26, and because we need to assess whether our radiative transfer codes are sufficiently accurate to study removal of the aerosol effect from the measurement of the fluorescence line height, we will examine this issue and thin cirrus clouds only if time permits.

c. Publications: None.

Whitecap Correction Algorithm

As the basic objectives of the experimental portion of this task has been realized (acquiring whitecap radiometric data at sea), experimental work is being suspended until the validation phase, except insofar as the radiometer is being operated at sea when it is sufficiently important to do so, e.g., it was operated during the SeaWiFS Initialization Cruise (MOCE- 4). Our basic goal for the rest of the project is to maintain experience in operating and maintaining the instrumentation in preparation for the validation phase of the contract, and to complete the analysis of the whitecap data acquired thus far.

5. Maintaining Measurement Capability

We need to maintain our ability to make whitecap measurements.

The instrumentation and data acquisition system has been maintained and will be ready for the MODIS Initialization Cruise.

6. Reduction and Analysis of Existing Data

We need to complete the analysis of the data already acquired.

a. Task Progress:

We have concentrated on a reanalysis of the Tropical Pacific whitecap data set that was acquired in 1996. This is a unique data set, as it was acquired in the trade winds with moderately high winds (8-12 m/s) and practically unlimited fetch and duration. We developed an alternative method of analysis that we believe is more robust and provides greater confidence in the results. The complete analysis is provided as **Appendix III**. Briefly, there were two significant results that emerged:

1. The whitecap augmented reflectance in the visible for a given wind speed in the 8-12 m/s range was found to be about 2.5 times less than that predicted by whitecap reflectance models [*Gordon and Wang*, 1994; *Koepke*, 1984].

2. The augmented reflectance in the NIR (860 nm) was approximately 80% that in the visible, and dependent on the reflectance (i.e., whitecaps that were brighter in the visible showed a greater reflectance decrease in the NIR than whitecaps with low reflectance in the visible). This NIR decrease is in agreement with reflectance observations of breaking waves in the surf zone [*Frouin, Schwindling and Deschamps*, 1996] and of ship-wake foam [*Moore, Voss and Gordon*, 1998].

Last year, the SeaWiFS Project informed us that the present whitecap algorithm (See MODIS Normalized Water-leaving Radiance Algorithm Theoretical Basis Document, Version 4, April 30, 1999) was causing the atmospheric correction algorithm to fail in the South Atlantic. We provided an algorithm adjustment (based on our earlier analysis of the Tropical Pacific whitecap data), and were informed by them that the algorithm

appeared to be working much better after the adjustment. That adjustment was similar, but not identical, to the one resulting from our reanalysis.

b. Anticipated Future Actions:

We will operate the whitecap radiometer during the MODIS Initialization and Validation Cruises.

c. Publications:

Spectral Reflectance of Whitecaps: Their Contribution to Water-Leaving Radiance, K.D. Moore, K.J. Voss, and H.R. Gordon, *Jour. Geophys. Res.* (Submitted).

In-water Radiance Distribution (BRDF)

During FY '99 our objectives for this task are: maintaining experience in operating and maintaining the instrumentation in preparation for the validation phase of the contract; acquiring more field data; and using the field data to develop a model of the BRDF as a function of the solar zenith angle and the water's chlorophyll concentration.

7. Maintaining Measurement Capability

We need to maintain our ability to make BRDF measurements.

The instrumentation and data acquisition system has been maintained (actually they have been deployed in two seperate field experiments) and will be ready for the MODIS Initialization Cruise.

8. Acquisition of More Field Data

To build and thoroughly test a BRDF model, we need to acquire data over a wider range of chlorophyll concentrations.

We deployed the radiance distribution camera (RADS) during INDOEX in the Indian Ocean in February-April 1999. The data are presently being reduced to provide the BRDF as a function of chlorophyll concentration during the cruise.

9. Build a BRDF Model

We need to develop a model relating the subsurface radiance distribution (BRDF) to the chlorophyll concentration of the water.

a. Task Progress

Our efforts to model the BRDF have yet to yield an acceptable model. We started by using an ocean model developed by Morel and coworkers [*Morel and Gentili*, 1991; *Morel and Gentili*, 1993; *Morel and Gentili*, 1996; *Morel, Voss and Gentili*, 1995]. This model, although often utilized in the literature, was not capable of reproducing our measurements of the distribution of subsurface upwelling radiance $L_u(\theta, \phi)$, normalized to nadir, for a chlorophyll concentration near 0.1 mg/m^3 with an accuracy sufficient to be useful in remote sensing. We believed that the departure of the computed $L_u(\theta, \phi)$ from the experimental distribution was due to the neglect of Raman scattering. Thus we undertook a reexamination of the contribution of Raman scattering to $L_u(\theta, \phi)$ in the light of recent measurement of the absorption coefficient of pure water [*Pope and Fry*, 1997] and the spectral variation of the Raman-scattering cross section [*Bartlett et al.*, 1998]. The results of this study [*Gordon*, 1999] showed that Raman scattering made a larger contribution than expected on the basis of earlier computations [*Waters*, 1995], and that the fraction of $L_u(\theta, \phi)$ contributed by Raman scattering in the blue did not significantly decrease with increasing chlorophyll concentration. Unfortunately, accounting for the effects of Raman scattering did not significantly improve the fit of the computed $L_u(\theta, \phi)$

to the experimental data. Therefore, the deficiency of the model must be elsewhere. There are two leading candidates: (1) the scattering phase function used for the particles is unrealistic; and (2) the assumption that scalar radiative transfer theory (polarization is ignored) is adequate is not correct. A third possibility is that the measured radiances are in error due to instrument self shading.

b. Anticipated Future Actions:

The phase function used to characterize the particle scattering was actually measured *in-situ* and has long been used to characterize particle scattering in the ocean [*Petzold*, 1972]. Therefore, we are looking first toward the use of scalar radiative transfer theory in the computations. Although very few computations have been carried out in the vector mode, the errors in the radiance computed using scalar theory can be roughly the same magnitude as encountered in our modeling of the BRDF [*Kattawar and Adams*, 1989; *Kattawar and Adams*, 1990; *Kattawar, Adams and Tanis*, 1988]. Thus, before experimenting with the particle phase function, we are including polarization in our computation of both the elastic and inelastic (Raman) scattering components. When this is complete, we will test the model again against the data acquired during the SeaWiFS initialization cruise and, if successful, against the data acquired during the INDOEX cruise.

In addition, we are collaborating with J.P. Doyle at JRC, Ispra, Italy, in modeling the self-shading characteristics of our BRDF instrument (RADS). This study uses a 3-d Monte Carlo radiative transfer code to compare the radiance distribution in the presence and the absence of RADS as a function of the optical properties of the water.

Pre-launch/Post-launch Atmospheric Correction Validation

The original objectives of this task were fourfold: (1) study aerosol optical properties over the oceans to assess the applicability of the aerosol models proposed for use in the atmospheric correction algorithm; (2) measure the aerosol optical properties (including their vertical distribution) from a ship during the initialization/calibration/validation cruises; (3) determine how accurately the radiance at the top of the atmosphere can be estimated based on measurements of sky radiance and aerosol optical thickness at the sea surface (i.e., vicarious calibration); and (4) utilize data from other sensors that have achieved orbit (OCTS, POLDER, SeaWiFS ...) to validate and fine-tune the correction algorithm. We have obtained a significant amount of data toward (1), designed, constructed, or purchased, instrumentation to acquire data for (2), completed (3), and (4) was discussed under the first activity above (Atmospheric Correction Algorithm Development). Objectives for the post-launch validation phase are: maintain experience in operating and maintaining the instrumentation in preparation for the validation phase of the contract; complete analysis of data already acquired; and participate in the validation phase.

10. Maintaining Measurement Capability

We need to maintain our ability to make atmospheric measurements at sea.

a. Task Progress:

We exercised our instrumentation – sun photometers, sky radiance camera, aureole camera, and micro pulse lidar (MPL) – during the INDEOX and the pre-INDOEX Cruise aboard the RV Ron Brown. Our MPL worked well during the pre-INDOEX cruise, but failed on the last day. As there were two other MPL units on the INDOEX leg, and E.J. Welton of our group was able to keep them operating, no data were lost because of our MPL failure. The aureole camera failed because of a disfunctioning CCD array, and was lost during the entire period. The sky radiance camera did not function during pre-INDOEX, was repaired for INDOEX, but then failed again. However, little data were lost as there was only one opportunity to acquire high-quality data, which requires a clear sky at large solar zenith angles ($> 60°$).

Our CIMEL sun/sky scanning radiometer has been repaired, recalibrated, and reinstalled at Fort Jefferson in the Dry Tortugas. It is now transmitting data to the AERONET network.

b. Anticipated Future Actions:

The MPL has been sent back to the manufacturer for an upgrade of the optical design that will prevent detector damage when the laser becomes misaligned (the cause of the failure during INDOEX). The aureole camera is being repaired. We expect our measurement capability to be intact for the MODIS Initialization Cruise.

11. Complete Analysis of Existing Data

We need to complete the analysis of the data acquired previously.

Semi-Annual Report (1 January – 30 June 1999) NAS5–31363

a. Task Progress:

During much of this reporting period our personnel were at sea participating in pre-INDOEX and in INDOEX. The highest priority was collecting the data during the field experiments, and the next priority was reduction and analysis of the data that was collected. Thus, analysis of existing data was placed on the "back burner" in favor of the new data sets. Because of this, the MPL data from the INDOEX cruises has been completely reduced along with the sun photometer data.

b. Anticipated Future Actions:

We will reduce the the remaining data from INDOEX next, after which we will work on data acquired in Hawaii during the MOCE-4 cruise, in particular the sky camera and aureole data.

Two new graduate students have joined our group to take over the responsibilities of E.J. Welton and J. Ritter who have left to work at GSFC and MSFC, respectively. Graduate student David Bates has learned how to operate the CIMEL system and reinstalled this system in the Dry Tortugas. He is also learning the MPL system and will work with it when it returns from the manufacturer. Finally, he is also beginning analysis of the existing CIMEL data. Graduate student Hong Du is learning to operate the aureole system and helping in the redesign of the instrument. We are currently rebuilding this instrument to improve its operation in the field. Along with learning to operate the instrument he will be investigating what options exist for reducing this data to aerosol properties.

c. Publications:

E.J. Welton, K.J. Voss, D.L. Savoie, and J.M. Prospero, "Measurements of Aerosol Optical Depth over the North Atlantic Ocean: Correlations with Surface Aerosol Concentrations" (Under revision to *Jour. Geophys. Res.*).

J.M. Ritter and K.J. Voss, " A new instrument to measure the solar aureole from an unstable platform." (Revised to *Jour. Atmos. Ocean. Tech.*).

B. Schmid, P.B. Russell, J.M. Livingston, S. Gasso, D.A. Hegg, D.R. Collins, R.C. Flagan, J.H. Seinfeld, E. Ostrom, K.J. Noone, P.A. Durkee, H.H. Jonsson, E.J. Welton, K.J. Voss, H.R. Gordon, P. Formenti, M.O. Andreae, V.N. Kapustin, T.S. Bates, and P.K. Quinn, "Clear column closure studies of urban-marine and mineral-dust aerosols using aircraft, ship, and ground-based measurements in ACE-2," (ALPS99, 18–22 January 1999, Meribel, France).

B. Schmid, J.M. Livingston, P.B. Russell, P.A. Durkee, H.H. Jonsson, D.R. Collins, R.C. Flagan, J.H. Seinfeld, S.A. Gasso, D.A. Hegg, E. Ostrom, K.J. Noone, E.J. Welton, K.J. Voss, H.R. Gordon, P. Formenti, and M.O. Andreae, "Clear sky closure studies of lower tropospheric aerosol and water vapor during ACE-2 using airborne sun photometer, airborne in-situ, space-borne, and ground-based measurements." (Submitted to *Tellus* Special Issue on ACE-2)

E.J. Welton, K.J. Voss, H.R. Gordon, H. Maring, A. Smirnov, B. Holben, B. Schmid, J.M. Livingston, P.B. Russell, P.A. Durkee, P. Formenti, and M.O. Andreae, "Ground-based Lidar Measurements of Aerosols During ACE-2: Instrument Description, Results, and Comparisons with other Ground-based and Airborne Measurements." (Submitted to *Tellus* Special Issue on ACE-2)

12. Post-launch Validation

We will participate in MODIS post-launch validation.

a. Task Progress:

We used the MPL and in-water radaince distribution system (RADS) during pre-INDOEX and INDOEX in January-April of 1999. In this case, SeaWiFS imagery will be used as a surrogate for MODIS in the validation program. The INDOEX cruise (and the associated pre-INDOEX, or ACE cruise) offered a unique opportunity to collect aerosol optical information, satellite data (SeaWiFS), and aerosol chemistry data. The pre-INDOEX cruise went from Norfolk, VA to Cape Town, South Africa. During this cruise, we were able to sample an extensive bio-mass burning plume that extended off of Africa into the Atlantic. We obtained MPL data along the ship track, which allows us to look at the vertical distribution of the aerosols, an important piece of information for these absorbing aerosols. In addition other workers on the ship were making chemical and other optical measurements along this track.

During the INDOEX cruise the focus was on the extensive pollution plume, produced on the Indian sub-continent, which extends over the Indian Ocean. The cruise track went from the clean air in the southern portion of the Indian ocean to the polluted air near India. We were able to collect the MPL information for this whole track along with RADS data. Other researchers on the ship measured additional in-water optics and aerosol chemistry. We were also obtaining SeaWiFS LAC data. For the clear days this data will be useful to investigate the performance of the atmospheric correction algorithms for this heavily polluted environment. It will also be valuable for developing models for the aerosol pollution in a manner similar to that described for Saharan dust in Section 3.

We ended up with approximately 55 days, or about 16,000 nautical miles of MPL data. In addition we had 27 in-water radiance distribution casts, in varying water types.

b. Anticipated Future Actions:

Given our experience with the aureole system during INDOEX we have repaired the camera portion and are rebuilding much of this system to improve operation. These repairs will be done in time for an expected MODIS initialization cruise. The other major effort will be in reducing the backlog of data we have acquired during the recent cruises.

Finally we anticipate participating in the MODIS initialization cruise. The timing of this cruise will, of course, depend on the launch of TERRA.

Detached Coccolith Algorithm

The objectives of our FY 99 effort are to complete analysis of cruise work done to date, continue new field data in the Gulf of Maine and Gulf of Mexico, use these data to improve algorithm performance and to apply and validate the coccolithophore algorithm using SeaWiFS data.

13. Processing of completed pre-launch cruises

a. Task Progress:

As of June 1999, all of our 1998 pre-launch cruise data has been processed, at least to first-order. Tables of time, inherent optical properties, and apparent optical properties have been submitted to the NASA SeaBass data base. Discrete samples from the 1998 field season have been worked up, with the exception of the suspended calcite data (due to lack of available time on the Graphite Furnace Atomic Absorption Spectrometer at the University of Maine). For this current "coccolithophore season," we have completed 7 transects across the Gulf of Maine. Discrete samples for this work have yet to be processed, except for the chlorophyll a concentrations. Another 7-day pre-launch cruise has just been completed aboard the research vessel Linke, in the Gulf of Maine in which coccolith concentration, water-leaving radiance, and inherent optical properties (including acid-labile backscattering) were measured.

b. Anticipated Future Actions:

Running of the suspended calcite samples from the 1998 field season will probably be done after this busy summer field season. Discrete samples from the 1999 field season will be processed as they become available.

c. Publications:

Balch, W. M., D. Drapeau, and J. Fritz, Monsoonal forcing of calcification in the Arabian Sea, *Deep Sea Res. II.* (Accepted, in revision).

14. New field efforts

a. Task Progress:

We have 13 more days of shiptime across the Gulf of Maine in 1999. These will specifically involve sampling for coccoliths and their related backscattering. We have added a Hobi Labs Hydroscat 2 to our underway sampling system. After an initial failure of the instrument's mother board, it is now functioning. This instrument will provide an estimate of the wavelength dependence of backscattering (at 470 and 680 nm).

b. Anticipated Future Actions:

We are involved in the planning of a coccolithophore cruise south of Iceland, for either summer 2000, or 2001. Remaining discrete samples for PIC, chlorophyll, and POC will be processed.

c. Publications: None.

15. Improving algorithm performance

a. Task Progress:

A second manuscript on our Arabian Sea results is in preparation at the time of this writing. This manuscript will specifically deal with the calibration of the acid-labile backscattering vs suspended calcite relationship in this region of known coccolithophore production and sedimentation. Moreover, the first continuous record of particulate inorganic carbon and particulate organic carbon, measured over ~ 3500 kilometers of ship track, will be presented.

b. Anticipated Future Actions:

Completion of manuscript, and beginning of the Gulf of Maine algorithm work.

c. Publications:

Balch, William M., David T. Drapeau, Terry L. Cucci, and Robert D. Vaillancourt, Katherine A. Kilpatrick, Jennifer J. Fritz, Optical backscattering by calcifying algae-Separating the contribution by particulate inorganic and organic carbon fractions *J. Geophys. Res.*, **104C**, 1541-1558 (1999).

Balch, W. M., D. Drapeau, B. Bowler, and J. Fritz. Continuous measurements of calcite-dependent light scattering in the Arabian Sea. *Deep Sea Res. II.* (In Preparation).

References

Bartlett, J. S., K. J. Voss, S. Sathyendranath and A. Vodacek, Raman scattering by pure water and seawater, *Applied Optics*, *37*, 3324–3332, 1998.

Chomko, R. and H. R. Gordon, Atmospheric correction of ocean color imagery: Use of the Junge power-law aerosol size distribution with variable refractive index to handle aerosol absorption,, *Applied Optics*, *37*, 5560–5572, 1998.

Ding, K. and H. R. Gordon, Atmospheric correction of ocean color sensors: Effects of earth curvature, *Applied Optics*, *33*, 7096–7016, 1994.

Frouin, R., M. Schwindling and P. Y. Deschamps, Spectral reflectance of sea foam in the visible and near-infrared: In-situ measurements and implications for remote sensing of ocean color and aerosols, *Jour. Geophys. Res.*, *101C*, 14,361–14,371, 1996.

Gordon, H. R., Remote sensing of ocean color: a methodology for dealing with broad spectral bands and significant out-of-band response, *Applied Optics*, *34*, 8363–8374, 1995.

Gordon, H. R., Atmospheric Correction of Ocean Color Imagery in the Earth Observing System Era, *Jour. Geophys. Res.*, *102D*, 17081–17106, 1997.

Gordon, H. R., Contribution of Raman scattering to water-leaving radiance: a reexamination, *Applied Optics*, *38*, 3166–3174, 1999.

Gordon, H. R., O. B. Brown, R. H. Evans, J. W. Brown, R. C. Smith, K. S. Baker and D. K. Clark, A Semi-Analytic Radiance Model of Ocean Color, *Jour. Geophys. Res.*, *93D*, 10909–10924, 1988.

Gordon, H. R., T. Du and T. Zhang, Remote sensing of ocean color and aerosol properties: resolving the issue of aerosol absorption, *Applied Optics*, *36*, 8670–8684, 1997.

Gordon, H. R., K. J. Voss, P. V. F. Banzon, R. E. Evans, D. K. Clark, L. Koval, M. Yuen, M. Yarbrough and M. Feinholz, SeaWiFS Calibration Initialization: Preliminary Results, 1998, Ocean Optics XIV, Hawaii, HI, November 1998.

Gordon, H. R. and M. Wang, Influence of Oceanic Whitecaps on Atmospheric Correction of SeaWiFS, *Applied Optics*, *33*, 7754–7763, 1994.

Kattawar, G. W. and C. N. Adams, Stokes vector calculations of the submarine light field in an atmosphere-ocean with scattering according to a Rayleigh phase matrix: Effect of interface refractive index on radiance and polarization, *Limnology and Oceanography*, *34*, 1453–1472, 1989.

Kattawar, G. W. and C. N. Adams, Errors in radiance calculations induced by using scalar rather than Stokes vector theory in a realistic ocean atmosphere system, *Society of Photo-Optical Instrumentation Engineers, Ocean Optics X*, *1302*, 2–12, 1990.

Kattawar, G. W., C. N. Adams and F. J. Tanis, Monte Carlo Calculations of the Computed Stokes Vector for an Inhomogeneous Atmosphere-Ocean System, *Society of Photo-Optical Instrumentation Engineers, Ocean Optics IX*, *925*, 398–406, 1988.

Koepke, P., Effective Reflectance of Oceanic Whitecaps, *Applied Optics*, *23*, 1816–1824, 1984.

Moore, K. D., K. J. Voss and H. R. Gordon, Spectral reflectance of whitecaps: Instrumentation, calibration, and performance in coastal waters, *Jour. Atmos. Ocean. Tech.*, *15*, 496–509, 1998.

Morel, A. and B. Gentili, Diffuse reflectance of oceanic waters: its dependence on Sun angle as influenced by the molecular scattering contribution, *Applied Optics*, *30*, 4427–4438, 1991.

Morel, A. and B. Gentili, Diffuse reflectance of oceanic waters. II. Bidirectional aspects, *Applied Optics*, *32*, 6864–6879, 1993.

Morel, A. and B. Gentili, Diffuse reflectance of oceanic waters. III. Implication of bidirectionality for the remote sensing problem, *Applied Optics*, *35*, 4850–4862, 1996.

Morel, A., K. J. Voss and B. Gentili, Bidirectional reflectance of oceanic waters: A comparison of modeled and measured upward radiance fields, *Jour. Geophys. Res.*, *100C*, 13,143–13,150, 1995.

Moulin, C., F. Dulac, C. E. Lambert, P. Chazette, I. Jankowiak, B. Chatenet and F. Lavenu, Long-term daily monitoring of Saharan dust load over ocean using Meteosat ISCCP-B2 data 2. Accuracy of the method and validation using Sun photometer measurements, *Jour. Geophys. Res.* , *102D*, 16959–16969, 1997.

Patterson, E. M., Optical properties of crustal aerosol: relation to chemical and physical characteristics, *Jour. Geophys. Res.*, *86C*, 3236–3246, 1981.

Petzold, T. J., Volume Scattering Functions for Selected Natural Waters, 1972, Scripps Institution of Oceanography, Visibility Laboratory, San Diego, CA. 92152, SIO Ref. 72–78.

Pope, R. M. and E. S. Fry, Absorption spectrum (380-700 nm) of pure water. II. Integrating cavity measurements, *Applied Optics*, *36*, 8710–8723, 1997.

Shettle, E. P., Optical aand Radiative Properties of a Desert Dust Model, in *Proceedings of the Symposium on Radiation in the Atmosphere*, edited by G. Fiocco, pp. 74–77, A. Deepak, Hampton, VA, 1984.

Waters, K. J., Effects of Raman scattering on water-leaving radiance, *Jour. Geophys. Res.*, *100C*, 13151–13161, 1995.

Appendices

I. OCEAN OBSERVATIONS WITH EOS/MODIS Algorithm Development and Post Launch Studies: Plans for FY 99.

II. Atmospheric Correction of Ocean Color Imagery: Use of the Junge Power-Law Size Distribution.

III. Spectral Reflectance of Whitecaps: Their Contribution to Water-Leaving Radiance.

Appendix I

NASA/GSFC Contract No. NAS5-31363

OCEAN OBSERVATIONS WITH EOS/MODIS
Algorithm Development and Post Launch Studies

Howard R. Gordon
University of Miami
Department of Physics
Coral Gables, FL 33124

Plans for FY 99

Preamble

The coming Fiscal Year (1999) was to be heavily focused on validation of MODIS-derived products. However, the delay of the launch of EOS AM1 requires some modification of the plan. Our approach for the coming year is to use SeaWiFS for *validating algorithms* (rather than MODIS-derived products) in a manner similar to the way the MODIS Land and Atmospheres Groups have already been using the MAS. In addition, the delay in the launch will allow us additional time to enhance the already existing algorithms prior to launch.

We break our effort for FY 99 into five distinct (although interrelated) units:

- Atmospheric Correction Algorithm Development
- Whitecap Correction Algorithm
- In-water Radiance Distribution (BRDF)
- Pre-launch/Post-launch Atmospheric Correction Validation
- Detached Coccolith Algorithm

In what follows, it will be seen that addressing the various tasks within these units requires fundamental studies, a through examination of SeaWiFS imagery, use of SeaWiFS imagery as a tool, and a maintenance of measurement and data-analysis capability through the prelaunch era into the formal validation phase. Developing the required capability of, and experience in, processing SeaWiFS imagery will also facilitate the efficient handling of MODIS imagery (e.g., for QA) in the post-launch era.

Atmospheric Correction Algorithm Development

Objectives and Proposed Activities (FY '99)

During FY '99 there are several objectives under this task. They are focused on ensuring the correctness of the basic correction algorithm and its implementation, improving the basic algorithm to provide for an accurate correction in the presence of strongly-absorbing aerosols, and addressing several MODIS-specific issues.

1. Validate/Improve the Basic MODIS Algorithm using SeaWiFS

We will begin the algorithm validation and improvement process using SeaWiFS imagery.

As we have been able to successfully process SeaWiFS imagery (reformatted to MODIS) using our MODIS code, we can be assured that the implementation is correct. Thus, we will concentrate on the science of the correction algorithm by using SeaWiFS to validate the water-leaving radiances and indicate any potential problems and potential improvements. For example, we have found using SeaWiFS data acquired during the "initialization" cruise in January and February of 1998, that using the 670-865 nm bands (the "6-8" algorithm) resulted in a somewhat better atmospheric correction than using the 765-865 nm bands (the "7-8" algorithm). This has important implications for MODIS, because it uses an algorithm that is similar to the 7-8 algorithm in SeaWiFS. However, the SeaWiFS band at 765 nm overlaps the O_2 "A" absorption band, while the corresponding MODIS band (748 nm) avoids it. Thus, we need to know whether the better performance of the 6-8 compared to 7-8 algorithm of SeaWiFS is due to the O_2 "A" band, or a more fundamental problem that could have an impact on MODIS.

2. Implement and Test the "Spectral Matching Algorithm"

We will continue our basic study of the "spectral matching" algorithm. Unlike the basic MODIS algorithm, the spectral matching algorithm has the potential for atmospheric correction in the presence of strongly-absorbing aerosols.

The spectral matching algorithm [Gordon *et al.*, "Remote sensing ocean color and aerosol properties: resolving the issue of aerosol absorption," *Applied Optics*, **36**, 8670-8684 (1997); Chomko and Gordon, "Atmospheric correction of ocean color imagery: Use of the Junge power-law aerosol size distribution with variable refractive index to handle aerosol absorption," *Applied Optics* , **37**, 5560-5572 (1998)] has already been implemented in an image processing environment. We will test its efficacy and document its performance (compared to the basic MODIS algorithm) using SeaWiFS imagery in regions in which the aerosol properties may be highly variable on a day-to-day basis, but the water properties are reasonably stable, e.g., the Middle Atlantic Bight (MAB) or the Tropical Atlantic and Caribbean. Our focus will be as complete an assessment as possible, so a decision can be made concerning its replacement of, or inclusion in, the basic MODIS algorithm. At a minimum, it will be used to provide a flag in the MODIS algorithm that will signal the probable presence of absorbing aerosols, and indicate that the quality of the derived products cannot be assured. However, the long-term goal is that it replace the basic algorithm.

3. Optical Properties of Wind-Blown Dust

We need quantitative estimates of the optical properties of wind-blown dust, e.g., from Africa, to provide a proper model to effect atmospheric correction using the standard MODIS algorithm.

The optical properties of wind-blown dust are required to effect atmospheric correction using the standard MODIS algorithm, and possibly the spectral matching algorithm as well. We have a unique opportunity now to use SeaWiFS imagery that was acquired over the Caribbean this year's particularly intense dust periods of July and August, simultaneous with our surface measurements of the aerosol vertical profile (using LIDAR) and aerosol optical thickness (using a CIMEL sun/sky radiometer) made from St. Johns, VI, to develop a model for African dust.

4. MODIS-Specific Issues

We need to address the detection and removal of thin cirrus clouds, methods for efficiently including earth-curvature effects, out-of-band corrections, BRDF effects on the diffuse transmittance, correct for polarization sensitivity of MODIS, and the efficacy of atmospheric correction for removal of the aerosol effect from the measurement of the fluorescence line height.

Of the issues listed under this heading, the first that we will pursue is the MODIS out-of-band corrections. As we now have the MODIS relative spectral response (RSR) functions from MCST, we can complete their incorporation into the algorithms following the procedures described by Gordon (1995) ["Remote sensing of ocean color: a methodology for dealing with broad spectral bands and significant out-of-band response", *Applied Optics*, **34**, 8363-8374 (1995)].

The second is incorporating the SBRS/MCST polarization-sensitivity data into the atmospheric correction module. This will be effected as described in Gordon, *et al.*, (1997) ["Atmospheric Correction of Ocean Color Sensors: Analysis of the Effects of Residual Instrument Polarization Sensitivity," *Applied Optics*, **36**, 6938-6948 (1997)].

The third issue to be examined is the BRDF effect. As described below (In-water Radiance Distribution), we propose to use our measurements of the BRDF to develop a model that can be applied to MODIS imagery. This model will be used to address the BRDF on the diffuse transmittance.

The forth issue in importance is efficiently including earth-curvature effects in the MODIS algorithm. Following Ding and Gordon ["Atmospheric correction of ocean color sensors: Effects of earth curvature," *Applied Optics*, **33**, 7096-7106 (1994)] this will most likely be a modification of the look-up tables for the top-of-the-atmosphere contribution from Rayleigh scattering. However, before actually embarking on an implementation, we will examine SeaWiFS imagery at high latitudes to assess the impact of neglecting earth-curvature in the algorithm.

Finally, because of uncertainty in the performance of MODIS Band 26, and because we need to assess whether our radiative transfer codes are sufficiently accurate to study

removal of the aerosol effect from the measurement of the fluorescence line height, we will examine this issue and thin cirrus clouds only if time permits.

An updated Algorithm Theoretical Basis Document (ATBD) for the Normalized Water-leaving Radiance algorithm will be prepared and submitted by April 30, 1999.

Whitecap Correction Algorithm

Objectives and Proposed Activities (FY '99)

Our basic goal for the rest of the project is to maintain experience in operating and maintaining the instrumentation in preparation for the validation phase of the contract, and to complete the analysis of the whitecap data acquired thus far.

5 Maintaining Measurement Capability

We need to maintain our ability to make whitecap measurements.

The basic objectives of the experimental portion of this task has been realized (acquiring whitecap radiometric data at sea), experimental work is being suspended until the validation phase, except insofar as the radiometer is being operated at sea when it is sufficiently important to do so, e.g., it was operated during the SeaWiFS Initialization Cruise (MOCE-4). This requires personnel capable of both maintaining and operating the instrumentation.

6. Reduction and Analysis of Existing Data

We need to complete the analysis of the data already acquired.

We have a significant amount of whitecap data that is yet to be reduced and analyzed. In addition, we need to reanalyze the Tropical Pacific whitecap data because of the surprisingly low reflectance increase due to whitecaps that we measured there. This is a unique data set, as it was acquired in the trade winds with moderately high winds (8-12 m/s) and practically unlimited fetch and duration. We have now developed an alternative method of analysis that we believe is more robust and will provide greater confidence in the results. Earlier this year, the SeaWiFS Project informed us that the present whitecap algorithm was causing the atmospheric correction algorithm to fail in the South Atlantic. We provided an algorithm adjustment (based on our earlier analysis of the Tropical Pacific whitecap data), and were informed by them that the algorithm appeared to be working much better after the adjustment. This example underscores the importance of *a detailed examination of as much SeaWiFS imagery as possible prior to the launch of MODIS.*

In-water Radiance Distribution (BRDF)

Objectives and Proposed Activities (FY '99)

During FY '99 our objectives for this task are: maintaining experience in operating and maintaining the instrumentation in preparation for the validation phase of the contract; acquiring more field data; and using the field data to develop a model of the BRDF as a function of the solar zenith angle and the water's chlorophyll concentration.

7. Maintaining Measurement Capability

We need to maintain our ability to make BRDF measurements.

This requires personnel capable of both maintaining and operating the instrumentation, as well as reducing the data.

8. Acquisition of More Field Data

To build and thoroughly test a BRDF model, we need to acquire data over a wider range of chlorophyll concentrations.

We will operate the Radiance Distribution Camera System (RADS) whenever the opportunity to acquire data over a wider range of chlorophyll concentrations presents itself. For example, we plan to participate in INDOEX in the Indian Ocean in January-February 1999. This will also provide an independent data set for validation of the MODIS algorithm using SeaWIFS. We will, of course, participate in the MODIS initialization cruise.

9. Build a BRDF Model

We need to develop a model relating the subsurface radiance distribution (BRDF) to the chlorophyll concentration of the water

The data acquired during the SeaWiFS initialization cruise showed that, at a solar zenith angle of ~37° (the mean encountered during the cruise) and a chlorophyll concentration of ~ 0.1 mg/m^3 (the approximate mean encountered during the cruise), an error of ~5% in the normalized water-leaving radiance $[L_w(l)]_N$ would be made if the measurement was carried out at nadir rather than at the angle appropriate to the viewing direction of the sensor. Since most investigators are only capable of measuring the in-water upwelling radiance at nadir, direct comparison of their measurements with MODIS (or SeaWiFS) data will result in an error at, or above, the level of error that is acceptable for the MODIS product. This error can be reduced by using a model (based on the chlorophyll concentration and solar zenith angle) to either correct the nadir measurement to the appropriate viewing angle, or to correct the MODIS product to provide the normalized water-leaving radiance *at nadir*. In either case, a model is required and we propose to build one that includes both elastic and inelastic (Raman) scattering, as it is evident that a considerable portion of the radiance in the blue-green (>10%) results from inelastic processes. In addition we will compare our measurements with the f/Q model of Morel [Morel and Gentili, "Diffuse reflectance of oceanic waters. III. Implication of bidirectionality for the remote sensing problem," *Applied Optics*, **35**, 4850--4862 (1996)] (which is being used in other models in the community). Construction of such a model may require that the in-water light field be simulated with a radiative transfer code that includes polarization.

Pre-launch/Post-launch Atmospheric Correction Validation

Objectives and Proposed Activities (FY '99)

The original objectives of this task were fourfold: (1) study aerosol optical properties over the oceans to assess the applicability of the aerosol models proposed for use in the atmospheric correction algorithm; (2) measure the aerosol optical properties (including their vertical distribution) from a ship during the initialization/calibration/validation cruises; (3) determine how accurately the radiance at the top of the atmosphere can be estimated based on measurements of sky radiance and aerosol optical thickness at the sea surface (i.e., vicarious calibration); and (4) utilize data from other sensors that have achieved orbit (OCTS, POLDER, SeaWiFS ...) to validate and fine-tune the correction algorithm. We have obtained a significant amount of data toward (1), designed, constructed, or purchased, instrumentation to acquire data for (2), completed (3), and (4) was discussed under the first activity above (Atmospheric Correction Algorithm Development). Objectives for the post-launch validation phase are: maintain experience in operating and maintaining the instrumentation in preparation for the validation phase of the contract; complete analysis of data already acquired; and participate in the validation phase.

10. Maintaining Measurement Capability

We need to maintain our ability to make atmospheric measurements at sea.

This requires personnel capable of both maintaining and operating the instrumentation, as well as reducing the data. We will continue to keep the CIMEL operation in the Dry Tortugas, including the monthly maintenance checks. We plan to use the MPL, aureole camera, and sky camera during INDOEX in January-February of 1999, and during the MODIS initialization cruise.

11. Complete Analysis of Existing Data

We need to complete the analysis of the data acquired previously.

We have been operating the CIMEL instrument in the Dry Tortugas almost continuously for several years. It worked well, largely due to the diligence of E.J. Welton in maintaining the instrument and the site. However, we have only scratched the surface in the data analysis. We have only looked at a few specific time periods, and need to examine the entire record. In particular, there are several periods when African dust was known to be present, and we can study its properties using the CIMEL data. Also, we have extracted specific days of the data set, believed to be dust, marine aerosol, or nonseasalt sulfate aerosols. On these days we are running our inversion method [Wang and Gordon, "Retrieval of the Columnar Aerosol Phase Function and Single Scattering Albedo from Sky Radiance over the Ocean: Simulations," *Applied Optics*, **32**, 4598-4609 (1993)] for recovering the phase function, to compare with that used by Nakajima *et al*. ["Retrieval of the Optical Properties of Aerosols from Aureole and Extinction Data," *Applied Optics*, **22**, 2951--2959 (1983)], used in the Aeronet Network). This work will be continuing.

Aureole and sky camera data acquired during the July Hawaii criuse are being analyzed, specifically for several locations while the cruise went near the volcanic plume to look at the retrieved size distribution of particulates in the plume. The aureole and sky cameras (including the sky polarization) were also operated during the MOCE-4 cruise, and these data are in the process of being reduced and analyzed as part of the SeaWiFS initialization.

12. Post-launch Validation

We will participate in MODIS post-launch validation.

We will use the MPL, aureole camera, and sky camera during INDOEX in January-February of 1999. In this case, SeaWiFS will be a surrogate for MODIS in the algorithm validation program. We will also participate in the MODIS initialization cruise; however, its scheduling will be dependent on the MODIS launch.

Detached Coccolith Algorithm

Objectives and Proposed Activities (FY '99)

The objectives of our FY 99 effort are to complete analysis of cruise work done to date, continue new field data in the Gulf of Maine and Gulf of Mexico, use these data to improve algorithm performance and to apply and validate the coccolithophore algorithm using SeaWiFS data.

13. Processing of completed pre-launch cruises

We have been collecting data on coccolith concentrations in several pre-launch cruises per year for the past several years. Most analyses have now been performed, and post-cruise calibrations of the scattering measurements have been done (calibration standards are always run before each cruise, but periodic distilled water checks are always run, and must be checked against published values to verify calibration). While basic interpretation of the prelaunch data have been done, much more data interpretation is in order. Thus, we propose to devote half of our time in FY 99 to further reduction of the pre-launch data. This also will involve using SeaWiFS data of water-leaving radiance at 550 nm to validate the algorithm, and comparing against shipboard measurements of suspended calcite. There was a coccolithophore bloom last year in the Bering Sea, in which the coccolithophore algorithm was implemented. Due to the fact that the bloom was extremely thick, we discovered that the look-up table must be re-run in order to apply the algorithm. This is now being done.

14. New field efforts

The other half of our effort will be devoted to pre- and post-launch cruises. We have several days of pre-launch cruises in the Gulf of Maine in September and October which will also have to be processed in the coming year. In April, 1999, we have 15

days of shiptime in the Gulf of Mexico between Tampa and Progresso, Mexico. We are including water-leaving radiance in our suite of continuous measurements, as sampled from a bridge-mounted Satlantic radiance sensor. We also will have 20 days of ship time next year in the Gulf of Maine in which we will collect coccolith concentrations, suspended calcite concentrations, inherent and apparent optical measurements.

15. Improving algorithm performance

Now that SeaWiFS imagery can be run with MODIS software, we intend to compare the suspended calcite concentrations estimated from space-based measurements, with ship-board measurements. Specifically, we will begin with satellite-derived measurements from blooms, and work into nonbloom waters, in order to estimate the limits of sensitivity of the algorithm. Given that next year's Gulf of Maine cruises will be "post-launch", hopefully, we can test the algorithm without having to work through SeaWiFS. However, initial validation of the algorithms will be effected with SeaWiFS data.

An updated Algorithm Theoretical Basis Document (ATBD) for the Detached Coccolith Concentration algorithm will be prepared and submitted by April 30, 1999.

MODIS Ocean Discipline Group Validation Plan

We will provide input to a revision of the Ocean Discipline Group's validation plan by March 30, 1999. The plan will be in both narrative and viewgraph forms.

Appendix II

ATMOSPHERIC CORRECTION OF OCEAN COLOR IMAGERY: USE OF THE JUNGE POWER-LAW DISTRIBUTION

Roman M. Chomko

UNIVERSITY OF MIAMI

ATMOSPHERIC CORRECTION OF OCEAN COLOR IMAGERY: USE OF JUNGE POWER-LAW SIZE DISTRIBUTION

By

Roman M. Chomko

A DISSERTATION

Submitted to the Faculty

of the University of Miami

in partial fulfilment of the requirements for

the degree of Doctor of Philosophy

Coral Gables, Florida

May 1999

UNIVERSITY OF MIAMI

A Dissertation Presented in Partial
Fulfilment of the Requirements for the Degree
Doctor of Philosophy

ATMOSPHERIC CORRECTION OF OCEAN COLOR IMAGERY: USE OF JUNGE POWER-LAW SIZE DISTRIBUTION

Roman M. Chomko

Approved:

Howard R. Gordon Professor of Physics	Steven G. Ullmann Interim Dean of the Graduate School
Kenneth J. Voss Associate Professor of Physics	George C. Alexandrakis Professor of Physics
G. Chris Boynton Research Assistant Professor of Physics	Robert H. Evans Research Professor of Meteorology and Physical Oceanography

Roman M. Chomko (PhD, Physics)

Atmospheric Correction of Ocean Color Imagery: Use of Junge Power-Law Size Distribution (May 1999)

Abstract of a doctoral dissertation at the University of Miami.

Dissertation supervised by Professor Howard R. Gordon

No. of pages in text 123.

In this study, a new atmospheric correction algorithm capable of simultaneously retrieving aerosol and ocean optical parameters under the presence of both highly- and weakly-absorbing aerosols has been developed. It is suggested that the radiative properties of realistic aerosols can be well simulated with those resulting from the Junge power-law aerosol models. The use of the latter makes it possible to vary the atmospheric radiative properties continuously through a variation of the aerosol parameters. The atmosphere is assumed to consist of two, plane parallel and horizontally homogeneous, layers with the Fresnel reflecting bottom boundary. The radiative properties of the ocean water are assumed to be those of Case 1 waters. A system of non-linear equations is constructed for the radiances detected by a multi-band remote sensor and, is subsequently solved using non-linear optimization procedures. The algorithm's performance has been studied with simulated test data. It is shown that the aerosol single scattering albedo (ϖ_0) and the pigment concentration (C) can be excellently retrieved to within 6% and 10% respectively even under the presence of the instrument calibration errors. However, because of significant differences in the scattering phase functions for the test and power-law distributions, large error is possible in the estimate of the aerosol optical thickness. The positive results for the pigment concentration C suggest that the detailed shape of the aerosol scattering phase function is not needed for the atmospheric correction of ocean color sensors. The relevant parameters are the single scattering albedo and the relative spectral variation of the optical depth. The vertical distribution of aerosols and a spectral variation of the aerosol's refractive index have adverse effects on the accuracy of retrievals. Fortunately, these cases are easily identifiable in the course of non-linear optimization procedure as long as the data "fit" objective function S_{LSQ} becomes relatively large, i.e., 5-6%, in contrast to less than 1% in other test cases. The algorithm was incorporated into the SeaWiFS image processing system SeaDAS. The results demonstrate that the algorithm's performance is superior to the NASA Standard Atmospheric Correction algorithm. A significant advantage of the new approach is that realistic multicomponent aerosol models are not required for the retrieval of C.

TO MY FAMILY

Vita

Roman M. Chomko was born in Boryslav, Lviv region, Ukraine (former USSR), on June 11, 1970, the younger son of Mykhaylo I. Chomko and Olga M. Chomko, chemical engineers at the Farba Co. In 1977, he entered the Secondary School No. 7 which he completed in 1987 with the "silver medal". During that time he was a multiple awardee of All-Union and Republican Olympiads in Physics and Mathematics and won a valuable Grand Prize at the second All-Union Conference in Mathematics (1987) conducted by the Moscow Institute of Physics and Technology. He was admitted to the Department of Physical and Quantum Electronics of the Moscow Institute of Physics and Technology (MIPT) in Summer, 1987. During the 1989/90 period as a part of his professional experience he worked at the REMA Biomedical Engineering Co. (Ukraine) as a research assistant and later as a head of a project that dealt with the computer data storage of ACG signals. Since 1990 he resumed his studies at MIPT and got involved in his MS research project at the Institue of Radio Engineering and Electronics of the USSR Academy of Sciences. His work related to study of quantum dots and later the IR spectroscopy. He obtained his BS degree with high honors in summer, 1992 and his MS degree and Diploma with high honors in summer, 1994. During the Spring, 1993 he worked part-time at the Digital Equipment Corporation (Moscow Branch) on the project related to the VAX/VMS "All-in-One" system. From mid-1993 through summer 1994 he was invited to work part-time as the Interbank Telecommunication Administrator at the TverUniversalBank (Moscow). He came to the University of Miami, Coral Gables, Florida, in August, 1994. He worked as a Research Assistant to Prof. Howard R. Gordon on a Ph.D. project related to the remote sensing atmospheric correction algorithms from February, 1996 till his graduation in May, 1999. He received his Ph.D. in May, 1999.

Acknowledgements

I owe a debt of gratitude to my research advisor, Dr. Howard R. Gordon, for suggesting quite an exhilarative topic of my dissertation work, for his advise, unfailing enthusiasm and encouragement during my stay at the University of Miami, for providing the first class computer resources and working conditions, and for financial support through his research grants. His energy and drive kept my project going through a lot of hard times.

I would like to thank all the other members of my dissertation committee for their valuable suggestions and corrections. My special thanks go to Dr. Kenneth Voss and the entire optics group for stimulating discussions.

If it were not for our computer "guru" Marco Monti, I would probably never see the end of my Unix/VAX problems. His handy advises and uninterruptable joy made my life much easier to live through in my soundless computer cage.

I also take this opportunity to thank Mrs. Judy Mallery and Ms. Lourdes Castro for making it possible to have countless coffee breaks in the mail-room.

I wish to thank all my friends for their patience and for not laughing too loud when I should say "just another couple of days..."

Finally, I would like to thank my family to who I dedicate this dissertation. Their unconditional love, trust, support, inspiration, patience, joy of life is inexplicable.

I greatfully acknowledge the support from the National Aeronautics and Space Administration, Goddard Space Flight Center, under contracts NAS5-31363 and NAS5-31734.

I. INTRODUCTION

The subjects of the atmospheric particulate turbidity and ocean color have been receiving considerable attention recently. An impetus for the renewed interest is scientific: the role of aerosol and phytoplankton in the global carbon cycle and possibly climate.[1]

Marine phytoplankton are the microscopic single-celled ocean plants, and are at the base of the marine food chain. Phytoplankton contain chemical chlorophyll-a and other pigments that absorb light, thus, providing the energy needed for photosynthesis. The rate of photosynthesis in phytoplankton is regarded as primary productivity. The study of the primary productivity and the global distribution of phytoplankton can provide answers to its role in the global climate forcing and carbon cycle.[2,3] Phytoplankton pigments absorb light mainly in the red (670 nm) and in the blue (440 nm) range of the spectrum, and reflect the light in the green (550 nm). By measuring the light exiting the ocean in the blue and green (the "ocean color"), the phytoplankton pigment concentration can be determined (pure water reflects the light in this region of the spectrum).

The passive remote satellite sensors provide an efficient and cost-effective way to study the variation of marine phytoplankton on a global scale. The light signal at the top of the atmosphere is comprised of two parts resulting from the radiative processes within: 1) the atmosphere itself (90-100%), and 2) the ocean (0-10%). Thus, the atmospheric radiative effects need to be removed. This problem is regarded as atmospheric correction.

Atmospheric correction is complicated by many factors. Chief among them are aerosols (a suspension of fine liquid and/or solid particles in a gas). The aerosols possess not only a complicated chemical character but also diverse physical and geographical properties: shape, size distribution, time variability, location, etc.[4,5] There is no way to predict their properties *a priori*.

The proof-of-concept ocean-color mission was the Coastal Zone Color Scanner (CZCS) on Nimbus-7 (1978-1986).[6,7] It demonstrated that the concentration of marine phytoplankton could be estimated from measurements of the radiance leaving the top of the atmosphere. This led to the development of more sophisticated ocean color sensors such as the Sea-Viewing Wide-Field-of-View color sensor (SeaWiFS),[8] the moderate resolution imaging spectrometer MODIS,[9] the polarization and directionality of the earth's reflectances instrument (POLDER),[10] etc.).

The first atmospheric correction algorithm that was capable of retrieving water-leaving radiances[6,7] was developed for the Coastal Zone Color Scanner, and utilized a simple single-scattering algorithm. Gordon and Wang[11] substantially improved it later including multiple-scattering effects and was successfully applied for SeaWiFS. This algorithm provided water-leaving radiances with the required accuracy for typical marine atmospheres. It failed, however, in cases when the atmosphere contained highly absorbing aerosols.

Recently, Gordon *et al.*[12] proposed an algorithm for Case 1 waters [13] (i.e., waters whose optical properties are controlled by phytoplankton and their immediate detrital material) that worked resonably well for both weakly and highly absorbing aerosol and was able to obtain similtaneously the pigment concentration. It systematically varied the ocean pigment concentration and aerosol models, selected a pre-set number of best fits (in an r.m.s. sense) and computed the average of the model parameters taken to be the results of retrievals. The candidate models were derived from the bimodal log-normal size distributions and refractive indices provided by Shettle and Fenn[14] as a function of relative humidity. The water-leaving radiance was computed on the basis of the semianalytic radiance model of ocean color of Gordon *et al.*[15]

For the CZCS imagery correction Zhao and Nakajima[16] also proposed an algorithm that was able to determine aerosol and ocean properties similtaneously. They employed models with Junge power-law size distributions with a single index of refraction and used water-leaving ratios instead of water-leaving radiance itself. They showed good retrievals

with simulated test data created by use of bimodal aerosol size distributions with the same index of refraction and concluded that the power-law size distribution was an adequate approximation to the now favored bimodal aerosol distributions.

This dissertation extends the work of Gordon *et al.*[12] through utilizing the Junge power-law models with variable refractive index and including non-linear optimization procedures to determine similtaneously aerosol and ocean water properties. We begin in Chapter 2 with the basic description of radiative transfer through the atmosphere-ocean coupled system. Chapter 3 provides the details of the proposed atmospheric correction algorithm. The performance of the newly developed algorithm is tested with simulated data is provided in Chapter 4. This algorithm has been incorporated into the SeaDAS image processing system for SeaWiFS and the results are demonstrated in Chapter 5. Chapter 6 concludes this work. The quasi-Newton minimization theory concepts are outlined in the Appendix.

II. RADIATIVE TRANSFER IN ATMOSPHERE-OCEAN SYSTEM

In the scalar approximation (the polarization ignored), the propagation of light through the plane-parallel, horizontally homogeneous atmosphere is governed by the Radiative Transfer Equation (RTE) [17,18] :

$$\cos\theta \ \frac{dL(\tau;\theta,\phi)}{d\tau} = -L(\tau;\theta,\phi) + J(\tau;\theta,\phi), \tag{2.1}$$

where θ and ϕ are the photon's polar and azimuth angles, the optical thickness $\tau \equiv \int_0^z c(z')dz$ where $c(z')$ is the extinction coefficient of the atmosphere at the geometrical depth z (assuming that $z = 0$ at the top of the atmosphere), and $L(\tau;\theta,\phi)$ is the radiance. $J(\tau;\theta,\phi)$ is the source function defined as

$$J(\tau;\theta,\phi) = \frac{\varpi_0}{4\pi} \int_0^{\pi} d\theta' \int_0^{2\pi} d\phi' \sin\theta' \ P(\tau;\theta',\phi';\theta,\phi) \ L(\tau;\theta',\phi'), \tag{2.2}$$

where $P(\tau;\theta',\phi';\theta,\phi)$ is the single scattering phase function from the direction (θ',ϕ') to (θ,ϕ). The single scattering albedo $\varpi_0 \equiv b(\tau)/c(\tau)$, where $b(\tau)$ is the scattering coefficient of the atmosphere at the optical depth τ. In order to obtain a unique solution in the atmosphere two boundary conditions are needed: (1) at the top of the atmosphere

$$L(0;\theta,\phi) = F_0\delta(\cos\theta - \cos\theta_0)\delta(\phi - \phi_0), \quad \theta < \pi/2, \tag{2.3}$$

where F_0 is the extraterrestrial solar irradiance, θ_0 and ϕ_0 are the sun's zenith and azimuth angles respectively, and (2) at the botom of the atmosphere

$$L(\tau_1;\theta_r,\phi_r) = \int r(\theta_i,\phi_i \rightarrow \theta_r,\phi_r) \ L(\tau_1;\theta_i,\phi_i) \ d\Omega_i, \tag{2.4}$$

where subscripts "r" and "i" stand for "reflected" and "incident" respectively, and $r(\theta_i,\phi_i \rightarrow \theta_r,\phi_r)$ is the surface's bidirectional reflectance distribution function (BRDF).

To represent the *atmosphere-ocean coupled system* we adopt a widely used plane-parallel horizontally homogeneous *two-layer model* for the atmosphere with the Fresnel reflecting

bottom boundary where the top layer contains a gas of molecules (for simplicity, referred to as a "*Rayleigh layer*") and the second bottom layer contains only aerosol particles unless specified otherwise ("*aerosol layer*"). Radiance entering the ocean is backscattered into the atmosphere in accordance with the semi-analytic model of Gordon et. al.[15]

Let us introduce a dimensionless quantity named *reflectance*

$$\rho(\lambda) = \frac{\pi L(\lambda)}{F_0(\lambda)\cos\theta_0}, \tag{2.5}$$

where L is the radiance, F_0 is the extraterrestrial solar irradiance, θ_0 is the solar zenith angle, λ is the wavelength. The radiance at the top of the atmosphere (TOA) can be written then as (Figure 2.1)

$$\rho_t = \rho_r + \rho_a + \rho_{ra} + \rho_g + t\rho_w + t\rho_{wc}, \tag{2.6}$$

where ρ_t is the total reflectance measured by a remote sensor, ρ_r is the reflectance resulting from the multiple scattering by the molecular (Rayleigh) gas only (i.e., without being scattered by aerosol), ρ_a is the reflectance resulting from the multiple scattering by the aerosol only (i.e., without being scattered by Rayleigh gas), ρ_{ra} is the interaction term that represents the reflectance resulting from scattering by both Rayleigh gas and aerosol, ρ_g the reflectance resulting from the sun glitter, ρ_{wc} is the reflectance resulting from whitecaps, ρ_w is the water-leaving reflectance and, finally, t is the diffuse transmittance function of the atmosphere.

As long as the ocean color sensors are equipped with tilting mechanisms, the term ρ_g can be omitted. Assuming further that $\rho_{wc} = 0$ the Eq. (2.6) simplifies to

$$\rho_t = \rho_r + \rho_a + \rho_{ra} + t\rho_w, \tag{2.7}$$

Our objective (and that of the atmospheric correction in general) is to obtain $\rho_w(\lambda)$ from the values of $\rho_t(\lambda)$. Below, a focus will be placed upon the computational aspects of each

of the terms shown in the Eq. (2.7).

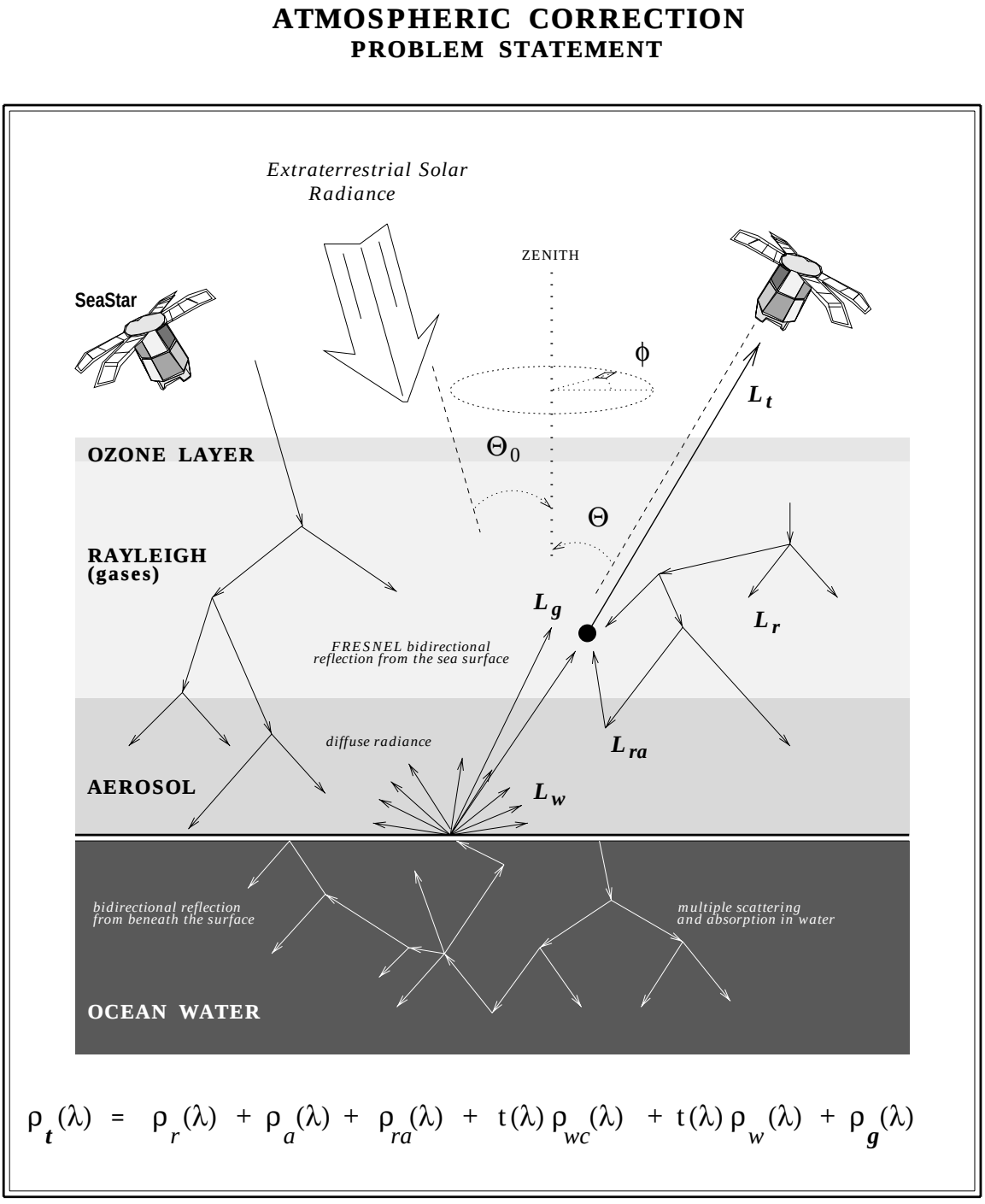

Figure 2.1. Atmospheric correction model.

Computation of $\rho_r(\lambda)$

Assuming that

- the air molecules are considered as molecules of a single gas;

- the scattering coefficient per unit mass of the air molecules κ_{air} and the acceleration of gravity g do not vary with the height;

- the molecular weight fraction of various atmospheric air molecules does not vary with the height,

a simple expression for the optical thickness τ_r may be obtained as the function of the optical thickness τ_{r0} corresponding to the standard surface pressure $P_0 = 1013.25$ mb and the ambient pressure P

$$\tau_r = \tau_{r0} \frac{P}{P_0}, \tag{2.8}$$

Hansen and Travis further derive an empirical relationship for τ_{r0} at STP:

$$\tau_{r0} = 0.008569\ \lambda^{-4}\ (1 + 0.0113\ \lambda^{-2} + 0.00013\ \lambda^{-4}), \tag{2.9}$$

where λ is the wavelength in [μm]. It should be noted, however, that more accurate computations may be performed without making the above assumptions,[19] but the deviation of the optical thicknesses of the Rayleigh gas for the atmospheric conditions provided by in the "U.S. Standard Atmosphere Supplements, 1976" [20,21] never exceeded 1% comparatively to those obtained with the equations (2.8)-(2.9) . Figure 2.2 demonstrates the results of the similar computations.

In the absence of the polarization of the incident radiation and the molecular anisotropy, the angular distribution of the light scattered by the molecular gas is given by the Rayleigh phase function $P(\Theta)$

$$P(\Theta) = 3/4\ (1 + \cos^2(\Theta)), \tag{2.10}$$

where Θ is the scattering angle.

For a given sun-viewing geometry, θ_0, θ and the ambient pressure P, Gordon *et al.*[22] show that the Rayleigh reflectance $\rho_r(\lambda)$ in the visible and near-infrared can be computed through

$$\rho_r(\lambda;\theta,\theta_0,\Delta\phi) = \frac{1-\exp(-\tau_r(\lambda)/\cos\theta)}{1-\exp(-\tau_{r0}(\lambda)/\cos\theta)}\rho_{r0}(\lambda;\theta,\theta_0,\Delta\phi), \tag{2.11}$$

where $\rho_{r0}(\lambda;\theta,\theta_0,\Delta\phi)$ is the reflectance of the Rayleigh gas at STP, and $\Delta\phi$ is the viewing azimuth angle relative to the sun.

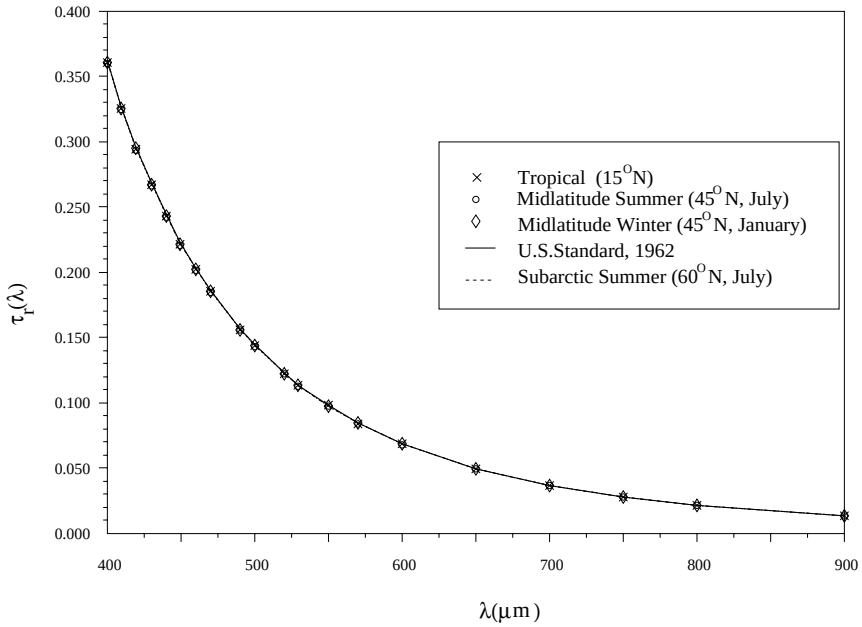

Figure 2.2 Rayleigh optical thickness $\tau_r(\lambda)$ for the U.S. Standard 1976 and four Supplements 1976 atmospheres

The Eqs. (2.8) - (2.11) along with the Radiative Transfer equation constitute a complete set of equations sufficient to determine the radiative properties and the reflectance $\rho_r(\lambda)$ of the Rayleigh gas. It is worth pointing out that the impact of the Rayleigh gas reflectance $\rho_r(\lambda)$ on the resulting total reflectance at the TOA, $\rho_t(\lambda)$, decreases rapidly from the blue to the near infrared (NIR) spectral range, more specifically, $\rho_r(\text{NIR})$ comprises just about

30-40% of ρ_t(NIR) depending mostly on the sun-viewing geometry, in contrast to 70-80% in the blue.

Computation of $\rho_a(\lambda) + \rho_{ra}(\lambda)$

The aerosol is composed of particles of extremely complex physical and chemical properties that depend on many factors like the aerosol origin, location, the time of a day, the wind speed, humidity, etc. They come in different shapes, forms and sizes. Their total unpredictability makes the problem of the atmospheric correction nearly untreatable.

We start with a simplification that the particulates are uniform spheres which is a valid assumption for the pure water aerosols found in abundance over large bodies of water, like, oceans. The theory of the scattering of electro-magnetic plane waves from dielectric spheres was originally developed by Mie[23] in 1908. More modern treatments of the theory along with further developments are given by van de Hulst[18] and Kerker.[24] The theory for the electro-magnetic scattering from spheroidal particles is provided by Mishchenko.[25]

In this work, we will adopt the Mie theory in the development of the atmospheric correction algorithm. There exists an extensive list of literature on the subject of the Mie theory, hence, below we provide only those properties that are directly used in the development of our algorithm.

The aerosol is characterized by its *index of refraction*

$$m(\lambda) = m_r(\lambda) - im_i(\lambda), \tag{2.12}$$

where $m_r(\lambda)$ and $m_i(\lambda)$ are respectively the real and imaginary part of the index of refraction. D'Almeida, Koepke and Shettle [4] provide the refractive indexes for the most common aerosols. They are partially reproduced in the form of a diagram in the Fig. 2.3.

It can be observed that the imaginary part $m_i(\lambda)$ of the index of refraction of water-soluble and dust aerosols have only a slight dependence on the wavelength, while the rest

are strongly dependent on the wavelength. Note, however, that neither oceanic (or sea-salt) nor sulfate (mostly existing over land) aerosol is ever found in its "pure" form and come as a mixture of various aerosols (for example, the *maritime* aerosol consists of 99%, by number, of the water-soluble and 1% of the oceanic components as defined by Shettle and Fenn[14]). In the atmospheric correction, we will make the assumption that the refractive

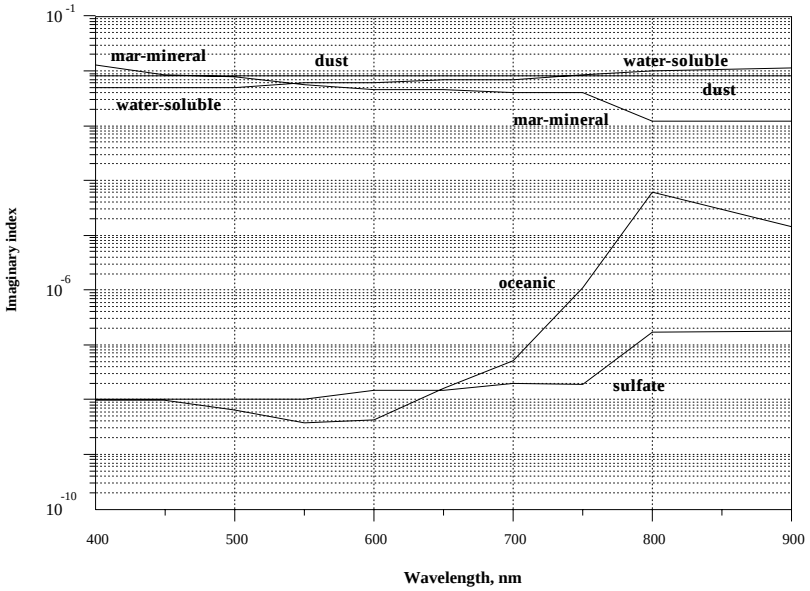

Figure 2.3. Imaginary part of the index of refraction $m_i(\lambda)$ for selected aerosols: water-soluble, dust, oceanic, maritime-mineral, sulfate. Based on the data provided by d'Almeida, Koepke and Shettle, 1991

index is independent of the wavelength.

Another aspect that determines the optical properties of aerosols is the spectrum of particle sizes. The smallest particles (typically called *Aitken nuclei*) range in size from $10^{-3}\mu$m to $10^{-1}\mu$m and have a little effect on the optical phenomena. The *condensation nuclei* or large particles are important, on the other hand. They range in size from $10^{-1}\mu$m to 1 μm. *Giant particles* are those greater then 1 μm in radius (see, Elterman[26,27] for the detailed classification). Deirmendjan (1960)[28] parameterized the aerosol size distribution

with the following equation

$$n(D) = \frac{dN(D)}{dD} = aD^{\alpha}e^{-bD^{\gamma}}, \tag{2.13}$$

where $n(D)$ is the size frequency at the diameter D, $dN(D)$ is the number of particles with diameters between D and $D + dD$ and a, α, b, and γ are positive constants determined by the type of the aerosol. Besides the fact that the parameters in (2.13) had a readily interpretable physical meaning, they fit fairly well with measurements on natural water clouds and aerosols. However, we will adopt another parameterization that proves to be convenient when dealing with aerosols that are a mixture of different types of aerosols, or *modes*: the *log-normal size distribution*

$$n(D) = \sum_{i=1}^{M} n_i(D), \tag{2.14}$$

where $n_i(D)$ is the size frequency at the diameter D for the i's component (mode) of the size distribution and M is the total number of modes. For the individual component $n_i(D)$ we have

$$n_i(D) = \frac{N_i}{\log_e(10)\sqrt{2\pi}\sigma_i D} \exp\left(-\frac{\log_{10}(D/D_i)}{2\sigma_i}\right), \tag{2.15}$$

where σ_i is the standard deviation, N_i is the total number density of the ith component, D_i is the mode's diameter. On the basis of the Eq. (2.15) Shettle and Fenn[14] and later d'Almeida, Koepke and Shettle[4] developed an extensive number of aerosol models having optical properties encountered under realistic conditions (some of them will be considered in later chapters in more detail). Having derived the scattering σ_{sca} and absorption σ_{abs} cross-sections from the Mie theory for individual particles of the diameter D, we can further compute quantities that directly govern the radiative transfer such as the scattering and absorption coefficients, k_{sca} and k_{abs}, respectively (note that the total extinction coefficients is defined to be the sum $k_{ext} = k_{sca} + k_{abs} \equiv c$), e.g.,

$$k_{sca} = \int_{D_1}^{D_2} \sigma_{sca}(D)n(D)dD, \tag{2.16}$$

where we explicitly restricted the range of diameters from D_1 to D_2 in the light of the above discussion. The coefficients k_{abs} and k_{ext} are defined by the similar expressions. The

single-scattering albedo (representing the fraction of the radiance removed from a beam of light by scattering) follows immediately from k-coefficients

$$\varpi_0 = k_{sca}/k_{ext}, \tag{2.17}$$

Figures 2.4 and 2.5 provide the single-scattering albedo $\varpi_0(\lambda)$ and the extinction coefficient $k_{ext}(\lambda)$ as the function of wavelength λ. These diagrams reveal a remarkable features of functional behaviours of $\varpi_0(\lambda)$ and $k_{ext}(\lambda)$. They are very smooth functions of the argument λ, and in particular, $k_{ext}(\lambda)$ demonstrates apparent log-linear relationship over the spectral range $400 - 900$ nm.

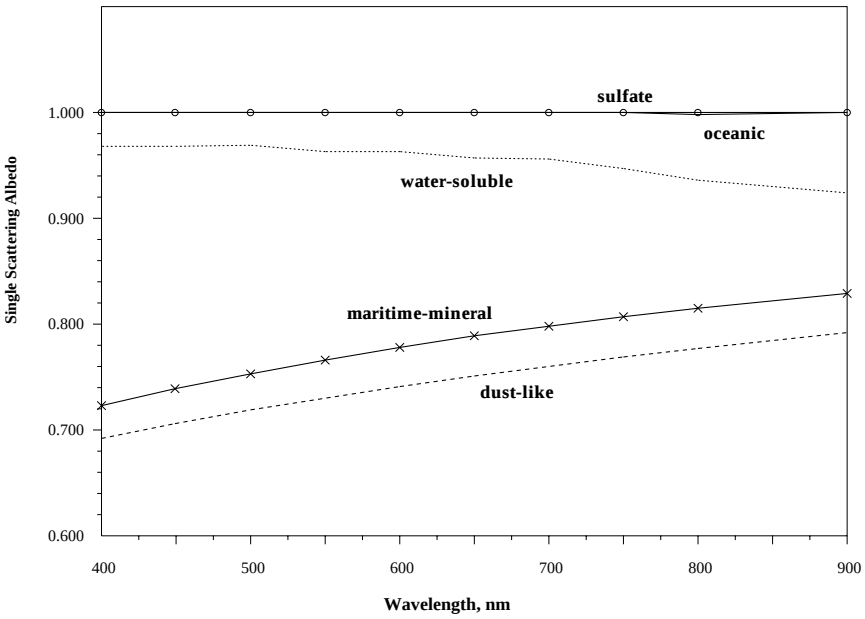

Figure 2.4 Single-scattering albedo $\varpi_0(\lambda)$ as the function of wavelength λ [μm], for selected aerosols: water-soluble, dust, oceanic, maritime-mineral, sulfate. Based on the data provided by d'Almeida, Koepke and Shettle, 1991

The angular distribution of the scattered light is called the phase function $P(\Theta)$, where Θ is the scattering angle. It is also computed from Mie theory in a manner similar to

k_{sca} in the Eq.(2.16). Examples of $P(\Theta)$ are provided in the next chapter. These optical

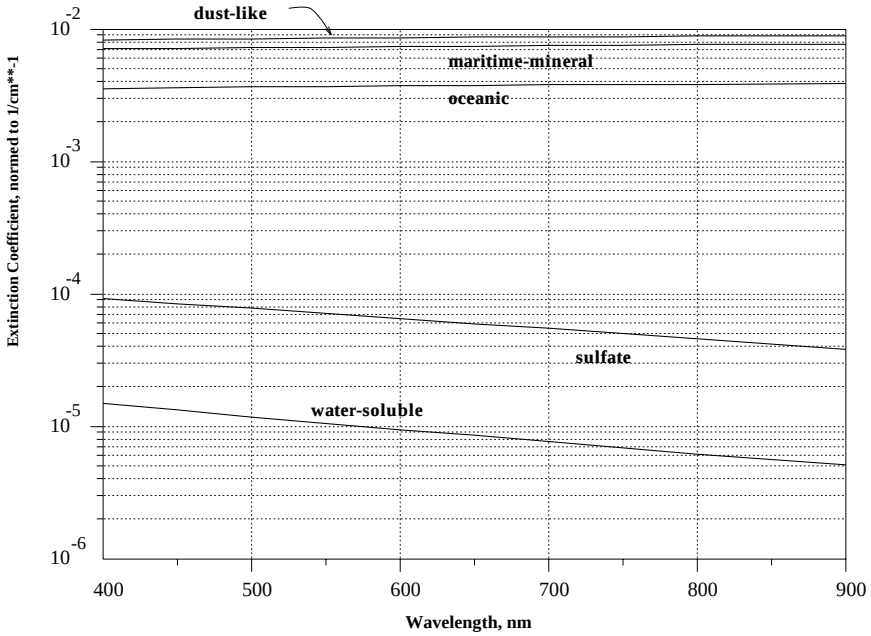

Figure 2.5 Extinction coefficient $k_{ext}(\lambda)$ as the function of wavelength λ [μm], for selected aerosols: water-soluble, dust, oceanic, maritime-mineral, sulfate. Based on the data provided by d'Almeida, Koepke and Shettle, 1991

parameters, k_{ext}, ϖ_0, and $P(\Theta)$ provide sufficient information to solve the radiative transfer equation (RTE) within the atmosphere for $\rho_a + \rho_{ra}$. Once computations of $\rho_a + \rho_{ra}$ are carried out for discrete values of $\theta, \theta_0, \Delta\phi$, and τ_a, it is necessary to make some approximations in order to interpolate between computed values in an image processing environment. In our work we extensively use the approach outlined by Gordon and Wang.[11] In particular, they have shown that the sum of the terms $\rho_a(\lambda) + \rho_{ra}(\lambda)$ at a given sun-viewing geometry is a smooth function of the aerosol optical thickness τ_a (Figure 2.6 demonstrates such a relationship for four of Shettle and Fenn's Maritime (M80), Tropospheric (T80), Coastal (C80), and Urban (U80) aerosol models, all at the relative humidity 80%) and can be adequately described by the four coefficients a, b, c, d as

$$\rho_a(\lambda) + \rho_{ra}(\lambda) = a(\lambda)\ \tau_a(\lambda) + b(\lambda)\ \tau_a^2(\lambda) + c(\lambda)\ \tau_a^3(\lambda) + d(\lambda)\ \tau_a^4(\lambda), \qquad (2.18)$$

Those coefficients are stored in the form of look-up tables (LUT). We will return to this

issue in later chapters where a further storage reduction technique is described in more detail. We conclude this subsection with a note that the dependence of $\rho_a(\lambda) + \rho_{ra}(\lambda)$ on

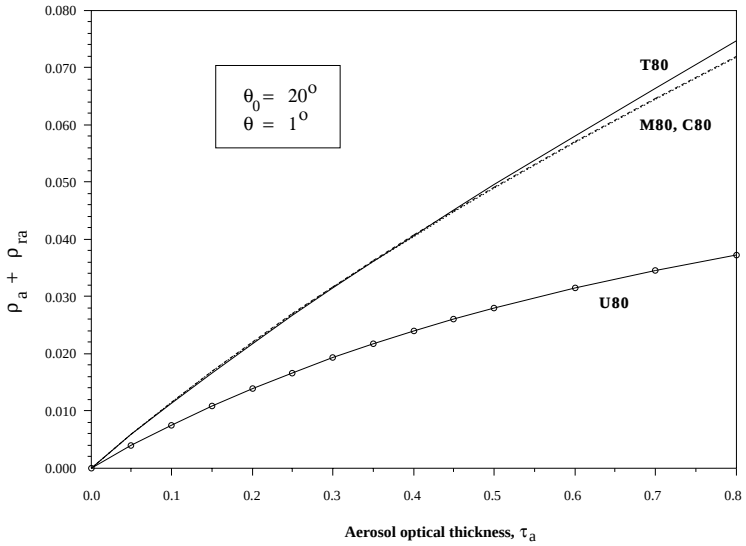

Figure 2.6 Reflectance $\rho_a(\lambda) + \rho_{ra}(\lambda)$ as a function of the aerosol optical thickness τ_a for the solar zenith angle $\theta_0 = 20°$ and viewing angle $\theta = 1°$. Based on the RTE computations

$\tau_r(\lambda)$ through the $\tau_r(\lambda)$ dependence on pressure is extremely small and is neglected.[29]

Computation of the diffuse transmittance $t(\lambda)$

The water-leaving radiance $L_w^{TOA}(\hat{\xi}_v)$ at the top of the atmosphere (TOA) is related to the water-leaving radiance $L_w(\hat{\xi}_v)$ at the bottom of the atmosphere through the diffuse transmittance $t(\hat{\xi}_v)$ function defined as

$$t(\hat{\xi}_v) = \frac{L_w^{TOA}(\hat{\xi}_v)}{L_w(\hat{\xi}_v)}, \tag{2.19}$$

where $\hat{\xi}_v$ is a unit vector directed from the sea-surface to a sensor and $L_w(\hat{\xi}_v)$ is the water-leaving radiance just above the sea-surface. While $t(\hat{\xi}_v)$ is a weak function of the aerosol radiative properties, its impact, generally speaking, cannot be neglected. It also has been shown[30] that $t(\hat{\xi}_v)$ is a function of the angular water-leaving radiance distribution. In this work, two assumptions have been examined:

1. The aerosol influence on $t(\hat{\xi}_v)$ is ignored and the water-leaving radiance just beneath the sea surface is uniform, and

2. The aerosol influence on $t(\hat{\xi}_v)$ is included.

Assumption 1 leads to a simple relation for $t(\hat{\xi}_v)$ empirically derived by Gordon and Clark.[31]

$$t(\lambda) \cong \exp\left[-\left(\frac{\tau_r(\lambda)}{2} + \tau_{Oz}\right)\left(\frac{1}{\cos\theta_0} + \frac{1}{\cos\theta_v}\right)\right], \tag{2.20}$$

where $\tau_r(\lambda)$ is the Rayleigh optical thickness, θ_0 and θ_v are the solar zenith angle and the sensor viewing angle with respect to the zenith, $\tau_{Oz}(\lambda)$ is the optical thickness of the ozone layer located just above the Rayleigh layer on TOA.

Computations of the diffuse transmittance $t(\hat{\xi}_v)$ under the Assumption 2 are more involved. Yang and Gordon (1998) replace (2.20) by

$$t(\hat{\xi}_v) = A(\theta_v)\, e^{-B(\theta_v)}, \tag{2.21}$$

where $A(\theta_v)$ and $B(\theta_v)$ are coefficients resulting from a fit to directly computed values of $t(\hat{\xi}_v)$. Note that these coefficients are the functions of the sensor polar angle only. Further, if the aerosol is non-absorbing, $t(\hat{\xi}_v)$ is only a weak function of the aerosol optical thickness τ_a, and independent of the aerosol vertical structure, and if the aerosol is absorbing $t(\hat{\xi}_v)$ is still independent of the aerosol vertical structure. In this work, Eq.(2.21) is used. This means we include no coupling of the ocean and atmosphere through $t(\lambda)$, and no bidirectional effects of $L_w(\hat{\xi}_v)$ on $t(\lambda)$.

Computation of the water-leaving reflectance $\rho_w(\lambda)$

Gordon *et al.*[15,31] defined the normalized water-leaving reflectance as

$$[\rho_w]_N = \left[\frac{\pi(1-\rho)(1-\overline{\rho})R}{m^2 Q(1-rR)}\right], \tag{2.22}$$

where ρ is the Fresnel reflectance of the sea surface for normal incidence; $\overline{\rho}$ is the Fresnel reflection albedo of the sea surface for irradiance from the Sun and sky; R is the irradiance

reflectance just beneath the sea surface ($R = E_u/E_d$, where E_u and E_d are the upwelling and downwelling irradiances just beneath the sea surface respectively); m is the index of refraction of water; and Q is the ratio of the upwelling radiance (at nadir) to the upwelling irradiance toward the zenith (Q equals π for a totally diffuse radiance distribution); r is the water-air interface reflectance for totally diffuse irradiance.

We will consider briefly the ocean optical properties for Case 1 waters only,[32–34] i.e., waters whose optical properties are controlled by phytoplankton and their immediate

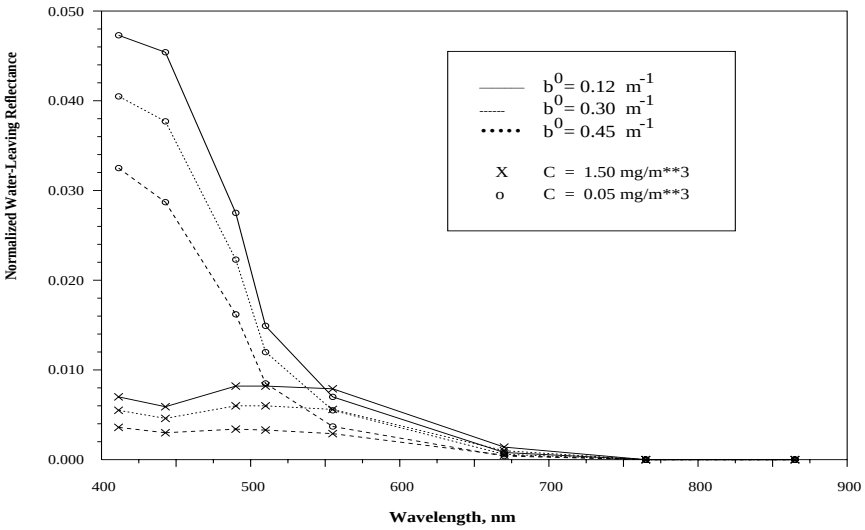

Figure 2.7 Normalized water-leaving reflectance $L_w(\lambda)$ as the function of wavelength λ [μm] for two pigment pigment concentrations 0.05 and 1.0 mg/m^3, and three values of the scattering parameter b^0: 0.12, 0.30, 0.45 m^{-1}.

detrital material. According to the bio-optical model developed by Gordon et al.,[15] ρ_w can be computed from two parameters: b^0 relating the scattering coefficient to the pigment concentration, and the pigment concentration itself (pigment concentration is defined as the sum of the concentrations of chlorophyll a and phaeophytin a). The value of b^0 was empirically determined[34] to be in the range from 0.12 to 0.45 m^{-1} having the average value of 0.30 m^{-1} for the pigment concentration C ranging from 0.05 mg/m^3 to 10 mg/m^3 for Case 1 waters. The Figure 2.7 provides sample computations of the normalized water-

leaving reflectance for pigment concentrations 0.05 mg/m^3, 1.0 mg/m^3 and three values of the scattering parameter b^0. Note the strong dependence of $[\rho_w]_N$ on C.

III. SPECTRUM OPTIMIZATION ATMOSPHERIC CORRECTION ALGORITHM

Of all developed aerosol models for spherically shaped particulates the Junge power-law aerosol models are the simplest, and are described by the size distribution

$$\frac{dN}{dD} = \begin{cases} K & , \quad D_0 < D \leq D_1 \\ K\ (D_1/D)^{\nu+1} & , \quad D_1 < D \leq D_2 \\ 0 & , \quad D \leq D_0, D > D_2 \end{cases} \tag{3.1}$$

where dN is the number of particles per unit volume with diameters between D and $D+dD$, K is the normalization constant such that $\int_0^\infty dN = 1$. It is sometimes more convenient to use the so called volume size distribution $dV(D)$ that can be obtained from the particle size distribution through the transformation of variables

$$dV(\ln D) = \frac{\pi}{6} D^3 dN(D), \tag{3.2}$$

Shown in the Fig. 3.1 are the volume size distributions for $\nu = 2.0, 3.0, 4.0$

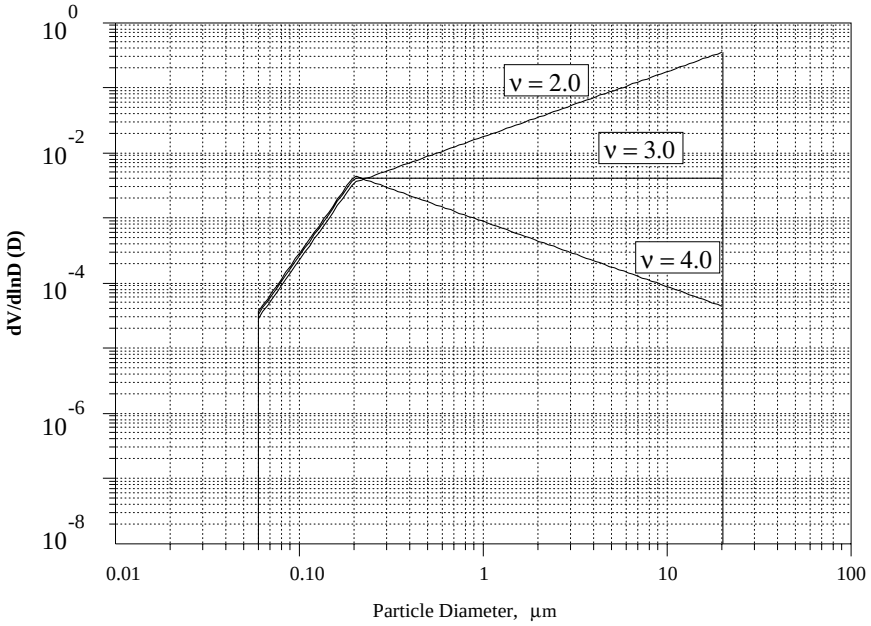

Figure 3.1. Volume size distribution for the Junge power-law aerosols with $\nu = 2.0, 3.0, 4.0$.

An outstanding feature of Junge power-law size distributions is that all their optical properties are controlled by just one parameter, ν. Van de Hulst[18] shows that if the particle refractive index is independent of λ, $D_1 = 0$ and $D_2 = \infty$, then $k_{ext} \propto \lambda^{-2+\nu}$ and, ϖ and $P(\Theta)$ are independent of λ. For the values of D_0, D_1 and D_2 used here, these facts are still approximately true. Figure 3.2 demonstrates the fraction of the extinction coefficients $c(\lambda)/c(\lambda = 865 \text{ nm})$ as the function of wavelength ($c \equiv k_{ext}$). Curves corresponding to different parameters of ν are easily identifiable and, in fact, are almost independent of the refractive index $m(m_r, m_i)$. Independent of the refractive index is also the amount of forward scattering as can be seen from Fig. 3.3. The amount of backward scattering is a strong function of the imaginary part m_i of the index of refraction m. As expected, the shape of the phase function $P(\Theta)$ doesn't vary much with wavelength (up to 30% at 120°).

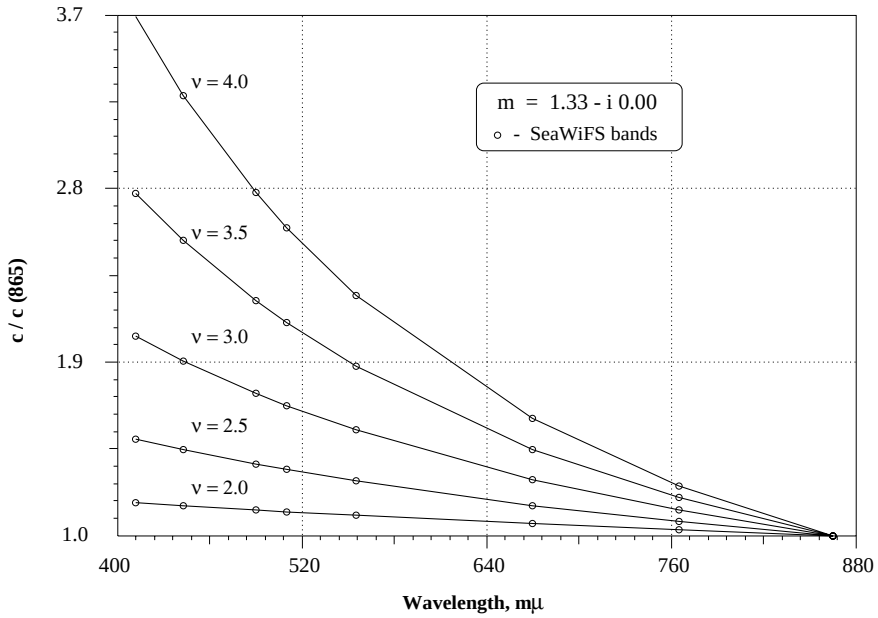

Figure 3.2. The fraction $c(\lambda)/c(865)$ as the function of wavelength for the Junge power-law aerosols with $\nu = 2.0(0.5)4.0$.

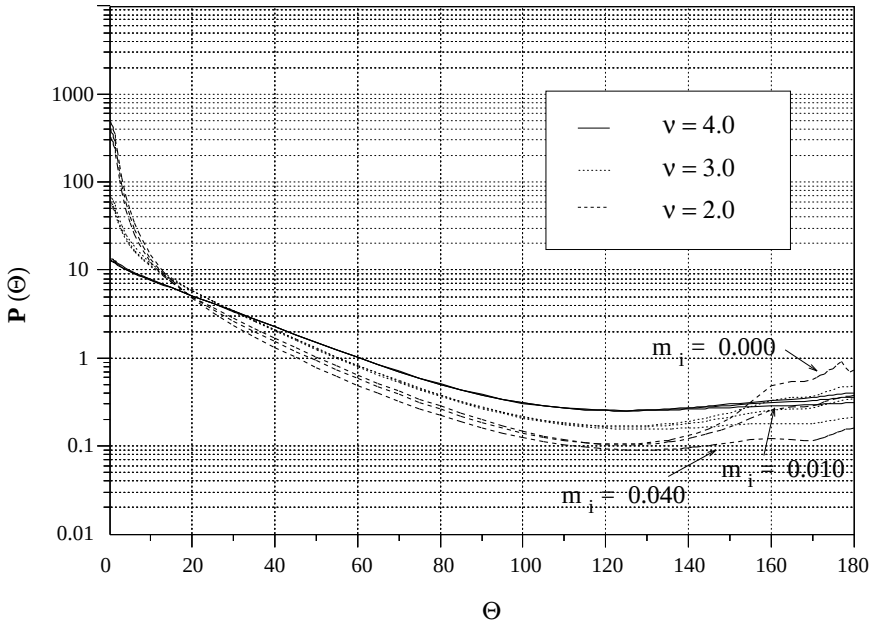

Figure 3.3. The scattering phase function $P(\Theta)$ as the function of the scattering angle Θ for the Junge power-law aerosols with $\nu = 2.0, 3.0, 4.0$ and selected m_i at $\lambda = 865$ nm.

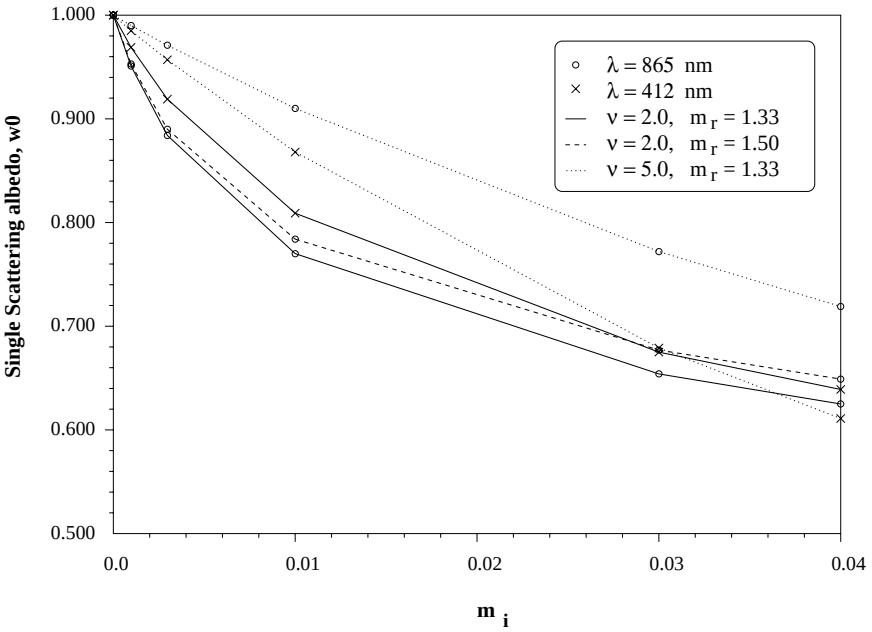

Figure 3.4. The single scattering albedo ϖ_0 as the function of the imaginary part of the index of refraction m_i for the Junge power-law aerosols with selected parameters of λ, ν and m_r.

Far more complex (see Fig. 3.3) is the behaviour of the single scattering albedo ϖ_0 on its parameters. The strongest variation appears to be with the imaginary part of the index of refraction m_i, in fact, it is an exponentially decreasing function of m_i and a weak function of the real part m_r of m. At higher m_i the single scattering albedo becomes a strong function of wavelength. The dependence on ν is moderately strong and highly non-linear.

In the Chapter 2 we have made a note of a smooth, almost linear, behaviour of the reflection function $\rho_a(\lambda) + \rho_{ra}(\lambda)$ on the aerosol optical thickness τ_a (see Eq. (2.15)). The purpose of the thesis is to exploit this property utilizing Junge power-law size distributions described above. We begin with the following

> **Proposition.** A reflectance field $\rho_t(\lambda) - \rho_r(\lambda)$ produced by essentially *any* aerosol and any ocean Case 1 waters can be adequately regenerated by the reflectance field resulting from the Junge power-law model aerosols described by a set of parameters $\{\nu, m_r, m_i; \tau_a\}$ and the ocean bio-optical model described by a set of parameters $\{C, b^0\}$. Furthermore, this set of values $\{\nu, m_r, m_i, \tau_a, C, b^0\}$ is unique.

If the above conjecture is true, and the parameters are obtained one way or another, we end up having a set of useful aerosol and ocean water characteristics. We now study this proposition using simulations.

Let us introduce some simplifying notation:

$$\begin{aligned} \rho_A(\lambda_j;\ \nu, m_r, m_i, \tau_a) &\equiv \rho_a(\lambda_j;\ \nu, m_r, m_i, \tau_a) + \rho_{ra}(\lambda_j;\ \nu, m_r, m_i, \tau_a), \\ \rho_{aW}(\lambda_j;\ C, b^0) &\equiv t^*(\lambda_j;\ \nu, m_r, m_i, \tau_a)\ \rho_w(\lambda_j;\ C, b^0), \\ \rho_W(\lambda_j;\ C, b^0) &\equiv t(\lambda_j)\ \rho_w(\lambda_j;\ C, b^0), \end{aligned} \tag{3.3}$$

where $t^*(\lambda_j;\ \nu, m_r, m_i, \tau_a)$ and $t(\lambda_j)$ are the diffuse transmittance functions in the sense of equations (2.21) and (2.20) respectively, $\rho_w(\lambda_j;\ C, b^0)$ is the water-leaving reflectance.

Typically, ocean color sensors measure the radiance in a finite number N of pre-selected spectral bands (the SeaWiFS color sensor, for instance, is supplied with N=8 bands in the visible and NIR spectral ranges). In general, N non-linear equations in the six variables $\{\nu, m_r, m_i, \tau_a, C, b^0\}$ can be written for N bands (see, Eq. (2.4):

$$\begin{aligned}
\rho_A(\lambda_1;\ \nu, m_r, m_i, \tau_a) + \rho_{aW}(\lambda_1;\ C, b^0) &= \rho_t(\lambda_1) - \rho_r(\lambda_1), \\
\rho_A(\lambda_2;\ \nu, m_r, m_i, \tau_a) + \rho_{aW}(\lambda_2;\ C, b^0) &= \rho_t(\lambda_2) - \rho_r(\lambda_2), \\
&\cdots\cdots\cdots\cdots\cdots\cdots \\
\rho_A(\lambda_N;\ \nu, m_r, m_i, \tau_a) + \rho_{aW}(\lambda_N;\ C, b^0) &= \rho_t(\lambda_N) - \rho_r(\lambda_N).
\end{aligned} \tag{3.4}$$

Note that each of variables $\{\nu, m_r, m_i, C, b^0)\}$ is subject to constraints:

$$\begin{aligned}
0 \ \le\ \nu\ (\min) \ \le\ \ \nu \ \le\ \nu\ (\max)\ , \\
0 \ \le\ m_i(\min) \ \le\ m_i \ \le\ m_i(\max)\ , \\
0 \ \le\ m_r(\min) \ \le\ \ m_r \le\ m_r(\max)\ , \\
0 \ \le\ C\ (\min) \ \le\ \ C \ \le\ C\ (\max)\ , \\
0 \ \le\ \ b^0(\min) \ \le\ \ b^0 \ \le\ \ b^0(\max)\ .
\end{aligned} \tag{3.5}$$

Here we assume $C(\min) = 0.1$ mg/m^3, $C(\max) = 1.5$ mg/m^3, $b^0(\min) = 0.12$ m^{-1}, $b^0(\max) = 0.45$ m^{-1}, and $\nu(\min) = 2.0$, $\nu(\max) = 4.5$, $m_r(\min) = 1.33$, $m_r(\max) = 1.50$, $m_i(\min) = 0.0$, $m_i(\max) = 0.04$. The ranges of b^0 and ν are consistent with oceanic and atmospheric measurements.

Now, we choose a *least-square objective function* (LSQ) $S_{\rm LSQ}(\nu, m_r, m_i, \tau_a, C, b^0)$ such that

$$S^2_{\rm LSQ}(\nu, m_r, m_i, \tau_a, C, b^0) = \frac{1}{N-1} \sum_{j=1}^{N} \left[1 - \frac{\rho_A(\lambda_j;\ \nu, m_r, m_i, \tau_a) + \rho_{aW}(\lambda_j;\ C, b^0)}{\rho_t(\lambda_j) - \rho_r(\lambda_j)} \right]^2 \tag{3.6}$$

where the numerator within the square brackets is to be calculated and the denominator is provided by a sensor (assuming that the reflectance $\rho_r(\lambda_j)$ can be calculated exactly for any wavelength given the ambient surface pressure, as has been discussed previously in the Chapter 2). The LSQ objective function serves as a measure of "goodness" in the fit of

$\rho_A + \rho_{aW}$ to $\rho_t - \rho_r$. In other words, at the solution point $\{\nu^*, m_r^*, m_i^*, \tau_a^*, C^*, b^{0^*}\}$ S_{LSQ} should attain its minimal value subject to constraints in (3.5).

A number of versatile methods exist to find such a solution,[35] although they might differ appreciably as to the convergence rate, the memory requirements, and the ability to coverge to the solution. In particular, methods belonging to the so-called *quasi-Newton class* [36] (see also the Appendix) that take advantage of the information contained in the Hessian matrix of a function (i.e., the square matrix of the second partial derivatives of the function calculated at a point) in calculating the step size and the direction of search appear to be adequate for our purposes. Powell[37] proves the convergence to a minimum for the Davidon-Fletcher-Powell (DFP)[35,35,38] *variable metric class* method (which also holds for Broyden-Fletcher-Goldfarb-Shanno (BFGS) algorithm) on a function with properties outlined above in Eqs.(3.4)-(3.5). However, to the best of our knowledge, the quasi-Newton class methods do not guarantee, in general, a convergence to a minimum. In this study we used a slightly modified `DZXMWD` routine from the commonly available International Mathematical & Statistical Library[39] (IMSL), which is based on the Harwell Library routine `VA10A` and incorporates a quasi-Newton method. To assure the convergence to a minimum in our non-linear optimization procedure a set of starting search points is taken, some of which are discarded after performing a few iterations based on their relative values. It has been observed that the resulting solution was the same (within a preset tolerance) whatever the number of starting search points chosen, meaning that the convergence to a global minimum was probably achieved, so it is believed as sufficient to use just one starting point in solving the system (3.4), and the result is the solution we want.

In the meantime, the system (3.4) subject to constraints (3.5) is solved in two different ways: 1) with a reduction of the number of variables, and 2) directly solving (3.4). Both ways have advantages and disadvantages on their own. Though this will be discussed later, here, we note that the system with a reduced number of variables becomes more stable, it achieves the desired accuracy of computations faster, and affirmatively provides the global minimum of the solution.

Solution 1.

It can be noted that the water-leaving radiances in the NIR bands (i.e., at λ = 765 nm, 865 nm for SeaWiFS) are generally extremely small comparatively to the radiances reflected by the atmosphere (indeed, they constitute, typically, no more then 0.1% of the total radiance measured by a sensor at the TOA). As a consequence, we disregard terms $\rho_w(\lambda_{\mathrm{NIR}};\ C, b^0)$, such that $\rho_{aW}(\lambda_7;\ C, b^0) = \rho_{aW}(\lambda_8;\ C, b^0) = 0$ in the system (3.4).

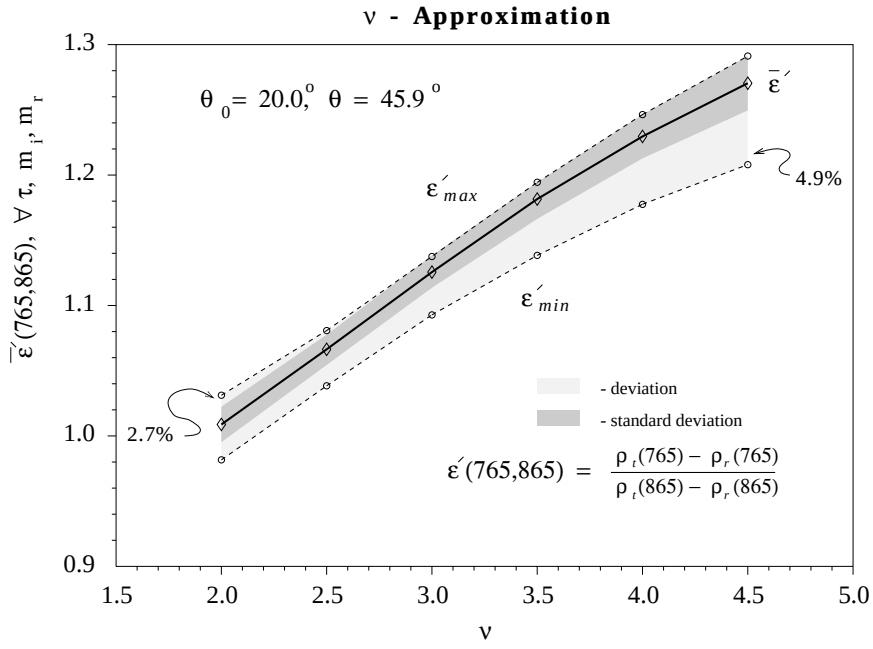

Figure 3.5. Relationship between $\varepsilon'(765, 865)$ and ν (solid curve) averaged over all combinations of four values of $\tau_a(865)$ (0.1, 0.2, 0.3, 0.4), six values of m_i (0.0, 0.001, 0.003, 0.010, 0.040), and two values of m_r (1.334 and 1.50), with $\theta_0 = 20°$ and $\theta = 45.9°$. Dashed curves represent the upper and lower envelopes of the relationship, and the darker region represents the standard deviation of the various cases about the mean for the given value of ν.

Gordon[40] has shown that the spectral variation of $\rho_a(\lambda_{\mathrm{NIR}}) + \rho_{ra}(\lambda_{\mathrm{NIR}})$ in the NIR depends mostly on the aerosol size distribution and only slightly on the refractive index,

thus the NIR bands can be used to determine the size distribution parameter ν. In fact, introducing a measured value

$$\varepsilon'(\lambda_s, \lambda_l) = \frac{\rho_a(\lambda_s) + \rho_{ra}(\lambda_s)}{\rho_a(\lambda_l) + \rho_{ra}(\lambda_l)}, \tag{3.7}$$

where λ_s and λ_l are the shorter and the longer of the two NIR bands available for the sensor, and averaging it over all model values of $\{\tau_a, m_r, m_i\}$,

$$\overline{\varepsilon}'(\lambda_s, \lambda_l) = \frac{1}{N_{m_r} + N_{m_i} + N_{\tau_a}} \sum_{i,r,k=1}^{N_{m_r}, N_{m_i}, N_{\tau_a}} \varepsilon'(\lambda_s, \lambda_l;\ m_i^{(i)}, m_r^{(r)}, \tau_a^{(k)}), \tag{3.8}$$

where N_{m_r} is the total number of preselected values $m_r^{(r)}$ for the real part of the refractive index, N_{m_r} is the total number of preselected values $m_i^{(i)}$ for the imaginary part of the refractive index, and N_{τ_a} is the total number of preselected values $\tau_a^{(k)}$ for the optical thickness τ_a. We can form an empirical relationship between $\overline{\varepsilon}'$ and the size distribution parameter ν. It is shown in Figure 3.5.

Once $\overline{\varepsilon}'(\lambda_s, \lambda_l)$ is computed from the sattelite imagery, it is a straightforward matter to determine the Junge power-law parameter ν^*, where the $*$ indicates the estimated value. From the tabulated values of $\rho_a(765) + \rho_{ra}(765)$ and $\rho_a(865) + \rho_{ra}(865)$ for each model from the set $\{m_r, m_i\}$, we derive the aerosol optical thickness τ_a at 865 nm (Fig. 2.5) through the Newton-Raphson iteration procedure[41]. This iteration proved to be fast and accurate. Note that the optical thicknesses $\tau_a(\lambda)$ for other wavelengths can be found (see, Fig. 3.2) because

$$\frac{c(\lambda)}{c(865)} = \frac{\tau_a(\lambda)}{\tau_a(865)}, \tag{3.9}$$

where $c(\lambda)$ is the extinction coefficient computed through Mie theory for each set $\{\nu, m_r, m_i\}$ and properly interpolated for the calculated value of ν^*.

In building the system (3.4) for the bands not containing the NIR wavelengths we have to assume some function for the diffuse transmittance of the water-leaving reflectance through the atmosphere. This has been discussed previously in the Chapter 2. Both Assumptions 1 and 2 (Eqs. (2.20) and (2.21) respectively) are easily introduced in these

computations. However, we will choose the simpler one of the two mentioned (i.e., we will use the Eq. (2.20). This will mean, in fact, that the reflectances $[\rho_a(\lambda)+\rho_{ra}(\lambda)]$ and $[\rho_W]$ are completely separable and unrelated to each other. While, in general, such an assumption is not justified, Yang and Gordon[30] showed that the diffuse transmittance $t(\lambda)$ for small optical thicknesses is only a weak function of the aerosol optical properties.

Thus, the total number of variables $\{\nu, m_r, m_i, \tau_a, C, b^0\}$ is reduced by two $\{\nu, \tau_a\}$. The system (3.4) no longer contains equations corresponding to the NIR bands and is re-written below for clarity:

$$\begin{aligned}
\rho_A(\lambda_1;\ \nu, m_r, m_i, \tau_a) + \rho_W(\lambda_1;\ C, b^0) &= \rho_t(\lambda_1) - \rho_r(\lambda_1), \\
\rho_A(\lambda_2;\ \nu, m_r, m_i, \tau_a) + \rho_W(\lambda_2;\ C, b^0) &= \rho_t(\lambda_2) - \rho_r(\lambda_2), \\
&\cdots\cdots\cdots\cdots\cdots\cdots \\
\rho_A(\lambda_{N-N_{\rm NIR}};\ \nu, m_r, m_i, \tau_a) + \rho_W(\lambda_N;\ C, b^0) &= \rho_t(\lambda_{N-N_{\rm NIR}}) - \rho_r(\lambda_{N-N_{\rm NIR}}).
\end{aligned} \tag{3.10}$$

Now, applying the quasi-Newton iteration subject to constraints (3.5) with the objective function $S_{\rm LSQ}$ from (3.6), we obtain the required solution $\{\nu^*, m_r^*, m_i^*, \tau_a^*, C^*, b^{0^*}\}$. A detailed graphical flow-chart in the Figure 3.6 demonstrates all the steps performed in this solution.

Solution 2.

In this case, the quasi-Newton iteration is applied to the full system of equations (3.4) (including the NIR bands) subject to same constraints (3.5) and the objective function $S_{\rm LSQ}$ from (3.6)

Discussion. The ultimate test of any correction algorithm is its stability and robustness. This was the main reason for introducing two solutions above (though in a sense similar). It is surely possible under realistic conditions to encounter aerosols with optical properties considerably different from those described by the simple Junge power-law aerosol models.

SPECTRUM OPTIMIZATION ALGORITHM Flow-Chart

1. Determine ν
   $\lambda = 765, 865$

$$\acute{\varepsilon}(765,865) = \frac{\rho_t(765) - \rho_r(765)}{\rho_t(865) - \rho_r(865)}$$

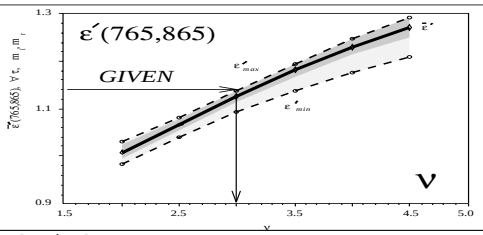

2. Determine τ_a ω
   λ = 865 nm

this curve is obtained from pre-computed LUT's for all λ, m_i, m_r *and given viewing geometry*

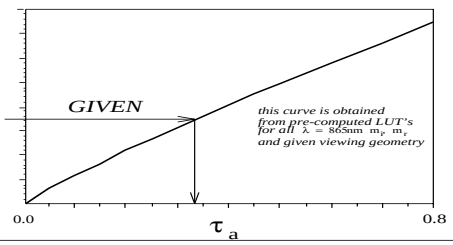

3. Determine τ_a at
$\lambda = 412, 443, 490, 510, 555, 670$

$$c / c(865) = \tau / \tau(865)$$

these values are computed from model's scattering parameters for all λ, m_i, m_r

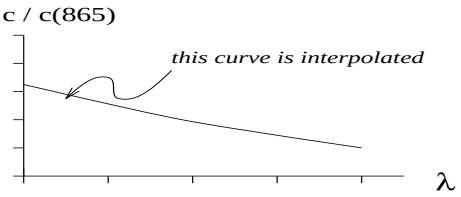

4. Determine $\rho_a + \rho_{ra}$

$\lambda = 412, 443, 490, 510, 555, 670$

this curve is obtained from pre-computed LUT's for all λ, m_i, m_r *and given viewing geometry*

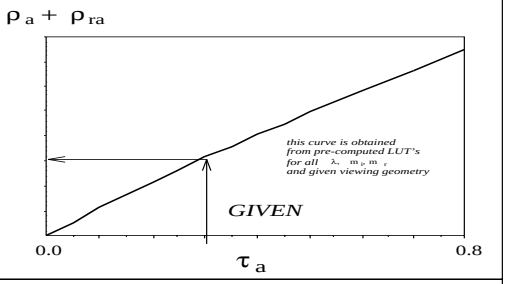

5. Solve system of NLE with LSQ-objective

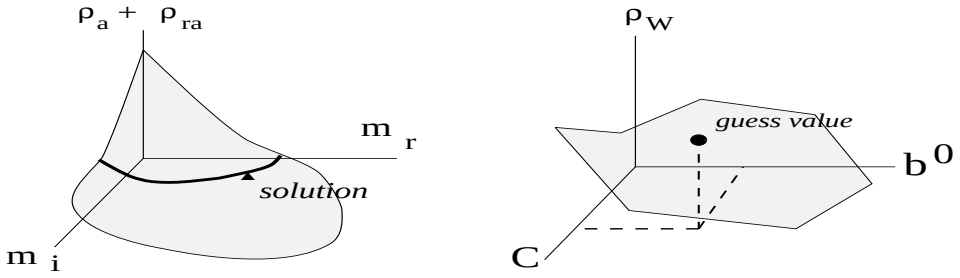

Note: the procedure might be thought as follows:
"guess" a value for C, b0 and calculate ρ_W
then find (mi,mr) such that $\rho_a + \rho_{ra} + \rho_W = \rho_t - \rho_r$

Figure 3.6. Atmospheric Correction Flow-Chart.

Yet, we require a good performance with a little noise, with the retrieved parameters as close to the real ones as possible.

An apparent drawback of the Solution 1 is its inability to obtain the exact parameters for pseudo data generated using the Junge power-law for the aerosols. The reason is the estimate of $\overline{\varepsilon}'(\lambda_s, \lambda_l)$ in (3.8). Since the deviation of ε_{exact} from $\overline{\varepsilon}$ might reach up to 3%, it is not possible to expect better accuracy in obtained values for $\{\nu, m_r, m_i\}$. On the other hand, the usage of (3.8) makes the algorithm's performance extremely stable in situations when the test aerosol is different from Junge power-law aerosol models. The retrieved parameters are obtained with the standard deviations never exceeding 15-20%. It also provides for a better global optimal solution. As will be shown in the later chapters, the algorithm is extremely robust when dealing with the experimental errors such as the sensor calibration errors, when dealing with the aerosol vertical structures, etc. The Solution 2, on the other hand, computes the parameters $\{\nu, m_r, m_i\}$ "exactly" but its results are less stable, the standard deviation reaching sometimes 30%.

While both the solutions are extremely time-efficient (about 2 sec for an image pixel on AlphaServer 2100), the Solution 1 is preferable to the Solution 2. However, the Solution 2, because of its direct approach, is more flexible, and can be easily extended to include, for example, the aerosol vertical structures. Here, the Solution 2 is used mostly to test the correctness of the computer code used in the implementation of the Solution 1.

IV. ALGORITHM'S PERFORMANCE WITH SIMULATED DATA

In the following subsections we generate and test the algorithm with simulated values for the radiances measured by the pseudo-sensors at the TOA. They will provide:

- a theoretical background on test aerosols or probable errors to be expected with actual color sensors;

- the results for the retrieved atmospheric-ocean parameters;

- a brief discussion of results.

A. Pseudo $\rho_t(\lambda)$ for Junge power-law test aerosol models

The purpose of this test is to examine the correctness of all interpolation procedures as well as the performance of the optimization itrerations.

A test data-set was simulated by computing $\rho_t(\lambda) - \rho_r(\lambda)$ for the Junge power-law aerosol models with $m = 1.50 - i0.002$ (characterized by low absorption) and an optical thickness $\tau_a(865) = 0.2$ at $\lambda = 865$ nm. Parameters for the ocean water properties were chosen to be $C = 0.1$ mg/m^3 and $b^0 = 0.3$ m^{-1} (the average value of b^0 for Case 1 waters[15]). Calculations were performed for seven sun-viewing geometries with the solar zenith angles $\theta_0 = 0°, 20°, 40°, 60°$ and, the sensor viewing at $\theta_v = 1°, 45°$ with respect to nadir and the azimuth angle $\phi_v = 90°$ (omitting the glitter at $\theta_0 = 0°, \theta_v = 1°$). The atmospheric correction scheme of the Solution 2 (namely, the direct solution of the system (3.4)) was employed in this case. The retrived results for parameters $\{\nu^*, m^*, \varpi_0^*, \tau_a^*(865), C^*, b^{0^*}\}$ are shown in the Table 4.1.

Table 4.1

a)

θ \ θ_o		**0°**	**20°**	**40°**	**60°**
1°	ν^*		*2.07*	*2.04*	*2.05*
	m^*		*1.500 - i 0.003*	*1.500 - i 0.002*	*1.500 - i 0.003*
45°	ν^*	*2.06*	*2.06*	*2.05*	*2.04*
	m^*	*1.500 - i 0.003*	*1.453 - i 0.002*	*1.500 - i 0.003*	*1.500 - i 0.002*

b)

θ \ θ_o		**0°**	**20°**	**40°**	**60°**
1°	ω_o^*		*0.910*	*0.930*	*0.929*
	τ_a^*		*0.24*	*0.20*	*0.20*
45°	ω_o^*	*0.924*	*0.932*	*0.929*	*0.934*
	τ_a^*	*0.20*	*0.22*	*0.20*	*0.20*

c)

θ \ θ_o		**0°**	**20°**	**40°**	**60°**
1°	C^*		*0.101*	*0.099*	*0.098*
	b_o^*		*0.30*	*0.30*	*0.30*
45°	C^*	*0.098*	*0.098*	*0.098*	*0.098*
	b_o^*	*0.30*	*0.30*	*0.30*	*0.30*

Table 4.1 Retrieved aerosol parameters for the Junge power-law test model with $m_r = 1.50, m_i = 0.002, \nu = 2.0, \tau_a(865) = 0.2$ and, the ocean water pigment concentration and the scattering parameter $C = 0.1$ mg/m^3 and $b^0 = 0.3$ m^{-1} respectively, for seven sun-viewing geometries. The correct value of ϖ_0 is 0.944.

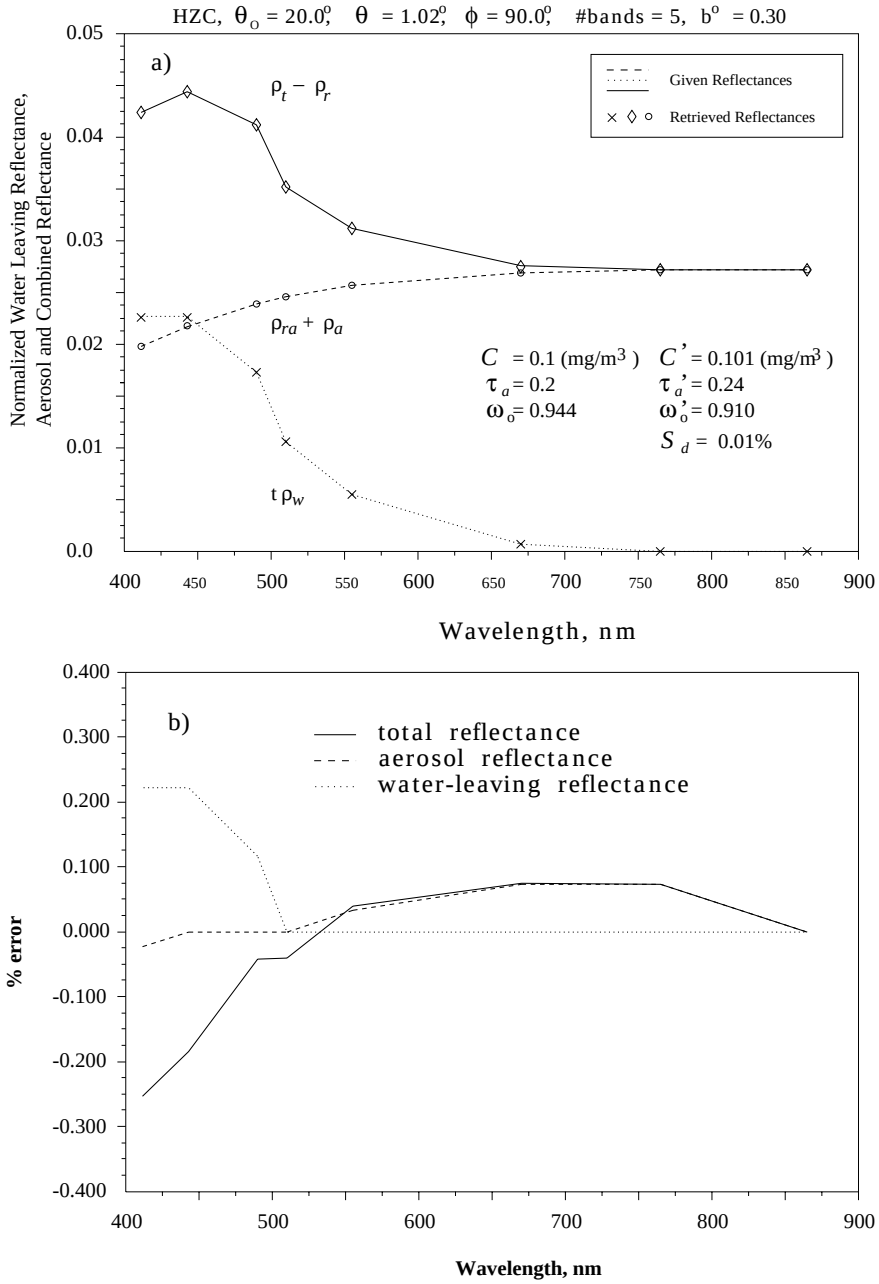

Figure 4.1. a) Retrieved the total, aerosol and water-leaving reflectances for the Junge power-law test model with $m_r = 1.50, m_i = 0.002, \nu = 2.0, \tau_a(865) = 0.2$ and, the ocean water pigment concentration and the scattering parameter $C = 0.1$ mg/m^3 and $b^0 = 0.3$ m^{-1} respectively, for the sun-viewing geometry $\theta_0 = 20°, \theta = 1°$. b) respective retrieval errors

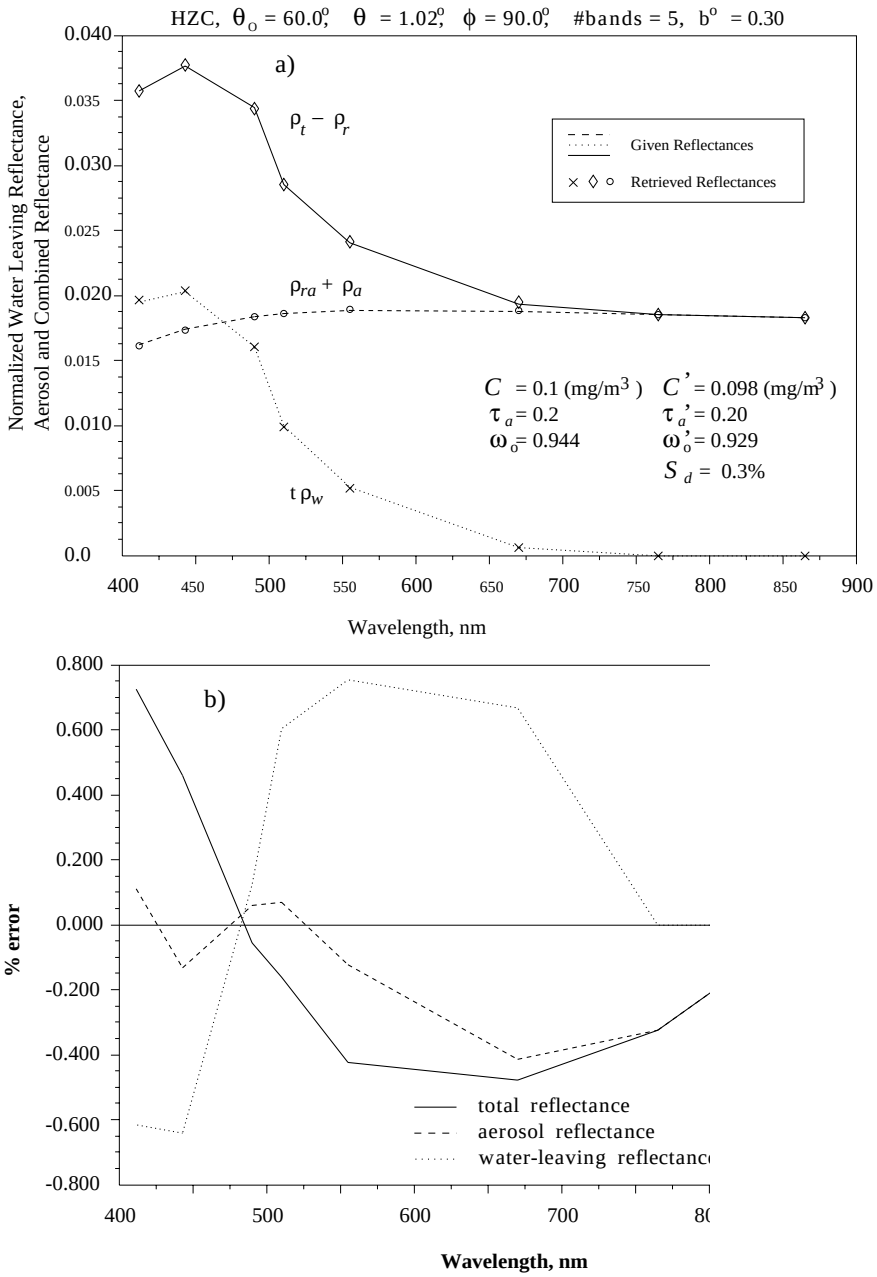

Figure 4.2. a) Retrieved the total, aerosol and water-leaving reflectances for the Junge power-law test model with $m_r = 1.50, m_i = 0.002, \nu = 2.0, \tau_a(865) = 0.2$ and, the ocean water pigment concentration and the scattering parameter $C = 0.1$ mg/m^3 and $b^0 = 0.3$ m^{-1} respectively, for the sun-viewing geometry $\theta_0 = 60°, \theta = 1°$. b) respective retrieval errors

The retrieved and given reflectances along with the error deviations are plotted in Fig. 4.1 and 4.2 for two sun-viewing geometries, $\theta_0 = 20°, \theta = 1°$ and $\theta_0 = 60°, \theta = 1°$, $\phi_0 = 90°$. Apparently, the aerosol and ocean water parameters are retrieved excellently: the maximum deviation for the single scattering albedo ϖ_0 never exceeded 3%, the deviation for the pigment concentration C never exceeded 2%. As expected in the previous chapters, the retrieval of the aerosol optical thickness $\tau_a(\lambda)$ is the most unstable (with respect to both the sun-viewing geometries and the other parameters), though stable enough to be acceptable. The results demonstrate that the adopted interpolation and optimization procedures work satisfactorily, so that other test cases should be considered. This also demonstrates that the algorithm was properly coded.

B. Pseudo $\rho_t(\lambda)$ for M80, C80, T80, U80 test aerosol models

The nomenclature M80, C80, T80, U80 stands for the Maritime, Coastal, Tropospheric and Urban models of Shettle and Fenn,[14] all at the relative humidity of 80%. The distinguished feature of these models is that they closely approximate optical properties of realistic aerosols and are characterized by the bimodal size distribution (see Eq. (2.12) with $i = 2$).

Table 4.2: Characteristics of the M80,C80,T80,U80 test aerosol models.

	Size Distribution			Refractive Index	
Aerosol Model	N_i	D_i	σ_i	412 nm	865 nm
M80	0.990000	0.06548	0.35	$1.446 - i\ 3.309\text{e}{-3}$	$1.436 - i\ 6.107\text{e}{-3}$
	0.010000	0.63600	0.40	$1.359 - i\ 5.165\text{e}{-9}$	$1.348 - i\ 1.381\text{e}{-6}$
C80	0.995000	0.06548	0.35	$1.446 - i\ 3.309\text{e}{-3}$	$1.436 - i\ 6.107\text{e}{-3}$
	0.005000	0.63600	0.40	$1.359 - i\ 5.165\text{e}{-9}$	$1.348 - i\ 1.381\text{e}{-6}$
T80	0.990000	0.06548	0.35	$1.446 - i\ 3.309\text{e}{-3}$	$1.436 - i\ 6.107\text{e}{-3}$
U80	0.999875	0.07028	0.35	$1.423 - i\ 3.473\text{e}{-2}$	$1.414 - i\ 3.412\text{e}{-2}$
	0.000125	1.16200	0.40	$1.415 - i\ 3.151\text{e}{-2}$	$1.406 - i\ 3.095\text{e}{-2}$

The size distribution parameters and values of the refractive index at two wavelengths

$\lambda = 412$ and 865 nm are tabulated in the Table 4.2. Figure 4.3 compares the volume size distribution $dV/d\ln D$ for the test models M80, C80, T80, U80 and the Junge power-law models with $\nu = 2.0, 3.0, 4.0$. All volume size distributions are normalized such that $\int_0^\infty dN = 1$ cm^{-3}. Figure 4.4 demonstrates the spectral variation of the aerosol optical thickness with respect to that at $\lambda = 865$ nm. We note a strong similarity of this almost log-linear behaviour with that of the Junge power-law models (see Fig. 3.2).

Table 4.3: The single-scattering albedo ϖ_0 of the M80,C80,T80,U80 test aerosol models.

Wavelength, nm	M80	C80	T80	U80
412	0.9924	0.9884	0.9758	0.7823
443	0.9929	0.9890	0.9761	0.7825
490	0.9935	0.9898	0.9763	0.7820
510	0.9938	0.9901	0.9764	0.7810
555	0.9936	0.9897	0.9737	0.7805
670	0.9944	0.9906	0.9715	0.7738
765	0.9939	0.9896	0.9634	0.7621
865	0.9934	0.9884	0.9528	0.7481

From Table 4.3 it can be observed that the spectral variation of the single-scattering albedo $\varpi_0(\lambda)$ is unsubstantial, being the highest for Tropospheric T80 models, again, a property which is similar to the Junge power-law models. Among all the models the Urban at the relative humidity of 80% possesses the lowest value of the single-scattering albedo ($\varpi_0^{\mathrm{U80}}(865) = 0.748$ comparatively to the M80 $\varpi_0^{\mathrm{M80}}(865) = 0.993$). The U80 model is referred to as the highly absorbing aerosol in contrast to M80, C80, T80 models which are usually referred to as the weakly absorbing aerosols.

The test-data set $[\rho_t(\lambda) - \rho_r(\lambda)]$ was created for M80, C80, T80, U80 aerosol models having the optical thicknesses $\tau_a(865) = 0.1, 0.2, 0.3$. The ocean water optical properties were chosen to be $b^0 = 0.3$ m^{-1} and three values of the pigment concentration $C = 0.1, 0.5, 1.0$ mg/m^3.

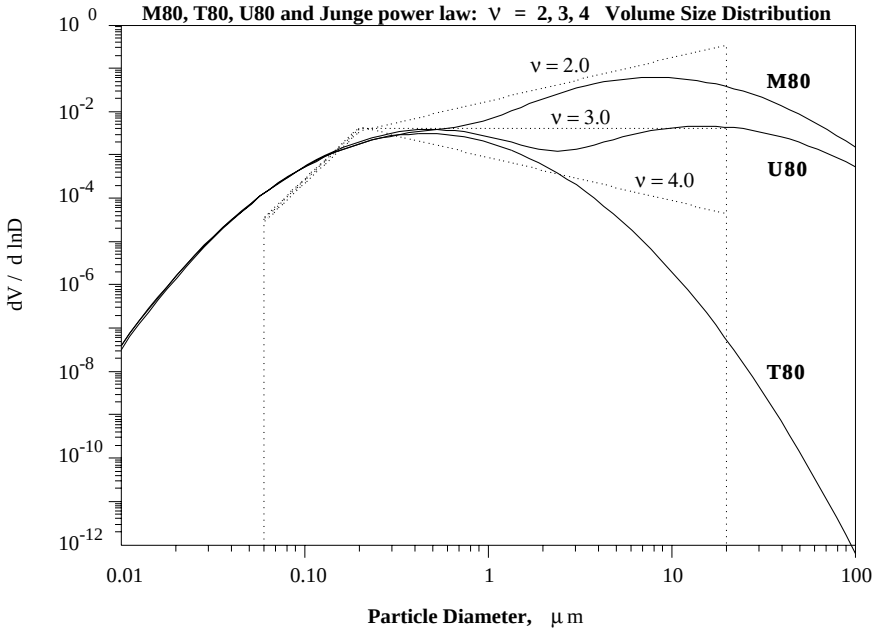

Figure 4.3. Volume size distributions for the M80, T80, U80 test aerosol models and the Junge power-law test model with $\nu = 2.0, 3.0, 4.0$.

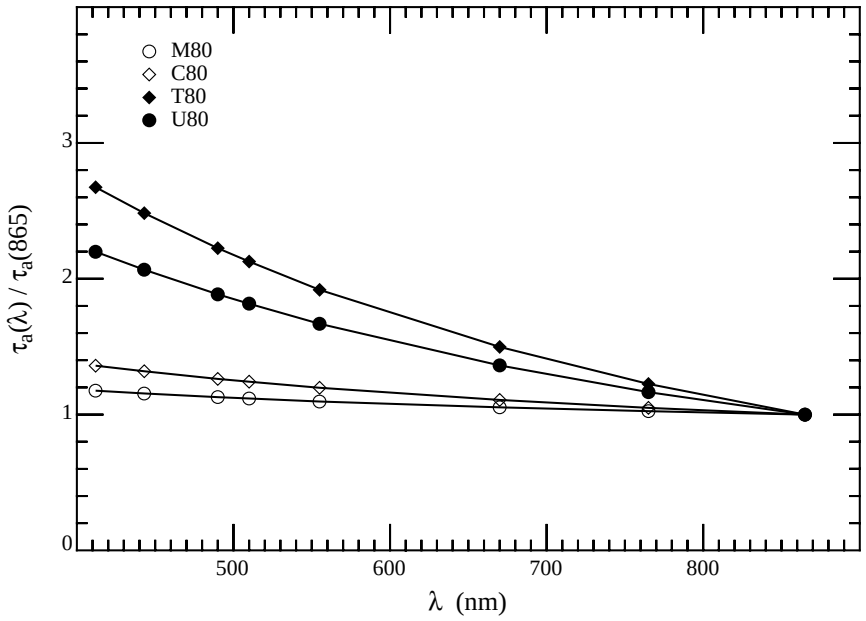

Figure 4.4. Spectral variation of the optical thickness $\tau_a(\lambda)/\tau_a(865)$ for the M80, C80, T80, U80 test aerosol models.

The solar zenith angles θ_0 were $0°, 20°, 40°, 60°$ and the viewing angles $\theta = 1°, 45°$ with respect to nadir (total of the seven sun-viewing geometries since $\theta_0 = 0°, \theta = 1°$ case was excluded as long as it would be strongly influenced by the Sun-glitter).

The retrievals were performed using the approach outlined in the previous chapter as Solution 1, where SeaWiFS bands 7 and 8 (at $\lambda = 765, 865$ nm respectively) were used to determine the Junge power-law parameter ν and the optical thicknesses $\tau_a(\lambda)$. Five bands 1 through 5 (at $\lambda = 412, 443, 490, 510, 555$ nm) were used in the non-linear optimization procedure, Eqs. (3.4)-(3.6).

The detailed analysis will be carried out for the aerosol models M80, T80, U80. The C80 aerosol test model behaves similarly to the M80 model. It should be noted that the M80 aerosol phase function is highly peaked in the forward direction because of the high presence of the giant particles in its particle size distribution. The U80 aerosol is highly absorbing, and the T80 aerosol model is characterized by a high reflectivity which is the consequence of the dominant presence of particles in the region of 0.5 μm characterized by the high scattering efficiency. As was mentioned before both M80 and T80 models are weakly-absorbing aerosols.

Figures 4.5 through 4.13 have been brought in to demonstrate an unessential dependence of the retrieved results on the sun-viewing geometry. The tests are shown for the case with $\tau_a(865) = 0.2$, the pigment concentration $C = 0.5$ mg/m^3, the water scattering parameter $b^0 = 0.3$ m^{-1}, and three sun-viewing geometries $\theta_0 = 20°, \theta = 1°, \phi = 90°$; $\theta_0 = 60°, \theta = 1°, \phi = 90°$; $\theta_0 = 40°, \theta = 45°, \phi = 90°$. In the latter geometry the optical path through the aerosol layer is the longest among all the geometries considered. Figures 4.7, 4.10, 4.13 clearly indicate that for this geometry the retrieved aerosol-ocean parameters are slightly poorer then for the other geometries. In all cases the aerosol reflectance are best retrieved for bands 7 and 8 (the ones that were used to obtain the Junge power-law parameters ν and $\tau_a(\lambda)$) and the worst near the band 6 (this band was not used during the solution of non-linear equations). Outstanding is the fact that the algorithm provides the

results equally well for the highly absorbing U80 and the weakly absorbing M80 aerosols. The average value of the objective function S_{LSQ} with respect to the sun-viewing geometries was 0.24% for M80, 0.17% for U80, and 0.31% for T80 aerosol models. These numbers were typical while working with all the above test models and indicate that the fit to the total aerosol reflectance $\rho_t(\lambda) - \rho_r(\lambda)$ was excellent.

It has been noticed in the previous chapter that the normalized water-leaving reflectance is the highest for waters with the low pigment concentration, i.e., $C = 0.1$ mg/m^{-3} (see Fig. 2.6). As a consequence, these waters' parameters should be the easiest to determine compared to waters with the high pigment concentration content, e.g., $C = 1.0$ mg/m^{-3}. This is validated for two aerosol optical thicknesses $\tau_a(865) = 0.1, 0.3$: $\tau_a(865) = 0.1$ in Figures 4.14 - 4.15 for M80, Figures 4.16 - 4.17 for T80, and Figures 4.18 - 4.19 for U80; and $\tau_a(865) = 0.3$ in Figures 4.20 - 4.21 for M80, Figures 4.22 - 4.23 for T80, and Figures 4.24 - 4.25 for U80. The results are provided for just one sun-viewing geometry $\theta_0 = 60°, \theta = 1°, \phi = 90°$. In U80 case, for example, for the optical thickness $\tau_a(865) = 0.1$ the retrieval of the pigment concentration C gave the error 0% for $C = 0.1$ mg/m^{-3} and 2.6% for $C = 1.0$ mg/m^{-3}.

The same figures demonstrate that with the increase of the aerosol optical thickness the aerosol parameters are retrieved better (the reflectance of aerosol increases), while the ocean parameters are retrieved more poorly. The ocean parameters are better retrieved for low τ_a. For example, for M80 model (Fig. 4.14 and 4.20) and the ocean pigment concentration $C = 0.1$ mg/m^{-3} the retrieval of C degraded from 4% for $\tau_a(865) = 0.1$ to 8% for $\tau_a(865) = 0.3$ while the single-scattering albedo $\varpi_0(865)$ improved from about 6% to 2% and $\tau_a(865)$ from about 30% to 7%.

The results for the single-scattering albedo $\varpi_0(865)$, the ocean pigment concentration C, and the water scattering parameter b^0 are summarized in Tables 4.4 - 4.6. All values

were averaged over the sun-viewing geometries as

$$\overline{\Delta} = \frac{1}{(N_i + N_j)} \sum_{i=1}^{N_i} \sum_{j=1}^{N_j} \Delta(\theta_0^{(i)}, \theta^{(j)}) \tag{4.1}$$

where Δ stands for one of the parameters $\varpi_0(865), C, b^0$ and, θ_0, θ are the sun and viewing zenith angle.

From Table 4.4 we observe that the error of the retrieval of the ocean pigment concentration C was on the average 3.6% for M80, 4.5% for C80, 10.3% for T80, and 5.1% for U80 test aerosol models. The algorithm's handling the highly absorbing aerosol case (U80) is outstanding. The single-scattering albedo ϖ_0 is remarkably well retrieved also (Table 4.5). For the weakly absorbing aerosols M80, C80 the average error was 2.7% and, for the highly absorbing aerosol U80 it was 2.6%. Notable is the stability of the algorithm's performance. The objective function S_{LSQ} was on the average 0.27% for M80, 0.28% for C80, 0.36% for T80, and 0.15% for U80 aerosol test models with its typical average standard deviation of 20% over all cases examined.

An intrinsic drawback of the algorithm is its inability to retrieve reasonably the aerosol optical thickness τ_a. The correct single-scattering phase function is a primary condition for that. The "true" and "retrieved" phase functions for the test cases M80 and U80 are shown in Figures 4.26 and 4.27 respectively. Meanwhile, Tables 4.4 and 4.6 suggest that the retrieval of the ocean water parameters C and b^0 is only a weak function of the single scattering phase function.

We end up this subsection with a note that only the first five out of six bands in visible were used in constructing the systen of non-linear equations (3.4), (3.6) subject to constraints (3.5). The addition of the Band 6 (670 nm) did not improve the result of retrievals. Indeed, the variation of the water-leaving reflectance $\rho_w(C, b^0)$ at this wavelength is small (but not negligible), thus downgrading the overall time-performance of the algorithm.

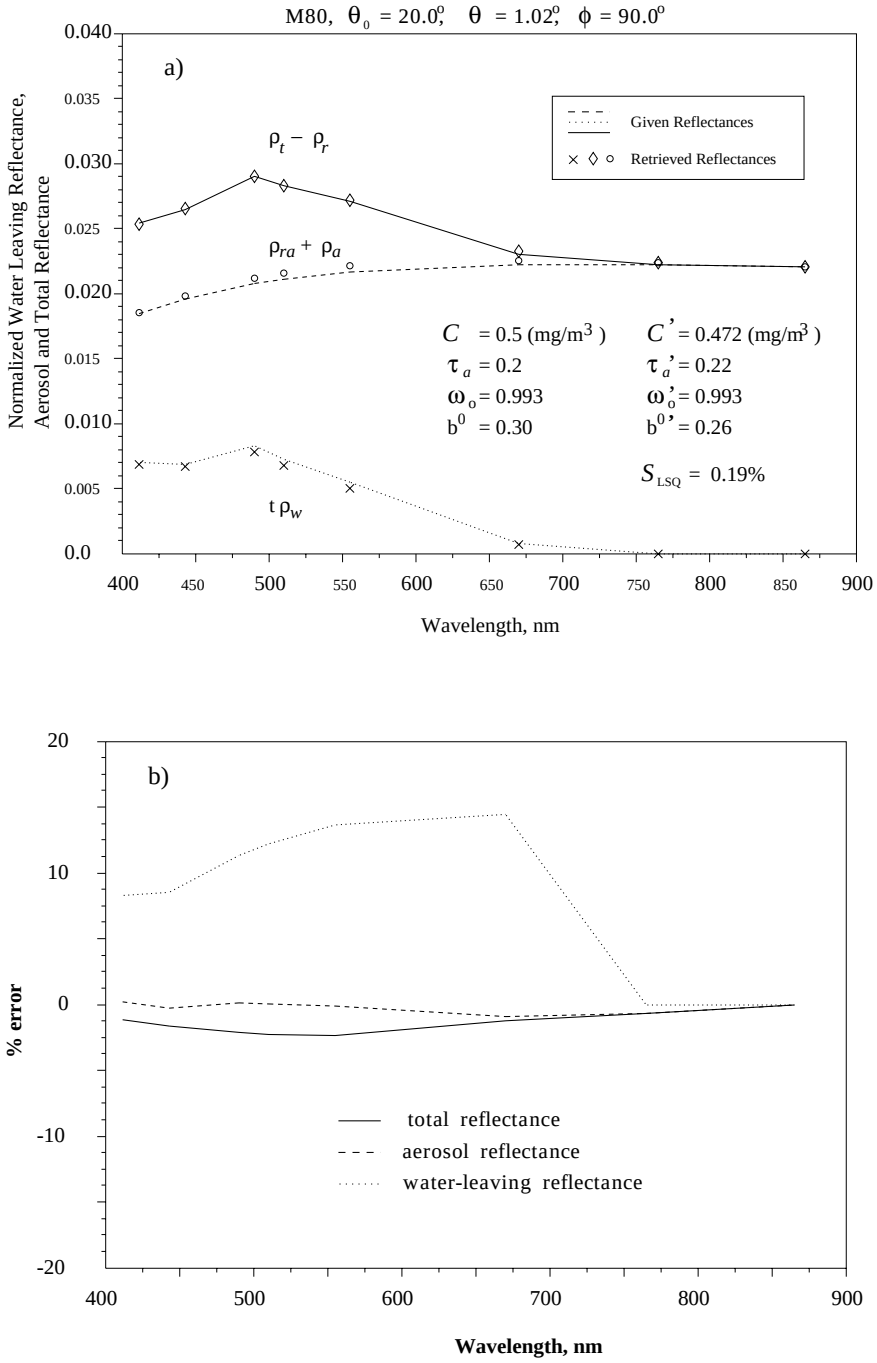

Figure 4.5 a) Retrieved the total, aerosol and water-leaving reflectances for the Maritime-80 test model having the optical thickness $\tau_a(865) = 0.2$ and, the ocean water pigment concentration and the scattering parameter $C = 0.5$ mg/m^3 and $b^0 = 0.3$ m^{-1} respectively, for the sun-viewing geometry $\theta_0 = 20°, \theta = 1°, \phi = 90°$. b) respective retrieval errors

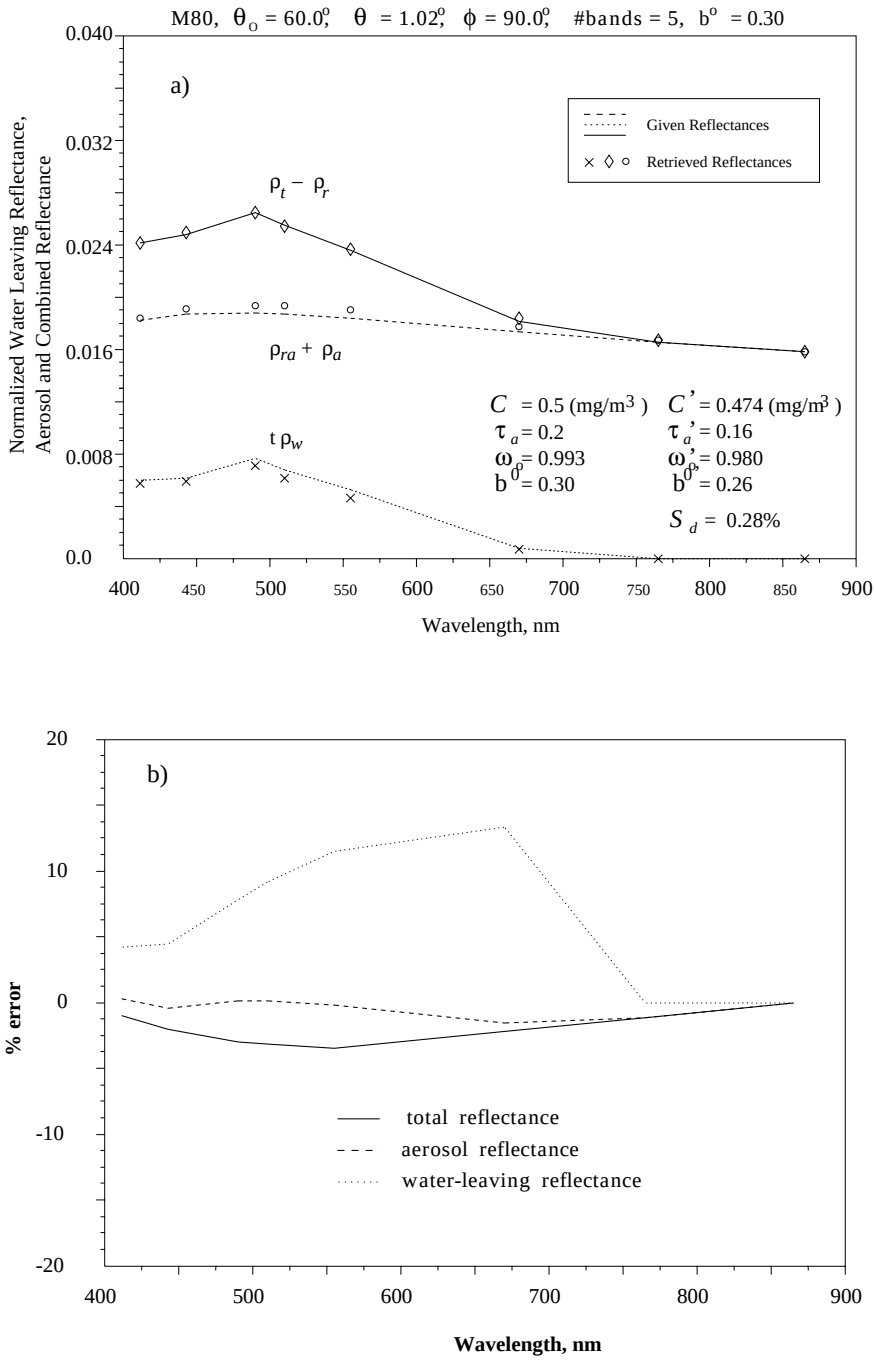

Figure 4.6 a) Retrieved the total, aerosol and water-leaving reflectances for the Maritime-80 test model having the optical thickness $\tau_a(865) = 0.2$ and, the ocean water pigment concentration and the scattering parameter $C = 0.5$ mg/m^3 and $b^0 = 0.3$ m^{-1} respectively, for the sun-viewing geometry $\theta_0 = 60°, \theta = 1°, \phi = 90°$. b) respective retrieval errors

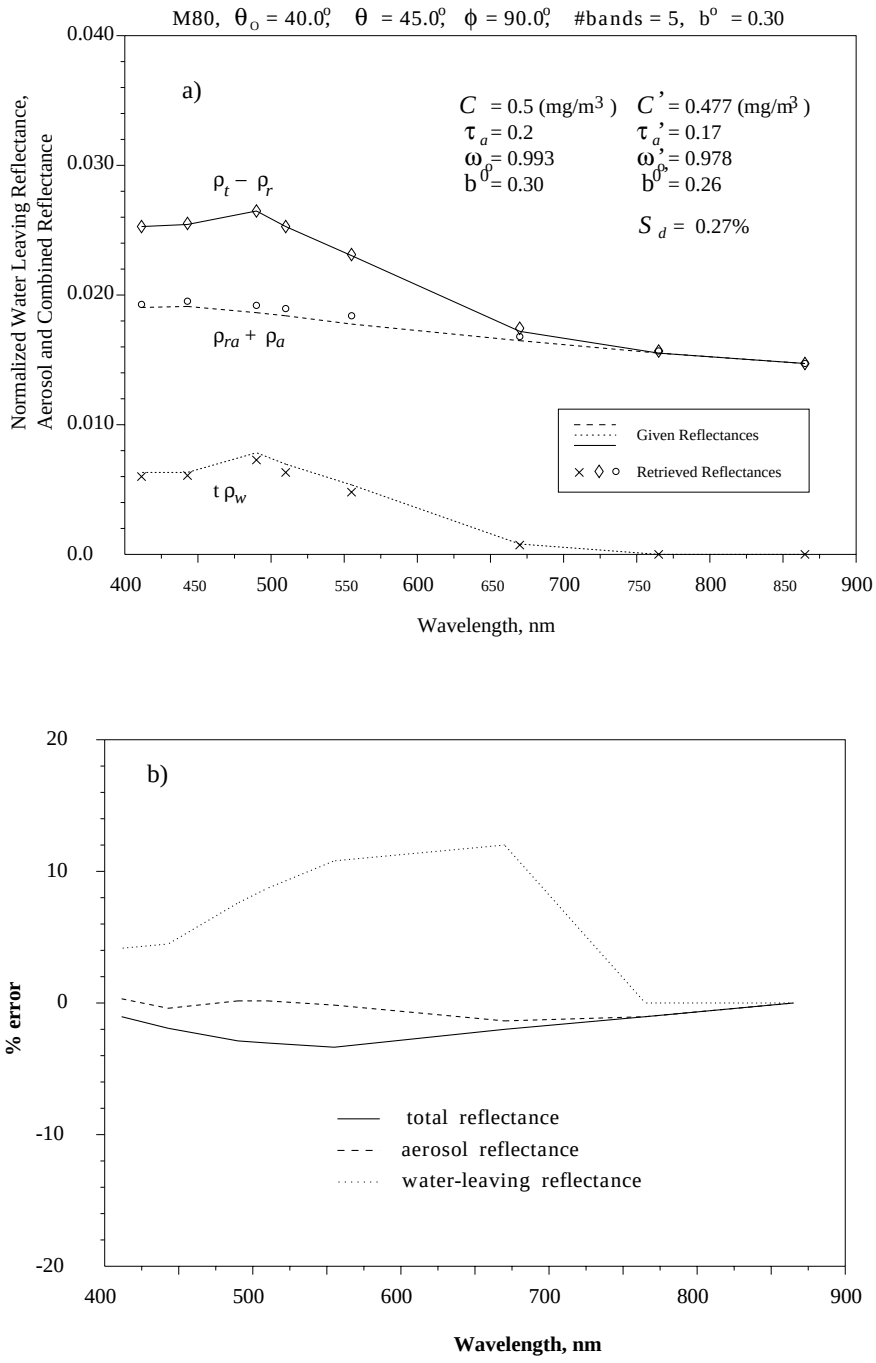

Figure 4.7 a) Retrieved the total, aerosol and water-leaving reflectances for the Maritime-80 test model having the optical thickness $\tau_a(865) = 0.2$ and, the ocean water pigment concentration and the scattering parameter $C = 0.5$ mg/m^3 and $b^0 = 0.3$ m^{-1} respectively, for the sun-viewing geometry $\theta_0 = 40°, \theta = 45°, \phi = 90°$. b) respective retrieval errors

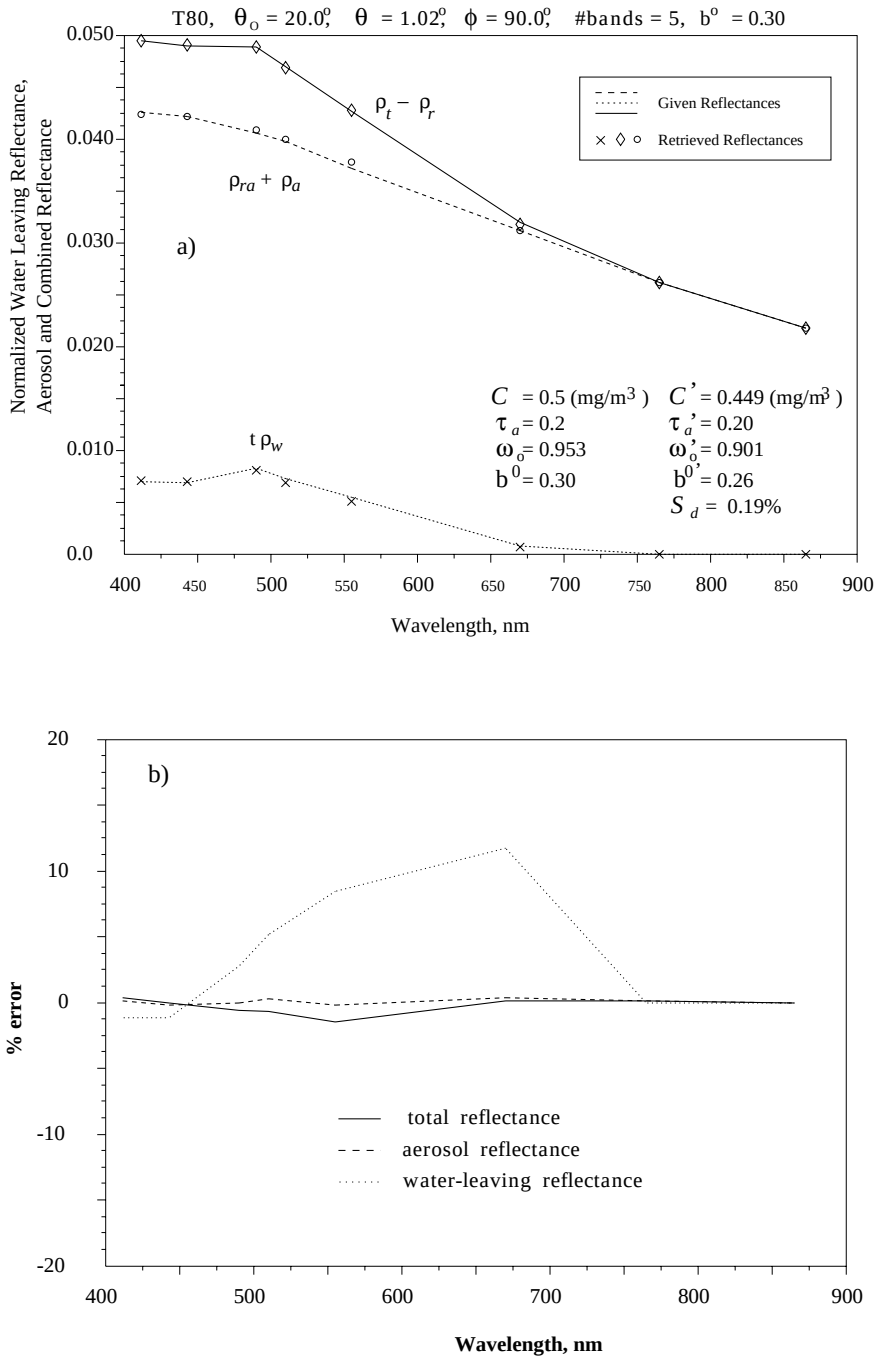

Figure 4.8 a) Retrieved the total, aerosol and water-leaving reflectances for the Tropospheric-80 test model having the optical thickness $\tau_a(865) = 0.2$ and, the ocean water pigment concentration and the scattering parameter $C = 0.5\,\mathrm{mg/m^3}$ and $b^0 = 0.3\,\mathrm{m^{-1}}$ respectively, for the sun-viewing geometry $\theta_0 = 20°, \theta = 1°, \phi = 90°$. b) respective retrieval errors

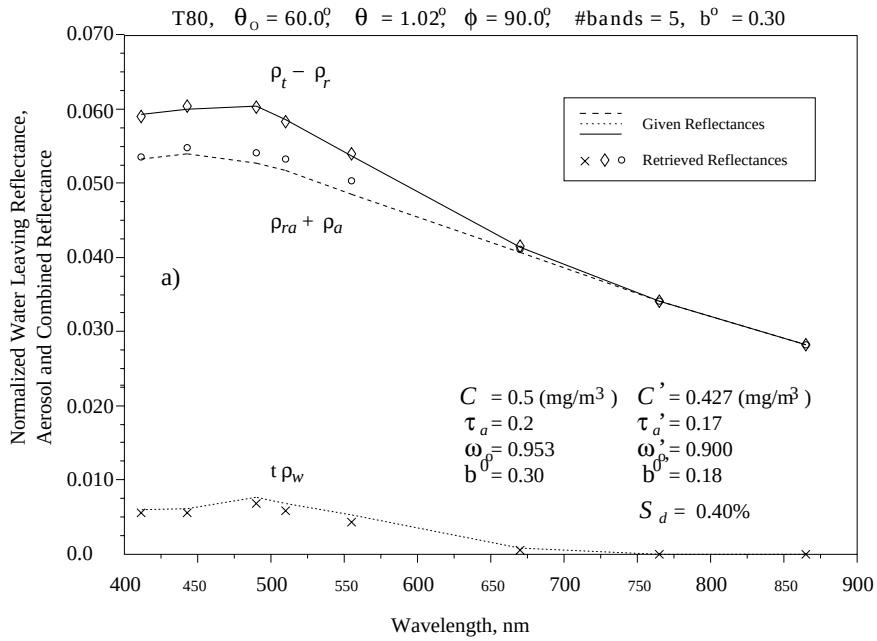

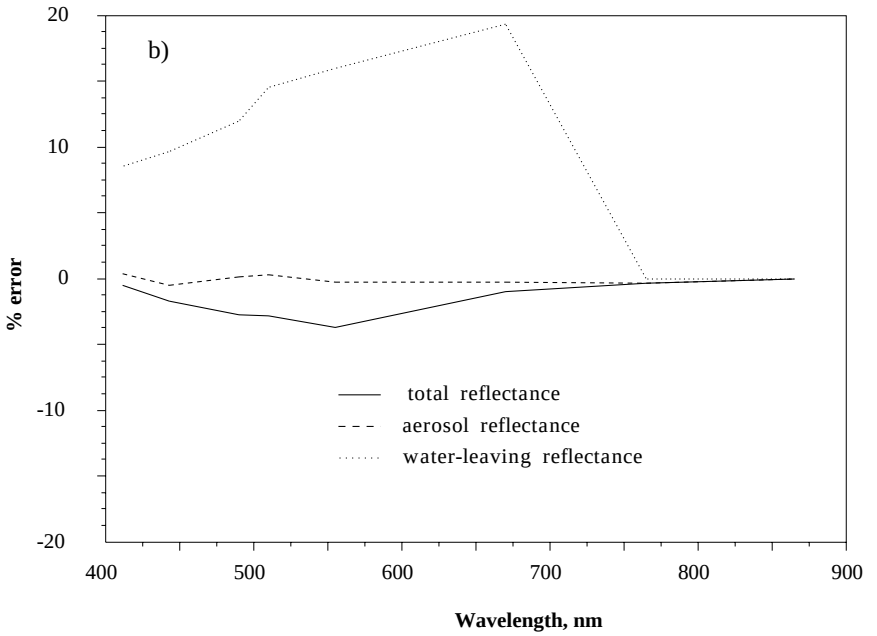

Figure 4.9 a) Retrieved the total, aerosol and water-leaving reflectances for the Tropospheric-80 test model having the optical thickness $\tau_a(865) = 0.2$ and, the ocean water pigment concentration and the scattering parameter $C = 0.5\,\mathrm{mg/m^3}$ and $b^0 = 0.3\,\mathrm{m^{-1}}$ respectively, for the sun-viewing geometry $\theta_0 = 60°, \theta = 1°, \phi = 90°$. b) respective retrieval errors

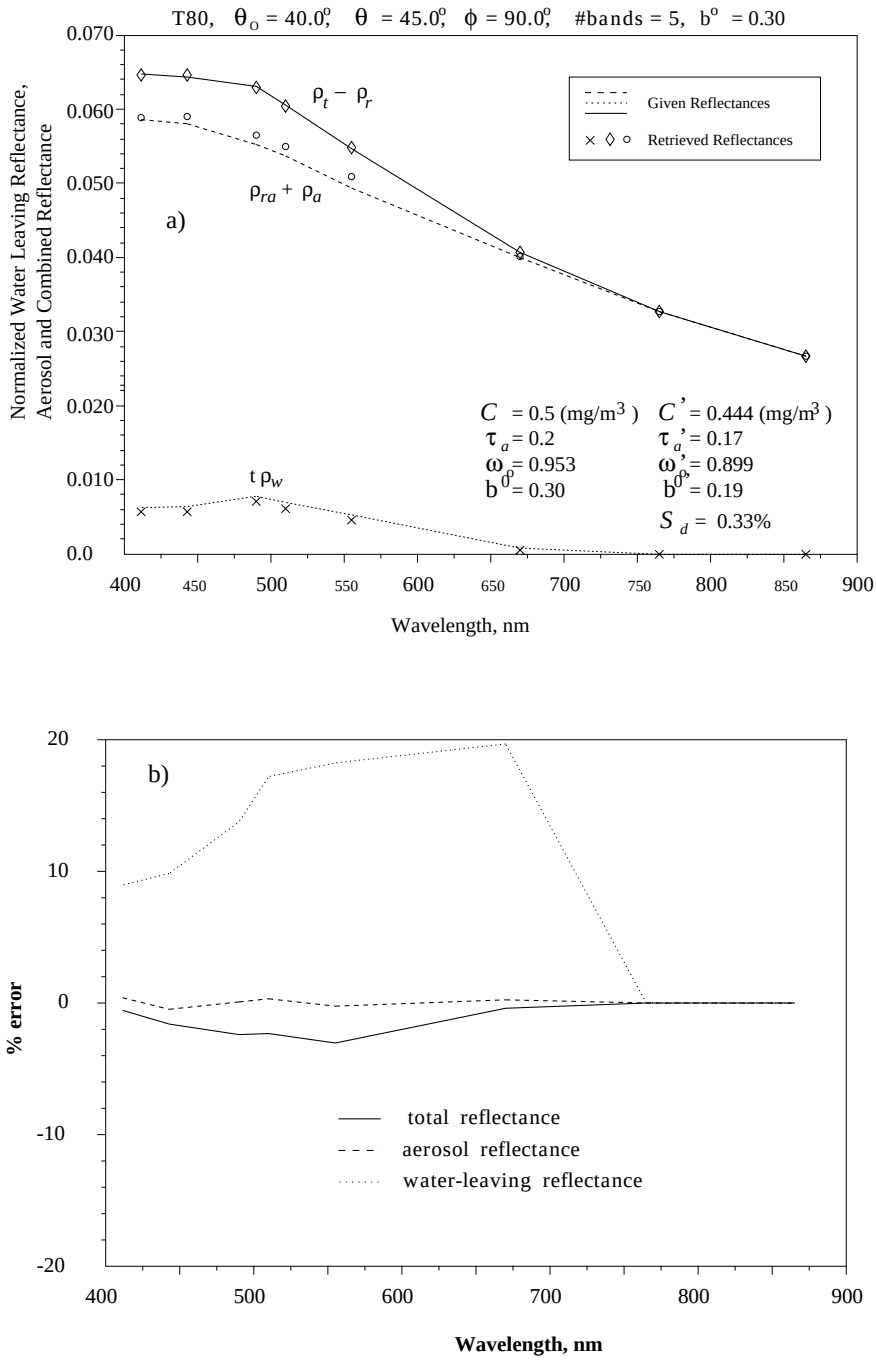

Figure 4.10 a) Retrieved the total, aerosol and water-leaving reflectances for the Tropospheric-80 test model having the optical thickness $\tau_a(865) = 0.2$ and, the ocean water pigment concentration and the scattering parameter $C = 0.5\ \mathrm{mg/m^3}$ and $b^0 = 0.3\ \mathrm{m^{-1}}$ respectively, for the sun-viewing geometry $\theta_0 = 40°, \theta = 45°, \phi = 90°$. b) respective retrieval errors

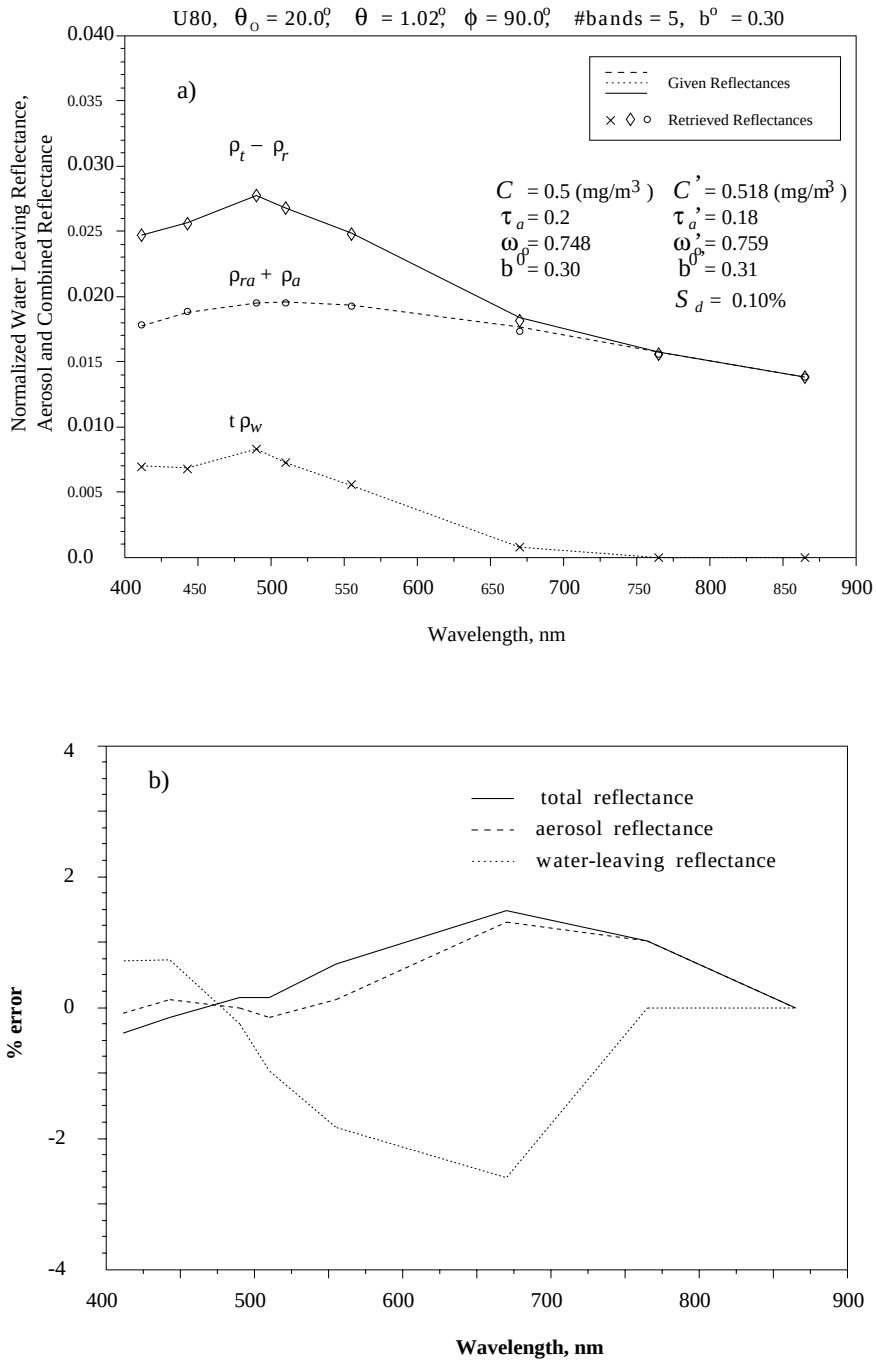

Figure 4.11 a) Retrieved the total, aerosol and water-leaving reflectances for the Urban-80 test model having the optical thickness $\tau_a(865) = 0.2$ and, the ocean water pigment concentration and the scattering parameter $C = 0.5$ mg/m^3 and $b^0 = 0.3$ m^{-1} respectively, for the sun-viewing geometry $\theta_0 = 20°, \theta = 1°, \phi = 90°$. b) respective retrieval errors

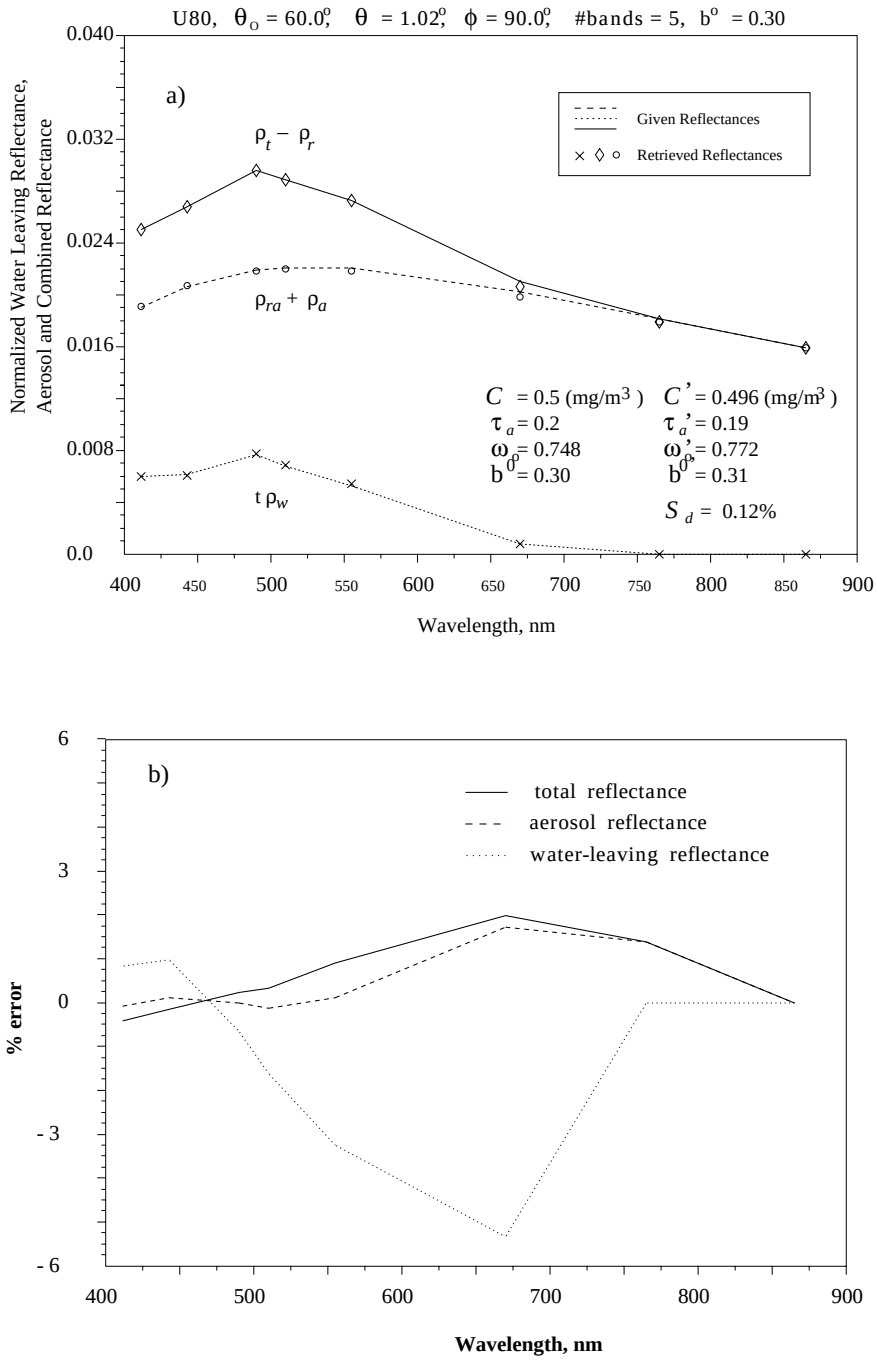

Figure 4.12 a) Retrieved the total, aerosol and water-leaving reflectances for the Urban-80 test model having the optical thickness $\tau_a(865) = 0.2$ and, the ocean water pigment concentration and the scattering parameter $C = 0.5$ mg/m^3 and $b^0 = 0.3$ m^{-1} respectively, for the sun-viewing geometry $\theta_0 = 60°, \theta = 1°, \phi = 90°$. b) respective retrieval errors

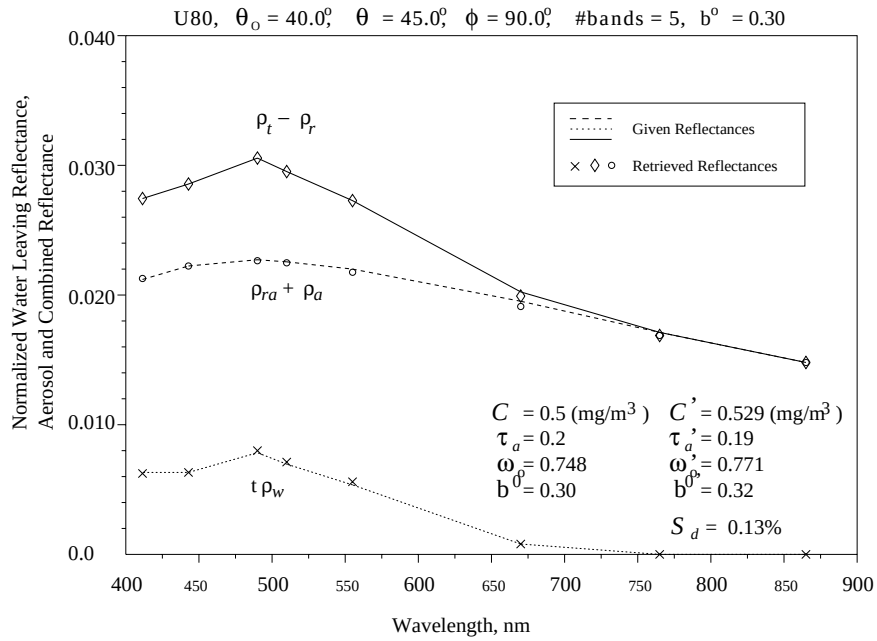

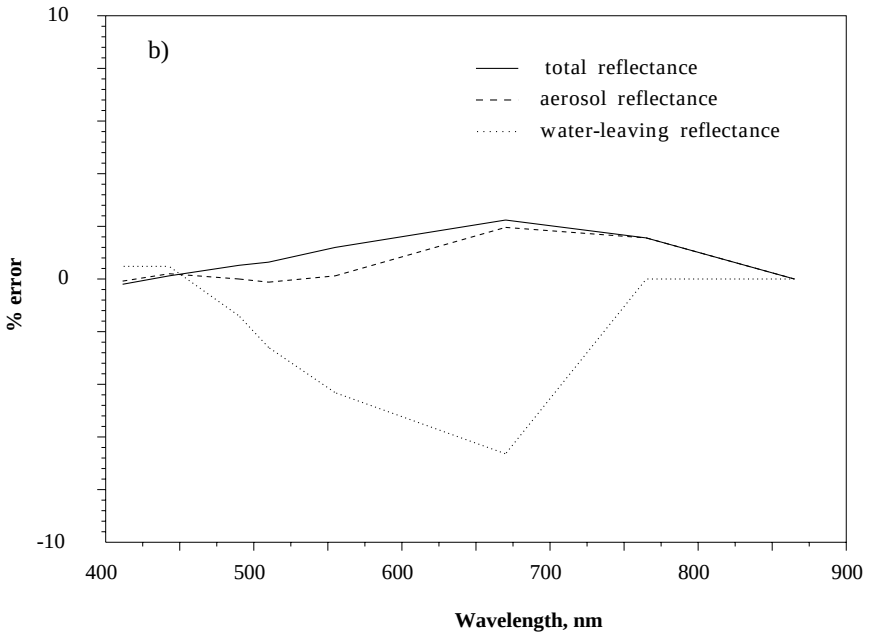

Figure 4.13 a) Retrieved the total, aerosol and water-leaving reflectances for the Urban-80 test model having the optical thickness $\tau_a(865) = 0.2$ and, the ocean water pigment concentration and the scattering parameter $C = 0.5$ mg/m^3 and $b^0 = 0.3$ m^{-1} respectively, for the sun-viewing geometry $\theta_0 = 40°, \theta = 45°, \phi = 90°$. b) respective retrieval errors

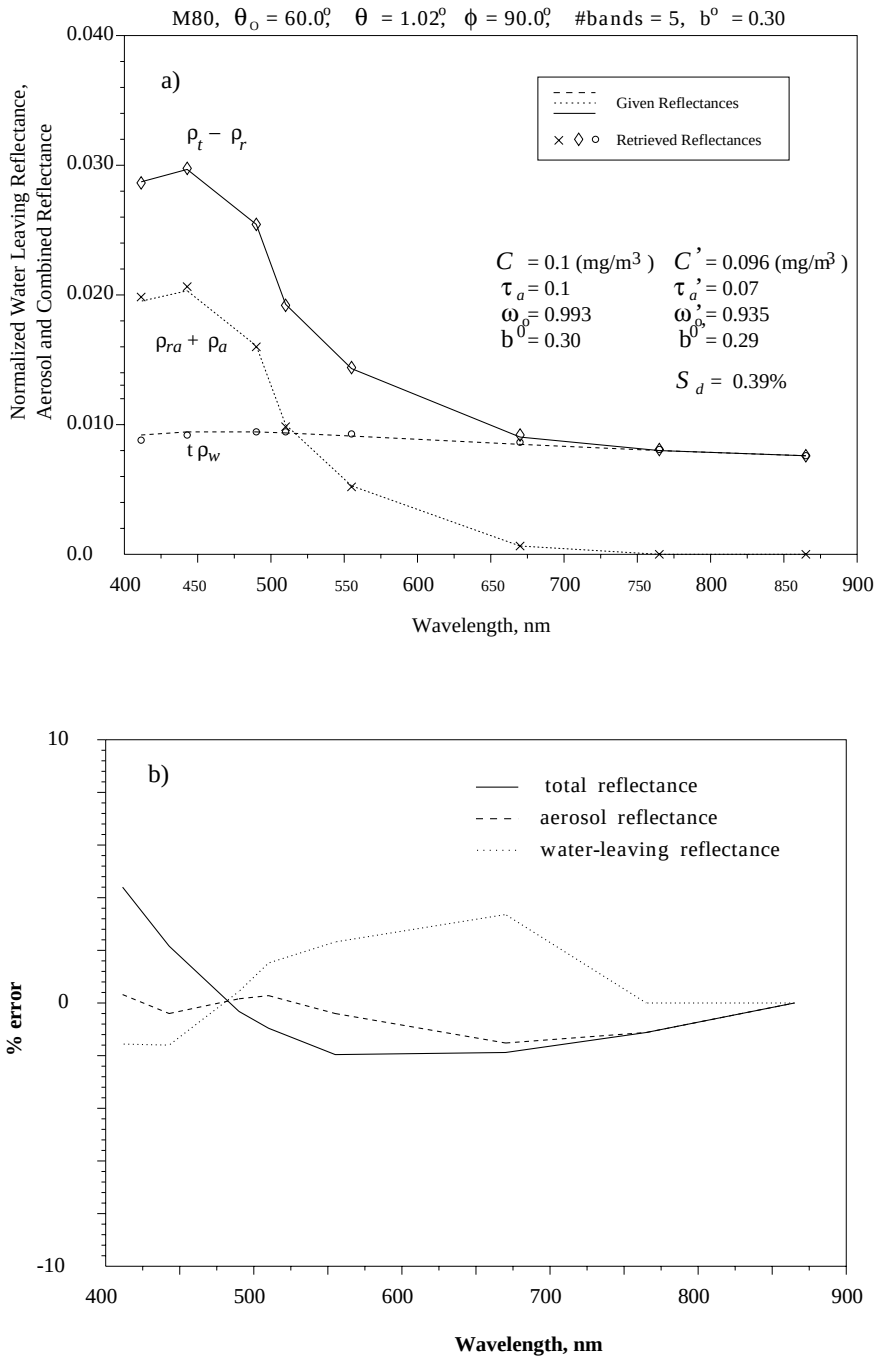

Figure 4.14 a) Retrieved the total, aerosol and water-leaving reflectances for the Maritime-80 test model having the optical thickness $\tau_a(865) = 0.1$ and, the ocean water pigment concentration and the scattering parameter $C = 0.1$ mg/m^3 and $b^0 = 0.3$ m^{-1} respectively, for the sun-viewing geometry $\theta_0 = 60°, \theta = 1°, \phi = 90°$. b) respective retrieval errors

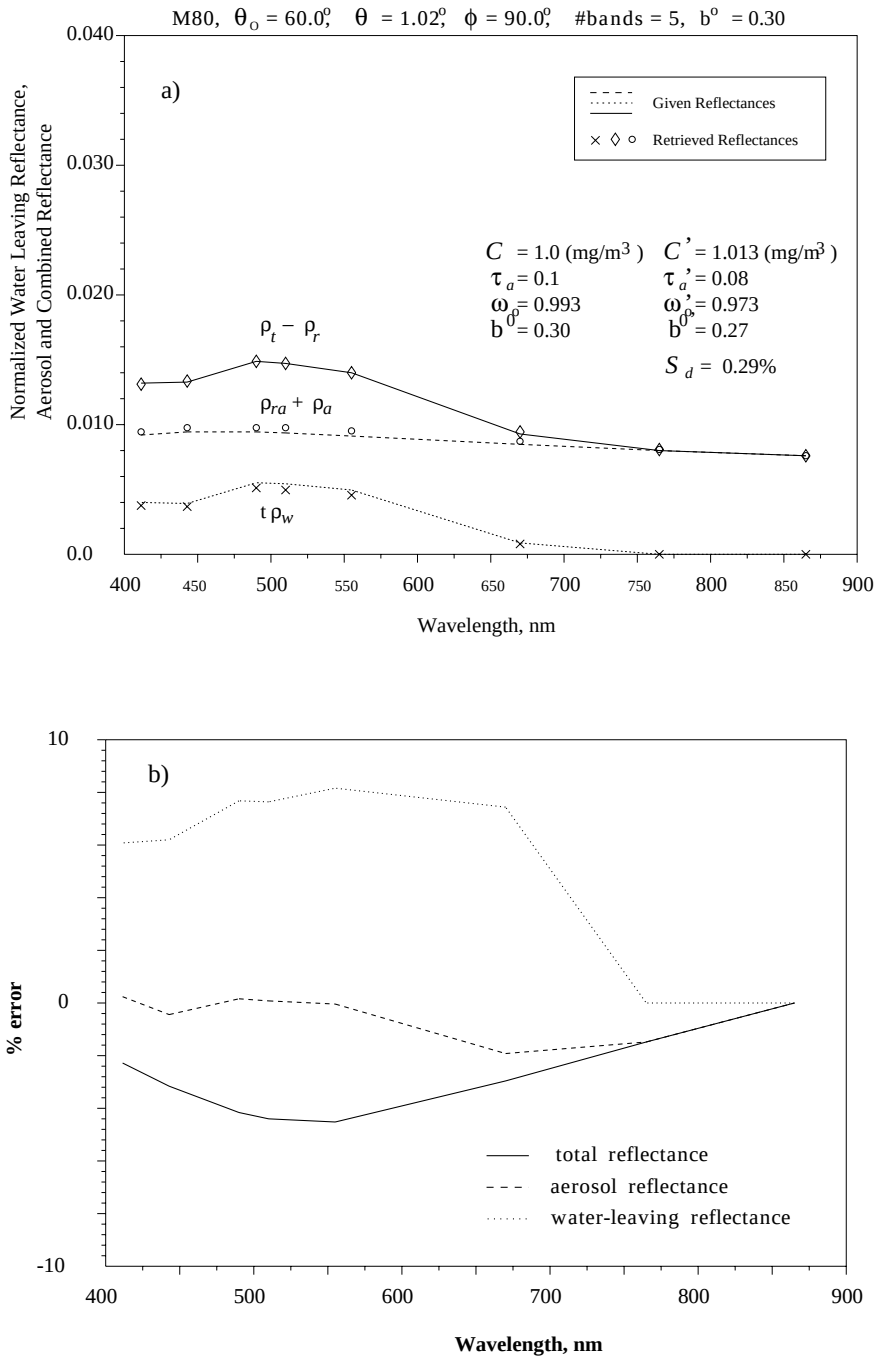

Figure 4.15 a) Retrieved the total, aerosol and water-leaving reflectances for the Maritime-80 test model having the optical thickness $\tau_a(865) = 0.1$ and, the ocean water pigment concentration and the scattering parameter $C = 1.0$ mg/m^3 and $b^0 = 0.3$ m^{-1} respectively, for the sun-viewing geometry $\theta_0 = 60°, \theta = 1°, \phi = 90°$. b) respective retrieval errors

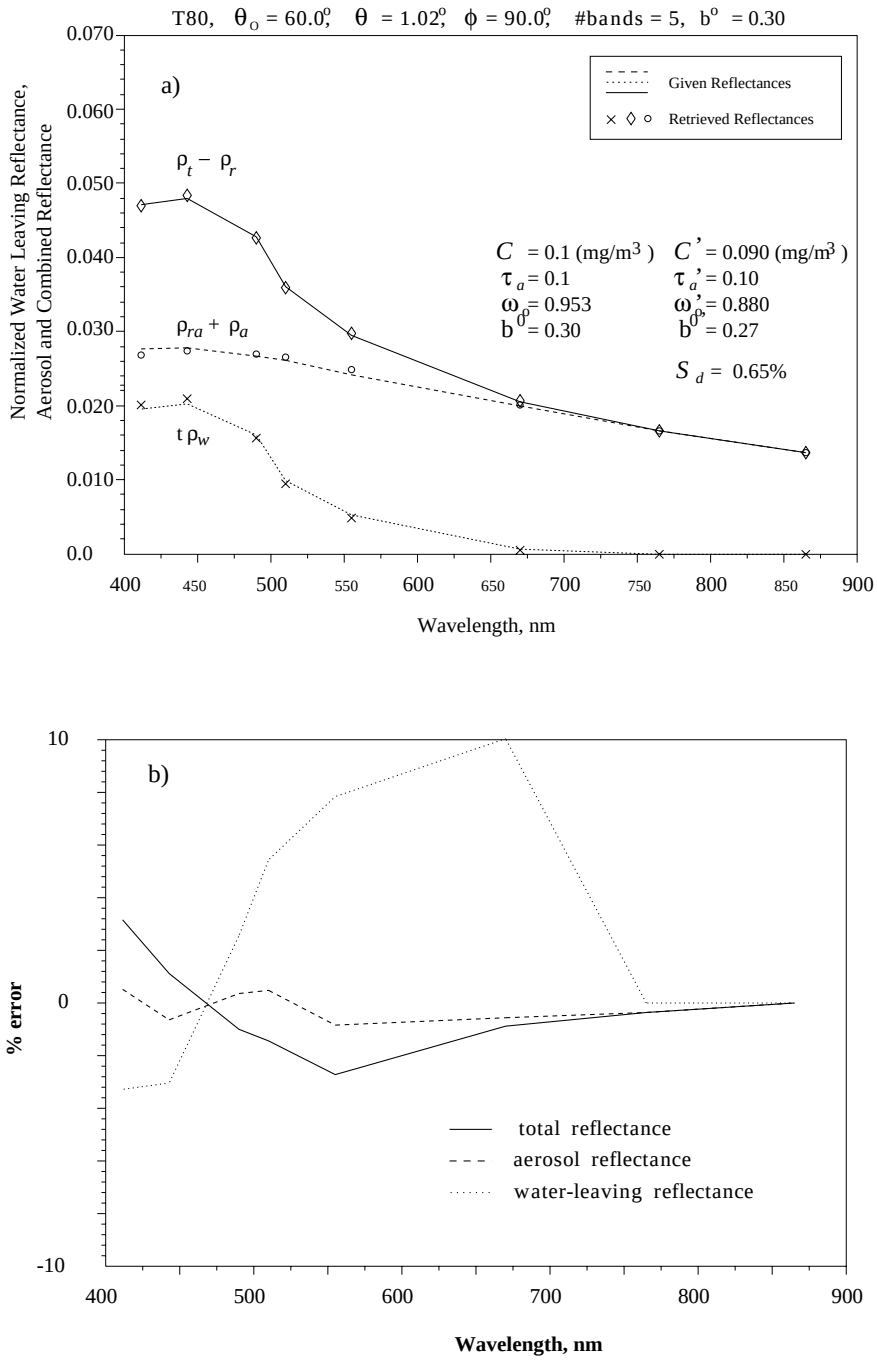

Figure 4.16 a) Retrieved the total, aerosol and water-leaving reflectances for the Tropospheric-80 test model having the optical thickness $\tau_a(865) = 0.1$ and, the ocean water pigment concentration and the scattering parameter $C = 0.1\,\mathrm{mg/m^3}$ and $b^0 = 0.3\,\mathrm{m}^{-1}$ respectively, for the sun-viewing geometry $\theta_0 = 60°, \theta = 1°, \phi = 90°$. b) respective retrieval errors

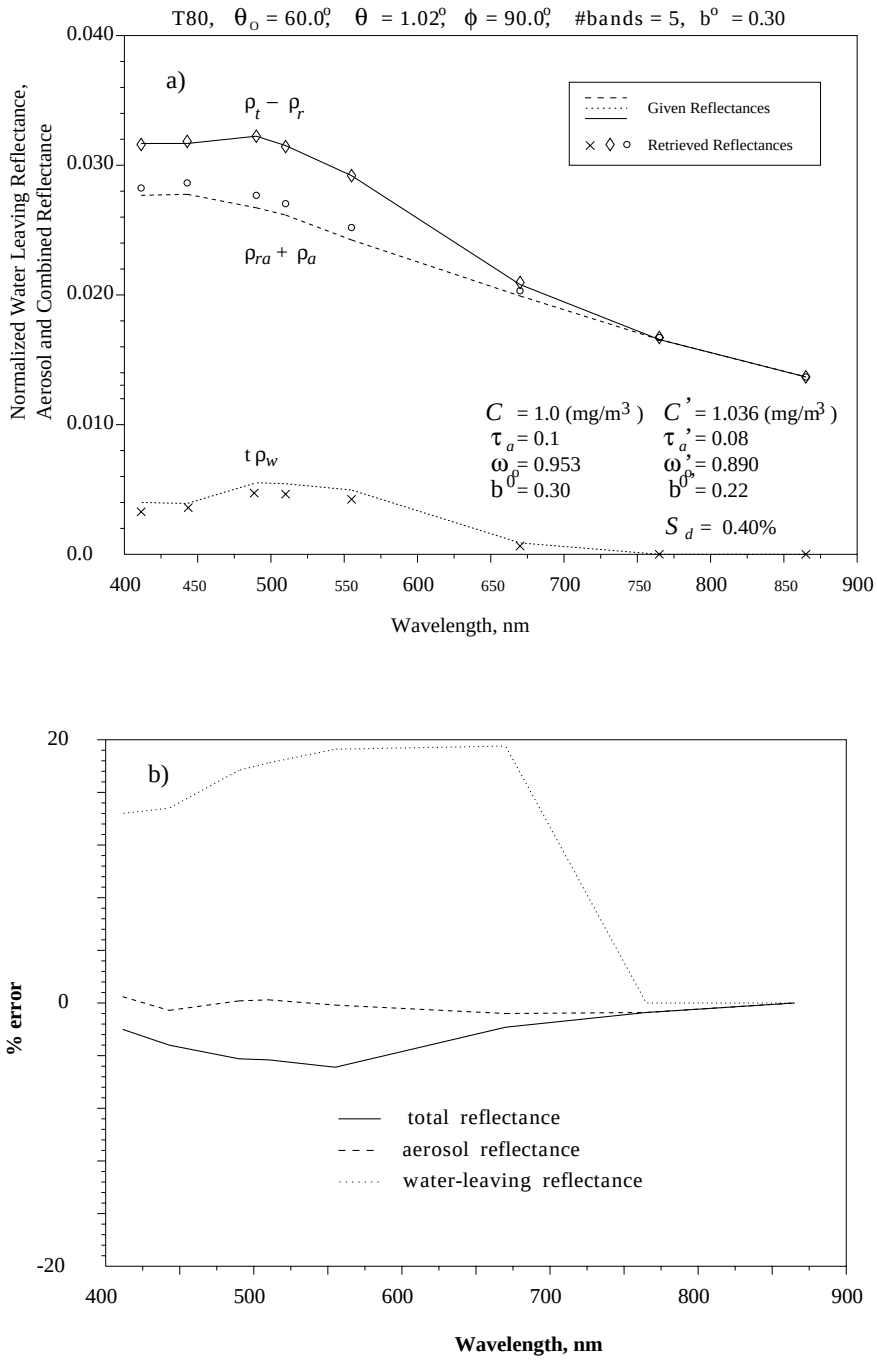

Figure 4.17 a) Retrieved the total, aerosol and water-leaving reflectances for the Tropospheric-80 test model having the optical thickness $\tau_a(865) = 0.1$ and, the ocean water pigment concentration and the scattering parameter $C = 1.0\,\mathrm{mg/m^3}$ and $b^0 = 0.3\,\mathrm{m^{-1}}$ respectively, for the sun-viewing geometry $\theta_0 = 60°, \theta = 1°, \phi = 90°$. b) respective retrieval errors

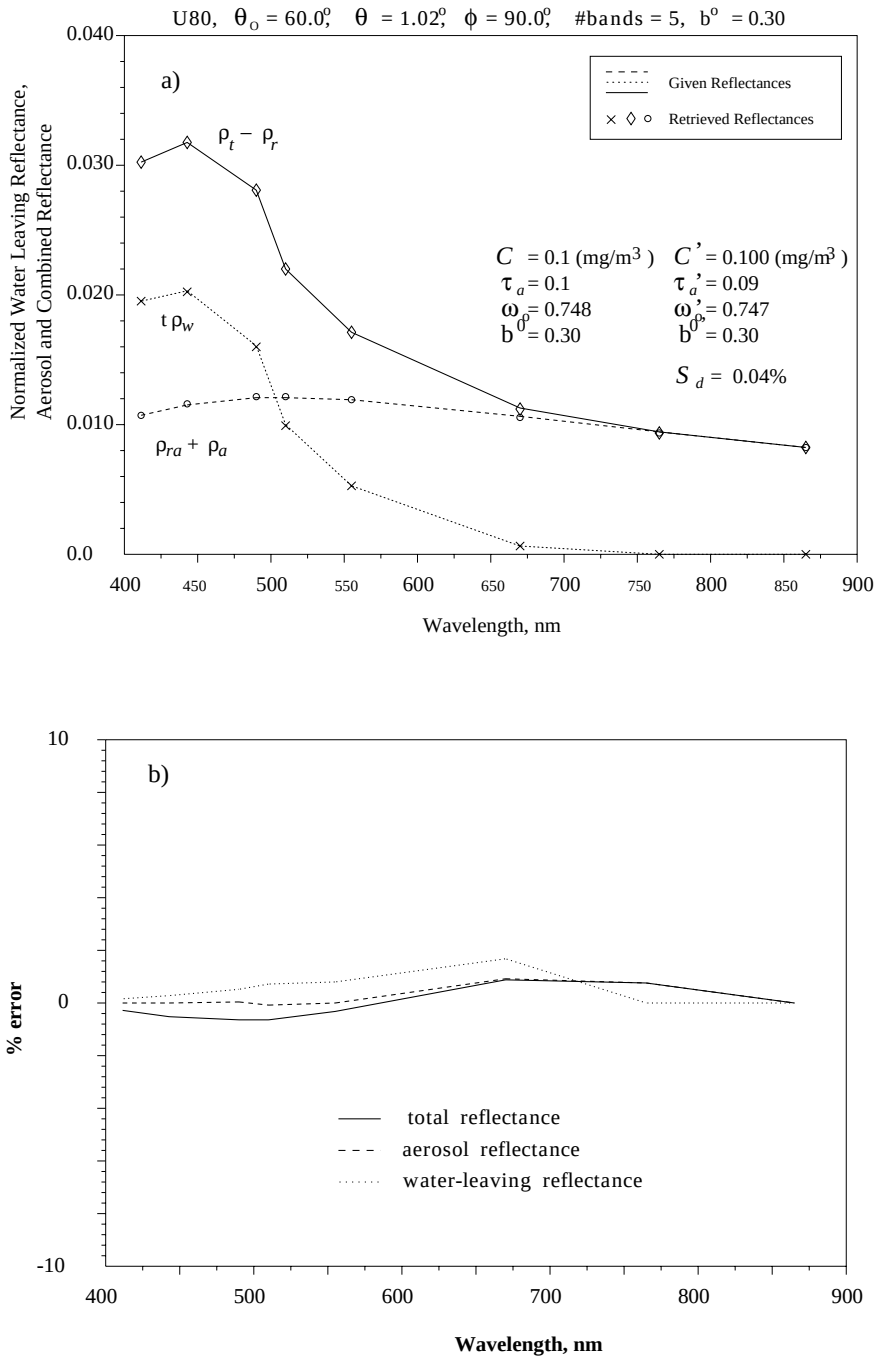

Figure 4.18 a) Retrieved the total, aerosol and water-leaving reflectances for the Urban-80 test model having the optical thickness $\tau_a(865) = 0.1$ and, the ocean water pigment concentration and the scattering parameter $C = 0.1$ mg/m^3 and $b^0 = 0.3$ m^{-1} respectively, for the sun-viewing geometry $\theta_0 = 60°, \theta = 1°, \phi = 90°$. b) respective retrieval errors

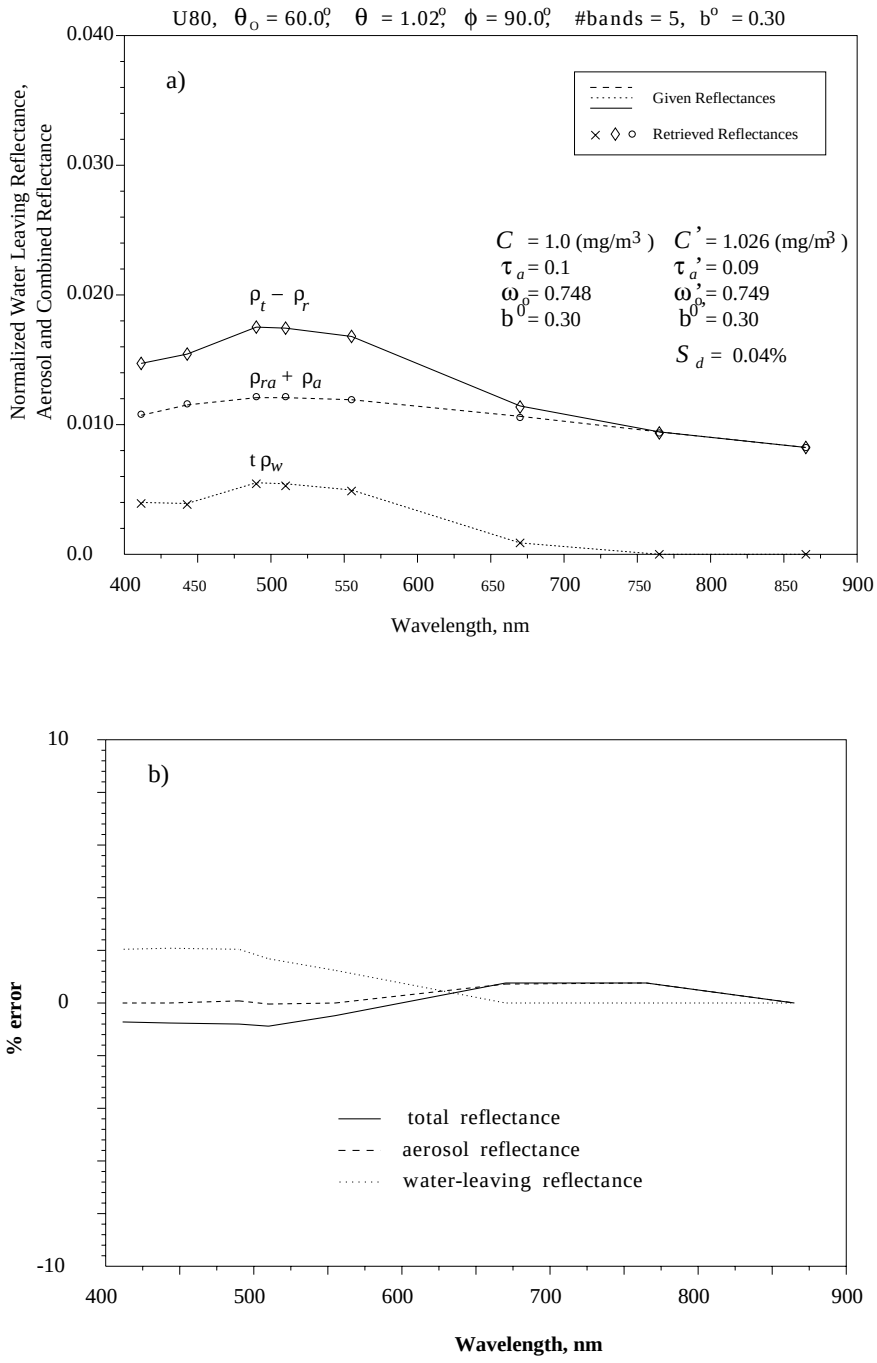

Figure 4.19 a) Retrieved the total, aerosol and water-leaving reflectances for the Urban-80 test model having the optical thickness $\tau_a(865) = 0.1$ and, the ocean water pigment concentration and the scattering parameter $C = 1.0$ mg/m^3 and $b^0 = 0.3$ m^{-1} respectively, for the sun-viewing geometry $\theta_0 = 60°, \theta = 1°, \phi = 90°$. b) respective retrieval errors

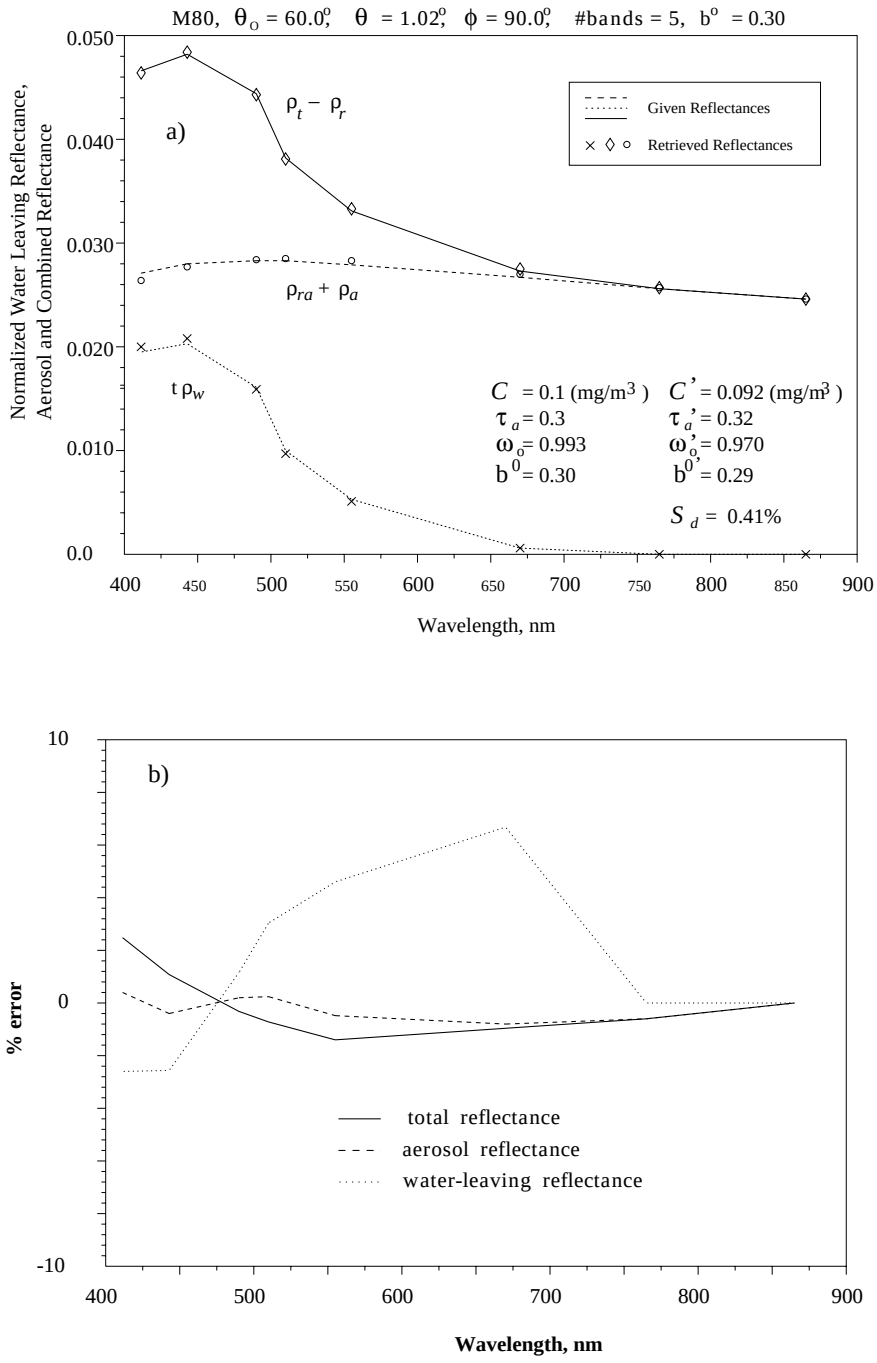

Figure 4.20 a) Retrieved the total, aerosol and water-leaving reflectances for the Maritime-80 test model having the optical thickness $\tau_a(865) = 0.3$ and, the ocean water pigment concentration and the scattering parameter $C = 0.1$ mg/m^3 and $b^0 = 0.3$ m^{-1} respectively, for the sun-viewing geometry $\theta_0 = 60°, \theta = 1°, \phi = 90°$. b) respective retrieval errors

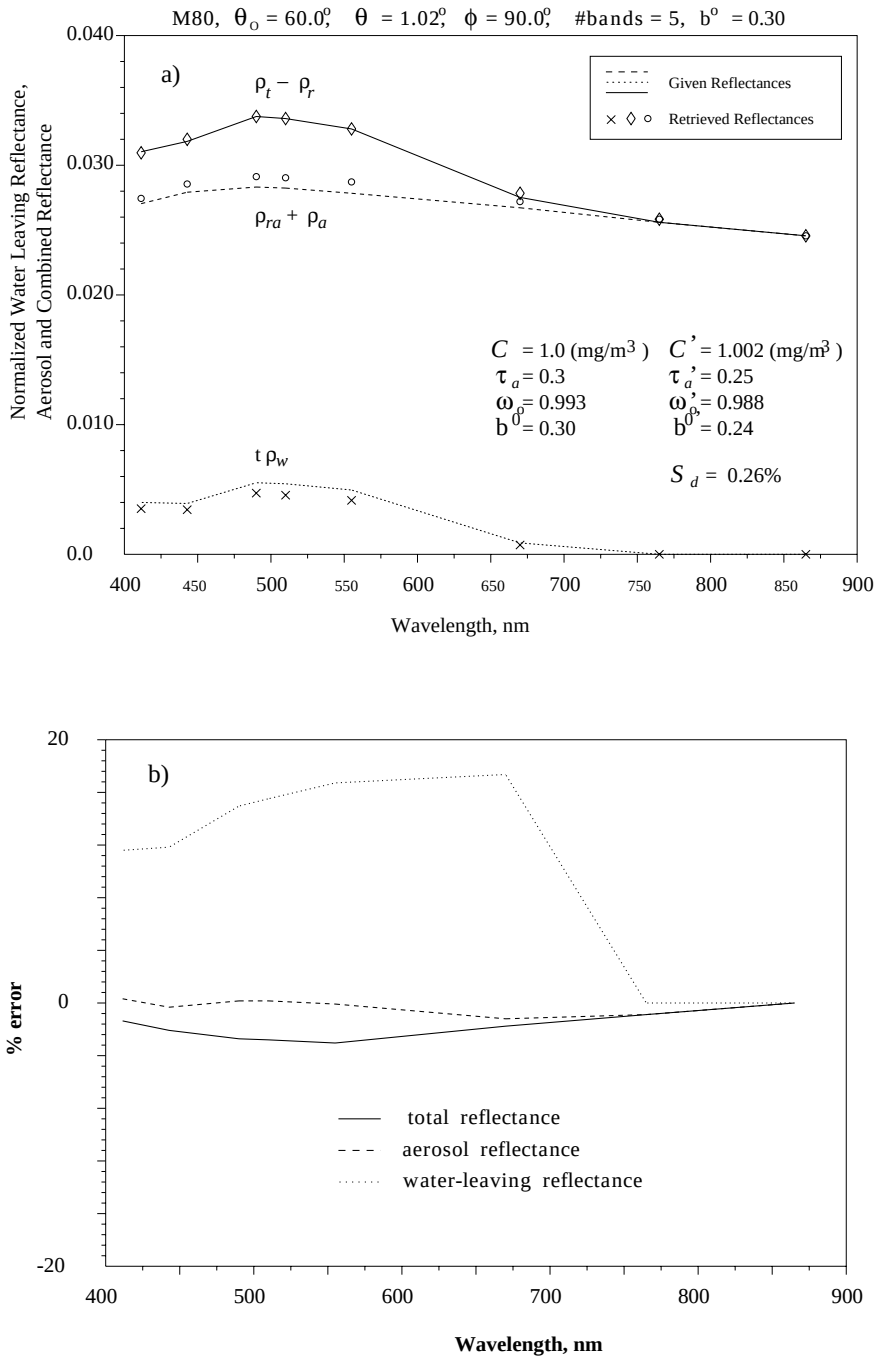

Figure 4.21 a) Retrieved the total, aerosol and water-leaving reflectances for the Maritime-80 test model having the optical thickness $\tau_a(865) = 0.3$ and, the ocean water pigment concentration and the scattering parameter $C = 1.0$ mg/m^3 and $b^0 = 0.3$ m^{-1} respectively, for the sun-viewing geometry $\theta_0 = 60°, \theta = 1°, \phi = 90°$. b) respective retrieval errors

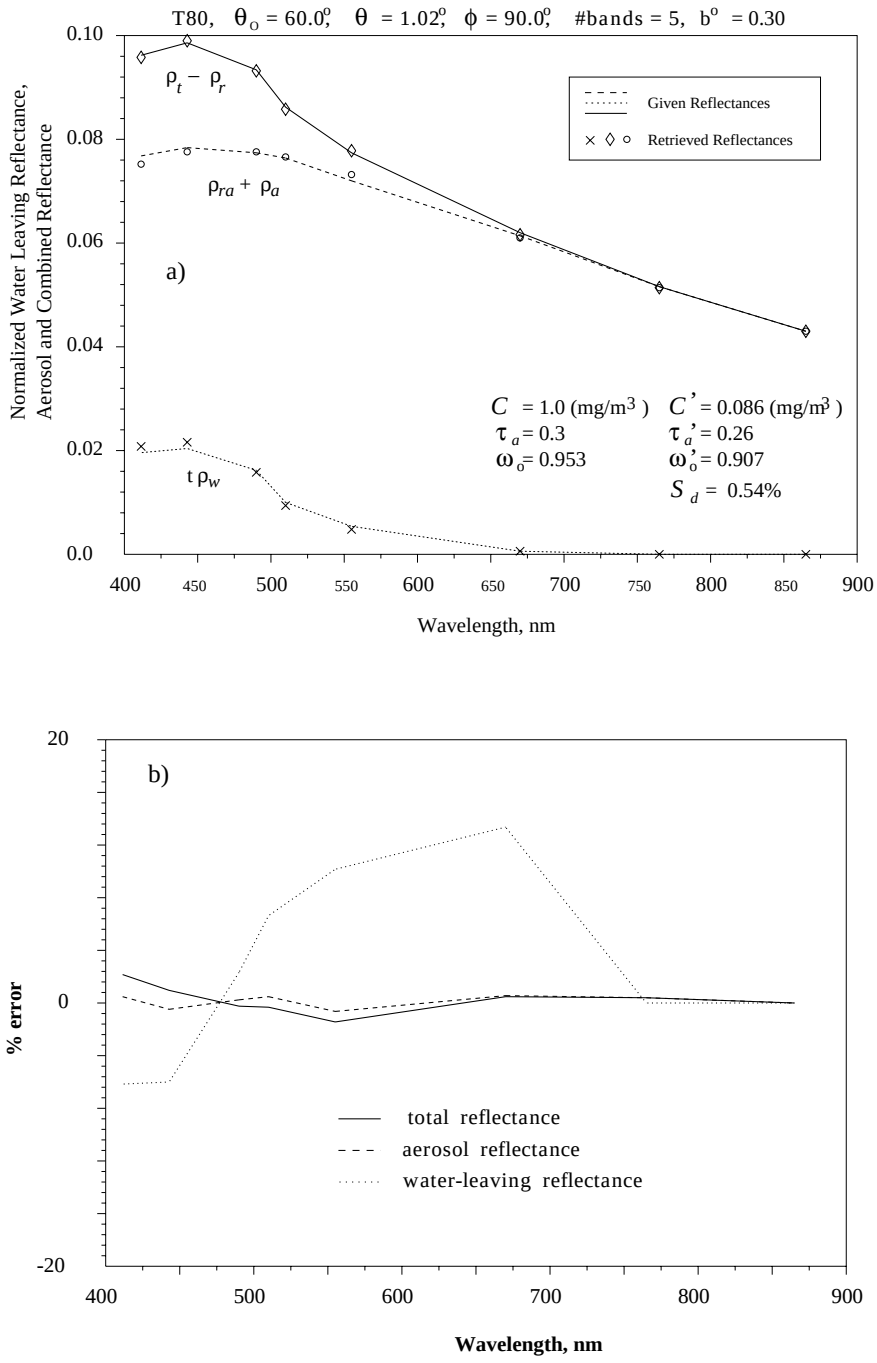

Figure 4.22 a) Retrieved the total, aerosol and water-leaving reflectances for the Tropospheric-80 test model having the optical thickness $\tau_a(865) = 0.3$ and, the ocean water pigment concentration and the scattering parameter $C = 0.1\,\mathrm{mg/m^3}$ and $b^0 = 0.3\,\mathrm{m}^{-1}$ respectively, for the sun-viewing geometry $\theta_0 = 60°, \theta = 1°, \phi = 90°$. b) respective retrieval errors

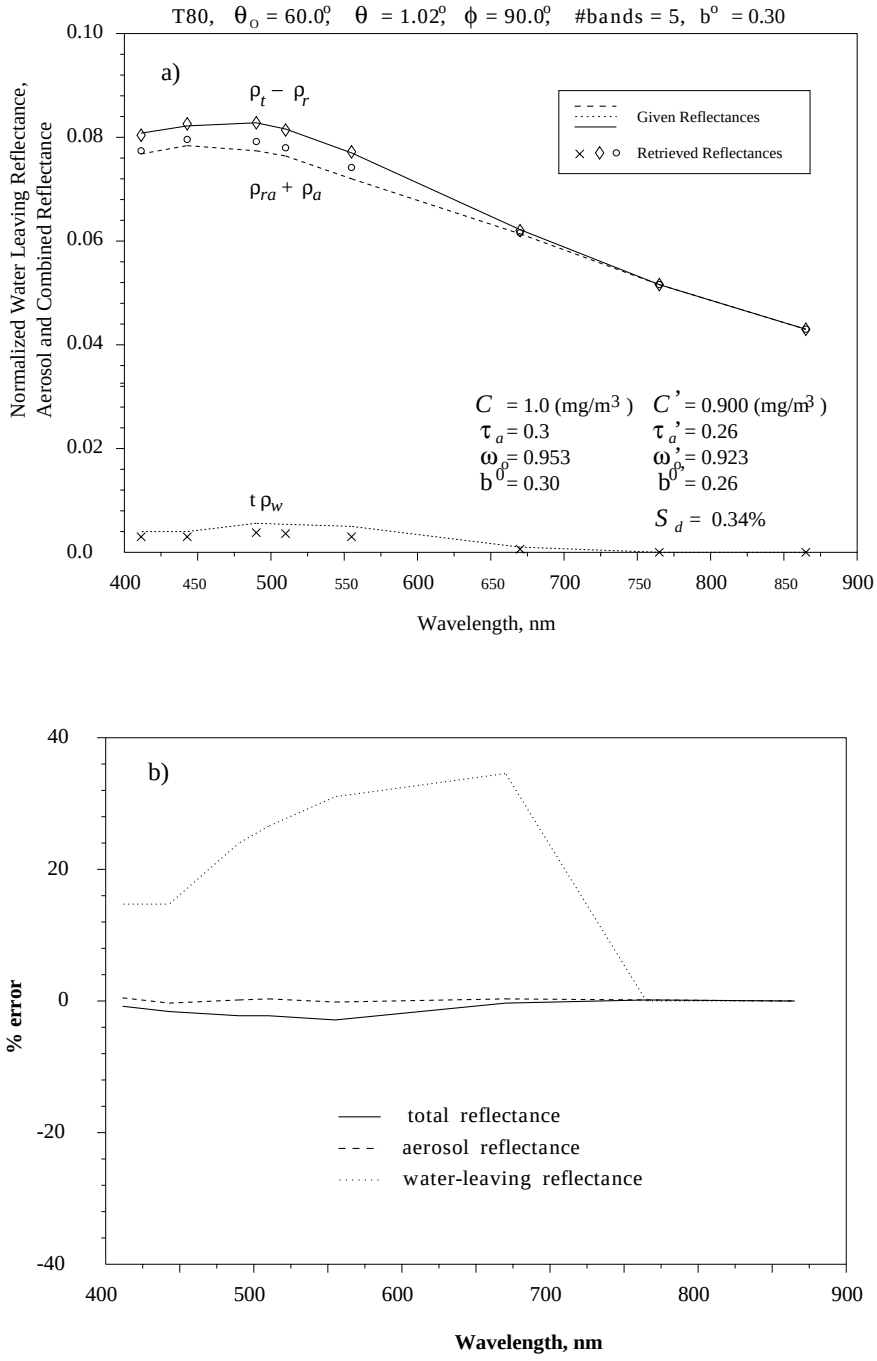

Figure 4.23 a) Retrieved the total, aerosol and water-leaving reflectances for the Tropospheric-80 test model having the optical thickness $\tau_a(865) = 0.3$ and, the ocean water pigment concentration and the scattering parameter $C = 1.0\,\mathrm{mg/m^3}$ and $b^0 = 0.3\,\mathrm{m^{-1}}$ respectively, for the sun-viewing geometry $\theta_0 = 60°, \theta = 1°, \phi = 90°$. b) respective retrieval errors

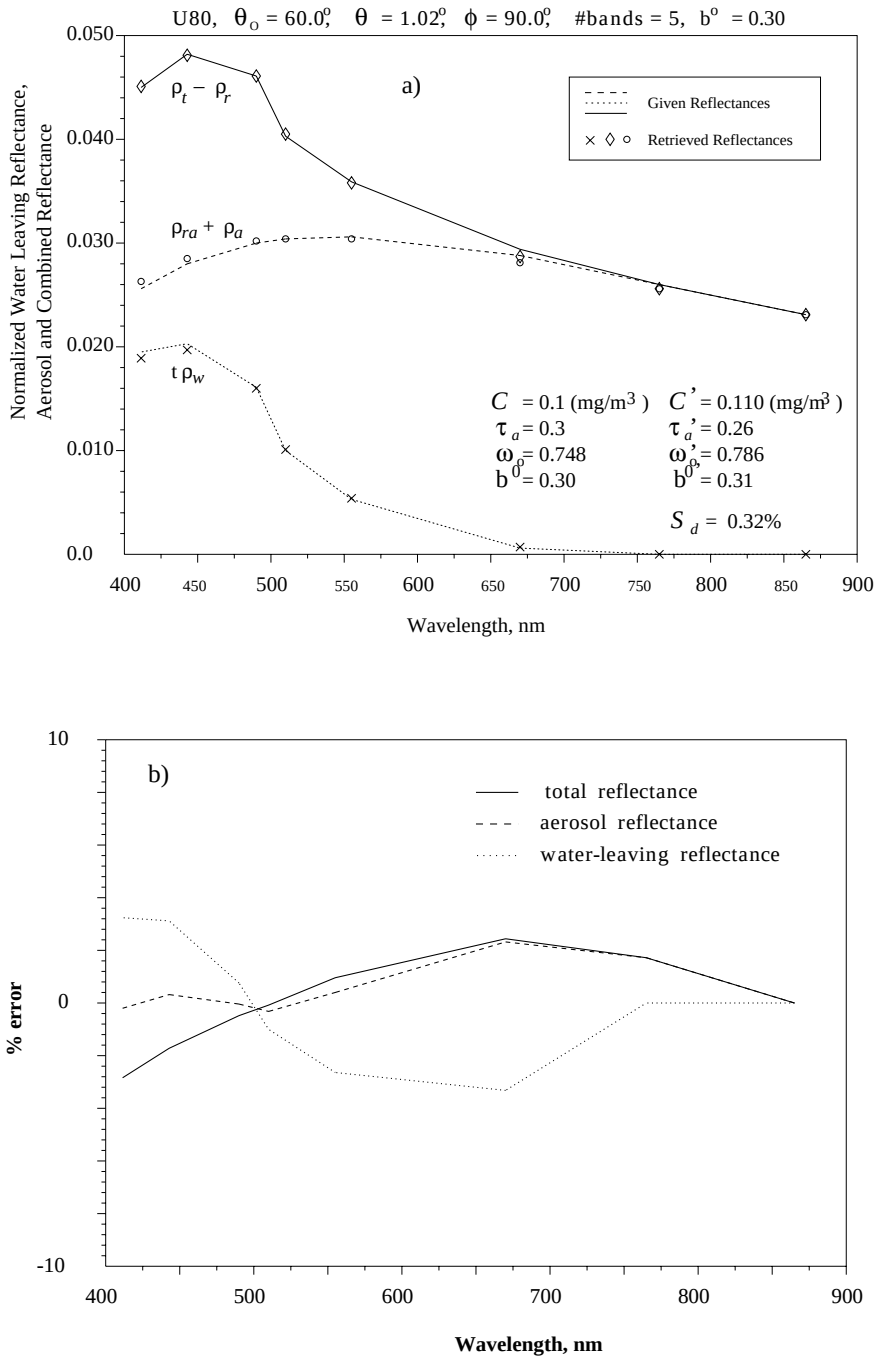

Figure 4.24 a) Retrieved the total, aerosol and water-leaving reflectances for the Urban-80 test model having the optical thickness $\tau_a(865) = 0.3$ and, the ocean water pigment concentration and the scattering parameter $C = 0.1$ mg/m^3 and $b^0 = 0.3$ m^{-1} respectively, for the sun-viewing geometry $\theta_0 = 60°, \theta = 1°, \phi = 90°$. b) respective retrieval errors

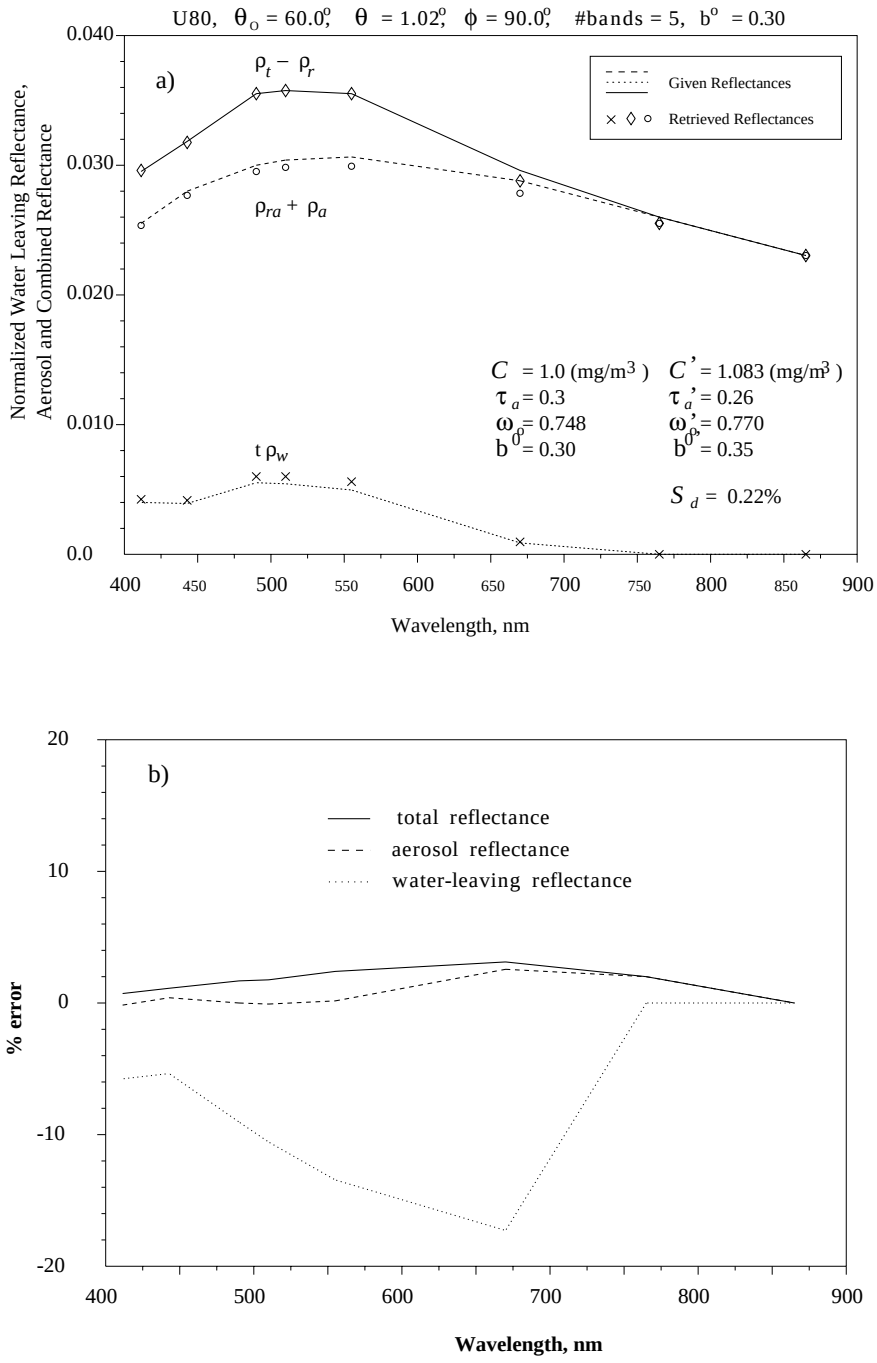

Figure 4.25 a) Retrieved the total, aerosol and water-leaving reflectances for the Urban-80 test model having the optical thickness $\tau_a(865) = 0.3$ and, the ocean water pigment concentration and the scattering parameter $C = 1.0$ mg/m^3 and $b^0 = 0.3$ m^{-1} respectively, for the sun-viewing geometry $\theta_0 = 60°, \theta = 1°, \phi = 90°$. b) respective retrieval errors

RETRIEVAL OF OCEAN's PIGMENT CONCENTRATION

Tabulated are mean values of retrieved C for seven Sun-Viewing Geometries and each of four hypothetical atmospheric aerosols (M80, C80, T80, U80). Also, provided are the standard deviations over viewing geometries divided by the mean (S_d) as well as the deviations from given parameters (D).

	C: mg/m^3	0.100			0.500			1.000		
		result	S_d	D	result	S_d	D	result	S_d	D
M80	$\tau_a(865) = 0.10$	**0.096**	1.8%	4.00%	**0.488**	1.8%	2.40%	**1.012**	1.1%	1.20%
$\omega_0 = 0.993$	$\tau_a(865) = 0.20$	**0.094**	2.9%	6.00%	**0.479**	3.7%	4.20%	**1.014**	2.3%	1.40%
	$\tau_a(865) = 0.30$	**0.093**	3.2%	7.00%	**0.473**	4.6%	5.40%	**1.010**	3.5%	1.00%

	C: mg/m^3	0.100			0.500			1.000		
		result	S_d	D	result	S_d	D	result	S_d	D
C80	$\tau_a(865) = 0.10$	**0.096**	2.1%	4.00%	**0.484**	2.1%	3.20%	**1.001**	1.9%	0.10%
$\omega_0 = 0.988$	$\tau_a(865) = 0.20$	**0.094**	3.2%	6.00%	**0.469**	1.7%	6.20%	**0.984**	4.3%	1.60%
	$\tau_a(865) = 0.30$	**0.093**	2.8%	7.00%	**0.459**	4.9%	8.20%	**0.959**	7.3%	4.10%

	C: mg/m^3	0.100			0.500			1.000		
		result	S_d	D	result	S_d	D	result	S_d	D
T80	$\tau_a(865) = 0.10$	**0.091**	4.9%	9.00%	**0.466**	4.0%	6.80%	**1.021**	6.1%	2.10%
$\omega_0 = 0.953$	$\tau_a(865) = 0.20$	**0.086**	1.9%	14.0%	**0.425**	9.9%	15.0%	**0.941**	7.0%	5.90%
	$\tau_a(865) = 0.30$	**0.090**	5.7%	10.0%	**0.412**	6.8%	17.6%	**0.874**	6.7%	12.6%

	C: mg/m^3	0.100			0.500			1.000		
		result	S_d	D	result	S_d	D	result	S_d	D
U80	$\tau_a(865) = 0.10$	**0.100**	0.8%	0.00%	**0.507**	0.7%	1.40%	**1.028**	1.9%	2.80%
$\omega_0 = 0.748$	$\tau_a(865) = 0.20$	**0.104**	1.4%	4.00%	**0.526**	2.7%	5.20%	**1.053**	3.2%	5.30%
	$\tau_a(865) = 0.30$	**0.110**	4.3%	10.0%	**0.552**	5.8%	10.4%	**1.070**	4.0%	7.00%

Table 4.4

RETRIEVAL OF AEROSOL's SINGLE-SCATTERING ALBEDO

Tabulated are mean values of retrieved ω_0 *for seven Sun-Viewing Geometries and each of four hypothetical atmospheric aerosols (M80, C80, T80, U80). Also, provided are the standard deviations over viewing geometries divided by the mean (* S_d *) as well as the deviations from given parameters (D).*

	C: mg/m^3	*0.100*			*0.500*			*1.000*		
		result	S_d	*D*	*result*	S_d	*D*	*result*	S_d	*D*
M80	$\tau_a(865) = 0.10$	**0.938**	2.5%	5.50%	**0.968**	1.9%	2.40%	**0.972**	2.2%	2.12%
$\omega_0 = 0.993$	$\tau_a(865) = 0.20$	**0.954**	2.2%	3.93%	**0.971**	2.4%	2.22%	**0.974**	2.5%	1.91%
	$\tau_a(865) = 0.30$	**0.963**	1.8%	3.02%	**0.976**	1.9%	1.22%	**0.979**	2.0%	1.41%

	C: mg/m^3	*0.100*			*0.500*			*1.000*		
		result	S_d	*D*	*result*	S_d	*D*	*result*	S_d	*D*
C80	$\tau_a(865) = 0.10$	**0.943**	2.3%	4.56%	**0.970**	1.7%	3.20%	**0.972**	1.7%	1.62%
$\omega_0 = 0.988$	$\tau_a(865) = 0.20$	**0.960**	2.1%	2.83%	**0.977**	1.7%	1.11%	**0.979**	1.8%	0.91%
	$\tau_a(865) = 0.30$	**0.969**	1.9%	1.92%	**0.981**	1.6%	0.71%	**0.983**	1.5%	0.51%

	C: mg/m^3	*0.100*			*0.500*			*1.000*		
		result	S_d	*D*	*result*	S_d	*D*	*result*	S_d	*D*
T80	$\tau_a(865) = 0.10$	**0.842**	4.9%	11.6%	**0.867**	4.5%	9.02%	**0.872**	4.4%	8.50%
$\omega_0 = 0.953$	$\tau_a(865) = 0.20$	**0.877**	1.9%	8.00%	**0.891**	2.0%	6.51%	**0.892**	1.9%	6.40%
	$\tau_a(865) = 0.30$	**0.902**	1.6%	5.35%	**0.914**	1.0%	4.09%	**0.918**	1.0%	3.67%

	C: mg/m^3	*0.100*			*0.500*			*1.000*		
		result	S_d	*D*	*result*	S_d	*D*	*result*	S_d	*D*
U80	$\tau_a(865) = 0.10$	**0.744**	4.7%	0.54%	**0.745**	4.3%	1.40%	**0.745**	4.4%	0.40%
$\omega_0 = 0.748$	$\tau_a(865) = 0.20$	**0.770**	0.8%	2.94%	**0.769**	0.8%	2.81%	**0.770**	1.3%	2.94%
	$\tau_a(865) = 0.30$	**0.788**	1.7%	5.35%	**0.777**	1.2%	3.88%	**0.773**	1.5%	3.34%

Table 4.5

RETRIEVAL OF WATER SCATTERING PARAMETER

Tabulated are mean values of retrieved b^0 *for seven Sun-Viewing Geometries and each of four hypothetical atmospheric aerosols (M80, C80, T80, U80). Also, provided are the standard deviations over viewing geometries divided by the mean (S_d) as well as the deviations from given parameters (D).*

	C: mg/m^3	0.100			0.500			1.000		
		result	S_d	D	result	S_d	D	result	S_d	D
M80	$\tau_a(865) = 0.10$	**0.294**	1.1%	2.00%	**0.274**	4.1%	8.67%	**0.273**	4.4%	3.20%
$\omega_0 = 0.993$	$\tau_a(865) = 0.20$	**0.289**	1.7%	3.67%	**0.258**	7.3%	14.%	**0.255**	8.2%	15.0%
	$\tau_a(865) = 0.30$	**0.286**	1.8%	4.67%	**0.249**	8.2%	17.0%	**0.246**	9.4%	18.0%

	C: mg/m^3	0.100			0.500			1.000		
		result	S_d	D	result	S_d	D	result	S_d	D
C80	$\tau_a(865) = 0.10$	**0.293**	1.6%	2.33%	**0.273**	4.9%	3.20%	**0.271**	5.3%	9.67%
$\omega_0 = 0.988$	$\tau_a(865) = 0.20$	**0.289**	2.2%	3.67%	**0.255**	8.0%	15.0%	**0.250**	9.0%	16.7%
	$\tau_a(865) = 0.30$	**0.287**	2.0%	4.33%	**0.247**	7.4%	17.7%	**0.239**	8.7%	20.3%

	C: mg/m^3	0.100			0.500			1.000		
		result	S_d	D	result	S_d	D	result	S_d	D
T80	$\tau_a(865) = 0.10$	**0.278**	6.5%	7.33%	**0.237**	18.%	21.0%	**0.234**	19.%	22.%
$\omega_0 = 0.953$	$\tau_a(865) = 0.20$	**0.270**	6.4%	10.0%	**0.200**	23.%	33.3%	**0.193**	23.7%	36.%
	$\tau_a(865) = 0.30$	**0.288**	5.1%	4.00%	**0.201**	20.%	33.0%	**0.186**	25.%	38.0%

	C: mg/m^3	0.100			0.500			1.000		
		result	S_d	D	result	S_d	D	result	S_d	D
U80	$\tau_a(865) = 0.10$	**0.297**	1.0%	1.00%	**0.298**	1.8%	0.67%	**0.298**	1.7%	0.67%
$\omega_0 = 0.748$	$\tau_a(865) = 0.20$	**0.302**	0.5%	0.67%	**0.316**	1.9%	5.33%	**0.319**	2.4%	6.33%
	$\tau_a(865) = 0.30$	**0.311**	1.5%	3.67%	**0.350**	8.2%	16.7%	**0.354**	8.1%	18.0%

Table 4.6

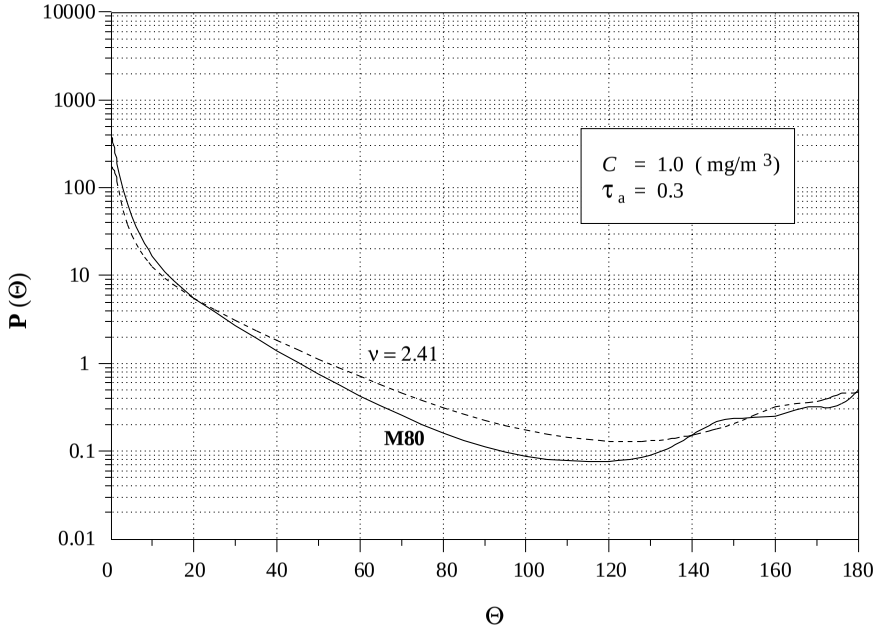

Figure 4.26 Comparison of the true (solid curve) and retrieved (dashed curve) single-scattering phase functions at 865 nm for M80 test aerosol model

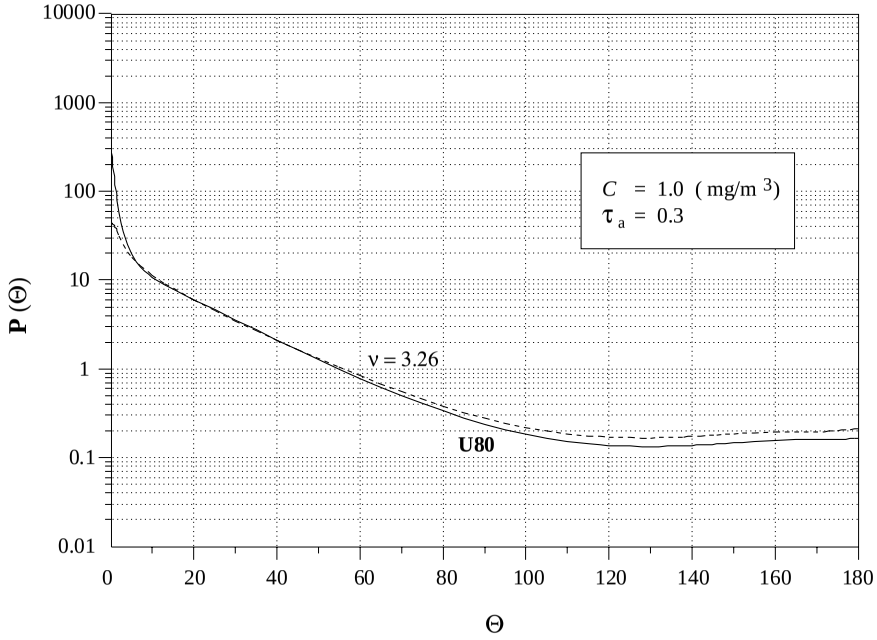

Figure 4.27 Comparison of the true (solid curve) and retrieved (dashed curve) single-scattering phase functions at 865 nm for U80 test aerosol model

C. Pseudo $\rho_t(\lambda)$ for M80, C80, T80, U80 test aerosol models with added sensor calibration error

To assess the effect of the sensor calibration errors in $\rho_t(\lambda)$ on the algorithm performance we adopt the approach outlined by Gordon.[42] The pseudo-reflectance data $\rho_t(\lambda)$ measured by a remote sensor were simulated for models M80, C80, T80, U80, as in the previous subsection, and a pseudo-calibration error added to all bands as follows:

$$\rho_t'(\lambda) = \rho_t(\lambda)\,[1 + \alpha(\lambda)], \tag{4.2}$$

where $\alpha(\lambda)$ is the fractional error in $\rho_t(\lambda)$, $\rho_t'(\lambda)$ is the pseudo-reflectance at the TOA measured by a sensor.

Table 4.7: Values of the Residual Radiometric Uncertainty after Effecting an In-Orbit Calibration Adjustment

λ_i, nm	Uncertainty, %
412	0.3
443	0.5
490	0.8
510	1.0
555	1.5
670	2.0
765	3.0
865	5.0

Gordon[42] has demonstrated an in-orbit calibration procedure for which the residual calibration error in all the visible bands will have the same sign as in NIR bands and, the magnitude of the error will progressively decrease from NIR to visible bands roughly as the Rayleigh reflectance ρ_r increases (which is calculated exactly and has the greatest impact on the total reflectance ρ_t in the blue). Assuming $\sim 5\%$ calibration error at 865 nm, following Gordon [42] the values of the residual radiometric uncertainty $\alpha(\lambda)$ for all bands after effecting the vicarious calibration procedure are provided in the Table 4.7. We consider both positive and negative calibration errors.

The retrieval of the ocean pigment concentration has been summarized in the Table 4.8 (positive calibration errors) and Table 4.9 (negative calibration errors) where parameter values were averaged over all sun-viewing geometries (Eq. (4.1)). The "true" and retrieved reflectances are shown for two particular cases with added positive calibration error: 1) M80 test aerosol, the low optical thickness $\tau_a(865) = 0.1$, the low pigment concentration $C = 0.1$ mg/m^3 and the geometry with $\theta_0 = 20°, \theta = 45.9°$ (Fig. 4.28); 2) U80 test aerosol, the high optical thickness $\tau_a(865) = 0.3$, the high pigment concentration $C = 1.0$ mg/m^3 and the geometry $\theta_0 = 40°, \theta = 1°$ (Figure 4.29). We can observe that the fit of the computed total reflectance $\rho_t(\lambda) - \rho_r(\lambda)$ to the given one was excellent, the objective function still being small (0.12%-0.40%) while the fits to the aerosol and water-leaving reflectances were slightly degraded.

The retrieval error for the pigment concentration C was 6% for the positive calibration errors and about 9% for negative calibration errors. Apparently, the negative calibration errors generally affect the retrievals more adversely. The reason is the way we determine the Junge power-law parameter ν, i.e., using the Eq. (3.7), which results in the larger values for ν when the errors are negative and the smaller when the errors are positive. The reflectivity of aerosols with the larger values of ν increases and the total reflectivity is compensated by varying the water scattering parameter b^0 in such a manner as to reduce the water-leaving reflectance keeping the pigment concentration almost unchanged. In contrast, the pigment concentration is varied when the ν decreases.

Compared to the results in the previous subsection, where the calibration errors were absent, the results were only slightly degraded. The average error of the retrieved pigment concentration for M80 case increased from 3.6% to 6% (the positive calibration error), for U80 case there was actually a decrease from 5.1% to 2.9% (the negative calibration error).

From the above discussion we can conclude that the algorithm performance should be relatively insensitive to the radiometric calibration errors of the magnitude expected after in-orbit calibration adjustment.

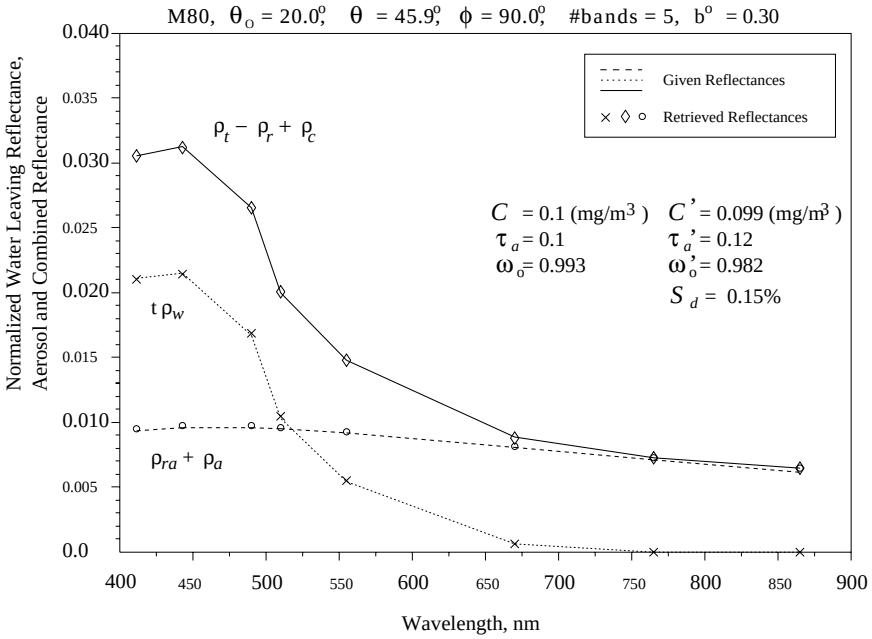

Figure 4.28 Retrieved the total, aerosol and water-leaving reflectances for the M80 test model with added positive calibration errors: $\tau_a(865) = 0.1$, the pigment concentration $C = 0.1$ mg/m^3, the water scattering parameter $b^0 = 0.3$ m^{-1}, the viewing geometry $\theta_0 = 20°, \theta = 45.9°$

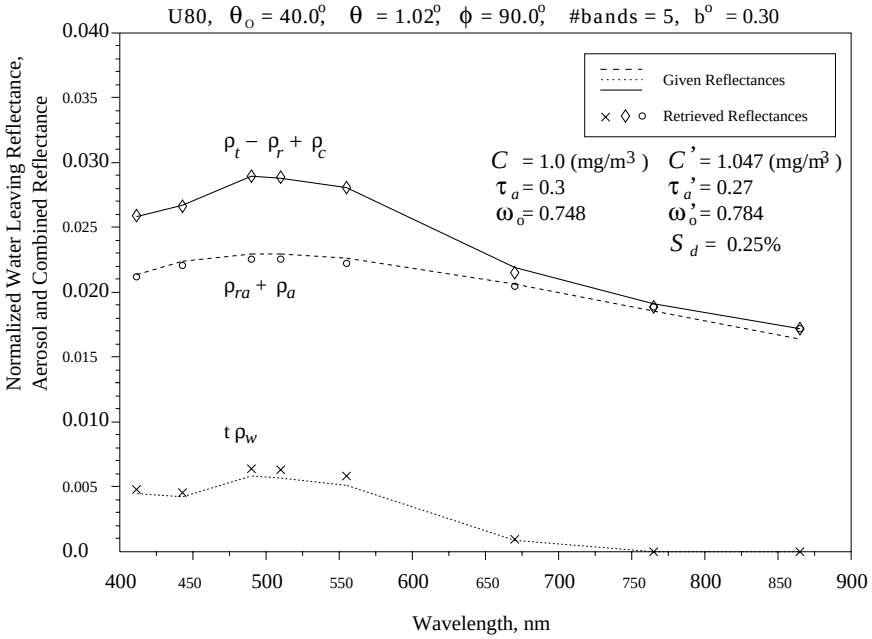

Figure 4.29 Retrieved the total, aerosol and water-leaving reflectances for the M80 test model with added positive calibration errors: $\tau_a(865) = 0.3$, the pigment concentration $C = 1.0$ mg/m^3, the water scattering parameter $b^0 = 0.3$ m^{-1}, the viewing geometry $\theta_0 = 40°, \theta = 1°$

RETRIEVAL OF OCEAN's PIGMENT CONCENTRATION
with positive calibration error

Tabulated are mean values of retrieved C for seven Sun-Viewing Geometries and each of four hypothetical atmospheric aerosols (M80, C80, T80, U80). Also, provided are the standard deviations over viewing geometries divided by the mean (S_d) as well as the deviations from given parameters (D).

	C: mg/m^3	*0.100*			*0.500*			*1.000*		
		result	S_d	*D*	*result*	S_d	*D*	*result*	S_d	*D*
M80	$\tau_a(865) = 0.10$	**0.098**	1.6%	2.00%	**0.494**	2.7%	1.20%	**1.011**	4.2%	1.10%
$\omega_0 = 0.993$	$\tau_a(865) = 0.20$	**0.097**	2.2%	3.00%	**0.487**	5.0%	2.60%	**0.999**	8.5%	0.10%
	$\tau_a(865) = 0.30$	**0.097**	2.2%	3.00%	**0.485**	6.2%	3.00%	**0.991**	11.%	0.90%

	C: mg/m^3	*0.100*			*0.500*			*1.000*		
		result	S_d	*D*	*result*	S_d	*D*	*result*	S_d	*D*
C80	$\tau_a(865) = 0.10$	**0.098**	1.6%	2.00%	**0.490**	3.6%	2.00%	**0.995**	6.3%	0.50%
$\omega_0 = 0.988$	$\tau_a(865) = 0.20$	**0.097**	2.2%	3.00%	**0.478**	7.1%	4.40%	**0.966**	12.%	3.40%
	$\tau_a(865) = 0.30$	**0.097**	2.6%	3.00%	**0.471**	10.%	5.80%	**0.940**	17.%	6.00%

	C: mg/m^3	*0.100*			*0.500*			*1.000*		
		result	S_d	*D*	*result*	S_d	*D*	*result*	S_d	*D*
T80	$\tau_a(865) = 0.10$	**0.095**	4.7%	5.00%	**0.487**	2.4%	2.60%	**1.037**	4.9%	3.70%
$\omega_0 = 0.953$	$\tau_a(865) = 0.20$	**0.093**	1.3%	7.00%	**0.470**	4.0%	6.00%	**0.935**	3.0%	6.50%
	$\tau_a(865) = 0.30$	**0.096**	4.4%	4.0%	**0.469**	2.1%	6.20%	**0.943**	2.7%	5.70%

	C: mg/m^3	*0.100*			*0.500*			*1.000*		
		result	S_d	*D*	*result*	S_d	*D*	*result*	S_d	*D*
U80	$\tau_a(865) = 0.10$	**0.103**	0.8%	3.00%	**0.519**	1.1%	3.80%	**1.043**	2.3%	4.30%
$\omega_0 = 0.748$	$\tau_a(865) = 0.20$	**0.109**	2.8%	9.00%	**0.543**	3.8%	8.60%	**1.062**	2.9%	6.20%
	$\tau_a(865) = 0.30$	**0.116**	5.7%	16.0%	**0.573**	6.4%	14.6%	**1.089**	3.6%	8.90%

Table 4.8

RETRIEVAL OF OCEAN's PIGMENT CONCENTRATION
with negative calibration error

Tabulated are mean values of retrieved C for seven Sun-Viewing Geometries and each of four hypothetical atmospheric aerosols (M80, C80, T80, U80). Also, provided are the standard deviations over viewing geometries divided by the mean (S_d) as well as the deviations from given parameters (D).

	C: mg/m^3	0.100			0.500			1.000		
		result	S_d	D	result	S_d	D	result	S_d	D
M80	$\tau_a(865) = 0.10$	**0.094**	2.3%	6.00%	**0.479**	2.3%	4.20%	**1.004**	0.8%	0.40%
$\omega_0 = 0.993$	$\tau_a(865) = 0.20$	**0.091**	4.0%	9.00%	**0.463**	4.6%	7.40%	**1.005**	2.2%	0.50%
	$\tau_a(865) = 0.30$	**0.090**	4.7%	3.00%	**0.452**	6.1%	9.60%	**0.998**	4.0%	0.20%

	C: mg/m^3	0.100			0.500			1.000		
		result	S_d	D	result	S_d	D	result	S_d	D
C80	$\tau_a(865) = 0.10$	**0.094**	2.6%	6.00%	**0.476**	2.5%	4.80%	**0.997**	0.9%	0.30%
$\omega_0 = 0.988$	$\tau_a(865) = 0.20$	**0.090**	4.7%	10.0%	**0.455**	5.2%	9.00%	**0.983**	2.2%	1.70%
	$\tau_a(865) = 0.30$	**0.088**	5.3%	12.0%	**0.438**	6.5%	12.4%	**0.964**	4.4%	3.60%

	C: mg/m^3	0.100			0.500			1.000		
		result	S_d	D	result	S_d	D	result	S_d	D
T80	$\tau_a(865) = 0.10$	**0.086**	10.%	5.00%	**0.437**	9.5%	12.6%	**1.038**	14.%	3.80%
$\omega_0 = 0.953$	$\tau_a(865) = 0.20$	**0.078**	14.%	22.0%	**0.377**	19.%	24.6%	**0.836**	3.4%	16.4%
	$\tau_a(865) = 0.30$	**0.081**	12.%	19.0%	**0.337**	15.%	32.6%	**0.640**	26.%	36.0%

	C: mg/m^3	0.100			0.500			1.000		
		result	S_d	D	result	S_d	D	result	S_d	D
U80	$\tau_a(865) = 0.10$	**0.098**	1.5%	2.00%	**0.496**	0.2%	0.80%	**1.021**	2.7%	2.10%
$\omega_0 = 0.748$	$\tau_a(865) = 0.20$	**0.099**	2.7%	1.00%	**0.507**	1.9%	1.40%	**1.033**	3.5%	3.30%
	$\tau_a(865) = 0.30$	**0.104**	3.2%	4.0%	**0.530**	4.7%	6.00%	**1.056**	4.1%	5.60%

Table 4.9

D. Pseudo $\rho_t(\lambda)$ for U80 test aerosol models with vertical structure

So far it has been assumed that the aerosol is located within a thin layer just above the sea-surface. Actually, this is hardly ever the case in the natural conditions. In their study Ding and Gordon[43] came to a conclusion that as long as the aerosol was weakly absorbing $\varpi_0 > 0.93$, its vertical distribution had a negligible effect on the multiple scattering algorithm they used. On the other hand, if ϖ_0 decreased, the results degraded substantially. So, only highly absorbing aerosols need to be studied when the vertical atmospheric profile is taken into account. Later, Gordon[40] provided a simple explanation arguing that the increase of the amount of the Rayleigh gas in the aerosol layer increases the average path length of photons through the layer, and in this manner increases total absorption. In addition, the reflectance of the Rayleigh layer ρ_r decreases for it is partially absorbed by the aerosol mixed up with the gas.

While the aerosol vertical distribution is quite a complicated function, the easiest way to assess its impact on the radiative transfer processes is through the use of our two-layer atmospheric model where the top layer contains only the Rayleigh gas and the bottom layer is a mixture of the Rayleigh gas and aerosol with a constant mixing ratio. Denoting the fraction of the Rayleigh gas in the bottom layer as γ, the optical thicknesses of the top and the bottom layers can be simply expressed as:

$$\tau_{\text{top}} = (1-\gamma)\,\tau_r, \qquad \tau_{\text{bot}} = \gamma\tau_r + \tau_a, \tag{4.3}$$

where τ_r and τ_a are the total Rayleigh gas and aerosol optical thicknesses. The nomenclature for the U80 aerosol model is given in the Table 4.10 below.

Table 4.10 Nomenclature for U80 models with vertical structure

Notation	Aerosol's top altitude, km	Fraction, γ
U80	up to 1 km	0.0
U280	2.0	0.21
U480	4.0	0.39

The spectral variation of the aerosol reflectance $\rho_a + \rho_{ra}$ for models U80, U280, U480 with $\tau_a(865) = 0.2$ is shown in the Figure 4.30.

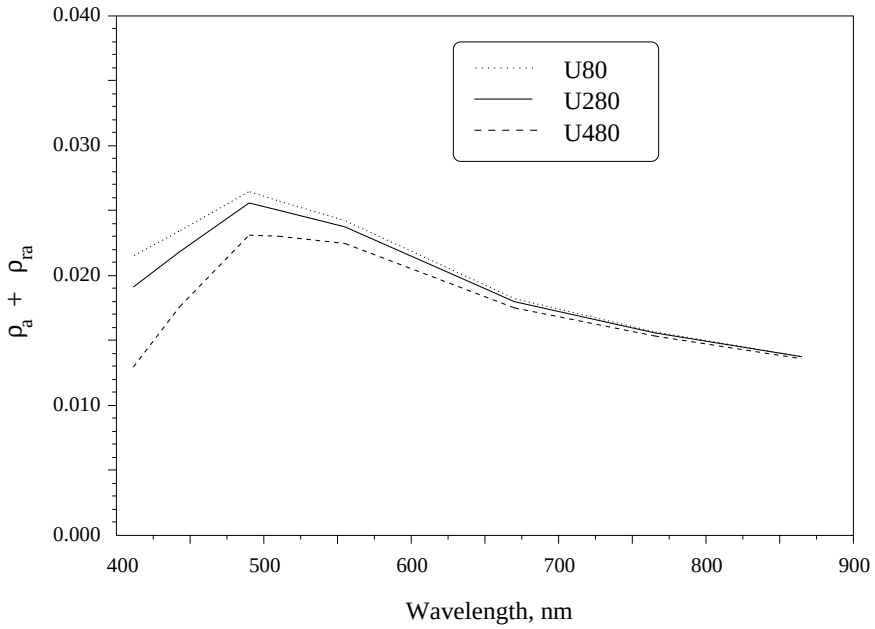

Figure 4.30 Spectral variation of $\rho_a + \rho_{ra}$ for test models U80, U280, U480: $\tau_a(865) = 0.2$, the viewing geometry $\theta_0 = 60°, \theta = 1°$

The aforementioned interpretation of this spectral behaviour can be clearly seen in this Figure. Indeed, the Rayleigh optical thickness τ_r in the blue is the largest comparatively to that in the NIR, thus the aerosol has the lower reflectivity in the blue part of the spectrum. In the NIR, in contrast, the amount of Rayleigh scattering is very low and has a small impact on the reflectance field.

To study the effect of the aerosol vertical distribution we generated data for the pseudo reflectance $\rho_t(\lambda)$ at the TOA using γ values as indicated in the Table 4.10. Again, we applied the Solution 1. In building the system (3.10) only the first five bands were used. Particular results for the viewing geometry $\theta_0 = 20°, \theta = 1°$, the optical thickness $\tau_a(865)$ and the ocean pigment concentration $C = 0.5$ mg/m^3 are shown in the Figures 4.11, 4.31,

4.32 for two vertical distributions U80, U280, U480 respectively.

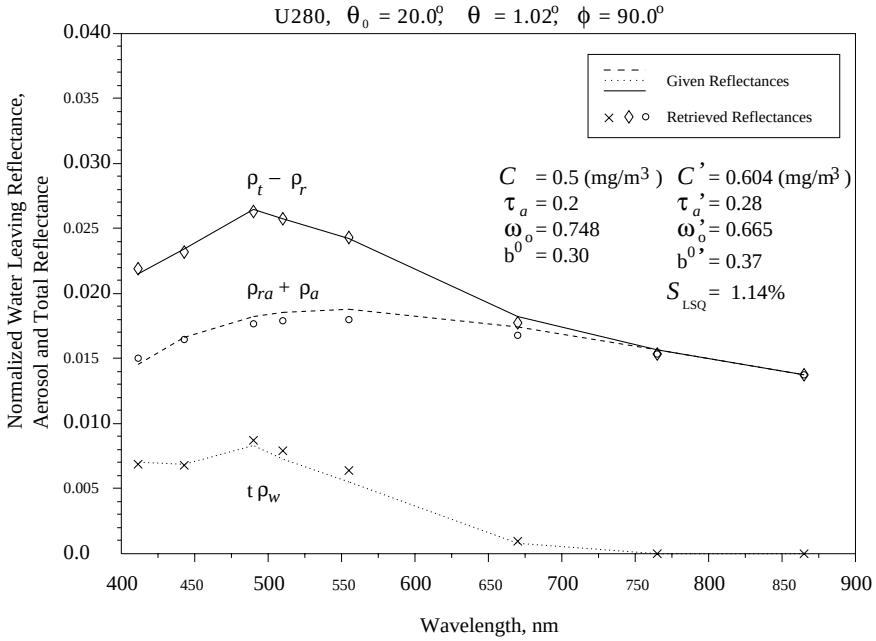

Figure 4.31 Retrieved the total, aerosol and water-leaving reflectances for the U280 test model: $\tau_a(865) = 0.2$, the pigment concentration $C = 0.5$ mg/m^3, the water scattering parameter $b^0 = 0.3$ m^{-1}, the viewing geometry $\theta_0 = 20°, \theta = 1°$

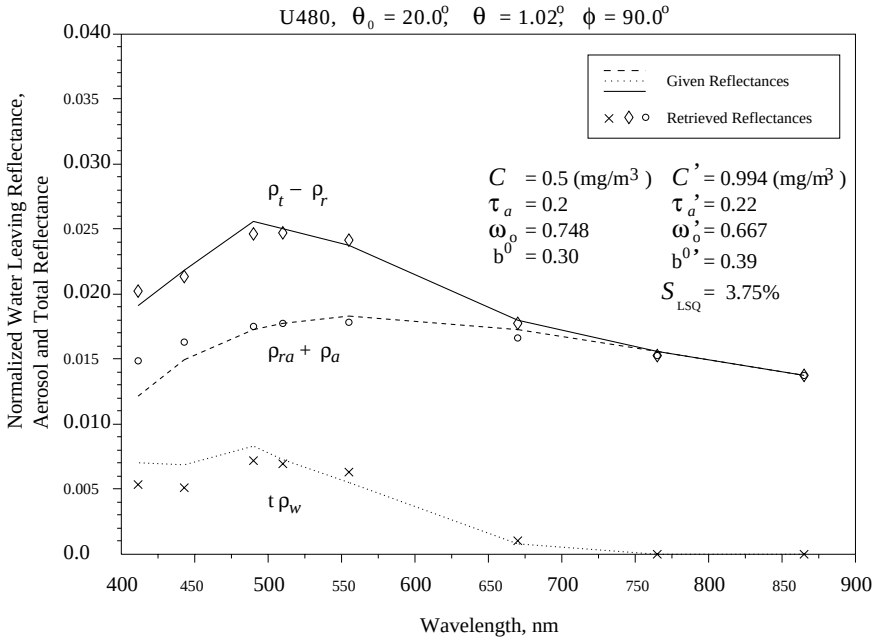

Figure 4.32 Retrieved the total, aerosol and water-leaving reflectances for the U480 test model: $\tau_a(865) = 0.2$, the pigment concentration $C = 0.5$ mg/m^3, the water scattering parameter $b^0 = 0.3$ m^{-1}, the viewing geometry $\theta_0 = 20°, \theta = 1°$

RETRIEVAL OF OCEAN's PIGMENT CONCENTRATION

Tabulated are mean values of retrieved C for seven Sun-Viewing Geometries and each of four hypothetical atmospheric aerosols (M80, C80, T80, U80). Also, provided are the standard deviations over viewing geometries divided by the mean (S_d) as well as the deviations from given parameters (D).

	C: mg/m^3	*0.100*			*0.500*			*1.000*		
		result	S_d	*D*	*result*	S_d	*D*	*result*	S_d	*D*
U80	$\tau_a(865) = 0.10$	**0.100**	0.8%	0.00%	**0.507**	0.7%	1.40%	**1.028**	1.9%	2.80%
$\omega_0 = 0.748$	$\tau_a(865) = 0.20$	**0.104**	1.4%	4.00%	**0.526**	2.7%	5.20%	**1.053**	3.2%	5.30%
	$\tau_a(865) = 0.30$	**0.110**	4.3%	10.0%	**0.552**	5.8%	10.4%	**1.070**	4.0%	7.00%

	C: mg/m^3	*0.100*			*0.500*			*1.000*		
		result	S_d	*D*	*result*	S_d	*D*	*result*	S_d	*D*
U280	$\tau_a(865) = 0.10$	**0.110**	2.8%	10.0%	**0.602**	9.8%	20.4%	**1.305**	11.%	30.5%
$\omega_0 = 0.748$	$\tau_a(865) = 0.20$	**0.122**	6.3%	22.0%	**0.575**	3.0%	15.0%	**1.120**	7.9%	12.0%
	$\tau_a(865) = 0.30$	**0.138**	12.%	38.0%	**0.631**	16.%	26.2%	**0.959**	8.6%	4.10%

	C: mg/m^3	*0.100*			*0.500*			*1.000*		
		result	S_d	*D*	*result*	S_d	*D*	*result*	S_d	*D*
U480	$\tau_a(865) = 0.10$	**0.120**	6.7%	20.0%	**0.941**	28.%	88.2%	**1.500**	0.0%	50.0%
$\omega_0 = 0.748$	$\tau_a(865) = 0.20$	**0.142**	14.%	42.0%	**1.198**	19.%	140.%	**1.500**	0.0%	50.0%
	$\tau_a(865) = 0.30$	**0.172**	25.%	72.0%	**1.084**	13.%	102.%	**1.500**	0.0%	50.0%

Table 4.11

The detailed summary of the retrieval of the ocean pigment concentration is given in the Table 4.11 for three vertical distributions with optical thicknesses $\tau_a(865) = 0.1, 0.2, 0.3$ and three ocean pigment concentrations $C = 0.1, 0.5, 1.0$ mg/m^3 Note how the quality of retrievals degraded when the optical thickness τ_a increased. In fact, the standard deviation of the retrieval of the pigment concentration increased from 2.8% at $\tau_a(865) = 0.1$ to 12%

at $\tau_a(865) = 0.3$ for U280 test case and from 6.7% at $\tau_a(865) = 0.1$ to 25% at $\tau_a(865) = 0.3$ for U480 test case (when $C = 0.1$ mg/m^3).

The retrievals of the water-leaving reflectance had the deviation ranging from 10% to 30% for U280 and, from 20% up to 60% for U480 case. This is explained as follows. Increasing the layer thickness causes $\rho_a(\lambda) + \rho_{ra}(\lambda)$ to become increasingly smaller as λ increases. The algorithm deals with that through both choosing the largest value of m_i available and increasing C to further reduce $\rho_t(\lambda) - \rho_r(\lambda)$ in the blue relative to the red.

The objective function S_{LSQ} on the average rose from 1.6% for U280 to 5.6% for U480 test case. No test case described in the previous subsections gave such large values for the objective function. This highlights the point that the vertical distribution for highly absorbing aerosols is a primary problem to deal with in any atmospheric correction algorithm.

Encouraging is the fact that the retrievals for U280 test case, in general, produced acceptable results. This can be used to improve the algorithm's performance when dealing with the aerosol vertical distribution. Indeed, if Look-Up Tables are created with the Junge power-law models having a vertical distribution up to 2 km, it will have a little impact on the results when weakly absorbing aerosols are present. In contrast, when dealing with highly absorbing aerosols the results for cases when the aerosol is all near the surface and when the aerosol is mixed up with gas up to 4 km will be equally good.

E. Pseudo $\rho_t(\lambda)$ for Maritime-Mineral test aerosol models

As has been noted before the Junge power-law aerosol models are characterized by a refractive index which does not vary with wavelength. To study the effect of a variable refractive index on our atmospheric correction results, we use the Maritime-Mineral test aerosol. Mineral component being of the crustal origin is frequently present in the maritime environment and is characterized by the trimodal log-normal size distribution. It is the mineral component that is responsible for the variation of the refractive index with wavelength. Though, its fraction compared to the maritime component is rather small (from 5% to 20% being a strong function of relative humidity), its impact on aerosol radiative properties is significant. In Chapter 2 we have made a remark that the higher the modality of the size distribution, the better it is approximated by the Junge power-law size distribution. This fact was used in our simulations.

The values of the refractive index for eight wavelengths and three Junge power-law parameters ν are tabulated below.

Table 4.12: Characteristics of the Maritime-Mineral test aerosol models.

		ϖ_0		
λ_i	$m = m_r - i\, m_i$	$\nu = 2.0$	$\nu = 3.0$	$\nu = 4.0$
412	$1.53 - i$ 1.20e−2	0.7679	0.8990	0.9297
443	$1.53 - i$ 9.10e−3	0.7978	0.9185	0.9445
490	$1.53 - i$ 7.94e−3	0.8158	0.9270	0.9498
510	$1.53 - i$ 7.34e−3	0.8252	0.9315	0.9528
555	$1.53 - i$ 5.40e−3	0.8576	0.9469	0.9637
670	$1.53 - i$ 4.30e−3	0.8863	0.9566	0.9687
765	$1.53 - i$ 3.16e−3	0.9146	0.9670	0.9752
865	$1.53 - i$ 1.20e−3	0.9645	0.9866	0.9898

The spectral variation of $\tau_a(\lambda)/\tau_a(865)$ is almost independent of the refractive index and is similar to that shown in Fig. 4.4. The typical spectral variation of the reflectance $\rho_a(\lambda) + \rho_{ra}(\lambda)$ is plotted in the Figure 4.33 for the case with $\theta_0 = 20°, \theta = 1°, \phi = 90°$ and

the optical thickness $\tau_a(865) = 0.2$. We note immediately the behaviour of the Maritime-Mineral test aerosol with $\nu = 2.0$: $0 < \epsilon' < 1$, cases that were not tabulated in the look-up tables (LUT), thus an extrapolation has to be performed in this case (remember that the selection of the set of $\{\nu, m_r, m_i\}$ was based on the possibility of linear interpolation). Now, reminding that the calculation of ν is based on the NIR bands exclusively (in the Solution 1), we might expect difficulties in solving the non-linear system of equations (3.4). Additionally, a strong dependence on the sun-viewing geometry might be expected (compare the results in Figures 4.34 - 4.36 to the results averaged over all sun-viewing geometries summarized in the Table 4.13) because of the increase in the ray path length.

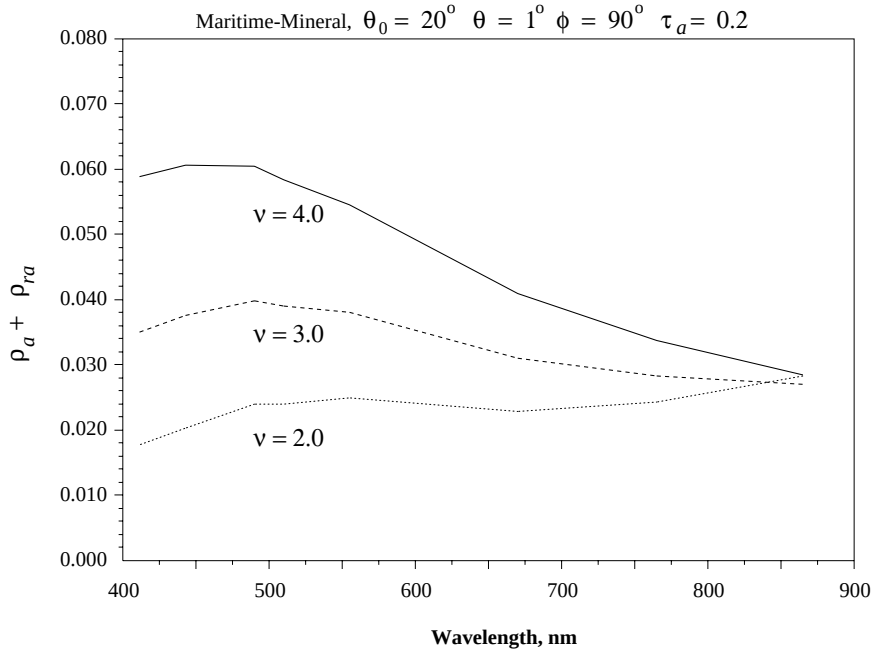

Figure 4.33 Reflectance $\rho_a(\lambda) + \rho_{ra}(\lambda)$ for the Maritime-Mineral test models with $\nu = 2.0, 3.0, 4.0$, $\tau_a(865) = 0.2$, the viewing geometry $\theta_0 = 20°, \theta = 1°$

Encountered problems are reminiscent to those with the aerosol vertical structure distribution from the previous subsection or the high reflectance T80 case from the Subsection B. Indeed, for the Maritime-Mineral case with $\nu = 4.0$ (see Fig. 4.34) the high reflectance

the algorithm achieves by increasing b^0 (which is constraint by the system (3.5)) and the aerosol optical thickness $\tau_a(\lambda)$ keeping C and ϖ_0 practically unchanged. This might not be the case, though, for other geometries. This leads sometimes to errors in C up to as much as 50% - 60%.

RETRIEVAL OF OCEAN's PIGMENT CONCENTRATION

Tabulated are mean values of retrieved C for seven Sun-Viewing Geometries and hypothetical atmospheric Maritime-Mineral aerosol.
Also, provided are the standard deviations over viewing geometries divided by the mean (S_d) as well as the deviations from given parameters (D).

	C: mg/m^3	0.100			0.500			1.000		
		result	S_d	D	result	S_d	D	result	S_d	D
maritime mineral $\nu = 2.0$ $\omega_0 = 0.965$	$\tau_a(865) = 0.10$	**0.107**	7.0%	7.00%	**0.525**	5.8%	5.00%	**1.018**	5.0%	18.0%
	$\tau_a(865) = 0.20$	**0.115**	14.%	15.0%	**0.577**	19.%	15.4%	**1.074**	11.%	7.40%
	$\tau_a(865) = 0.30$	**0.123**	22.%	23.0%	**0.599**	22.%	19.8%	**1.256**	17.%	25.6%

	C: mg/m^3	0.100			0.500			1.000		
		result	S_d	D	result	S_d	D	result	S_d	D
maritime mineral $\nu = 3.0$ $\omega_0 = 0.987$	$\tau_a(865) = 0.10$	**0.110**	3.0%	10.0%	**0.516**	2.2%	3.20%	**0.959**	3.2%	4.00%
	$\tau_a(865) = 0.20$	**0.130**	11.%	30.0%	**0.578**	9.2%	15.6%	**0.948**	7.8%	5.20%
	$\tau_a(865) = 0.30$	**0.157**	24.%	57.0%	**0.654**	11.%	30.8%	**1.009**	17.%	0.90%

	C: mg/m^3	0.100			0.500			1.000		
		result	S_d	D	result	S_d	D	result	S_d	D
maritime mineral $\nu = 4.0$ $\omega_0 = 0.990$	$\tau_a(865) = 0.10$	**0.111**	2.5%	20.0%	**0.497**	1.4%	0.60%	**0.914**	3.5%	8.60%
	$\tau_a(865) = 0.20$	**0.139**	14.%	39.0%	**0.568**	11.%	13.6%	**0.836**	4.8%	16.4%
	$\tau_a(865) = 0.30$	**0.195**	34.%	95.0%	**0.708**	14.%	41.6%	**1.093**	31.%	9.30%

Table 4.13

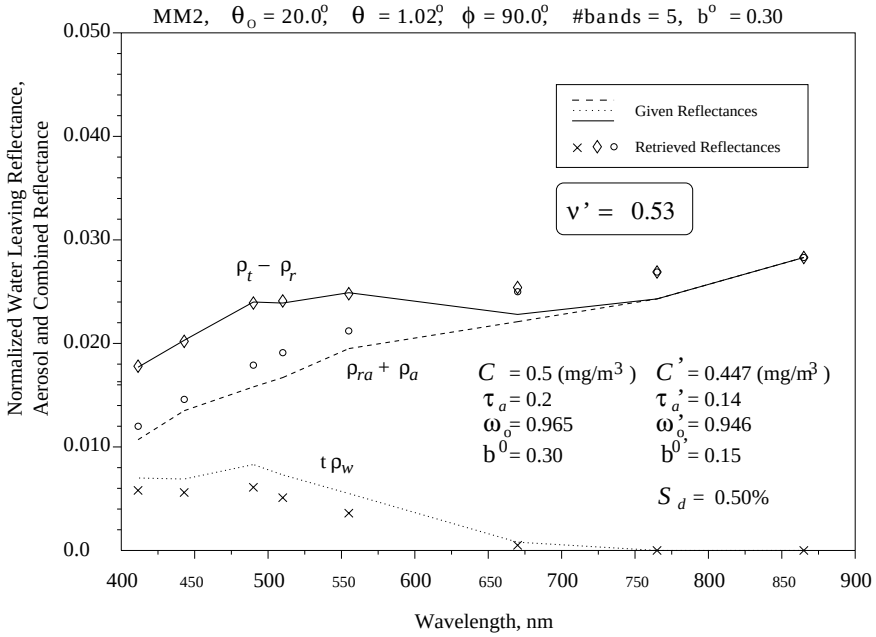

Figure 4.34 Retrieved the total, aerosol and water-leaving reflectances for the Maritime-Mineral test model with $\nu = 2.0$: $\tau_a(865) = 0.2$, the pigment concentration $C = 0.5$ mg/m^3, the water scattering parameter $b^0 = 0.3$ m^{-1}, the viewing geometry $\theta_0 = 20°, \theta = 1°$

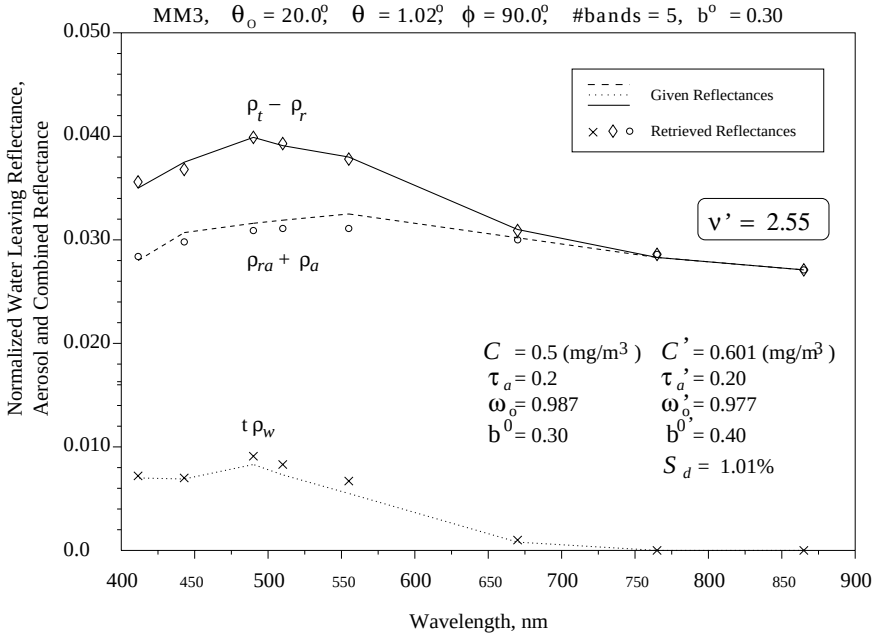

Figure 4.35 Retrieved the total, aerosol and water-leaving reflectances for the Maritime-Mineral test model with $\nu = 3.0$: $\tau_a(865) = 0.2$, the pigment concentration $C = 0.5$ mg/m^3, the water scattering parameter $b^0 = 0.3$ m^{-1}, the viewing geometry $\theta_0 = 20°, \theta = 1°$

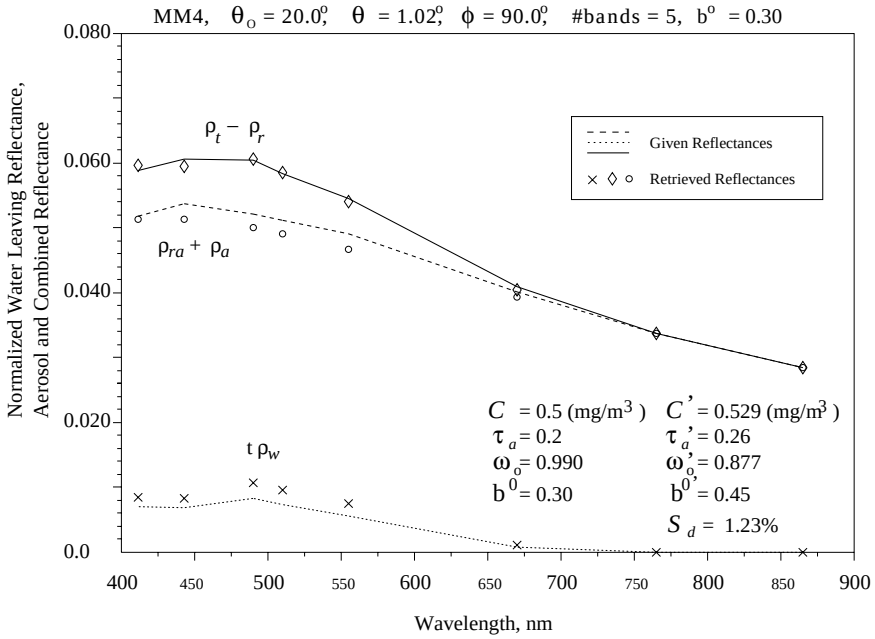

Figure 4.36 Retrieved the total, aerosol and water-leaving reflectances for the Maritime-Mineral test model with $\nu = 4.0$: $\tau_a(865) = 0.2$, the pigment concentration $C = 0.5$ mg/m^3, the water scattering parameter $b^0 = 0.3$ m^{-1}, the viewing geometry $\theta_0 = 20°, \theta = 1°$

While the values of the single-scattering albedo $\varpi_0(865)$ were within 5% - 6% range in the NIR, they made no sense in the blue, particularly for $\nu = 2.0$ test model.

The objective function was on the average equal to 1.2% (again, in building the system (3.10) only the information from the first five bands was used). In some individual cases S_{LSQ} was as small as $0.4 - 0.8\%$ making it difficult to use this objective function for an identification of the maritime-mineral aerosols. Note, that with the Junge power-law models we cannot estimate the spectral variation of the refractive index, so just observing a large objective function value S_{LSQ} will not recognize whether it happened because of the aerosol vertical distribution or because of the spectral variation of the refractive index.

V. TESTING SPECTRUM OPTIMIZATION WITH SeaWiFS

The SeaWiFS, the Sea-viewing Wide Field-of-view Sensor, was launched by NASA in August 1997. Its purpose is to examine oceanic factors that affect global change and to assess the ocean's role in the global carbon cycle, as well as other biogeochemical cycles.[8]

Major instrument parameters have been summarized in the Table 5.1. The selection of of the SeaWiFS bands was based on the spectral absorption characteristics of some common in-water optical constituents, mean extraterrestrial irradiances, and spectral transmittance of the atmospheric constituents oxygen and water vapor. SeaWiFS produces two types of science data: LAC (Local Area Coverage), with a nominal ground resolution of 1.13 km (1,285 picture elements, or pixels, per scan line) and GAC (Global Area Coverage), with a nominal ground resolution of 4.5 km, which is subsampled from LAC data every fourth line and every fourth pixel (such that is comprised of 248 pixels per scan line). There are four **Levels** of SeaWiFS data products:

0 Raw radiance counts from all bands and instrument telemetry.

1A All Level-0 data, appended calibration and navigation data, and reformatted instrument and selected spacecraft telemetry.

2 Derived from corresponding Level-1A GAC product by applying the sensor calibration, the atmospheric corrections, and bio-optical algorithms.

3 Binned (a global, equal-area grid whose grid cells, or "bins", are approximately 81 km^2) data product that consists of the accumulated data for all Level-2 GAC products corresponding to a period of one day, 8 days, a calendar month, or a calendar year.

Table 5.1: Major Parameters and Characteristics of the SeaWiFS ocean color sensor.

Instrument Bands					
Band	Center Wavelength [nm]	Wavelength FWHM [nm]	Saturation Radiance [mW $cm^{-2}\mu m^{-1}$ sr^{-1}]	Input Radiance [mW $cm^{-2}\mu m^{-1}$ sr^{-1}]	SNR
1	412	402-422	13.63	9.10	499
2	443	433-453	13.25	8.41	674
3	490	480-500	10.50	6.56	667
4	510	500-520	9.08	5.64	640
5	555	545-565	7.44	4.57	596
6	670	660-680	4.20	2.46	442
7	765	745-785	3.00	1.61	455
8	865	845-885	2.13	1.09	467
Sensor Accuracy					
Radiance Accuracy:		<5% absolute each band			
Relative Precision:		<1% linearity			
Between Band Precision:		<5% relative band-to-band (over 0.5-0.9 full scale)			
Polarization:		<2% sensitivity (all angles)			
Nadir Resolution:		1.1km LAC; 4.5km GAC			
Mission Characteristics					
Orbit Type:		Sun Synchronous at 705 km			
Equator Crossing:		Noon ±20 min., descending			
Saturation Recovery:		<10 samples			
Modulation Transfer Function:		≥0.3 at Nyquist			
Swath width (at equator):		2,801 km LAC (±58.3°)			
		1,502 km GAC (±45.0°)			
Scan Plane Tilt:		$+20°, 0°, -20°$			
Digitization:		10 bits			

It is the Level-2 data product generation, or more exactly, its atmospheric correction part, that we will be concerned with in this chapter.

To facilitate a rapid processing, display, analysis, and quality control of all SeaWiFS products, GSFC NASA created a comprehensive image analysis product named SeaDAS[44].

The NASA Standard Atmospheric Correction algorithm has been developed by Gordon and Wang.[11] It will not be described here since it can be found in published literature elsewhere.[11,45] This algorithm has proven to be fast, reliable and simple to implement. Our purpose will be to compare the performances of the aforementioned NASA Standard Correction and the Spectrum Optimization Algorithm (described in Chapter 2) within the SeaDAS image processing system.

Table 5.2:
Comparative Methodology between the
NASA Standard and Spectrum Optimization Algorithms.

	Method or Structure	
Function	NASA Standard Correction	Spectrum Optimization
Aerosol Assumptions*	12 models for M,C,T models at 4 relative humidities	72 models for Junge Power-Law models: 6 values of ν, 2 of m_r, 6 of m_i
Data Storage†	LUT for $\rho_a(\rho_{as}) + \rho_{ra}(\rho_{as})$	LUT for $\rho_a(\tau_a) + \rho_{ra}(\tau_a)$
Aerosol Properties:	Bands 7 and 8 are used to determine $\overline{\epsilon}'(765, 865)$ LUTs are used to bracket the best 2 models. Further interpolation provides an "average" model.	Bands 7 and 8 are used to determine ν : given $\overline{\epsilon}'(765, 865)$. Then $\tau_a(865)$ is determined for each m_r, m_i combination using Newton-Raphson iteration.
Aerosol Reflectance $\rho_a(\lambda_s) + \rho_{ra}(\lambda_s)$	Based on extrapolation of the "average" model into the visible	Quadratic interpolation for scattering parameters for LUT models.
Water-Leaving Reflect. $\rho_w(\lambda)$	Computed directly	Non-linear optimization using Bands 1 through 5 (Band 6 is optional)
Diffuse Transmit. $t(\lambda)$	Bidirectional effects not included	Bidirectional effects not included

* M, C, T, U shortcuts stand for Maritime, Coastal, Tropospheric, Urban models

† ρ_{as} stands for the single-scattering reflectance.

From the Table 5.2 we can make a note on the way the pigment concentrations are obtained by each of the algorithms: the NASA Standard Correction algorithms utilizes two bands (centered at 490 nm and 555 nm), while the Spectrum Optimization algorithm uses the first five bands (the usage of Band 6 is optional). This is why we might expect better retrievals of the pigment concentration with the latter algorithm.

For atmospheric correction experiments we select two L1A_GAC images that were taken on October 6, 1997 (corresponds to the 279th day of a year) and October 8, 1997 (DAY-281). We consider the same grid cell with its top left corner at (Lat,Lon) = (42°84",78°43") and the bottom right corner at (29°12",63°77") Since the time difference between the pictures is only two days and, the "productivity" (i.e. the production of organic material by algae and some bacteria that exist at the lowest levels of the oceanic food chain that utilize the sunlight or chemical energy as their source of energy) during fall is not high, the change in the pigment concentration is not expected to be large. DAY-279 is characterized by a highly turbid atmosphere, in contrast to the clear sky DAY-281. The true color pictures of those days are shown in Fig. 5.1. Figures 5.2 and 5.3 show Level-1A raw data for each of eight bands. After applying calibration and other metereological data, we perform Level-2 product generation using both algorithms.

The results of retrieving the pigment concentration are demonstrated in Figures 5.4 - 5.7. It can be noticed that the pigment concentration for DAY-281 obtained by NASA Standard Correction and Spectrum Optimization algorithms differ very little. Indeed, during DAY-281 we expect the aerosol to be completely of Maritime nature and of very small optical thickness, the case which both algorithms performed very well during initial testing. A sharp contrast in performance appears while processing the DAY-279 image. From Figure 5.5 we note a drastic change in pigment concentration comparatively to that of DAY-281 produced by NASA Standard Correction Algorithm. More precisely, retrieved concentrations for DAY-279 were from 2 to 3 times as large as that for DAY-281. Spectrum Optimization Algorithm results (Figures 5.6, 5.7) are substantially better, showing no large variations in the pigment concentration for DAY-279 and DAY-281. Needless to

say, Spectrum Optimization results are typically much smoother comparatively to results obtained by NASA Standard Correction Algorithm.

We further analyzed the water-leaving radiances retrieved by the algorithms. In order to escape the contamination of pictures by clouds, we extract subimages from our L2_GAC products. Histogram analysis is performed on water-leaving radiances for Band 2 (443 nm) and 5 (555 nm) for both days (the top corner of the subimage is located at (Lat,Lon)=(39°60",70°33") and the bottom right corner at (Lat,Lon)=(37°80",67°32").

NASA Standard Correction Algorithm:

For DAY-281 this algorithm (Fig. 5.8b) indicated two peaks of the water-leaving radiance for Band 2: first at 1100 (mW cm^{-2} um^{-1} sr^{-1}) with the full width at half maximum (FWHM) of about 200 (mW cm^{-2} um^{-1} sr^{-1}) and the second at 1390 (mW cm^{-2} um^{-1} sr^{-1}) with FWHM of about 110 (mW cm^{-2} um^{-1} sr^{-1}). For DAY-279 FWHM's were much wider (the second peak was almost unidentifiable) and shifted about 500 (mW cm^{-2} um^{-1} sr^{-1}) toward higher values of radiances, suggesting that the atmospheric correction algorithm underestimated the aerosol component.

For Band 5, both days showed a single peak, although that for DAY-279 was again shifted toward higher values and had FWHM more then triple that of DAY-281.

Spectrum Optimization Algorithm:

For DAY-281 this algorithm (Fig. 5.10b) for both bands indicated the results similar to those obtained by NASA Standard Correction Algorithm. The results differ for DAY-279. FWHM were almost unchanged, though the radiances shifted toward higher values as well. The second radiance peak for Band 2 is clearly visible (the noise in the histogram may be the result of the image' small size).

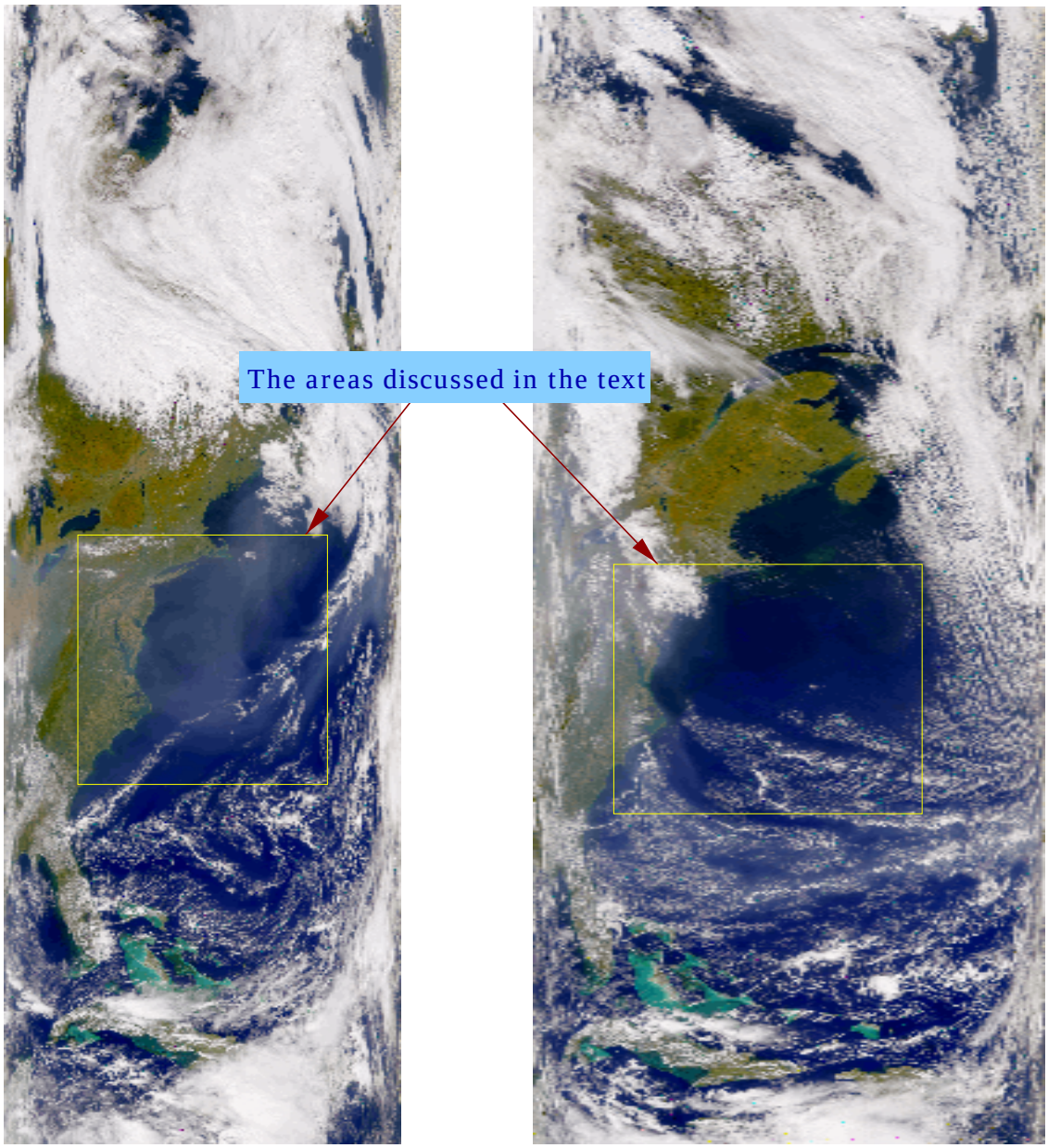

Figure 5.1 "True color" images taken by SeaWiFS on October 6, 1997 (Day-279) and October 8, 1997 (Day-281).

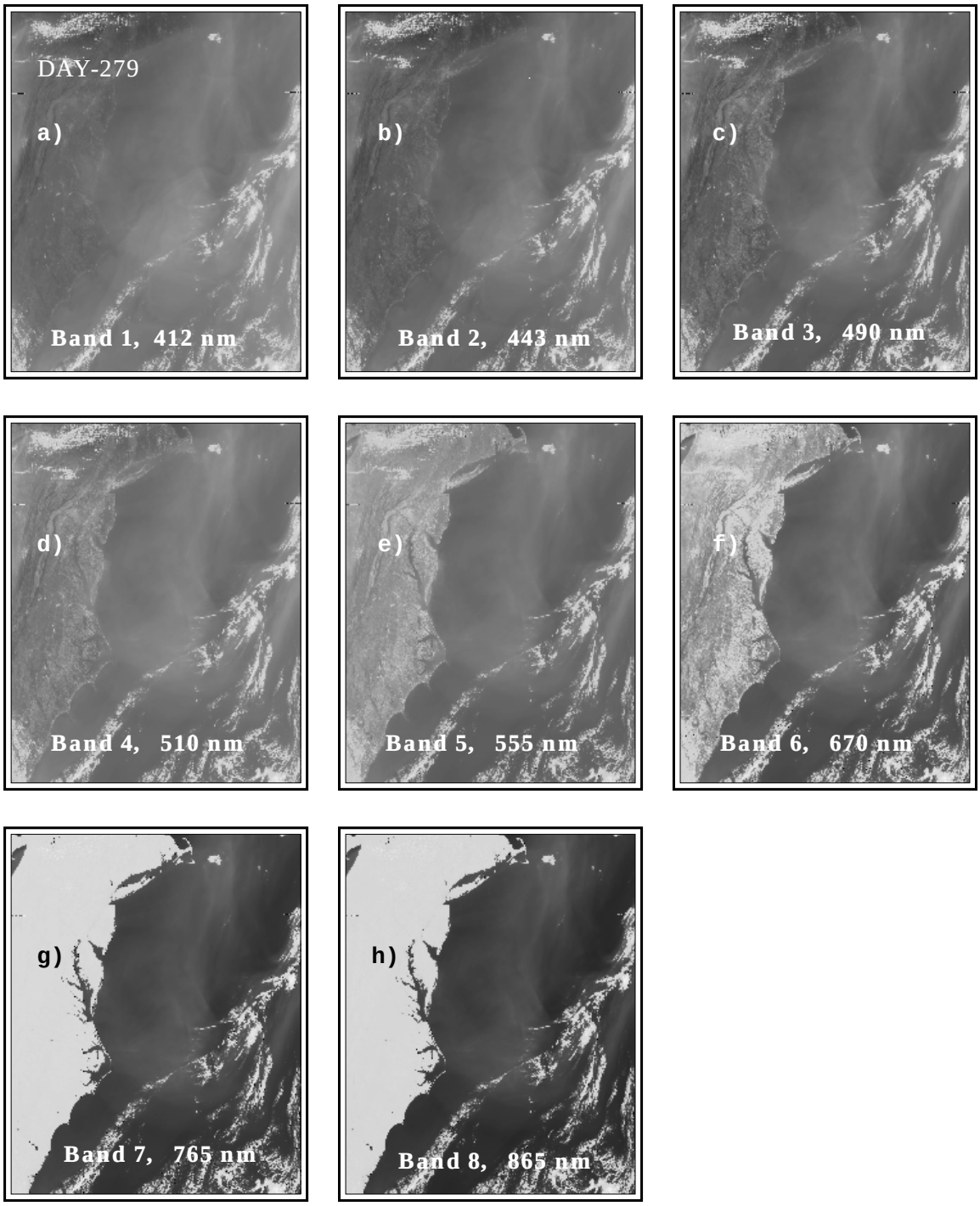

Figure 5.2 Raw data images for Bands 1 through 8 taken by SeaWiFS on October 6, 1997 (Day-279).

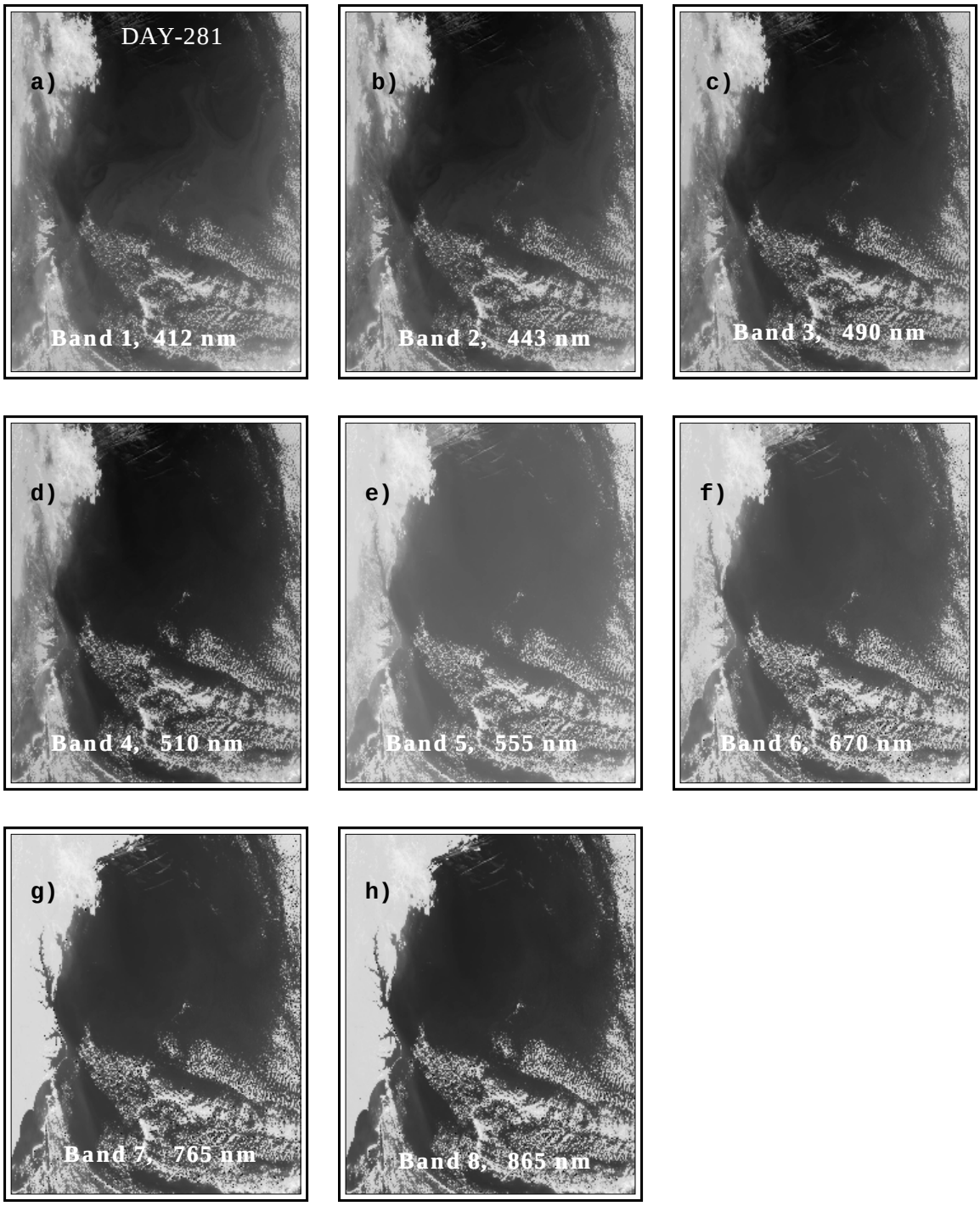

Figure 5.3 Raw data images for Bands 1 through 8 taken by SeaWiFS on October 8, 1997 (Day-281).

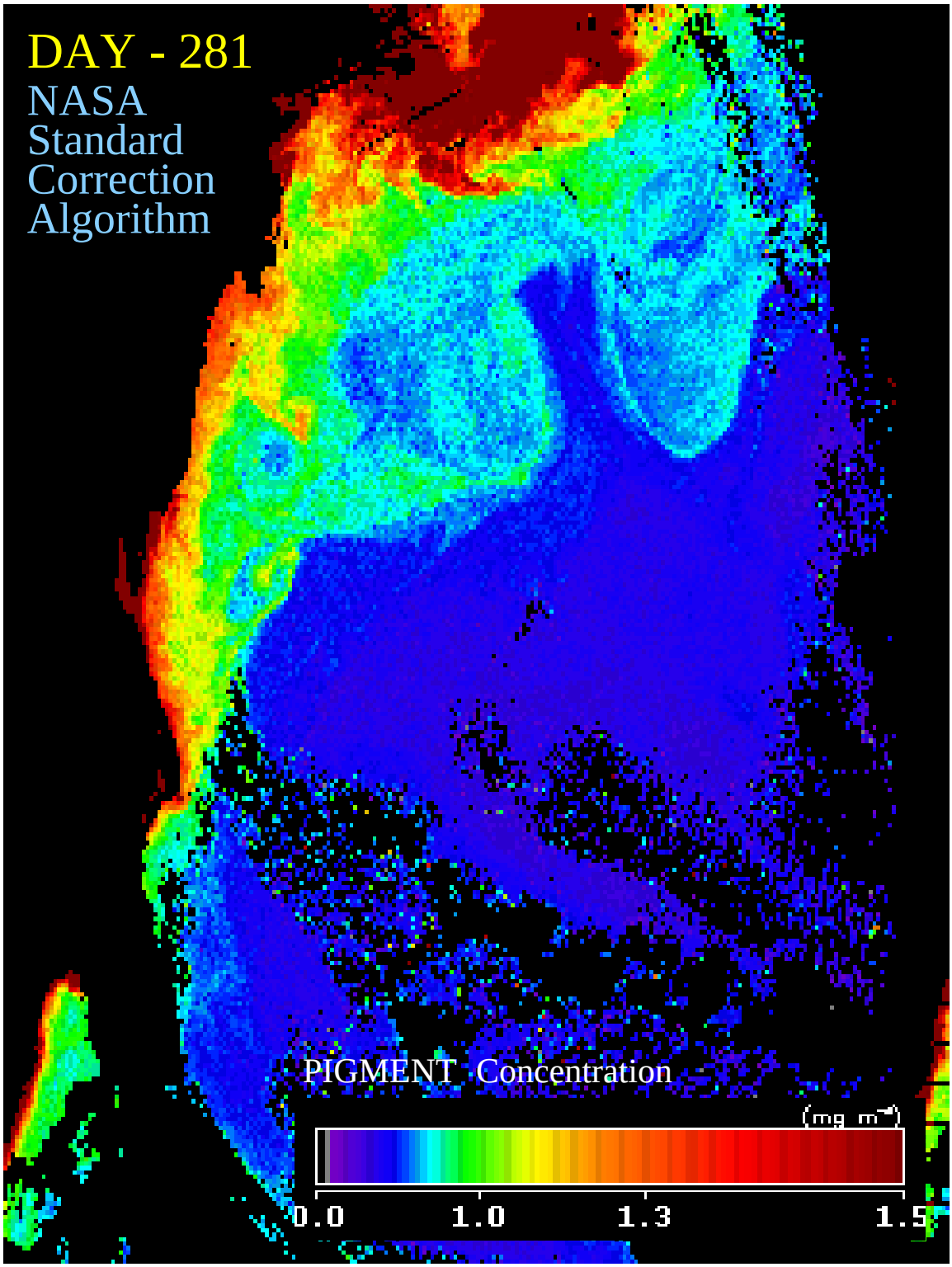

Figure 5.4 Level-2 pigment concentration obtained using the NASA Standard Algorithm for Day-281

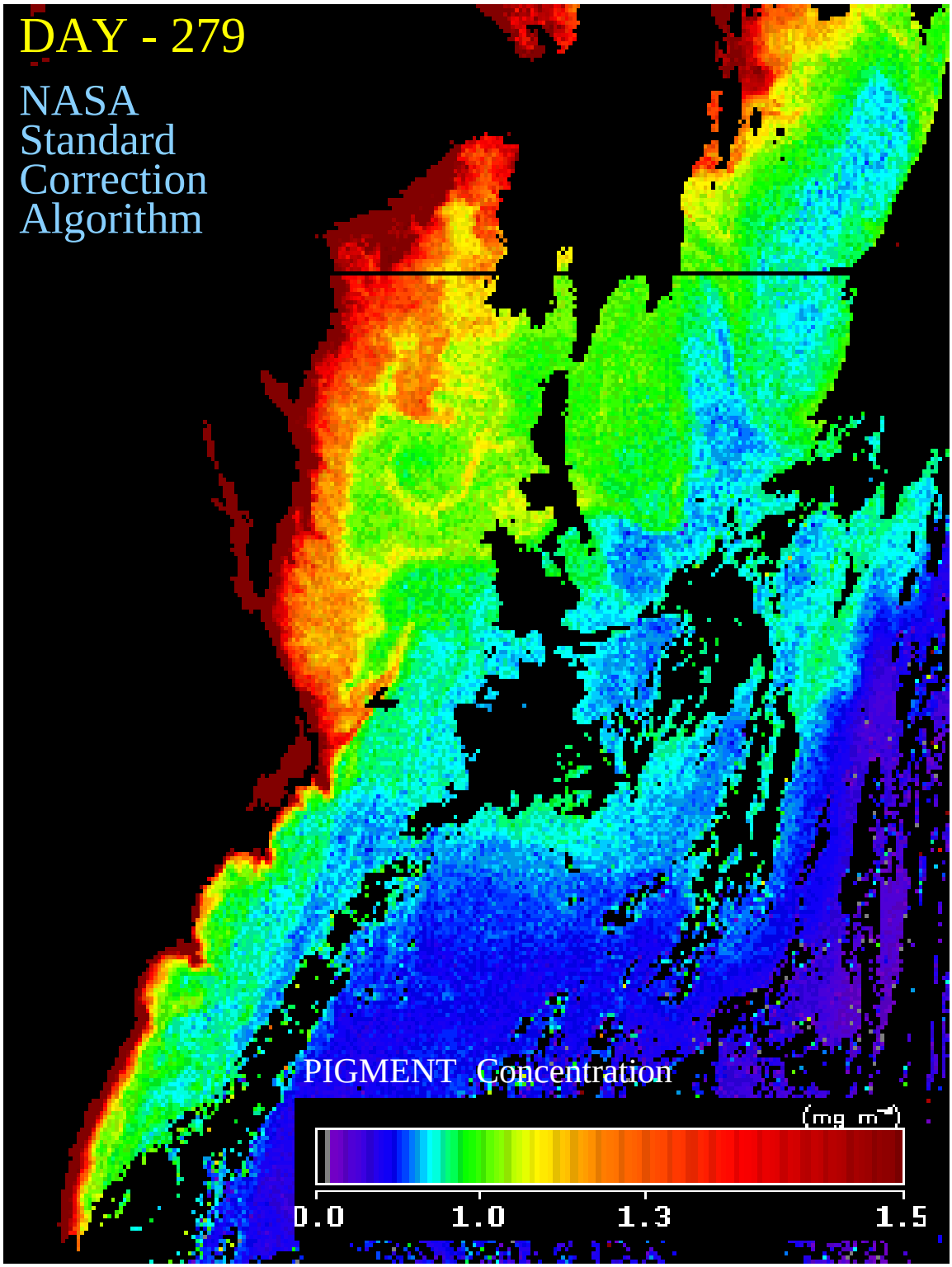

Figure 5.5 Level-2 pigment concentration obtained using the NASA Standard Algorithm for Day-279

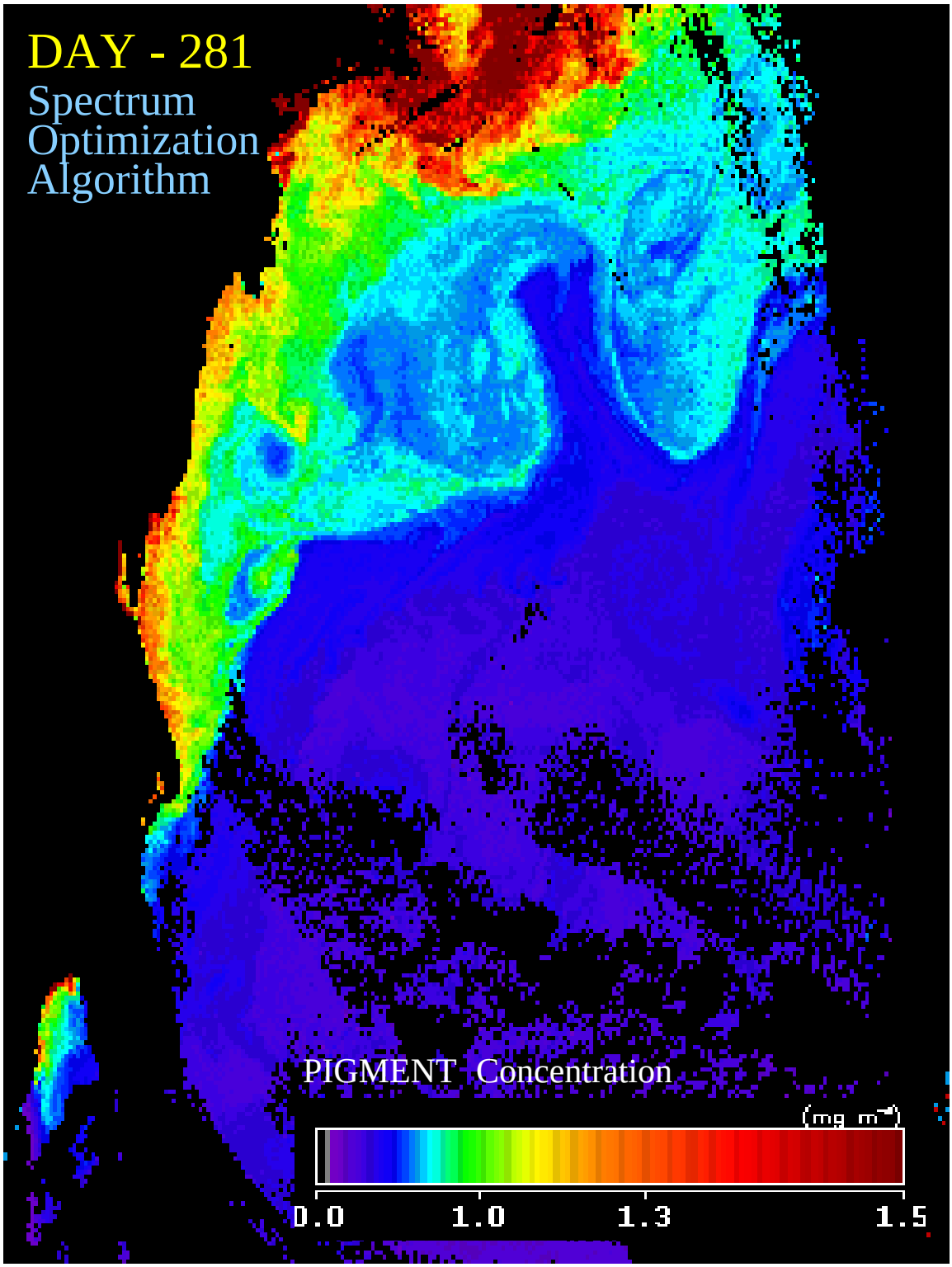

Figure 5.6 Level-2 pigment concentration obtained using the Spectrum Optimization Algorithm for Day-281

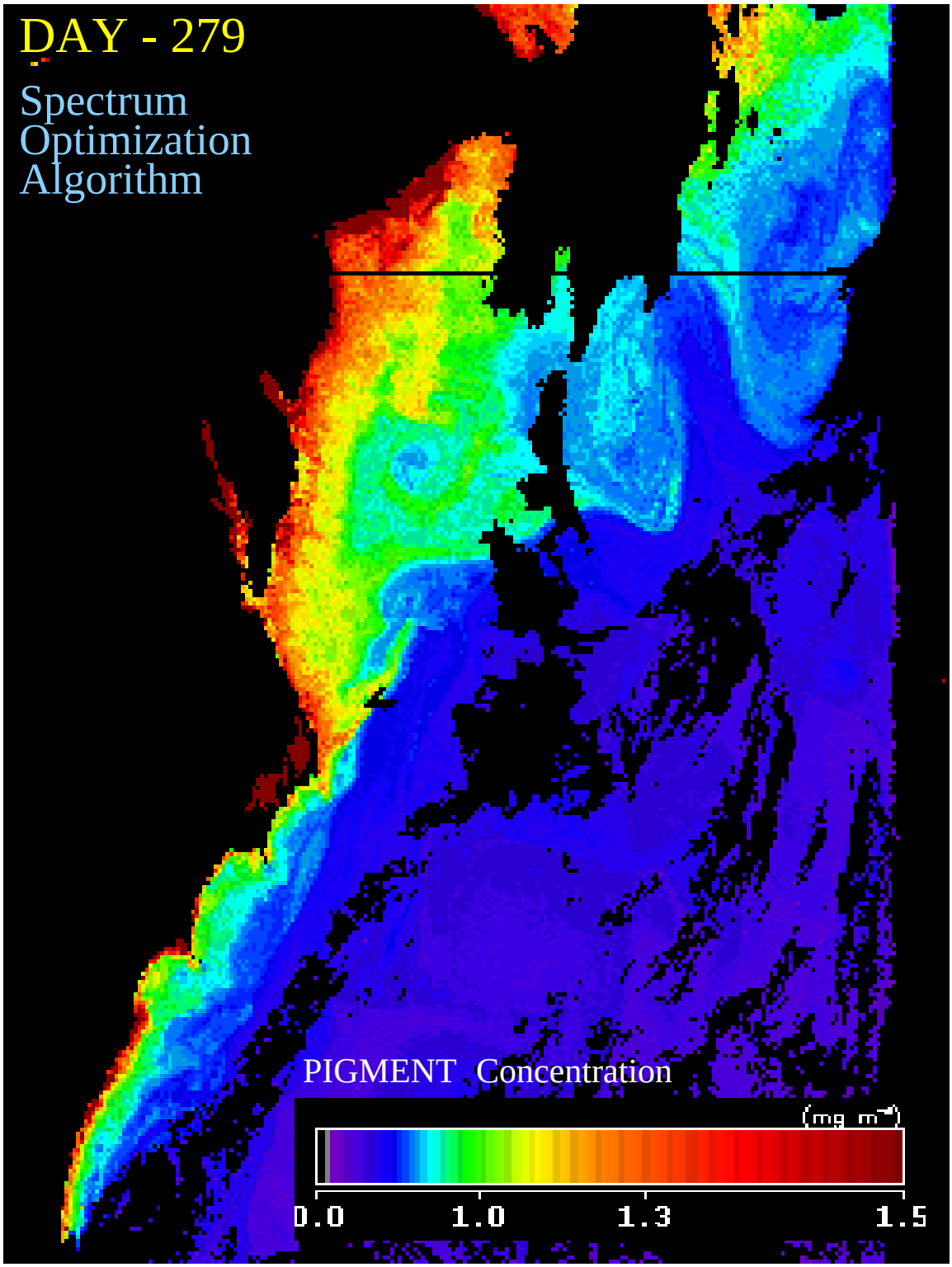

Figure 5.7 Level-2 pigment concentration obtained using the Spectrum Optimization Algorithm for Day-279

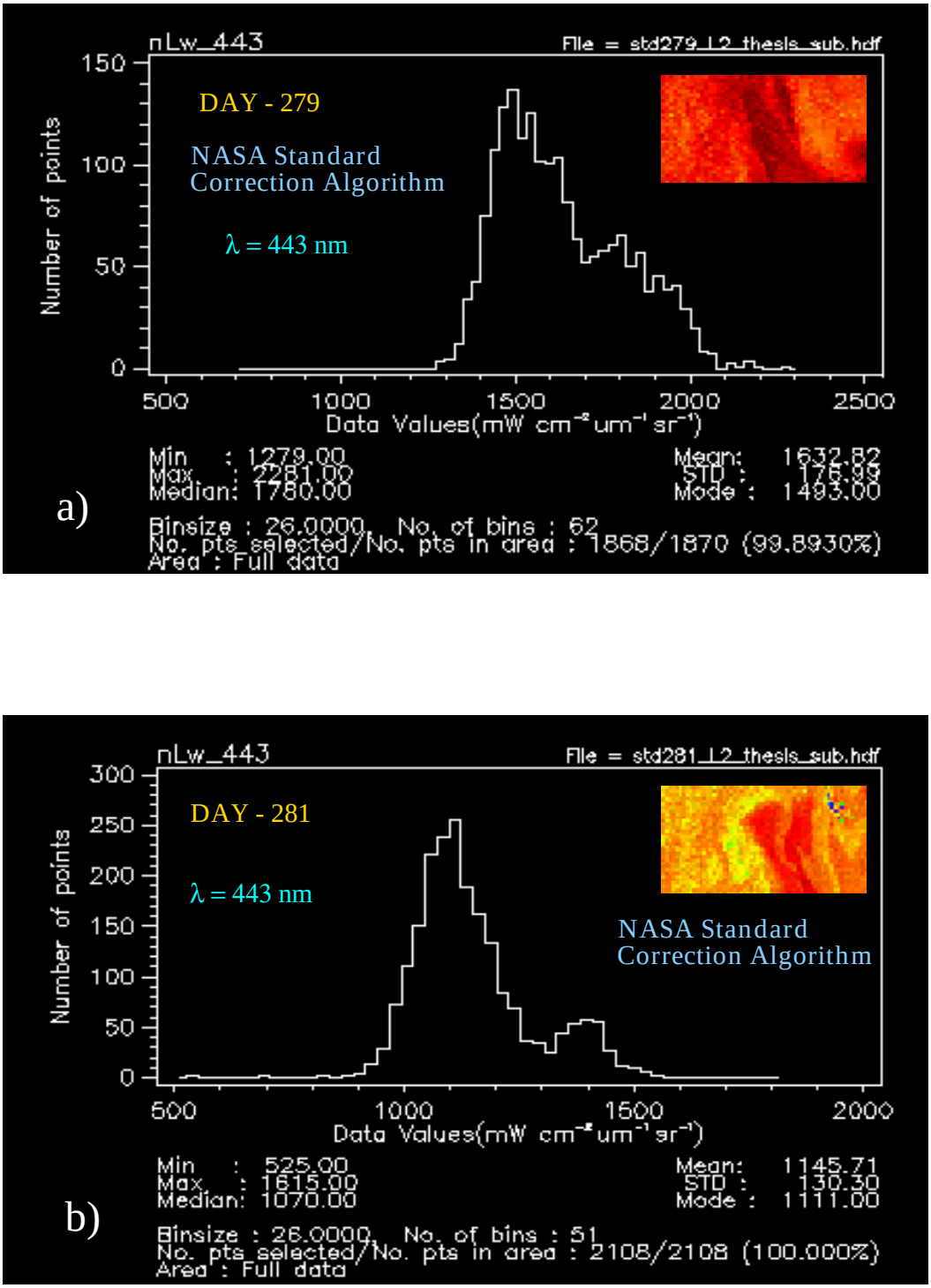

Figure 5.8 Level-2 Band 2 (443 nm) image obtained using the NASA Standard Correction Algorithm for a) Day-279, b) Day-281 and, corresponding histograms

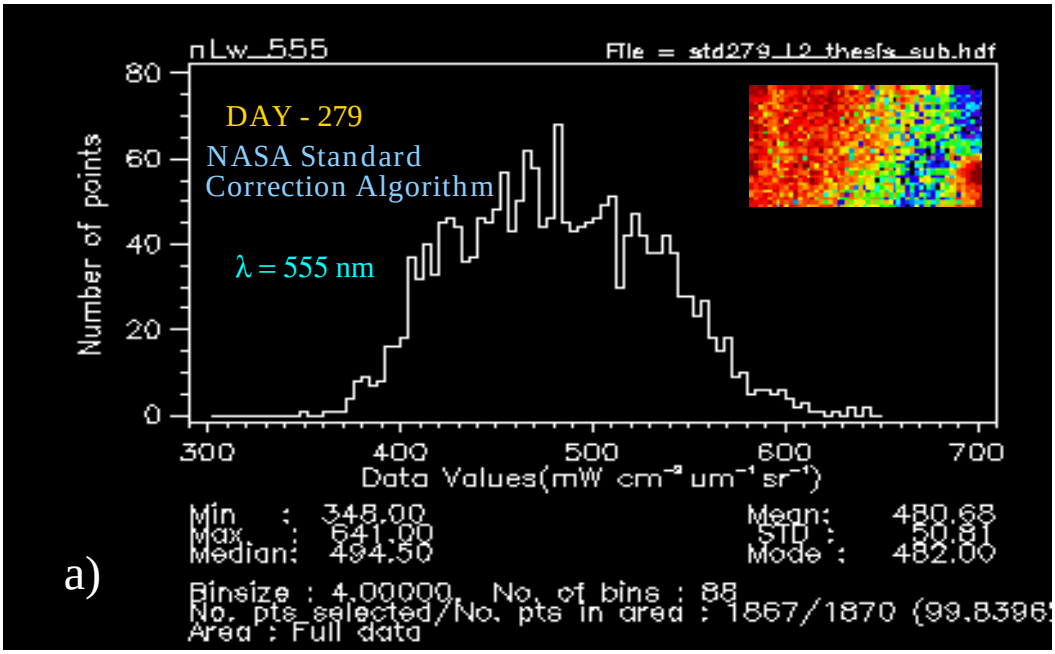

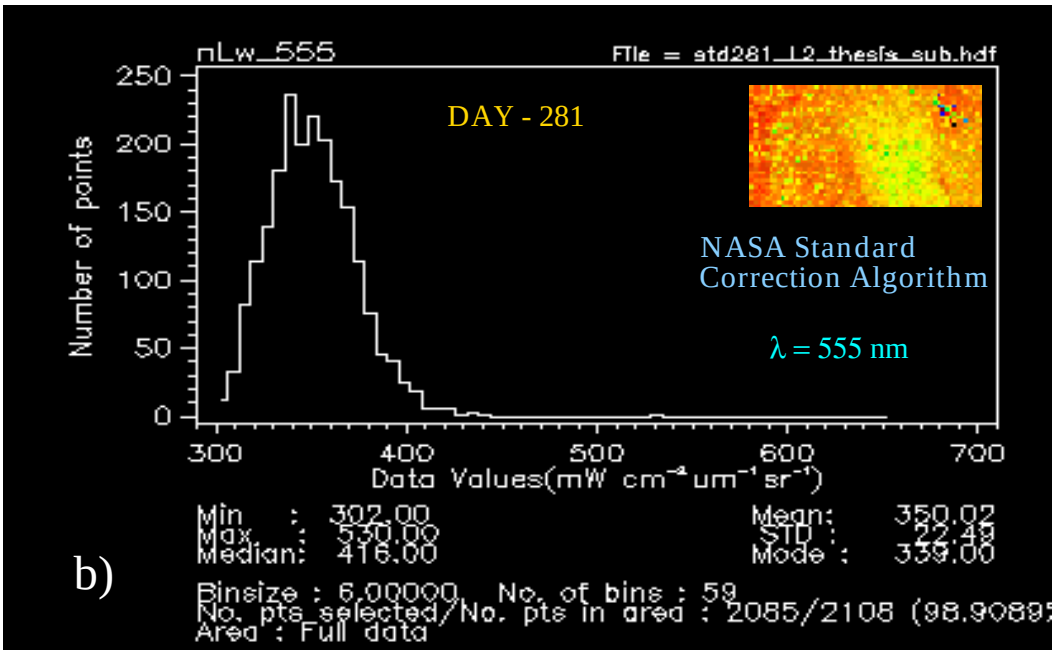

Figure 5.9 Level-2 Band 5 (555 nm) image obtained using the NASA Standard Correction Algorithm for a) Day-279, b) Day-281 and, corresponding histograms

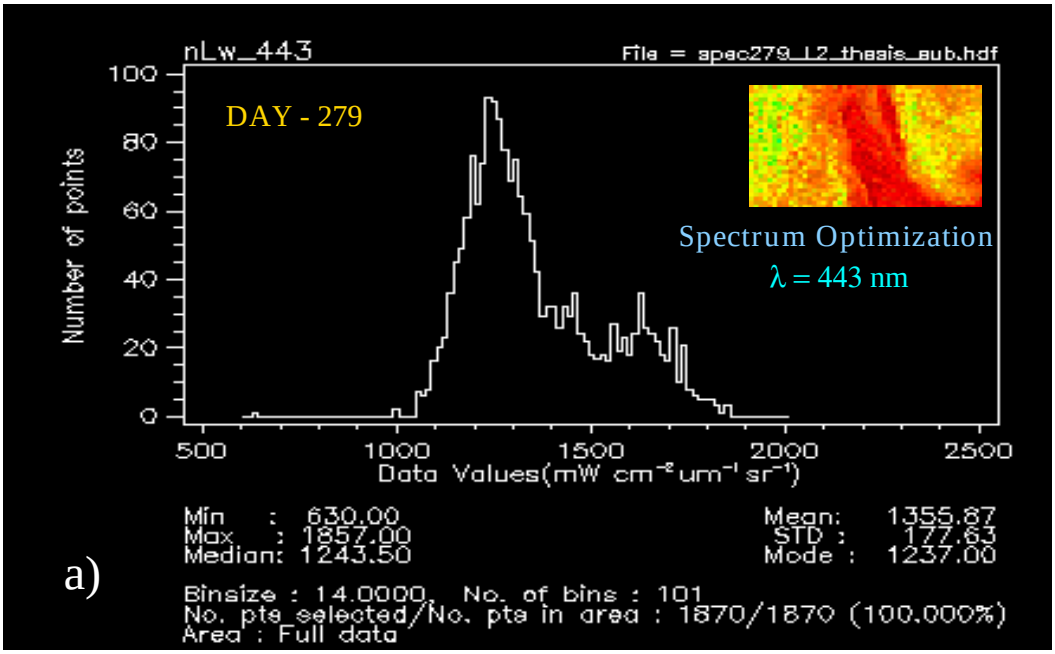

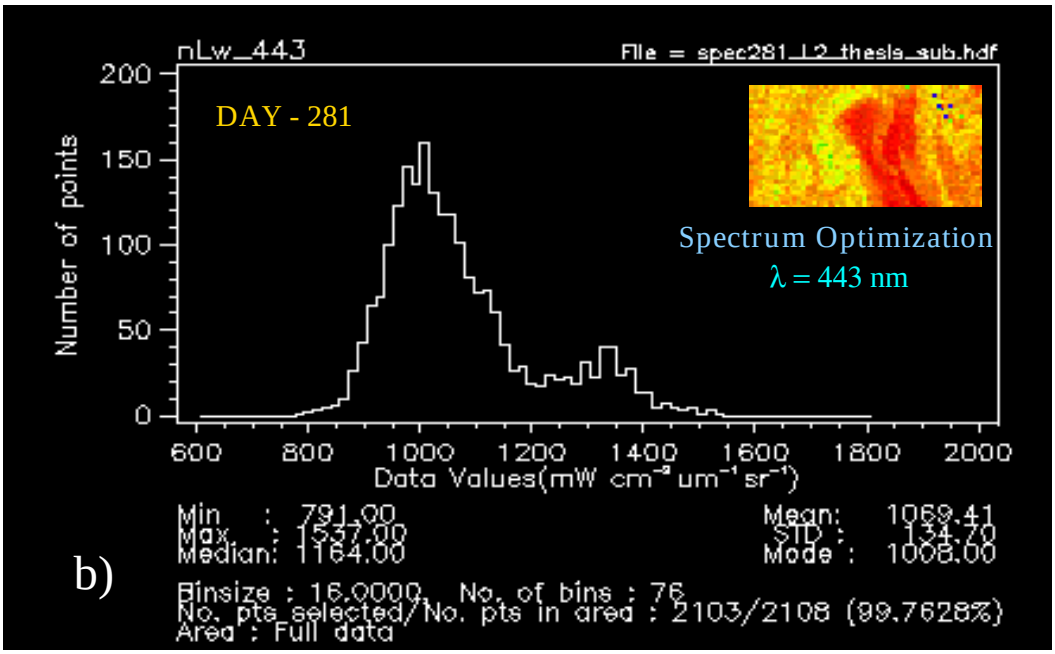

Figure 5.10 Level-2 Band 2 (443 nm) image obtained using the Spectrum Optimization Algorithm for a) Day-279, b) Day-281 and, corresponding histograms

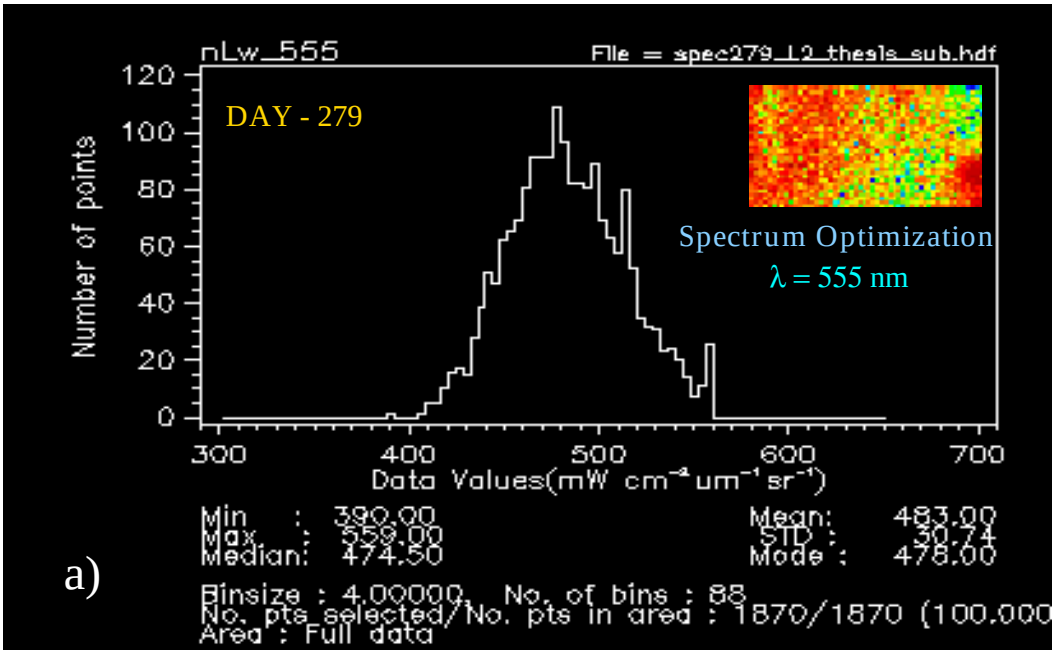

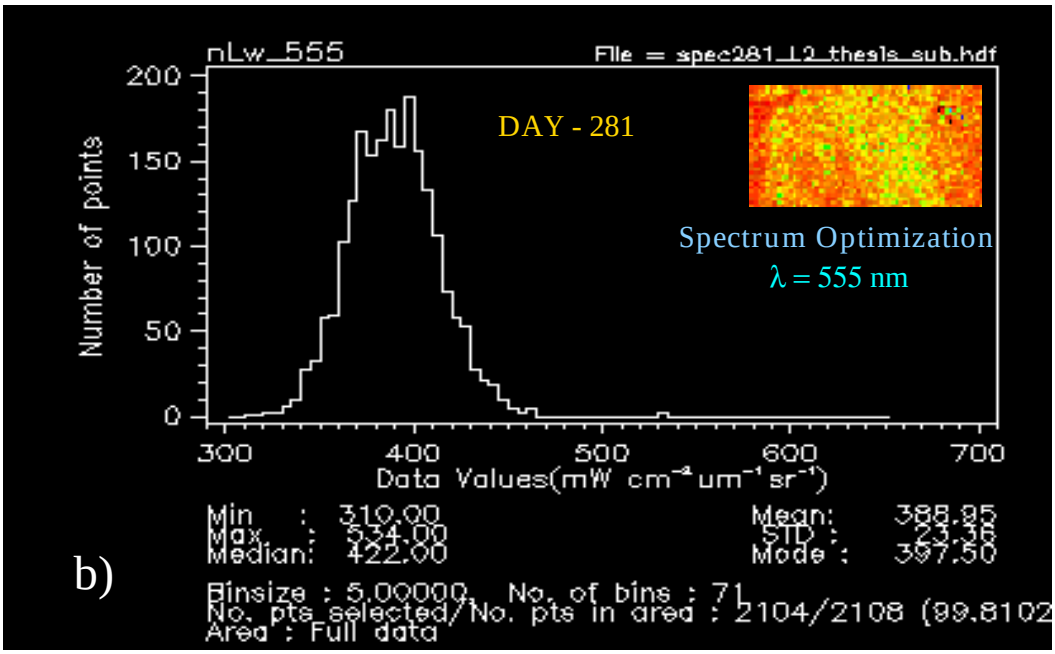

Figure 5.11 Level-2 Band 5 (555 nm) image obtained using the Spectrum Optimization Algorithm for a) Day-279, b) Day-281 and, corresponding histograms

Conclusion. The results presented in this chapter show that:

- Spectrum Optimization algorithm (SO) was successfully implemented in an image processing environment.

- SO produced excellent C for both days (in spite of turbid atmosphere on DAY-279) in agreement with the predictions in Chapter 4.

- SO produced normalized water-leaving radiances (nLw) with narrower distributions than NASA Standard algorithm and with smaller shift to higher nLw on DAY-279.

- compared to the results of NASA Standard Correction Algorithm, SO produced less noisy images, i.e., more water features were observed (the aspect is not understood at present).

VI. CONCLUSION

An atmospheric correction algorithm based on the non-linear optimization procedures capable of retrieving simultaneously the aerosol and ocean water optical properties under the presence of both highly and weakly absorbing aerosols has been developed in this dissertation. The Junge power-law with variable refractive index have been choosen as the model aerosols, since their radiative properties can be varied continuously via the parameters $\{\nu, m = m_r - im_i\}$, providing a possibility to make use of non-linear optimization techniques.

The algorithm performance with the simulated data revealed the robustness of the method when dealing with both highly and weakly absorbing atmospheric aerosols. In fact, the objective function S_{LSQ}, the "measure of the quality of the data fit", was extremely small, i.e., 0.27% for the Maritime-80 and 0.15% for the Urban-80 test aerosol models. The retrieval of the ocean pigment concentration was surprisingly accurate, the error reaching on the average 3.5% for Maritime-80, and 5.1% for Urban-80 models. The error in the single-scattering albedo ϖ_0 was on the average 3%. As long as the phase functions of the Junge power-law aerosol models does not reproduce properly the phase functions of realistic aerosols, the retrieval of the optical thickness $\tau(\lambda)$ was noticably poorer then that of other parameters. The error was sometimes as high as 30-40%. Unfortunately, this is a drawback of the algorithm. On the other hand, the fact that the other parameters, such as the pigment concentration and the single-scattering albedo, were obtained within an acceptable accuracy sets forward a suggestion as to whether the actual form of the phase function is necessary for that purpose.

We studied further the effects of the calibration errors after effecting an in-orbit calibration adjustment. The result of retrievals was not substantially worse. In the case of the pigment concentration the error was on the average 6% for positive calibration errors and 9% for the negative ones.

The presence of the aerosol vertical structure has adversely affected the results of the atmospheric corrections. The impact was so strong in cases when the aerosol was uniformly mixed with the Rayleigh gas that the results could have hardly been called valid. It is suggested, however, to use the Junge power-law models which are partially mixed up with gas. In this case, the error of retrievals is expected to be that of the error when calibration uncertainty is present in the radiance data.

The effects of the variable refractive index with respect to the wavelength has been also analyzed. The maritime-mineral aerosols are appropriate representatives of this class of aerosols. The study shows that the retrieval of the pigment concentration is still acceptable (the error was within 25%), though the accuracy of the other parameters degraded substantially. However, both cases, the aerosol vertical distribution and the refractive index variable with the wavelength were easily recognized by the algorithm. The objective function S_{LSQ} was on the average 10-15% for the aerosol vertical distribution and 1.2% for the maritime-mineral aerosols.

The algorithm has been successfully incorporated into the SeaWiFS image processing system SeaDAS. Images of the sea surface have been corrected for two days with two distinctive aerosol present: turbid and non-turbid. In both cases, the retrieval of the pigment concentration produced similar results, in contrast, to those obtained with the NASA Standard Correction Algorithm, which failed in the case of the turbid atmosphere. The water-leaving radiances for two days were compared with the help of image histograms that revealed a general shift of radiances' peaks in all bands toward higher values which might be a consequence of an incorrect calibration adjustment supplied to the algorithm.

Though the extensions to the algorithm are yet to be studied, this work demonstrates a general applicability of the method to ocean color remote sensing.

APPENDIX: Foundations of Quasi-Newton Optimization Methods

In this Appendix laid out will be the basic theoretical foundation of the non-linear programming (optimization) methods belonging to the so-called quasi-Newton class of methods. The theory will be supported with an examplary Davidon-Fletcher-Powell algorithm solution. Apparently, it is impossible to describe in a small section all the cornerstones of this wide field of computer science. So, the purpose is limited to highlighting the major building blocks of any optimization procedure, the knowledge of which provides the pavement for better and ellegant problem understanding and solving.

A.1 Notation, Terminology and Definitions.

Consider the n-dimensional euclidian space E^n. A point $\mathbf{x} = [x_1, \ldots, x_n]^T$ in this space is a column vector of its components $x_1, \ldots, x_n$. In general, it will be assumed that the problem arising functions $f(\mathbf{x})$ are smooth, that is continuous and continuously differentiable ($\mathcal{C}^1$). Let us have two other $\mathcal{C}^1$ functions $h_j(\mathbf{x})$ and $g_j(\mathbf{x})$. Then, the non-linear optimization problem might be stated as follows.

Minimize

$$f(\mathbf{x}), \quad \mathbf{x} \in E^n \tag{A.1}$$

subject to m linear and/or non-linear constraints:

$$h_j(\mathbf{x}) = 0, \quad j = 1, \ldots, m \tag{A.2}$$

and $(p - m)$ linear and/or non-linear non-equality constraints:

$$g_j(\mathbf{x}) \geq 0, \quad j = m + 1, \ldots, p \tag{A.3}$$

Now, a function $\phi(\mathbf{x})$ is called *convex* over the domain $\mathcal{R}$ if for any two vectors, say $\mathbf{x}_1$ and $\mathbf{x}_2 \in \mathcal{R}$ the following inequality is satisfied:

$$\phi(\theta\mathbf{x}_1 + (1-\theta)\mathbf{x}_2) \leq \theta\phi(\mathbf{x}_1) + (1-\theta)\phi(\mathbf{x}_2), \qquad 0 \leq \theta \leq 1 \tag{A.4}$$

In other words, a convex function $\phi(\mathbf{x})$, by its classical definition (A.4), cannot have any value larger then the values of the function obtained by linear interpolation between $\phi(\mathbf{x}_1)$ and $\phi(\mathbf{x}_2)$. A differentiable convex function has the following properties:

a) $\phi(\mathbf{x}_2) - \phi(\mathbf{x}_1) \geq \nabla^T\phi(\mathbf{x}_1)\,(\mathbf{x}_2 - \mathbf{x}_1)$ for $\forall\mathbf{x}_1, \mathbf{x}_1$

b) the Hessian matrix (see below) is positive definite

c) $\phi(\mathbf{x})$ has only one extremum.

The convexity of a set of points $\{\mathbf{x}_j\}$ is defined the same way, i.e. all the vectors $\mathbf{x} = \theta\mathbf{x}_1 + (1-\theta)\mathbf{x}_2,\ \forall\mathbf{x}_1, \mathbf{x}_2,\ 0 \leq \theta \leq 1$, should belong to the set $\{\mathbf{x}_j\}$. Other seven types of convexity, very relevant to the optimization problems, have been discussed by Ponstein.[46]

For the norm of a vector $\|\mathbf{x}\|$ we choose the common L_2-norm, defined as

$$\|\mathbf{x}\|_2 = \sqrt{(\mathbf{x}^T\mathbf{x})} \tag{A.5}$$

Note, as has been pointed out by Powell,[47] L_1-norm, defined as $\|\mathbf{x}\|_1 = \sum_{i=1}^{n} x_i$, very often leads to bad-conditioning in the approximation methods.

Iterative procedures generate a sequence of points $\mathbf{x}^{(1)}, \mathbf{x}^{(2)}, \ldots, \mathbf{x}^{(k)}, \ldots$, or $\{x^{(k)}\}$ (where k indicates the iteration number) converging to a fixed, [48,49] stationary point $\mathbf{x}^*$ which provides the solution (or optimal value solution) to a problem.[35]

For any iteration $\mathcal{C}^1$-function $f(\mathbf{x}^{(k)})$ at the iteration point $\mathbf{x}^{(k)}$ there is a vector of its

first partial derivatives, or gradient vector, $\nabla f(\mathbf{x}^{(k)})$

$$\begin{pmatrix} \partial f(\mathbf{x}^{(k)})/\partial x_1 \\ \partial f(\mathbf{x}^{(k)})/\partial x_2 \\ \vdots \\ \partial f(\mathbf{x}^{(k)})/\partial x_n \end{pmatrix} = \nabla f(\mathbf{x}^{(k)}) \equiv \nabla f^{(k)} \tag{A.6}$$

If $f(\mathbf{x}^{(k)})$ is twice continuously differentiable ($\mathcal{C}^2$), then there exists a matrix of its second partial derivatives or, *Hessian matrix* $\mathbf{H}(\mathbf{x}^{(k)})$, written as

$$\begin{pmatrix} \partial f(\mathbf{x}^{(k)})/\partial x_1^2 & \dots & \partial f(\mathbf{x}^{(k)})/\partial x_1 \partial x_n \\ \vdots & \ddots & \vdots \\ \partial f(\mathbf{x}^{(k)})/\partial x_n \partial x_1 & \dots & \partial f(\mathbf{x}^{(k)})/\partial x_n^2 \end{pmatrix} = \nabla^2 f(\mathbf{x}^{(k)}) \equiv \mathbf{H}(\mathbf{x}^{(k)}) \tag{A.7}$$

This matrix is square and symmetric. In the n-dimensional Euclidian space we define a line as a set of points

$$\mathbf{x} = \mathbf{x}(\lambda) = \mathbf{x}' + \lambda \mathbf{s} \tag{A.8}$$

for all λ, a fixed point $\mathbf{x}'$ and any vector $\mathbf{s}$ collinear with the line (see Fig.A.1).

From (A.8) we can determine derivatives of $f(\mathbf{x})$ along the line:

$$\frac{d}{d\lambda} = \sum_i \frac{dx_i(\lambda)}{d\lambda} \frac{\partial}{\partial x_i} = \sum_i s_i \frac{\partial}{\partial x_i} = \mathbf{s}^T \nabla \tag{A.9}$$

The slope of $f(\mathbf{x})$ along the line at any point $\mathbf{x}(\lambda)$ is

$$\frac{df}{d\lambda} = \mathbf{s}^T \nabla f \equiv \nabla^T f \ \mathbf{s} \tag{A.10}$$

The curvature along the line is

$$\frac{d^2 f}{d\lambda^2} = \frac{d}{d\lambda} \frac{df}{d\lambda} = \mathbf{s}^T \nabla (\nabla^T f \ \mathbf{s}) = \mathbf{s}^T \nabla^2 f \ \mathbf{s} \tag{A.11}$$

where ∇f and $\nabla^2 f$ are evaluated at $\mathbf{x}(\lambda)$.

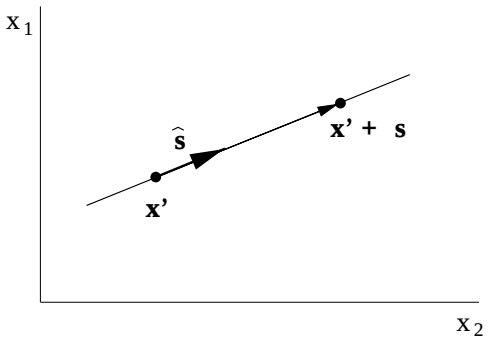

Figure A.1 Definition of a line.

Assume that $\mathbf{x}^{(k)}$ is some point of an iteration. Expanding $f(\mathbf{x})$ in the vicinity of $\mathbf{x}^{(k)}$ into the Taylor series, truncating all terms of orders higher then two, we obtain:

$$f(\mathbf{x}) - f(\mathbf{x}^{(k)}) \approx (\nabla f(\mathbf{x}^{(k)}))^T \ (\mathbf{x} - \mathbf{x}^{(k)}) + \frac{1}{2} \ (\mathbf{x} - \mathbf{x}^{(k)})^T \ \nabla^2 f(\mathbf{x}^{(k)}) \ (\mathbf{x} - \mathbf{x}^{(k)}) \quad (A.12)$$

where $\nabla^2 f(\mathbf{x}^{(k)}) \equiv \mathbf{H}(\mathbf{x}^{(k)})$ is the Hessian matrix. Note, for a quadratic unconstrained functions (Eq. (A.12)), the necessary conditions for $\mathbf{x}^*$ to be a local minimum is

1. $f(\mathbf{x})$ is differentiable at $\mathbf{x}^*$,
2. $\nabla f(\mathbf{x}^*) = \mathbf{0}$,
3. (*sufficient condition*) the Hessian is positive definite.

A.2 Steepest Descent Method.

Before continuing, it can be observed that the iteration step from the point $\mathbf{x}^{(k)}$ to $\mathbf{x}^{(k+1)}$ may be viewed as

$$\mathbf{x}^{(k+1)} = \mathbf{x}^{(k)} + \Delta\mathbf{x}^{(k)} = \mathbf{x}^{(k)} + \lambda^{(k)} \ \hat{\mathbf{s}}^{(k)} = \mathbf{x}^{(k)} + \lambda^{*(k)} \ \mathbf{s}^{(k)} \quad (A.13)$$

where $\hat{\mathbf{s}}^{(k)}$ is a unit vector in the direction of $\Delta\mathbf{x}^{(k)}$, $\mathbf{s}^{(k)}$ is a generic vector in the direction $\Delta\mathbf{x}^{(k)}$, $\lambda^{(k)}$ and $\lambda^{*(k)}$ are scalars such that $\Delta\mathbf{x}^{(k)} = \lambda^{(k)} \ \hat{\mathbf{s}}^{(k)} = \lambda^{*(k)} \ \mathbf{s}^{(k)}$.

In the search for a reliable direction $\hat{\mathbf{s}}^{(k)}$ one may suggest to pick it up in the direction

of the greatest decrease of $f(\mathbf{x})$ with respect to its variable $\mathbf{x}$, i.e.

$$\hat{\mathbf{s}}^{(k)} = -\frac{\nabla f(\mathbf{x}^{(k)})}{\|\nabla f(\mathbf{x}^{(k)})\|}, \tag{A.14}$$

where $\|\nabla f(\mathbf{x}^{(k)})\|$ is the chosen norm of a vector. Plugging this back into Eq. (A.13), we obtain the following step

$$\begin{aligned} \mathbf{x}^{(k+1)} &= \mathbf{x}^{(k)} - \lambda^{(k)} \frac{\nabla f(\mathbf{x}^{(k)})}{\|\nabla f(\mathbf{x}^{(k)})\|} \\ &= \mathbf{x}^{(k)} - \lambda^{*(k)} \ \nabla f(\mathbf{x}^{(k)}) \end{aligned} \tag{A.15}$$

where $\lambda^{*(k)}$ is a variable parameter in the Eq. (A.8). In order to provide the best step possible, it is needed to perform a one-dimensional (in $\lambda^{*(k)}$) search for a minimum of $f(\mathbf{x}^{(k+1)})$ (the concept of the one-dimensional search has been well-developed and can be found elsewhere in literature. However, in the author's opinion, the one described by Armijo[50] proved to be very fast and extremely robust in real problems). Thus, we arrive at the point $\mathbf{x}^{(k+1)}$. Proceeding this way with $\mathbf{x}^{(k+2)}, \ldots$, the optimal value solution $\mathbf{x}^*$ may be found that satisfies some requirements for a termination: value of $f(\mathbf{x})$, $\mathbf{x}$ itself, smallness of λ, zeroing of $\nabla f(\mathbf{x})$, etc. At the solution point $\mathbf{x}^*$, typically, the Hessian is determined and, if it is not positive definite, the $\mathbf{x}$ should be moved from its position one way or another (or *penalized*), like in the case of having a saddle point.

Returning back to the Eq. (A.15), we may observe that formally $\lambda^{(k)}$ can be found from the condition of minimum of a function (note, this is not generally true for constrained problems):

$$\frac{df(\mathbf{x}^{(k)} + \lambda^{(k)} \ \hat{\mathbf{s}}^{(k)})}{d\lambda} = 0 \tag{A.16}$$

If $f(\mathbf{x})$ is a quadratic function (i.e. representable by (A.12)), then from (A.12)

$$(\nabla f(\mathbf{x}^{(k)}))^T \ \hat{\mathbf{s}}^{(k)} + (\hat{\mathbf{s}}^{(k)})^T \ \mathbf{H}(\mathbf{x}^{(k)}) \ \lambda \ \hat{\mathbf{s}}^{(k)} = 0 \tag{A.17}$$

So that,

$$\lambda^{(k)} = -\frac{(\nabla f(\mathbf{x}^{(k)}))^T \ \hat{\mathbf{s}}^{(k)}}{(\hat{\mathbf{s}}^{(k)})^T \ \mathbf{H}(\mathbf{x}^{(k)}) \ \hat{\mathbf{s}}^{(k)}} \tag{A.18}$$

A.3 Newton Method

Let us try to look at the minimum of $f(\mathbf{x})$ in the direction of $\Delta\mathbf{x}^{(k)}$, i.e.

$$\frac{\partial\ f(\mathbf{x}^{(k)})}{\partial\ \Delta\mathbf{x}} = 0 \tag{A.19}$$

From (A.12) this yields

$$0 = \nabla f(\mathbf{x}^{(k)}) + \nabla^2 f(\mathbf{x}^{(k)})\ \mathbf{x}^{(k)} \tag{A.20}$$

so that,

$$\mathbf{x}^{(k)} = -\ \frac{\nabla f(\mathbf{x}^{(k)})}{\nabla^2 f(\mathbf{x}^{(k)})} \tag{A.21}$$

or,

$$\mathbf{x}^{(k+1)} = \mathbf{x}^{(k)} - [\nabla^2 f(\mathbf{x}^{(k)})]^{-1}\ \nabla f(\mathbf{x}^{(k)}) \tag{A.22}$$

This would provide the solution if only $f(\mathbf{x})$ were strictly quadratic. Generally speaking, it is not ever the case. Conforming (A.22) to (A.15), we obtain the following

$$\mathbf{x}^{(k+1)} = \mathbf{x}^{(k)} - \lambda^{(k)} \frac{[\nabla^2 f(\mathbf{x}^{(k)})]^{-1}\ [\nabla f(\mathbf{x}^{(k)})]}{\|[\nabla^2 f(\mathbf{x}^{(k)})]^{-1}\ [\nabla f(\mathbf{x}^{(k)})]\|} \tag{A.23}$$

or,

$$\mathbf{x}^{(k+1)} = \mathbf{x}^{(k)} - \lambda^{*(k)}\ \mathbf{H}^{-1}(\mathbf{x}^{(k)})\ \nabla f(\mathbf{x}^{(k)}) \tag{A.24}$$

Observe that in contrast to the Steepest Descent method the search direction is now given by

$$\mathbf{s}^{(k)} = -\mathbf{H}^{-1}(\mathbf{x}^{(k)})\ \nabla f(\mathbf{x}^{(k)}) \tag{A.25}$$

Well, numerical complexities of this approach are apparent: 1) the second derivatives should be computed; 2) a matrix inversion is required. All this makes the method extremely unpractical.

A.4 Quasi-Newton or Variable Metric Methods

This section will provide the way to approximate the inverse Hessian matrix $\mathbf{H}^{-1}(\mathbf{x}^{(k)})$ without actually computing it (from here the term "quasi-Newton"). [35,38] Denoting

$$\mathbf{\Psi}(\mathbf{x}^{(k)}) \approx \mathbf{H}^{-1}(\mathbf{x}^{(k)}) \tag{A.26}$$

the Eq. (A.24) becomes

$$\mathbf{x}^{(k+1)} = \mathbf{x}^{(k)} - \lambda^{*(k)}\ \mathbf{\Psi}(\mathbf{x}^{(k)})\ \nabla f(\mathbf{x}^{(k)}) \tag{A.27}$$

(note, $\mathbf{\Psi}(\mathbf{x}^{(k)})$ corresponds to the identity matrix in the Steepest Descent method and, is typically called the *direction matrix*).

From analytical geometry it is known that for quadratic functions the Hessian matrix is symmetric. Using (A.12) and noting that $\mathbf{H}(\mathbf{x}^{(k)})$ is set, i.e. constant, and, constant also are the $(\nabla f(\mathbf{x}^{(k)}))^T$ and $f(\mathbf{x}^{(k)})$, we find the gradient of $f(\mathbf{x})$ to be

$$\begin{aligned}\nabla f(\mathbf{x}) &= (\nabla f(\mathbf{x}^{(k)}))^T + \frac{1}{2}\ (\mathbf{H}(\mathbf{x}^{(k)}) + \mathbf{H}^T(\mathbf{x}^{(k)}))\ (\mathbf{x} - \mathbf{x}^{(k)}) \\ &= (\nabla f(\mathbf{x}^{(k)}))^T + \mathbf{H}(\mathbf{x}^{(k)})\ (\mathbf{x} - \mathbf{x}^{(k)})\end{aligned} \tag{A.28}$$

where we used the rule of the gradient of the scalar product of vectors $\mathbf{x}$ and $\mathbf{Hx}$.

Premultiplying both sides by $\mathbf{H}^{-1}(\mathbf{x}^{(k)})$,

$$\mathbf{x}^{(k+1)} - \mathbf{x}^{(k)} = \mathbf{H}^{-1}(\mathbf{x}^{(k)})\ [\nabla f(\mathbf{x}^{(k+1)}) - \nabla f(\mathbf{x}^{(k)})] \tag{A.29}$$

Trying to find $\Delta\mathbf{\Psi}^{(k)}$

$$\mathbf{H}^{-1}(\mathbf{x}^{(k)}) \approx \omega\ \mathbf{\Psi}^{(k+1)} = \omega\ (\mathbf{\Psi}^{(k)} + \Delta\mathbf{\Psi}^{(k)}) \tag{A.30}$$

where ω is a scaling parameter, it is introduced since functions are typically non-quadratic, the technique we already used before in (A.24). At stage $(k+1)$ we are provided with $\mathbf{x}^{(k)}, \nabla f(\mathbf{x}^{(k)}), \nabla f(\mathbf{x}^{(k+1)})$ and $\mathbf{\Psi}^{(k)}$. Let $\Delta\mathbf{g}^{(k)} = \nabla f(\mathbf{x}^{(k+1)}) - \nabla f(\mathbf{x}^{(k)})$. Then

$$\mathbf{\Psi}^{(k+1)}\ \Delta\mathbf{g}^{(k)} = \frac{1}{\omega}\Delta\mathbf{x}^{(k)} \tag{A.31}$$

or,

$$\Delta\Psi^{(k)}\ \Delta\mathbf{g}^{(k)} = \frac{1}{\omega}\Delta\mathbf{x}^{(k)} - \Psi^{(k)}\ \Delta\mathbf{g}^{(k)} \tag{A.32}$$

Eq. (A.32) may be viewed as a system of n^2 equations in n^2 variables. Once it is solved, the information on $\Delta\Psi^{(k)}$ becomes available. By direct substitution it can be verified that

$$\Delta\Psi^{(k)} = \frac{1}{\omega}\ \frac{\Delta\mathbf{x}^{(k)}\ \mathbf{y}^T}{\mathbf{y}^T\ \Delta\mathbf{g}^{(k)}} - \frac{\Psi^{(k)}\ \Delta\mathbf{g}^{(k)}\ \mathbf{z}^T}{\mathbf{z}^T\Delta\mathbf{g}^{(k)}} \tag{A.33}$$

is the solution where $\mathbf{y}$ and $\mathbf{z}$ are *arbitrary* vectors. The freedom of choosing $\mathbf{y}$ and $\mathbf{z}$ leads to a variety of quasi-Newton methods. Some examples are:

Broyden:

$$\mathbf{y} = \mathbf{z} = \Delta\mathbf{x}^{(k)} - \Psi^{(k)}\ \Delta\mathbf{g}^{(k)} \tag{A.34}$$

$$\Delta\Psi^{(k)}_{\text{Broyden}} = \frac{[\Delta\mathbf{x}^{(k)} - \Psi^{(k)}\ \Delta\mathbf{g}^{(k)}]\ (\Delta\mathbf{x}^{(k)})^T\ \Psi^{(k)}}{\Delta\mathbf{g}^{(k)}\ (\Psi^{(k)})^T\mathbf{x}^{(k)}} \tag{A.35}$$

Davidon-Fletcher-Powell:

$$\mathbf{y} = \Delta\mathbf{x}^{(k)}, \qquad \mathbf{z} = \Psi^{(k)}\ \Delta\mathbf{g}^{(k)} \tag{A.36}$$

$$\Delta\Psi^{(k)}_{\text{DFP}} = \frac{[\Delta\mathbf{x}^{(k)}]\ [\Delta\mathbf{x}^{(k)}]^T}{[\Delta\mathbf{x}^{(k)}]^T\ [\Delta\mathbf{g}^{(k)}]} - \frac{\Psi^{(k)}\ [\Delta\mathbf{g}^{(k)}]\ [\Delta\mathbf{g}^{(k)}]^T\ [\Psi^{(k)}]^T}{[\Delta\mathbf{g}^{(k)}]^T\ \Psi^{(k)}\ [\Delta\mathbf{g}^{(k)}]} \tag{A.37}$$

Broyden-Fletcher-Goldfarb-Shanno:

$$\begin{aligned}\Delta\Psi^{(k)}_{\text{BFGS}} = &\left(1 + \frac{[\Delta\mathbf{g}^{(k)}]^T\ \Psi^{(k)}\ \Delta\mathbf{g}^{(k)}}{\Delta\mathbf{x}^{(k)}\ \Delta\mathbf{g}^{(k)}}\ \frac{\Delta\mathbf{x}^{(k)}\ [\Delta\mathbf{x}^{(k)}]^t}{[\Delta\mathbf{x}^{(k)}]^T\ \Delta\mathbf{g}^{(k)}}\right) \\ &- \left(\frac{\mathbf{x}^{(k)}\ [\Delta\mathbf{g}^{(k)}]^T\ \Psi^{(k)} + \Psi^{(k)}\ [\Delta\mathbf{g}^{(k)}]\ [\mathbf{x}^{(k)}]^T}{[\mathbf{x}^{(k)}]^T\ \Delta\mathbf{g}^{(k)}}\right)\end{aligned} \tag{A.38}$$

It should be noted, however, that BFGS algorithm has been derived from other suggestions and is given here for completeness since it is complementary to DFP algorithm.

Once the $\Delta\Psi^{(k)}$ are computed, (A.27) should be used to determine the length of the "next" step $\Delta\mathbf{x}^{(k)}$ through one-dimensional search, namely, minimizing $\lambda^{*(k)}$. Again, the iteration procedure is repeated until some of terminating conditions are met.

A.5 Example: analytical DFP minimization

As an example let us try to minimize an unconstrained function of two variables:

$$f(x_1, x_2) = 2\ (x_1 - 1)^2 + 3\ (x_2 - 2)^2 \qquad (Ae.1)$$

○

This simple quadratic function reaches its minimum $f(x_1, x_2) = 0$ at the point $\mathbf{x}^* = [1 \quad 2]^T$. We are trying to use the information from the previous subsections to perform all the required iterations assuming that the function and its derivatives can be computed analytically everywhere.

Step 0.

Let $\mathbf{x}^{(0)} = [5 \quad 5]^T$ be a starting iteration point and the inverse hessian matrix $\mathbf{\Psi}^{(0)} = \mathbf{I}$ (identity matrix). The function value is $f(\mathbf{x}^{(0)}) = 59$. The general formula for the gradient of the function $f(\mathbf{x})$ can be computed to be

$$\nabla f(\mathbf{x}) = \begin{bmatrix} 4x_1 - 4 \\ 6x_2 - 12 \end{bmatrix} \qquad (Ae.2)$$

Step 1.

The formula for the step function (A.27) becomes:

$$\mathbf{x}^{(1)} = \mathbf{x}^{(0)} - \lambda^{*(0)}\ \mathbf{\Psi}^{(0)}\ \nabla f(\mathbf{x}^{(0)}) \qquad (Ae.3)$$

or,

$$\begin{bmatrix} x_1^{(1)} \\ x_2^{(1)} \end{bmatrix} = \begin{bmatrix} 5 \\ 5 \end{bmatrix} - \lambda^{*(0)} \begin{bmatrix} 16 \\ 18 \end{bmatrix} \qquad (Ae.4)$$

For purposes of illustration we use the analytical minimum of $f(\mathbf{x}^{(1)})$ in $\lambda^{*(0)}$, i.e.

$$f(\mathbf{x}^{(1)}) = 59 - 580\ \lambda^{*(0)} + 1484\ (\lambda^{*(0)})^2 \qquad (Ae.5)$$

and,

$$\frac{d\ f(\mathbf{x}^{(1)})}{d\ \lambda^{*(0)}} = 0 = -580 + 2968\ \lambda^{*(0)} \qquad (Ae.6)$$

So that, $\lambda^{*(0)} = 0.195418$. From $(Ae.3)$ we determine the first iteration point $\mathbf{x}^{(1)}$:

$$\mathbf{x}^{(1)} \equiv \begin{bmatrix} x_1^{(1)} \\ x_2^{(1)} \end{bmatrix} = \begin{bmatrix} 1.873315 \\ 1.482476 \end{bmatrix} \qquad (Ae.7)$$

We complete the step with the other relevant results:

$$f(\mathbf{x}^{(1)}) = 2.3288 \qquad \Delta\mathbf{x}^{(0)} = \begin{bmatrix} -3.126685 \\ -3.517524 \end{bmatrix} \qquad \nabla f(\mathbf{x}^{(1)}) = \begin{bmatrix} 3.493260 \\ -3.105144 \end{bmatrix}$$

$$\Delta\mathbf{g}^{(0)} = \begin{bmatrix} -12.506740 \\ -21.105144 \end{bmatrix} \qquad \mathbf{\Psi}^{(0)} = \begin{bmatrix} 1 & 0 \\ 0 & 1 \end{bmatrix} \qquad (Ae.8)$$

The update to the approximate inverse hessian matrix $\mathbf{\Psi}^{(0)}$ can be found using (A.37):

$$\Delta\mathbf{\Psi}^{(0)} = \frac{\begin{bmatrix} -3.126685 & 0 \\ -3.517524 & 0 \end{bmatrix} \begin{bmatrix} -3.126685 & -3.517524 \\ 0 & 0 \end{bmatrix}}{[-3.126685 \quad -3.517524] \begin{bmatrix} -12.506740 \\ -21.105144 \end{bmatrix}}$$

$$- \frac{\begin{bmatrix} 1 & 0 \\ 0 & 1 \end{bmatrix} \begin{bmatrix} -12.506740 & 0 \\ -21.105144 & 0 \end{bmatrix} \begin{bmatrix} -12.506740 & -21.105144 \\ 0 & 0 \end{bmatrix} \begin{bmatrix} 1 & 0 \\ 0 & 1 \end{bmatrix}}{[-12.506740 \quad -21.105144] \begin{bmatrix} 1 & 0 \\ 0 & 1 \end{bmatrix} \begin{bmatrix} -12.506740 \\ -21.105144 \end{bmatrix}}$$

$$= \begin{bmatrix} -0.173645 & -0.341543 \\ -0.341543 & -0.630937 \end{bmatrix}$$

And,

$$\mathbf{\Psi}^{(1)} = \begin{bmatrix} 0.826355 & -0.341543 \\ -0.341543 & -0.369063 \end{bmatrix} \qquad (Ae.9)$$

Step 2.

As before, the formula for the step function (A.27):

$$\mathbf{x}^{(2)} = \begin{bmatrix} x_1^{(2)} \\ x_2^{(2)} \end{bmatrix} = \begin{bmatrix} 1.873315 \\ 1.482476 \end{bmatrix} - \lambda^{*(1)} \begin{bmatrix} 3.947213 \\ -2.339044 \end{bmatrix} \qquad (Ae.10)$$

The step size:

$$f(\mathbf{x}^{(2)}) = 2.328851 - 21.051708\ \lambda^{*(1)} + 47.574360\ (\lambda^{*(1)})^2 \qquad (Ae.11)$$

and,

$$\frac{d\, f(\mathbf{x}^{(2)})}{d\, \lambda^{*(1)}} = 0 = -21.051708 + 95.148720\, \lambda^{*(1)} \qquad (Ae.12)$$

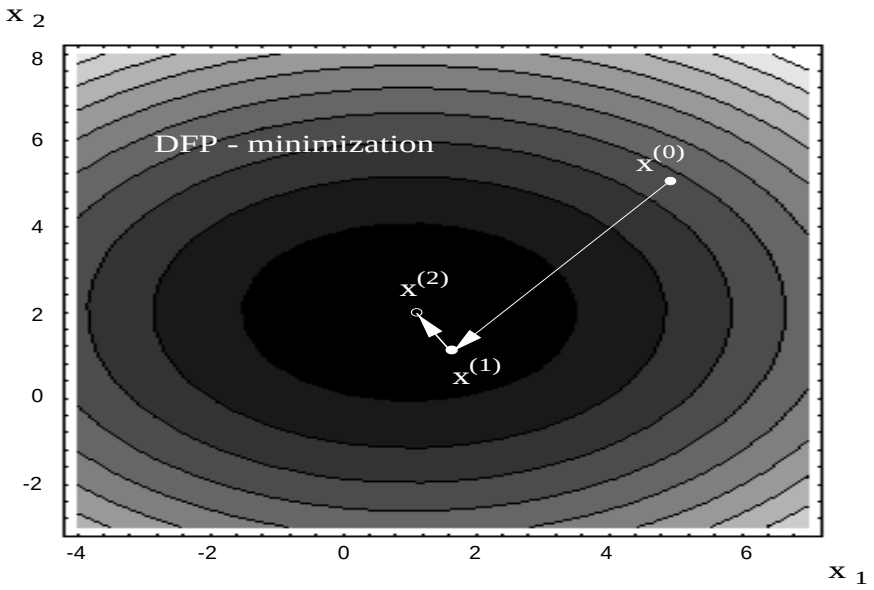

Figure A.2 Steps in minimization of function $f(x_1, x_2) = 2\,(x_1 - 1)^2 + 3\,(x_2 - 2)^2$ using DFP-algorithm.

Such that, $\lambda^{*(1)} = 0.220707$. The second iteration point becomes:

$$\mathbf{x}^{(2)} \equiv \begin{bmatrix} x_1^{(2)} \\ x_2^{(2)} \end{bmatrix} = \begin{bmatrix} 1.002140 \\ 1.998700 \end{bmatrix} \qquad (Ae.13)$$

The other relevant results:

$$f(\mathbf{x}^{(2)}) = 1.4236 \times 10^{-5} \qquad \Delta\mathbf{x}^{(1)} = \begin{bmatrix} -0.871175 \\ 0.516224 \end{bmatrix} \qquad \nabla f(\mathbf{x}^{(2)}) = \begin{bmatrix} 0.00856 \\ -0.00780 \end{bmatrix}$$

$$\Delta\mathbf{g}^{(1)} = \begin{bmatrix} -3.4847 \\ -3.1129 \end{bmatrix} \qquad \mathbf{\Psi}^{(1)} = \begin{bmatrix} 0.826355 & -0.341543 \\ -0.341543 & -0.369063 \end{bmatrix} \qquad (Ae.14)$$

The second inverse hessian update leads to:

$$\Delta\mathbf{\Psi}^{(1)} = \begin{bmatrix} -0.5764 & -0.3415 \\ -0.3415 & -0.2024 \end{bmatrix} \qquad (Ae.15)$$

or,

$$\mathbf{\Psi}^{(2)} = \begin{bmatrix} 0.250 & -2.78 \times 10^{-11} \\ -2.78 \times 10^{-11} & -0.16667 \end{bmatrix} \qquad (Ae.16)$$

Thus,

$$\mathbf{x}^{(3)} = [1.00 \quad 2.00] \qquad f(\mathbf{x}^{(3)}) = 6.71 \times 10^{-15}$$

Discussion.

Even this simple example shows some general behaviour of DFP (and other quasi-Newton) iterations. The function values become minimized much faster well before the iteration point reaches the desired optimal value point. The fact that in this demonstration we reached the minimum in three steps is the result of the given function $f(\mathbf{x})$ being quadratic. Indeed, quasi-Newton methods on each iteration select the direction of the appropriate conjugate directions (similar to Conjugate Gradient methods that were not considered here) and, in case of two-dimensional function there are just two of such directions.

REFERENCES

1. R.J. Charlson, S.E. Schwartz, J.M. Hales, R.D. Cess, J.A. Coakley, J.E. Hansen & D.J. Hofmann, "Climate Forcing by Anthropogenic Aerosols," *Science* 255 (1992), 423–430.

2. S. E. Schwartz, "Are global cloud albedo and climate controlled by marine phytoplankton," *Nature* 336 (1988), 441–445.

3. J. L. Sarmiento, T. M. C. Hughes, R. J. Stouffer & S. Manabe, "Simulated Response of the Ocean Carbon Cycle to Anthropogenic Climate Warming," *Nature* 393 (1998), 245–249.

4. G.A. d'Almeida, P. Koepke & E.P. Shettle, *Atmospheric Aerosols — Global Climatology and Radiative Characteristics*, A. Deepak Publishing, Hampton, VA, 1991.

5. J. E. Hansen & A. A. Lacis, "Sun and Dust versus Greenhouse Gases: an assessment of their relative roles in Global Climate Change," *Nature* 364 (1990), 713–719.

6. H.R. Gordon, D.K. Clark, J.L. Mueller & W.A. Hovis, "Phytoplankton pigments derived from the Nimbus–7 CZCS: initial comparisons with surface measurements," *Science* 210 (1980), 63–66.

7. O.B. Brown, R.H. Evans, J.W. Brown, H.R. Gordon, R.C. Smith & K.S. Baker, "Phytoplankton Blooming of the U.S. East Coast: A Satellite Description," *Science* 229 (1985), 163–167.

8. Stanford B. Hooker, Wayne E. Esaias, Gene C. Feldman, Watson W. Gregg & Charles R. McClain, *SeaWiFS Technical Report Series: Volume 1, An Overview of SeaWiFS and Ocean Color*, NASA, Greenbelt, MD, Technical Memorandum 104566, July 1992.

9. Vincent V. Salomonson, W. L. Barnes, Peter W. Maymon, Harry E. Montgomery & Harvey Ostrow, "MODIS: Advanced Facility Instrument for Studies of the Earth as a System," *IEEE Geosci. Rem. Sens.* 27 (1989), 145–152.

10. P.Y. Deschamps, F.M. Bréon, M. Leroy, A. Podaire, A. Bricaud, J.C. Buriez & G. Sèze, "The POLDER Mission: Instrument characteristics and scientific objectives," *IEEE Trans. Geoscience and Remote Sensing* 32 (1994), 598–615.

11. H.R. Gordon & M. Wang, "Retrieval of water-leaving radiance and aerosol optical thickness over the oceans with SeaWiFS: A preliminary algorithm," *Applied Optics* 33 (1994), 443–452.

12. H.R. Gordon, T. Du & T. Zhang, "Remote Sensing of Ocean Color and Aerosol properties: resolving the Issue of Aeosol Absorption," *Applied Optics* 36 (1997), 8670–8684.

13. A. Morel & L. Prieur, "Analysis of Variations in Ocean Color," *Limnology and Oceanography* 22 (1977), 709–722.

14. E.P. Shettle & R.W. Fenn, "Models for the Aerosols of the Lower Atmosphere and the Effects of Humidity Variations on Their Optical Properties," Air Force Geophysics Laboratory, Hanscomb AFB, MA 01731, AFGL–TR–79-0214, 1979.

15. H.R. Gordon, O.B. Brown, R.H. Evans, J.W. Brown, R.C. Smith, K.S. Baker & D.K. Clark, "A Semi-Analytic Radiance Model of Ocean Color," *Jour. Geophys. Res.* 93D (1988), 10909–10924.

16. F. Zhao & T. Nakajima, "Simultaneous Determination of Water-Leaving Reflectance and Aeosol Optical Thickness from Coastal Zone Color Scanner Measurements," *Applied Optics* 36 (1997), 6949–6956.

17. S. Chandrasekhar, *Radiative Transfer*, Oxford University Press, Oxford, 1950, 393 pp.

18. H.C. van de Hulst, *Multiple Light Scattering*, Academic Press, New York, 1980, 739 pp.

19. A. Bucholtz, "Rayleigh-scattering calsulations for the Terrestrial Atmosphere," *Applied Optics* 34 (1995), 2765–2773.

20. COESA, "U.S. Standard Atmosphere Supplements, 1976," U.S. Government Printing Office, Washington, D.C. 1976.

21. COESA, "U.S. Standard Atmosphere 1976," U.S. Government Printing Office, Washington, D.C. 1976.

22. H.R. Gordon, J.W. Brown & R.H. Evans, "Exact Rayleigh Scattering Calculations for use with the Nimbus-7 Coastal Zone Color Scanner," *Applied Optics* 27 (1988), 862–871.

23. G. Mie, "Beiträge zur Optik trüber Medien, speziell kollidalen Metall-lösungen," *Ann. Phys.* 25 (1908), 377–445.

24. M. Kerker, *ICES Electromagnetic Scattering, Vol. 5*, Pergamon Press, New York, 1963, 592 pp.

25. M.I. Mishchenko & L.D. Travis, "Light scattering by polydispersions of randomly oriented spheroids with sizes comparable to wavelengths of observation," *Applied Optics* 33 (1994), 7206–7225.

26. L. Elterman, "UV, Visible, and IR Attenuation for Altitudes to 50 km, 1968," AFCRL, Bedford, MA, Report AFCRL-68-0153, April 1968.

27. L. Elterman, "Vertical Attenuation Model with Eight Surface Meteorological Ranges 2 to 13 Kilometers," AFCRL, Bedford, MA, Report AFCRL-70-0200, March 1970.

28. D. Deirmendjan, "Scattering and Polarization properties of Polydispersed Suspensions with Partial Absorption," *Quart. J. R. Met. Soc.* 85 (1960).

29. H.R. Gordon, *personal communication.*

30. H. Yang & H.R. Gordon, "Remote Sensing of ocean color: assessment of water-leaving bidirectional effects on atmospheric diffuse transmittance," *Applied Optics* 36 (1997), 7887–7897.

31. H.R. Gordon & D.K. Clark, "Clear water radiances for atmospheric correction of coastal zone color scanner imagery," *Applied Optics* 20 (1981), 4175–4180.

32. A. Morel, "In-water and Remote Measurement of Ocean Color," *Boundary-Layer Meteorology* 18 (1980), 177–201.

33. A. Bricaud, A. Morel & L. Prieur, "Optical Efficiency Factors of Some Phytoplankters," *Limnology and Oceanography* 28 (1983), 816–832.

34. H.R. Gordon & A.Y. Morel, *Remote Assessment of Ocean Color for Interpretation of Satellite Visible Imagery: A Review*, Springer-Verlag, New York, 1983, 114 pp.

35. R. Fletcher, *Practical Methods of Optimization* Vol.1,2, John Wiley and Sons, Ltd., 1980.

36. P. E. Gill & W. Murray, "Quasi-Newton Methods for uncostrained optimization," *J. Inst. Maths. Appl.* **9** (1972), 91–108.

37. M. J. D. Powell, "Some global convergence properties of a variable metric algorithm for minimization without exact line searches," Atomic Energy Research Establishment, Harwell, Oxfordshire, UK, 1975, AERE Harwell Report CSS15, 1975.

38. Yu. G. Evtushenko, *Numerical Optimization Techniques*, Springer-Verlag NY Inc., 1985.

39. IMSL, *Reference Manual* Vol.4, IMSL Inc., 1982.

40. H.R. Gordon, 1996, Atmospheric Correction of Ocean Color Imagery in the Earth Observing System Era, submitted to Jour. Geophys. Res..

41. W. H. Press, S. A. Teukolsky, W. T. Vetterling & B. P. Fannery, *Numerical Recipes in FORTRAN: The Art of Scientific Computing*, Cambridge University Press, New York, NY, 1992.

42. H.R. Gordon, "In-orbit calibration strategy for ocean color sensors," *Remote Sensing Environ.* 63 (1998), 265–278.

43. K. Ding & H.R. Gordon, "Analysis of the influence of O_2 A-band absorption on atmospheric correction of ocean color imagery," *Applied Optics* 34 (1995), 2068–2080.

44. "SeaDAS: the SeaWiFS Data Analysis System,"1998, Proceedings of the 4th Pacific Ocean Remote Sensing Conference, Qingdao, China, July 28-31, 1998.

45. Y.J. Kaufman, D. Tanré, H.R. Gordon, T. Nakajima, J. Lenoble, R. Frouin, H. Grassl, B.M. Herman, M.D. King & P.M. Teillet, "Passive Remote Sensing of Tropospheric Aerosol and Atmospheric Corrections of the aerosol Effect,"*Jour. Geophys. Res.* 102D (1997), 16815–16830.

46. J. Ponstein, "Seven Kinds of Convexity,"*SIAM Review* 9 (1967), 115–119.

47. M. J. D. Powell, *Approximation Theory and Methods*, Cambridge University Press, 1981.

48. P. Wolfe, "Convergence Conditions for Ascend Methods. II: some corrections.,"*SIAM Review* 13 (1971), 185–188.

49. D.M. Hwang & C.T. Kelley, "Convergence of Broyden's Method in Banach Spaces,"*SIAM J. Optimization* 2 (1992), 505–532.

50. L. Armijo, "Minimization of Functions having Lipshitz Continuous First Partial Derivatives,"*Pacific Journal of Mathematics* 16 (1966), 1–3.

Table of Contents

APPENDIX III

Spectral Reflectance of Whitecaps: Their Contribution to Water-Leaving Radiance

Karl D. Moore, Kenneth J. Voss, Howard R. Gordon

Physics Dept., University of Miami

Coral Gables, FL 33124

Submitted to

Journal of Geophysical Research

Abstract

A radiometric system, deployed from a ship, is used to measure directly the influence of the presence of breaking waves (whitecaps) on the upwelling radiance above the sea surface. Estimates of their remote-sensing augmented spectral reflectance, i.e., the temporally-averaged or spatially-averaged *increase* in the ocean's reflectance over and above the reflectance in the absence of breaking waves, are provided from measurements in the Tropical Pacific. The accuracy of these estimates is dependent on the ability to determine radiometrically the background reflectance of the water. In the visible, the remote-sensing augmented spectral reflectance of whitecaps measured in the open ocean is found to be essentially independent of wavelength, ~0.001 at a wind speed of ~9 m/s, and ~0.002 at ~12 m/s. This is a factor of ~2.5 *less* than predicted earlier based on the statistical relationship between fractional coverage and wind speed, and the estimated average reflectance of individual whitecaps. In the near infrared (860 nm), the remote-sensing augmented spectral reflectance falls to 80% of its value in the visible.

Introduction

Due to the relatively small radiance backscattered into the atmosphere from below the ocean surface (the water-leaving radiance) in comparison to the total light arriving at a space-borne ocean-color sensor, the usefulness of ocean color data depends primarily on the accuracy of atmospheric correction algorithms [*Gordon and Morel,* 1983]. Atmospheric correction over the ocean is effected by measurement of the upwelling signal arriving at the satellite at spectral bands where the radiance backscattered out of the ocean is known to contribute very little or no signal [*Gordon and Wang*, 1994a]. Utilization of spectral bands beyond ~740 nm in Case 1 waters, i.e., waters in which the optical properties are determined by phytoplankton, their decay products, and the water itself [*Gordon and Morel*, 1983], can be justified in the absence of whitecaps due to the strong absorption properties of liquid water in the near infrared (NIR). When waves break on the sea surface, the presence of the resulting whitecaps occurring within a satellite image pixel increases the radiometric signal by an amount dependent on the whitecap coverage and their reflectance. This increase in apparent surface reflectance *over and above* that in the absence of breaking waves is referred to here as the *augmented reflectance*. [In this paper, we consider whitecaps to be any near-surface manifestation that results from breaking waves. Such manifestations include what could be called subjectively, “thick foam” (a lattice of bubbles floating on the sea surface), “thin foam” (a single layer of bubbles on the surface), and “subsurface bubbles” (air injected into the water during the breaking process). They do not include surface roughness normally associated with “sun glitter.” Historically, the whitecap coverage (or fractional coverage) was usually taken to be the fraction of the sea surface covered by thick foam.] Previous researchers have used a whitecap reflectance of 50% - 100% [*Payne*, 1972; *Maul and Gordon* , 1975; *Gordon and Jacobs* , 1977] and have assumed it to be constant at all wavelengths. Laboratory measurements carried out by *Whitlock et al.* [1982] yielded a value of ~55% in the visible part of the spectrum for thick foam in clear water, and showed that it diminishes with increasing wavelength beyond ~0.8 μm, with 5% decrease at 0.85 μm, 10% at 1.02 μm , and 50% at 1.65 μm. *Koepke* [1984] determined the effective reflectance of whitecaps

to be 22% in the visible, taking into consideration the decrease in reflectance and increase in area of an individual whitecap as it ages. He then combined this wavelength-independent estimate of the effective reflectance with the fractional area of the sea surface covered with whitecaps as a function of wind speed [*Monahan and O'Muircheartaigh*, 1980] to obtain the overall reflectance of whitecaps for different wind speeds. Using Koepke's model for the reflectance as a function of wind speed, and the *Whitlock et al.* [1982] spectral variation of foam reflectance, *Gordon and Wang*, [1994b] carried out simulations that suggested that adequate atmospheric correction of ocean color sensors could be made at wind speeds ~10-12 m/s even in the presence of large errors (~factor of 2) in estimating the contribution to the sensor radiance due to whitecaps.

Recently, field measurements of the reflectance of foam generated by breaking waves in the surf zone [*Frouin et al*., 1996] indicated a larger spectral variation in reflectance than reported by *Whitlock et al*. [1982]. *Frouin et al*. [1996] found the reflectance decreased by 40% at 0.87 μm, 50% at 1.02 μm, and 95% at 1.65 μm relative to the reflectance at 440 nm. The greater spectral variation in reflectance found in their field data, when compared to the laboratory foam measurements of Whitlock, is thought to be due to the strong absorption properties of water at the longer wavelengths. This absorption attenuates light reflected from submerged bubbles that are forced into the water column by the breaking waves. Using the spectral variation reported by *Frouin et al*. [1996], *Gordon* [1997] recomputed their influence on atmospheric correction and found whitecaps to be a far more serious problem than *Gordon and Wang* [1994b].

In addition to the spectral differences between foam measured in the laboratory and in the field, estimates of whitecap fractional coverage for different wind speeds are found to be quite noisy [*Blanchard*, 1971*; Monahan*, 1971*; Ross and Cardone*, 1974; *Wu* , 1979; *Toba and Chaen*, 1973; *Monahan and O'Muircheartaigh*, 1980,1986]. Typically, fractional coverage (W) has been related to wind speed (U) through an equation of the form $W = \alpha U^{\beta}$. The values of α and β vary with geographic location, air and sea temperature as well as wind speed range. These relationships remain noisy, despite attempts to fine tune particular data sets, due to the dynamic nature and interdependence of the many parameters involved in whitecap formation. Whitecap coverage is primarily dependent on wind speed, but also on other factors such as fetch and duration [*Cardone*, 1969], water temperature [*Miyake and Abe*, 1948], air temperature, stability of the lower atmosphere defined by the air/water temperature differential [*Monahan and O'Muircheartaigh*, 1986], salinity [*Monahan and Zietlow*, 1969], and even surface tension variations due to the presence of organic films [*Garrett*, 1967]. A slightly different approach by *Wu* [1988] relates whitecap coverage to wind-friction velocity, being proportional to the square root of the wind stress which depends strongly on atmospheric stability conditions. *Bortkovskii and Novak* [1993] assessed whitecap and foam coverage with particular dependence on the sea surface temperature which effects sea water viscosity and wind friction.

To date, the influence of whitecaps on the upwelling water-leaving radiance has been estimated by utilizing and combining the work of different researchers as described above. In this paper, a measurement system deployed from a ship is used to directly determine the augmented spectral reflectance resulting from the presence of breaking waves on the sea surface. Our measurement system provides spectral reflectance data from individual whitecaps — in various stages of growth and decay — and, by integrating over time, estimates of the augmented

spectral reflectance relevant to remote sensing can be determined. The principal reason we undertook the present investigation was to see if the *Frouin et al.* [1996] spectral measurements in the surf zone were applicable to real oceanic whitecaps. A secondary motivation was to validate the whitecap reflectance versus wind speed relationship proposed by *Koepke* [1984].

Instrument System

The whitecap reflectance measurement system is described in detail elsewhere [*Moore et al*., 1998]. The system consists of a 6-channel radiometer with narrow field of view and bands with a nominal 10 nm spectral width centered at 410, 440, 510, 550, 670 and 860 nm. It is held over the water surface by means of a boom extended from the bow of a ship providing an unobstructed view of the water surface. The field of view (FOV) of an individual channel on the sea surface is ~14 cm in diameter. Simultaneously, a deck unit with a cosine collector and matching spectral bands measures downwelling irradiance so that the reflectance of the water surface can be calculated. A TV camera is mounted next to the radiometer to provide a visual reference, and whenever the radiometric data are acquired the associated video frame is time and date marked and recorded onto video tape to assist in later analysis. Air and water temperature, wind speed and direction are measured simultaneously with the radiometric data at a rate of ~7 times a second continuously for about 30 seconds (providing 200 contiguous samples), after which global positioning (GPS) data, universal time, and location are recorded. This acquisition sequence is repeated until a time determined by the operator. This radiometric rate allows several sample points of a large individual whitecap to be captured as well as providing an adequate data set over a time period of reasonably constant sea state and sky conditions. However, note that for a ship speed of 10 kts (5 m/s) the samples are ~70 cm apart, so the radiometer will rarely view the same area of the ocean surface twice.

Once the system has been installed on a ship, only periodic measurements of the dark current are necessary. This requires bringing the radiometer in from the boom and covering both the radiometer and the deck cell with light tight caps. This is necessary only when significant temperature changes are encountered such as when conditions change from early morning to noon, or from dark, overcast, rainy conditions to bright sunshine. The radiometer can also be angled up to 20 deg. from nadir in order to minimize the effects of specular sun and sky glitter.

The purpose of the video camera was to remove events attributable to sun glitter from the analysis. Unfortunately, separating whitecaps from sun glitter was much more difficult than anticipated, and usually could not be done acccurately. Thus, most of the data reported here were acquired under overcast conditions (no sun glitter).

Data Description

Data used in this paper are from a ~6,000 km transit through equatorial waters of the Pacific Ocean from Manzanillo, Mexico (19.03 deg. N, 104.20 deg. W) to Honolulu, Hawaii (21.20 deg. N, 157.55 deg. W). This 13-day cruise took place in November 1996 abroad the NOAA ship R/V Ka'imimoana. Conditions were uniform with air/water temperature and wind speed/direction changing only by a relatively small amount over time. Fetch was typically greater than 1000 km

and duration could be considered unlimited. Data were acquired far from land and for the most part, water temperature was ~22-23C with air temperature ~20-23C. Wind speeds ranged from ~8 m/s to ~13 m/s and wind direction changed from an initial northerly direction at the beginning of the transect to an easterly and southerly direction as the Trade winds were crossed. Wind speed was constant within 1-2 m/s for days at a time. The sky conditions were mainly broken and scattered with some overcast periods. The data used in the analysis were collected under overcast conditions during 3 days of the transect. Reflectance data were acquired for wind speeds between ~9-12 m/s. Stability of the lower atmosphere, defined by the air temperature / water temperature differential, varied from neutral to slightly unstable.

Data Reduction Procedure

The radiometric data collected were reduced to produce dark background-subtracted and radiometrically-corrected reflectance values, R, from the six up- and downwelling channels. This reflectance is defined as $R(\lambda) = \pi L(\lambda)/E(\lambda)$, where $L(\lambda)$ is the upward radiance leaving the sea surface, and $E(\lambda)$ is the downward irradiance falling onto the sea surface from the sun and sky. If the surface were lambertian (L independent of the viewing direction) then R would be the surface *albedo*. The radiometric correction process consists of three steps [*Moore et al*., 1998] briefly reviewed here.

First: ratios of upwelling radiance to downwelling irradiance are formed from the dark-subtracted signals for each channel. These six ratios are then multiplied by a radiometric absolute calibration factor relating the channels in the radiometer to those in the deck cell. This was established using a calibrated 1000W (FEL) quartz halogen lamp source and a calibrated Spectralon reflectance plaque. The deck cell was positioned 50 cm in front of the source and measurements taken. For the radiometer, the reflectance plaque replaced the deck cell, and the radiometer viewed the plaque at a 45 deg. angle.

Second: a multiplicative factor was used to correct for spectral differences between the radiometer and deck cell and for differences between laboratory and field illumination conditions.

Third: each channel of the deck cell was corrected for solid angle response for operation under natural illumination due to the slight deviation in angular response of the deck cell collector from a true cosine response. Correction factors for different angular distributions of the downwelling light field are required for the various sky conditions that may be encountered. A set of correction factors were established for sky conditions such as overcast, or clear with different solar zenith angles, to correct solid angle response.

After applying these corrections we are left with a time series of spectral reflectance from the sea surface, examples of which are shown in Fig. 1. Figure 1a provides a 15 s record of the reflectance of two whitecaps passing within the radiometer FOV. It shows (1) that all spectral channels have essentially the same view of the whitecap, (2) that the reflectance of the whitecaps

throughout the visible is essentially independent of wavelength, and (3) that the whitecap reflectance at 860 nm is significantly lower than that in the visible, in agreement with the surf-zone observations of *Frouin et al.* [1996]. Figure 1b shows a longer record of the reflectance at 410 nm.

We wish to estimate the augmented reflectance [AR(λ)] associated with each whitecap event recorded in the time series. To automatically discriminate whitecaps and foam from the background reflectance we filtered each data set. The filter works in three steps on each wavelength individually. An example of the process steps is shown in Fig. 2. Because whitecaps are associated with rapid changes in the surface reflectance, the first step is to determine the data points for which the reflectance has changed by ±0.001 from the previous data point. For these data points, we believe there is a whitecap (or whitecap fragment) in the radiometer FOV. After this process is complete and candidate whitecaps have been determined, the background surface and subsurface reflectance must be eliminated. For each whitecap event we subtract the average of the first non-whitecap data point before and after the event. We are then left with individual cases of the enhanced reflectance (the *augmented* reflectance) due to the whitecap event. [This subtraction process inevitably leads to a few events with small *negative* augmented reflectance; however, their contribution to the final result will be negligible.] Finally we eliminate the events for which the augmented reflectance is less than 0.01. This last step, referred to as a threshold, is somewhat arbitrary; however, it results in fractional coverage estimates that are similar to those found by other investigators for similar wind speeds, e.g., *Monahan* [1971]. We will discuss the implications of this step below. Because the Fresnel surface reflectance is a much higher portion of the total reflectance for the red channels, the data are significantly noisier (especially at 860 nm) and this procedure is much less reliable in the red than in the blue channels. This filtering procedure was validated by comparing the video record and the radiometric record. The filter (without the threshold test) passes candidate events that we subjectively consider to be whitecaps; however, it also can pass events that are only associated with changes in reflected skylight (due to the rough nature of the surface). These latter events are completely removed by the thresholding test. Thus, employing only steps 1 and 2, the contribution to the reflectance due to breaking waves will be overestimated. Using the threshold test (step 3) reduces this overestimation, and in fact, may *underestimate* their contribution somewhat.

Within the context of ocean color remote sensing, the remote-sensing augmented reflectance (RSAR(λ)) is simply the increase in the water-leaving radiance (averaged over a single pixel, typically ~1 km^2) due to the presence of breaking waves on the surface. If the remote sensor had sufficient spatial resolution, one could in principle measure RSAR(λ) by subtracting the radiance measured in whitecap-free areas from the radiance averaged over a large number of pixels that include whitecaps and open water, after accounting for the transmission loss in the atmosphere. RSAR is then the average reflectance which the whitecaps have added to the surface reflectance. We attempt to effect the same determination at 410 nm by replacing the spatial average over ~1 km^2 by the time average of AR(410) over an ~14 cm diameter circle on the sea surface. The remote-sensing augmented reflectance at 410 nm was determined from the radiometer record by taking the sum of AR(410) for the reflectance "events" that passed these filters (Fig. 2) and dividing by the total number of records. Using the events that passed steps 1 and 2 of the filter provides an upper limit to RSAR(410) because examination of the video record shows that

events are passed that (subjectively) are not associated with whitecaps. These nonwhitecap events are removed (possibly along with some whitecap-associated events) by the threshold in step 3. Computation of RSAR(410) for the events that passed all three steps of the filter produces a lower limit to the augmented reflectance; however, as comparison with the video record indicated that the first-two steps of the filter often passed nonwhitecap events, we believe the lower limit is closer to the actual augmented reflectance.

We can estimate the fractional coverage, *W*, by simply taking the ratio of the number of records containing events to the total number of records. This estimate will be higher than previous estimates (based on photography [*Monahan, 1971; Koepke, 1984*]) for two reasons: (1) steps 1 and 2 of the filter pass events that are not whitecaps; and (2) a small whitecap that is detected, but does not fill the radiometer FOV, will be included in the estimate of *W* as if it did fill the FOV. For the wind speeds observed here (9-12 m/s), *W* was ~30% for events that passed steps 1 and 2, but fell to ~2-3% for events that passed the threshold as well. This latter range for *W* is more consistent with earlier estimates for these wind speeds.

In Fig. 3, we present RSAR(410), as a function of wind speed, resulting from the analysis of 11 data sets. Each of the 11 data points was for an average acquisition time of 45 minutes. Values of RSAR(410) that result from employing all three steps of the filter are indicated by the large triangles (▲). To determine if the threshold in our filter was eliminating too much data, we also looked at RSAR(410) for which the threshold filter was set to 0. In other words we accepted all data for which the change in reflectance was greater than 0.001 from the previous point and for which the reflectance, after subtracting the background, was greater than zero. By comparison with the video records, this procedure appeared to include many low reflectance, nonwhitecap events, and should be a very conservative upper estimate of RSAR(410). Note that in this case the fractional coverage estimate increases to 30%, obviously too high, even considering the nature of the sampling. RSAR(410) for the zero threshold case is shown in Fig. 3 as our upper limit (small filled triangles: ▼).

To relate augmented reflectance to wind speed the power law relationship of *Koepke* [1984] has been modified from $RSAR(410) = 6.49 \times 10^{-7}\ U^{3.52}$ to $RSAR(410) = 0.4 \times 6.49 \times 10^{-7}\ U^{3.52}$, where *U* is the wind speed in meters per second. This is the lower solid line in Fig. 3. Possible correlations between the augmented reflectance and other parameters such as water temperature, air temperature, stability of the lower atmosphere, humidity, salinity, barometric pressure, wave height, sea swell were investigated. None could be established mainly due to the small variation in the parameters during the transect.

Because the filter scheme did not work reliably for the red wavelengths, another technique was used to determine the spectral variation of $AR(\lambda)$. This was accomplished by passing the record for the wavelength λ through the first two steps of the filter and comparing the result with the record for the 410 nm band passed through all three steps of the filter. If the filtered 410 nm band record indicated a whitecap, its augmented reflectance along with the augmented reflectance of the same event in the λ band were recorded. Figure 4 compares the values of $AR(\lambda)$ and AR(410) for individual events for one of the records that we examined. For each λ (except 860 nm) the line on the figure is a 1:1 line. The noisy appearance in these figures is

partially due to the fact that each channel looks at a slightly different part of the surface. Clearly, for all channels (except 860 nm) the data fall near the 1:1 line. For 860 nm, the line shown is a least-squares fit (to an exponential) to the data. It clearly follows the 1:1 line reasonably well for low AR; however, for large AR, AR(860) is significantly less than AR(410). The depression of AR(860) at large values is similar to that noted by *Frouin et al.* [1996] for breaking surface and *Moore et al.* [1998] for ship wakes.

Clearly, this analysis suggests that the reflectance of whitecaps at 860 nm decreases relative to that in the visible and that the fractional decrease is greater at larger AR(λ), i.e., AR(860)/AR(λ) decreases as AR(λ) increases. The brightest whitecaps (here AR(λ)~0.3) show a reflectance decrease of ~50% from the visible to 860 nm. Using the exponential relationship between AR(860) and AR(410) shown in Fig. 4, we can compute RSAR(860) for an entire record using AR(410) for each event to find AR(860), and averaging AR(860) over the record. The result is that for the range 9-12 m/s, RSAR(860)/RSAR(410)≈0.8, with the ratio decreasing slightly as the wind speed increases. As the wind speed increases the occurrence of larger whitecaps increases. These larger whitecaps individually have the lowest ratio of AR(860nm)/AR(410nm), which lowers the overall ratio RSAR(860)/RSAR(410) for that wind speed.

Concluding remarks

We have determined the remote-sensing augmented reflectance in the open ocean for the 410 – 670 nm range to be ≈ 0.001 at a wind speed of 9 m/s, increasing to ≈ 0.002 near 12 m/s (Fig. 3). These values are lower than previously derived values of whitecap optical influence (Fig. 3). Using the *Koepke* [1984] effective reflectance of 22% and the fractional coverage determined by wind speed for water temperature above 14C [*Monahan and O'Muircheartaigh*, 1980] yields values that are greater than 2.5 times our values from 9 to 12 m/s. Applying the fractional coverage relationship which takes into account atmospheric stability [*Monahan and O'Muircheartaigh*, 1986], our results are even lower than those for a stable atmosphere (Fig. 3). However, the *Monahan and O'Muircheartaigh* [1986] model does provide a significantly better fit to the data than the *Koepke* [1984] model. Also, the 860 nm value of RSAR, which will be dependent on the amount and depth of bubbles forced into the water column, is found to be approximately 20% lower than the RSAR in the visible for wind speeds 9-12 m/s in the open ocean. This is approximately half the depression observed by *Frouin et al.* [1996] in the surf zone, suggesting less violent wave breaking is manifest in the open ocean at these wind speeds.

The goal of this study was to determine the augmented reflectance contribution from whitecaps as viewed from satellites and, in particular, its spectral dependence. Although most of our open ocean analysis utilized only data acquired during overcast conditions (to eliminate sun glint), some data for partly cloudy and clear skies were examined. This partly cloudy/clear sky data possessed an augmented reflectance spectrum similar to the overcast cases. Thus, we believe that our RSAR results should be reasonably representative of clear sky situations, and useful for estimating the whitecap contribution to the reflectance measured by ocean color sensors.

Notation

$AR(\lambda)$	augmented reflectance at wavelength λ.
$RSAR(\lambda)$	remote-sensing augmented reflectance at wavelength λ.
T_{air}	air temperature
T_{water}	water surface temperature
ΔT	temperature differential ($\Delta T = T_{water} - T_{air}$)
U	wind speed in meters per second
W	fractional coverage of whitecaps and foam

Acknowledgments. This research was funded by NASA / EOS - MODIS, Goddard Space Flight Center under contract #NAS5-31363. We would like to thank Al Chapin for his help in the design and construction of the equipment. We would like to thank the NOAA personnel: CDR Mark Koehn, CDR Tim Wright, LCDR John Herring, and Dr. Michael McPhaden for allowing us to join their transit aboard the R/V Ka'imimoana.

References

Blanchard, D. C., Whitecaps at sea. *J. Atmos. Sci., 28,* 645, 1971.

Bortkovskii, R. S., and V. A. Novak, Statistical dependencies of sea state characteristics on water temperature and wind-wave age. *J. of Marine Systems*, *4*, 161-169, 1993.

Cardone, V. J., Specification of the wind field distribution in the marine boundary layer for wave forecasting. *Rep. TR 69-1,* Geophys. Sci. Lab., New York Univ., New York, December 1969.

Frouin, R., M. Schwindling and P. Y. Deschamps, Spectral Reflectance of Sea Foam in the Visible and Near Infrared: In Situ Measurements and Remote Sensing Implications. *J. Geophys. Res., 101C,* 14361-14371, 1996.

Garrett, W. D., The influence of surface-active material on the properties of air bubbles at the air/sea interface. *Rep. Naval Research Lab*., 6545, Washington D.C., 14 pp., 1967.

Gordon, H. R, Atmospheric correction of ocean color imagery in the Earth Observing System era. *Jour. Geophys. Res. 102D,* 17081-17106, 1997.

Gordon, H. R., and M. M. Jacobs, Albedo of the Ocean-Atmosphere System: Influence of Sea Foam. *Applied Optics, 16*, 2257-2260, 1977.

Gordon, H. R., and A. Morel, *Remote Assessment of Ocean Color for Interpretation of Satellite Visible Imagery: A* Review, Springer-Verlag, New York, 1983.

Gordon, H. R., and M. Wang, Retrieval of water-leaving radiance and aerosol optical thickness over the oceans with SeaWiFS: A preliminary algorithm, *Applied Optics, 33*, 443-452, 1994a.

Gordon, H. R., and M. Wang, Influence of oceanic whitecaps on atmospheric correction of SeaWiFS, *Applied Optics, 33,* 7754-7763, 1994b.

Koepke, P., Effective Reflectance of Oceanic Whitecaps. *Applied Optics, 23*, 1816-1824, 1984.

Maul, G. A., and H. R. Gordon, On the Use of Earth Resources Technology Satellite (LANDSAT-1) in Optical Oceanography. *Remote Sensing Environment, 4*, 95, 1975.

Miyake, Y., and T. Abe, A study on the foaming of sea water. *J. Marine Res., 7*, 67-73, 1948.

Monahan, E. C., and C. R. Zietlow, Laboratory comparisons of fresh-water and salt-water whitecaps. *J. Geophys. Res., 74,* 6961-6966, 1969.

Monahan, E. C., Oceanic whitecaps. *J. Physical Oceanogr., 1,* 139-144, 1971.

Monahan, E. C., and I. G. O'Muircheartaigh, Optimal power-law description of oceanic whitecap coverage dependence on wind speed. *J. Phys. Oceanogr., 10*, 2094-2099, 1980.

Monahan, E. C., and I. G. O'Muircheartaigh, Whitecaps and passive remote sensing of the ocean surface. *Int. J. Remote Sens., 7*, 627-642, 1986.

Moore, K. D., Voss, K. J., Gordon, H. R., 1997: Spectral reflectance of whitecaps: Instrumentation, calibration and performance in coastal waters. *J. Atmospheric and Oceanic Technology,* 15, 496-509, 1998.

Payne, R. E., Albedo of the Sea Surface. *J. Atmospheric Physics, 29*, 959-970, 1972.

Ross, D. B., and V. J. Cardone, Observations of oceanic whitecaps and their relation to remote measurements of surface wind speed. *J. Geophys. Res., 79*, 444-452, 1974.

Salmonson, V. V., W. L. Barnes, P. W. Maymon, E. H. Montgomery and H. Ostrow, MODIS: Advanced facility instrument for studies of the earth as a system, *IEEE Geosci. Rem. Sens., 27*, 145-152, 1989.

Toba, Y., and M. Chaen, Quantitative expression of the breaking of wind waves on the sea surface. *Rec. Oceanogr. Works, 12*, 1-11, 1973.

Whitlock, C. H., D. S. Bartlett, and E. A. Gurganus, Sea foam reflectance and influence on optimum wavelength for remote sensing of ocean aerosols. *Geophys. Res. Letters, 9*, 719-722, 1982.

Wu, J., Oceanic whitecaps and sea state. *J. Phys. Oceanogr., 9*, 1064-1068, 1979.

Wu, J., Variation of whitecap coverage with wind stress and water temperature. *J. Phys. Oceanogr., 18*, 1448-1453, 1988.

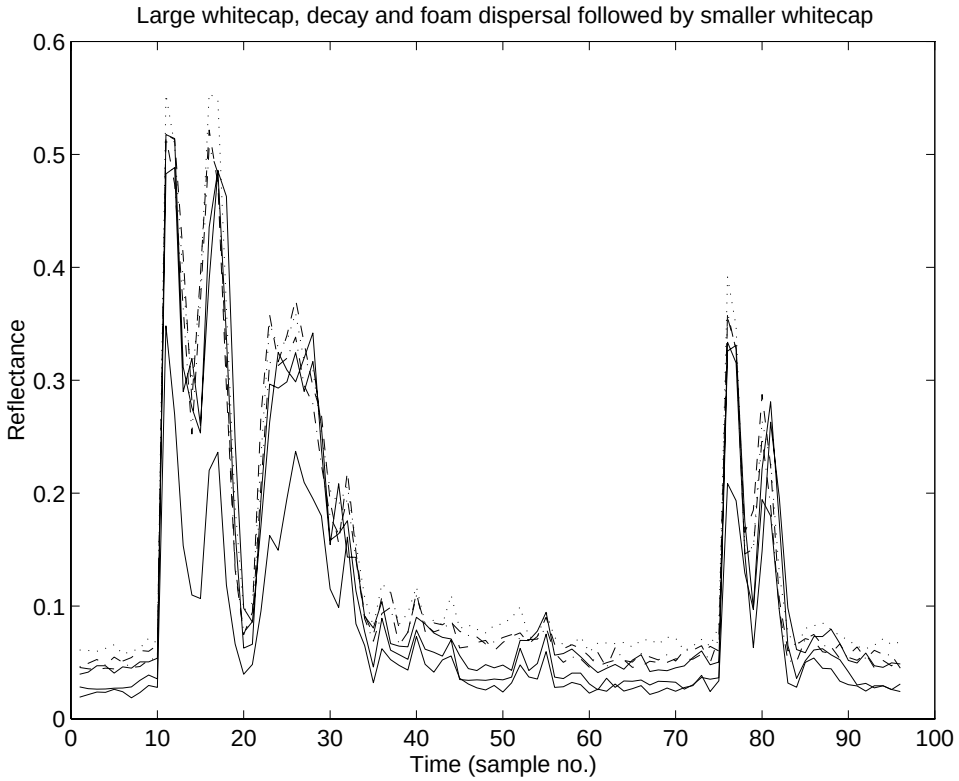

Figure 1a. An approximately 15 second record of the reflectance of two whitecaps passing within the field of view of the radiometer. The lowest line corresponds to 860 nm.

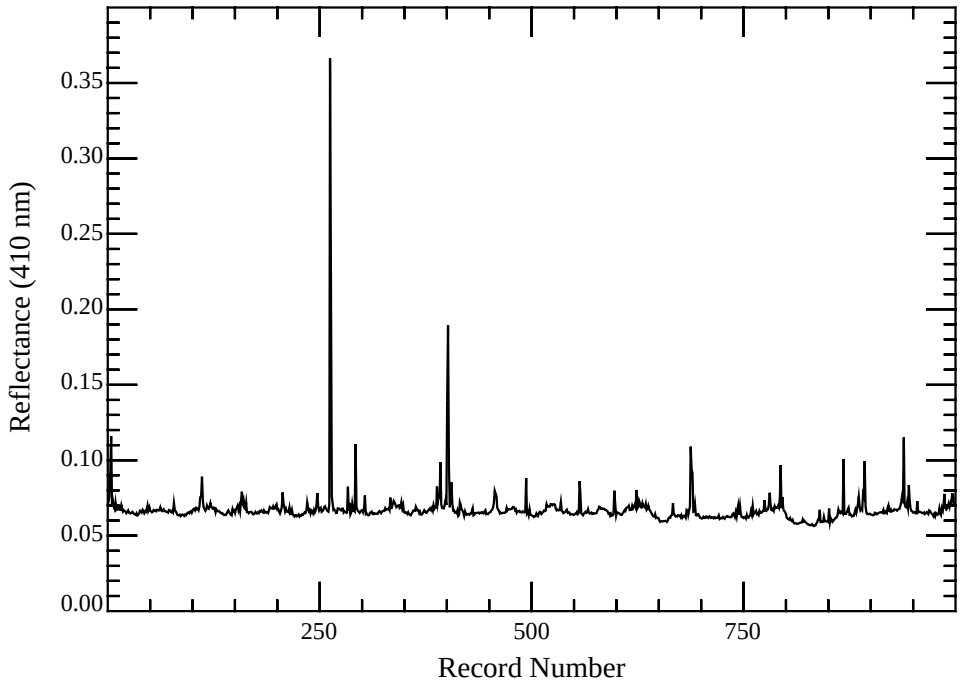

Figure 1b. Time series of the reflectance of the sea surface at 410 nm. The record covers 1000 samples at about 7 samples per second.

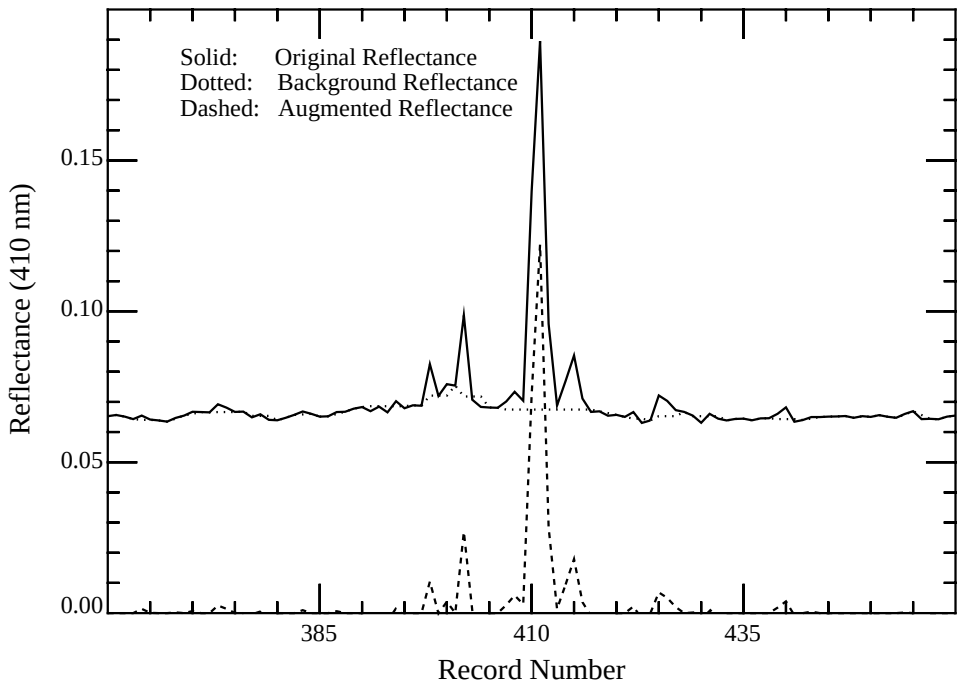

Figure 2. Sample record for Figure 1b showing the operation of the filter at 410 nm. The solid line is the recorded surface reflectance. The dotted line is the background reflectance (reflectance in the absence of whitecaps).

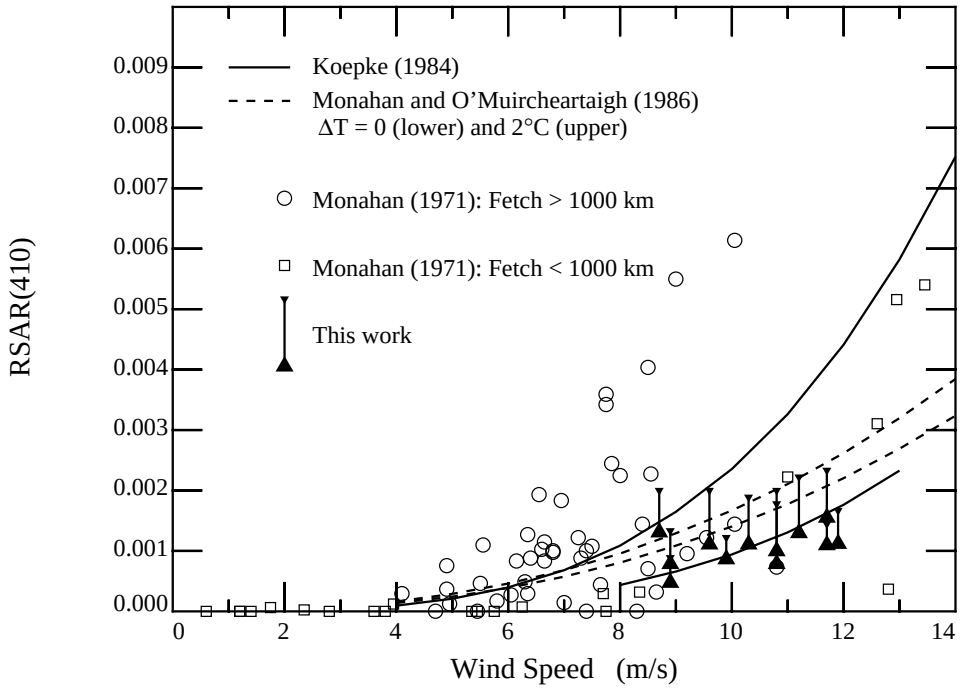

Figure 3. Remote-sensing augmented reflectance of whitecaps at 410 nm. The large solid triangles are our measurements for whitecap events that have passed all three steps of the filter. The small solid triangles are our measurements for events that have passed steps 1 and 2 of the filter (no threshold). The open symbols are the *Monahan* [1971] fractional coverages multiplied by 0.22 (the *Koepke* [1984] effective whitecap reflectance). The upper solid line is the *Koepke* [1984] whitecap reflectance model. The dashed lines are the *Monahan and O'Muircheartaigh* [1986] model (also multiplied by 0.22) for a neutrally stable ($\Delta T = 0°$C, lower dashed line) and an unstable ($\Delta T = 2°$C, upper dashed line). The lower solid line is the *Koepke* [1984] whitecap reflectance model multiplied by 0.4.

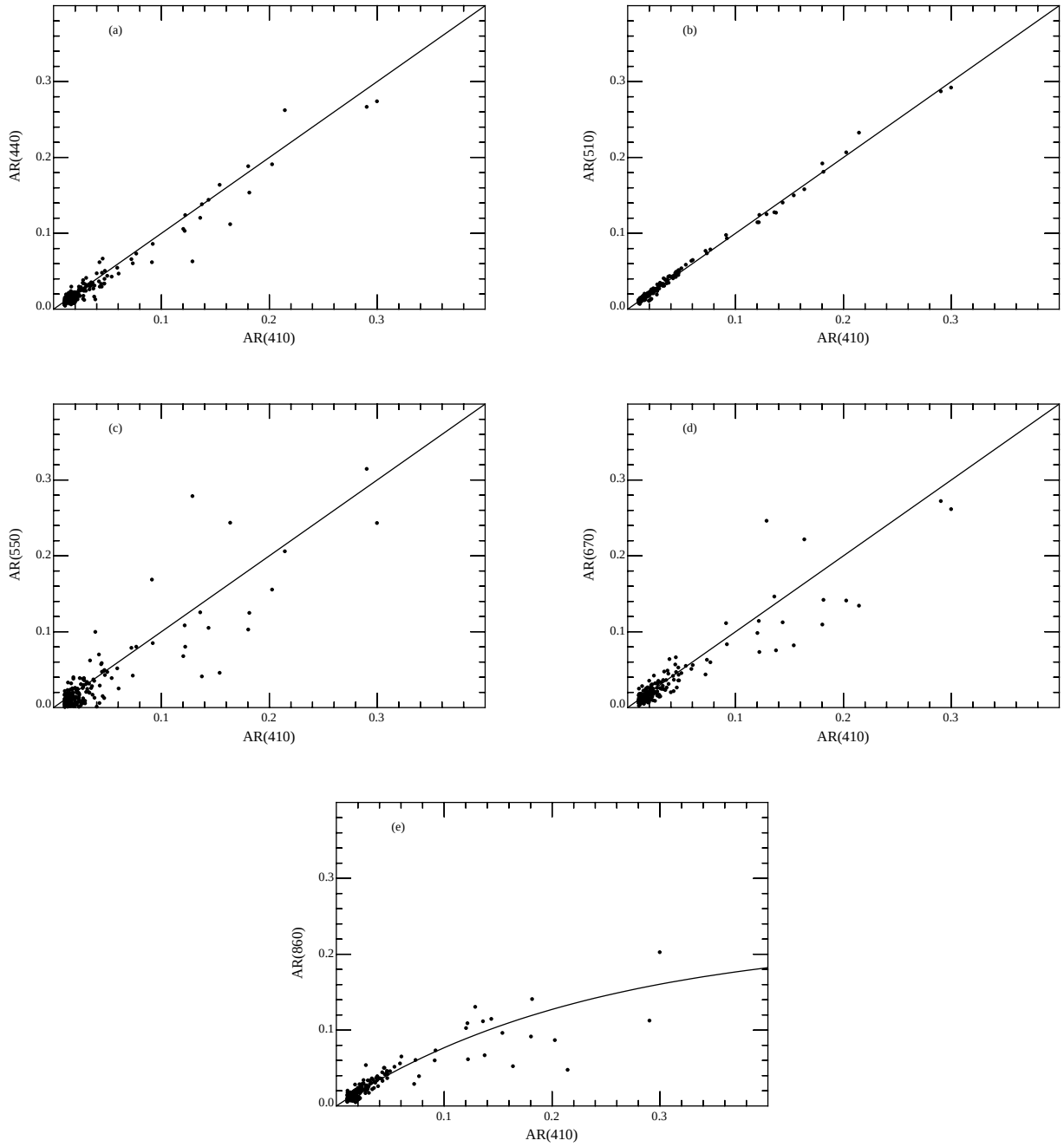

Figure 4. Comparison of $AR(\lambda)$ and $AR(410)$ for individual whitecap events. The solid lines on all graphs [except $AR(860)$ vs. $AR(410)$] are 1:1 lines. For the $AR(860)$ vs. $AR(410)$ graph (e) the curve is given by $AR(860) = 0.22\big[1-\exp[-4.2\,AR(410))]\big]$. (a) $AR(440)$ vs. $AR(410)$; (b) $AR(510)$ vs. $AR(410)$; (c) $AR(550)$ vs. $AR(410)$; (d) $AR(670)$ vs. $AR(410)$; (e) $AR(860)$ vs. $AR(410)$.